

---

**Theoretical and computational investigations of  
electrochemical CO<sub>2</sub> reduction to CO: Effects at  
the interface**

---

PhD Thesis

Technical University of Denmark

Department of Physics

Catalysis Theory Center

Sudarshan Vijay

February 2022



**Theoretical and computational investigations of electrochemical CO<sub>2</sub> reduction to CO: Effects at the interface**

PhD Thesis

**Author**

Sudarshan Vijay

`vijays@fysik.dtu.dk`

**Supervisors**

**Associate Professor Karen Chan**

Catalysis Theory Center

Department of Physics

Technical University of Denmark

`kchan@fysik.dtu.dk`

**Professor Jens Kehlet Nørskov**

Catalysis Theory Center

Department of Physics

Technical University of Denmark

`jkno@dtu.dk`

# Abstract

This PhD thesis presents theoretical and computational approaches to modelling the electrochemical reduction of carbon dioxide (CO<sub>2</sub>R) to carbon monoxide (CO). CO is the simplest product of CO<sub>2</sub>R, but accurately determining its rate limiting step and reaction kinetics across materials remains a challenge. In this thesis, we present a unified view of CO<sub>2</sub>R to CO by developing theoretical and computational models to account for different and sometimes competing effects at the electrochemical interface.

We begin by looking at the electrode side of the reaction by developing an approach to accurately determine adsorption energies, a central quantity to our goal of understanding CO<sub>2</sub>R, directly from temperature programmed desorption (TPD) experiments. Our method fits the long-tail of the TPD curve to an expression for the configurational entropy, allowing us to determine reliable adsorption energies as well as adsorbate-adsorbate interaction parameters and compare them against our computations.

We explore trends in adsorption energies for different intermediates, such as C\* and O\* by developing a model combining the Newns-Anderson model of chemisorption with the orthogonalisation term of the Hammer-Nørskov *d*-band model. By parameterising this model to Density Functional Theory (DFT) calculations, we describe the conditions for adsorption energies of different reacting species to scale with one another.

We then turn to studying two potentially pertinent effects besides those caused by the metal electrode. First, we discuss the effect of interfacial water

on steps and terraces of Gold through *ab-initio* molecular dynamics simulations. We find that including dynamics of interfacial water causes the adsorption of CO to weaken on steps, while staying roughly constant on terraces, contrary to static DFT calculations performed in vacuum.

Second, we study the influence of the interfacial field on the free energy of reaction intermediates of CO<sub>2</sub>R. To include these effects, we develop a computational method to determine the charge transfer coefficient of electrochemical reactions using just the atom-centred forces from a single DFT calculation performed at a saddle point.

We find that a particular group of materials, namely single atoms embedded on graphene, produce large surface dipole moments which interact strongly with the interfacial field. This stabilisation through the surface dipole moments of adsorbed CO<sub>2</sub>, the first reaction intermediate of CO<sub>2</sub>R, leads to specific chemical signatures observed within our model. One such signature is pH dependencies of current densities towards CO. Our predictions of these pH dependencies are in excellent agreement with available experiments, supporting the hypothesis that dipole-field interactions determine the reaction kinetics of CO<sub>2</sub>R. Based on these results, we suggest a general design principle to find more active catalysts for CO<sub>2</sub>R, by looking for materials with narrow width of their *d*-states.

Through a combination of theoretical and computational studies, we determine the reaction mechanism for CO<sub>2</sub>R to CO, as well as the underlying effects which influence a material's activity for this reaction.



## Resumé

Denne ph.d.-afhandling præsenterer teoretiske og beregningsmæssige tilgange til modellering af den elektrokemiske reduktion af kuldioxid ( $\text{CO}_2\text{R}$ ) til kulilte ( $\text{CO}$ ).  $\text{CO}$  er det mest simple produkt af  $\text{CO}_2\text{R}$ , men nøjagtig bestemmelse af dets hastighedsbegrænsende trin og reaktionskinetik på tværs af materialer er fortsat en udfordring. I denne afhandling præsenterer vi et samlet syn på  $\text{CO}_2\text{R}$  til  $\text{CO}$  ved at udvikle teoretiske og beregningsmodeller til at tage højde for forskellige, og i nogle tilfælde konkurrerende, effekter ved den elektrokemiske grænseflade.

Vi behandler først elektrodesiden af reaktionen ved at udvikle en tilgang til nøjagtigt at bestemme adsorptionsenergier, en central størrelse for vores mål om at forstå  $\text{CO}_2\text{R}$ , direkte fra eksperimenter med temperaturprogrammeret desorption (TPD). Vores metode parametriserer den lange hale af TPD-kurven til et udtryk for den konfigurationelle entropi, med hvilken vi kan bestemme pålidelige adsorptionsenergier såvel som adsorbat-adsorbat-interaktionsparametre og sammenligne dem med vores beregninger.

Vi undersøger tendenser i adsorptionsenergier for forskellige mellemprodukter, såsom  $\text{C}^*$  og  $\text{O}^*$ , ved at udvikle en model, der kombinerer Newns-Anderson-modellen for kemisorption med ortogonaliseringsleddet fra Hammer-Nørskov d-båndsmodellen. Ved at parametrisere denne model til Density Functional Theory (DFT) beregninger, kan vi beskrive de nødvendige betingelser for at adsorptionsenergier for forskellige reagerende specier skalerer med hinanden.

Vi beskæftiger os herefter med to potentielt relevante effekter udover dem, der er direkte resultat af metalelektroden. Først diskuterer vi effekten af grænsefladevand på henholdsvis trin og plane overflader af guld gennem ab-initio molekylærdynamik simuleringer. Vi finder, at ved at inkludere grænsefladevands dynamiske egenskaber svækkes adsorptionen af  $\text{CO}$  på trin, mens den forbliver nogenlunde konstant på plane overflader, i modsætning til statiske DFT-beregninger udført i vakuum.

Derudover studerer vi grænsefladefeltets indflydelse på den frie energi af

reaktionsmellemprodukter af  $\text{CO}_2\text{R}$ . For at inkludere disse effekter udvikler vi en beregningsmetode til at bestemme ladningsoverførselskoefficienten for elektrokemiske reaktioner udelukkende ved hjælp af de atomcentrerede kræfter fra en enkelt DFT-beregning udført ved et sadelpunkt.

Vi finder, at en bestemt gruppe af materialer, nemlig enkelte atomer indlejret i grafen, producerer store overfladedipolmomenter, som interagerer stærkt med grænsefladefeltet. Denne stabilisering gennem overfladedipolmomenterne af adsorberet  $\text{CO}_2$ , det første reaktionsmellemprodukt af  $\text{CO}_2\text{R}$ , fører til specifikke kemiske signaturer observeret i vores model. En af disse signaturer er pH-afhængigheden af strømtegheder til  $\text{CO}$ . Vores forudsigelser af disse pH-afhængigheder er i tæt overensstemmelse med tilgængelige eksperimenter, hvilket understøtter hypotesen om, at dipol-felt-interaktioner bestemmer reaktionskinetikken for  $\text{CO}_2\text{R}$ . Baseret på disse resultater foreslår vi et generelt designprincip til at finde mere aktive katalysatorer for  $\text{CO}_2\text{R}$  ved at lede efter materialer med smalle d-tilstande.

Gennem en kombination af teoretiske og beregningsmæssige undersøgelser bestemmer vi reaktionsmekanismen for  $\text{CO}_2\text{R}$  til  $\text{CO}$ , såvel som de underliggende effekter, som påvirker et materiales aktivitet for denne reaktion.

# Preface

This thesis is submitted in partial fulfilment of the PhD degree in Physics at the Technical University of Denmark (DTU). The work presented herein was performed at the Catalysis Theory Center, Technical University of Denmark between March 2019 to February 2022. The studies have been supervised by Karen Chan and Jens K Nørskov. The research leading to these results received funding from the European Union’s Horizon 2020 research and innovation program under grant agreement no. 851441, SELECTCO2, and from the VILLUM Centre for the Science of Sustainable Fuels and Chemicals (no. 9455) from VILLUM FONDEN. Part of the computations reported in this thesis were performed on the Juelich Supercomputing Centre through support from PRACE (project ID: 2020235596).



# Acknowledgments

First, I would like to thank Karen Chan for the support, advice and freedom to work on varied and challenging problems in catalysis during my PhD. Despite the ever-increasing size of her group at the Catalysis Theory Center, she always found the time to discuss science and provide suggestions and ideas about the projects we worked on. I am grateful to Jens Nørskov for his continued mentorship and support, especially when it comes to discussions about the fundamental concepts of catalysis. In particular, I am grateful to both Karen and Jens for inculcating in me an appreciation for catalysis and more broadly, the importance of performing good scientific research. I would also like to thank Thomas Bligaard for his help and support, especially during the last few months of my PhD.

I have learnt a great deal from my peers and colleagues at the Catalysis Theory Center. I benefitted immensely from discussions about electrocatalysis and beyond with Joseph Gauthier, Georg Kastlunger, Hendrik Heenen, Vanessa Bukas and Henrik Kristoffersen. Over the last three years I also had the pleasure of sharing a lively workspace with them as well as Oliver Siig, Ahmed Elnabawy, Sara Kelly, Hector Prats, Kasun Gunasooriya, Anjali Patel, Nitish Govindarajan, Sze-Chun Tsang, Andreas Vishart, Aoni Xu, Mianle Xu, Sihang Liu, Roberto Schimmenti, Hao Li, Megha Anand, Naiwrit Karmodak, Zhenbin Wang, Ang Cao and Christina Abraham. The discussions, scientific or otherwise, made my PhD a lot of fun.

I would like to specially thank Kathrine Nielsen for her help in ensuring

that the administrative aspects of my PhD were always in order, as well as all the support over the last few months. I would also like to acknowledge administrative help from Lone Coe and Marianne Balle during the early stages of my PhD. Special thanks also to Ole Nielsen for his technical support and guidance on the use of computing resource at DTU Physics.

I thoroughly enjoyed my external research stay at the group of Nicola Marzari at École Polytechnique Fédérale de Lausanne. It was a wonderful learning experience, and I am grateful for detailed discussions with Nicola as well as members of his group including Thibault Sohier and Francesco Libbi.

I had the pleasure of collaborating with a few research groups during my PhD. I would like to specially acknowledge Peter Strasser and Wen Ju for their continued collaboration on single atom catalysis, Brian Seger for discussions about electrocatalysis on gold, Hong Li for discussions on Lithium-sulfur batteries and Bingjun Xu and Xiaoxia Chang for collaborations on IR and Raman spectroscopy. I am delighted to acknowledge discussions with Johannes Voss about implementation of root finding procedures in kinetic models.

Finally, I would like to thank my parents for their support not just during my PhD at DTU, but also during other stages of my career.

# List of Publications

## Paper 1

**How to extract adsorption energies, adsorbate-adsorbate interaction parameters, and saturation coverages from temperature programmed desorption experiments**

Sudarshan Vijay, Henrik H. Kristoffersen, Yu Katayama, Yang Shao-Horn, Ib Chorkendorff, Brian Seger and Karen Chan  
Phys. Chem. Chem. Phys., **2021**, 23, 24396-24402

## Paper 2

**Interaction of CO with Gold in an Electrochemical Environment**

Sudarshan Vijay, Thomas V. Hogg, Johan Ehlers, Henrik H. Kristoffersen, Yu Katayama, Yang Shao Horn, Ib Chorkendorff, Karen Chan and Brian Seger  
J. Phys. Chem. C **2021**, 125, 32, 17684-17689

## Paper 3

**Dipole-Field Interactions Determine the CO<sub>2</sub> Reduction Activity of 2D Fe-N-C Single-Atom Catalysts**

Sudarshan Vijay, Joseph A. Gauthier, Hendrik H. Heenen, Vanessa J. Bukas, Henrik H. Kristoffersen, and Karen Chan  
ACS Catal. **2020**, 10, 7826-7835

## **Paper 4**

**Unified mechanistic understanding of CO<sub>2</sub> reduction to CO on transition metal and single atom catalysts**

Sudarshan Vijay, Wen Ju, Sven Brückner, Sze-Chun Tsang, Peter Strasser, Karen Chan

Nat Catal **2021**, 4, 1024-1031

## **Paper 5<sup>1</sup>**

**Limits to scaling relations between adsorption energies?**

Sudarshan Vijay, Karen Chan and Jens K Nørskov

To be submitted.

## **Paper 6<sup>2</sup>**

**Force-based method to determine the potential dependence in electrochemical barriers**

Sudarshan Vijay, Georg Kastlunger, Joseph A. Gauthier, Anjali Patel and Karen Chan.

To be submitted.

---

<sup>1</sup>Part of Chapter 5 of this thesis

<sup>2</sup>Part of Chapter 7 of this thesis



# Contents

<b>Abstract</b>	<b>iii</b>
<b>Resumé</b>	<b>v</b>
<b>Preface</b>	<b>vii</b>
<b>Acknowledgments</b>	<b>ix</b>
<b>List of Publication</b>	<b>xi</b>
<b>List of Figures</b>	<b>xxiv</b>
<b>List of Tables</b>	<b>xxv</b>
<b>1 Introduction</b>	<b>1</b>
1.1 Closing the carbon cycle . . . . .	1
1.2 Electrochemical reduction of CO <sub>2</sub> . . . . .	3
1.3 Outline of Thesis . . . . .	4
<b>2 Theory of heterogeneous catalysis</b>	<b>7</b>
2.1 Potential energy surface: An atomistic view of chemisorption . . .	8
2.2 Electronic structure view of the chemisorption energy . . . . .	9
2.2.1 Newns-Anderson model of chemisorption . . . . .	9
2.2.2 Hammer-Nørskov model . . . . .	16
2.3 Impact of environment on adsorption energies . . . . .	17

2.3.1	Coverage dependence of the chemisorption energy . . . . .	17
2.3.2	Adsorption free energy . . . . .	18
2.4	Adsorption free energy in electrocatalysis . . . . .	21
2.4.1	Dependence on the potential and pH . . . . .	22
2.4.2	Dependence on interfacial field . . . . .	23
2.5	Micro-kinetic modelling . . . . .	23
<b>3</b>	<b>Theory and methods</b>	<b>25</b>
3.1	The electronic structure problem . . . . .	25
3.2	Density functional theory . . . . .	26
3.2.1	Hohenberg-Kohn theorems . . . . .	27
3.2.2	Kohn-Sham framework . . . . .	28
3.2.3	Exchange-correlation energy . . . . .	30
3.2.4	Atom-centred forces . . . . .	31
3.3	Nudged elastic band method . . . . .	32
3.4	<i>ab-initio</i> molecular dynamics . . . . .	33
<b>4</b>	<b>Benchmark of DFT adsorption energies with temperature programmed desorption (TPD)</b>	<b>35</b>
4.1	Introduction . . . . .	36
4.2	Background on TPD . . . . .	37
4.3	Summary of procedure . . . . .	39
4.4	CO adsorption on gold . . . . .	40
4.4.1	Illustration of fitting procedure . . . . .	40
4.4.2	Equilibrium coverages from TPD . . . . .	43
4.4.3	Benchmark of exchange correlation functionals . . . . .	46
4.5	Water adsorption on gold . . . . .	48
4.6	CO adsorption on metal-doped graphene . . . . .	50
4.7	Conclusion and outlook . . . . .	51
4.8	Computational methods . . . . .	51

<b>5</b>	<b>Scaling relations with the Newns-Anderson and <math>d</math>-band model</b>	<b>53</b>
5.1	Introduction . . . . .	53
5.2	Model development . . . . .	55
5.2.1	Hybridisation with $sp$ and $d$ states of the metal . . . . .	56
5.2.2	Orthogonalisation energy . . . . .	59
5.2.3	Comparison with previous models of chemisorption . . . . .	61
5.3	Results and discussion . . . . .	64
5.3.1	Chemisorption energies of carbon and oxygen do not scale . . . . .	64
5.3.2	Parameterisation of model . . . . .	65
5.3.3	Saturation of energy causes scatter in scaling relations . . . . .	68
5.4	Conclusion . . . . .	71
5.5	Computational methods . . . . .	72
5.A	Appendix: Continuous variation of parameters . . . . .	73
<b>6</b>	<b>Impact of interfacial water on adsorption energies</b>	<b>75</b>
6.1	Introduction . . . . .	76
6.2	Revisiting CO adsorption on gold . . . . .	78
6.3	Pb adsorption on gold . . . . .	80
6.4	Simultaneous water and CO adsorption . . . . .	83
6.5	Conclusion . . . . .	84
6.6	Computational methods . . . . .	85
<b>7</b>	<b>Charge transfer coefficients from atom-centered forces</b>	<b>87</b>
7.1	Introduction . . . . .	87
7.2	Extrapolation procedures in practice . . . . .	90
7.3	Model development . . . . .	92
7.4	Application to electrocatalytic reactions . . . . .	97
7.5	Conclusion . . . . .	100
7.6	Computational Methods . . . . .	101
<b>8</b>	<b>Dipole-field interactions in CO<sub>2</sub>R</b>	<b>103</b>
8.1	Introduction . . . . .	103

8.2	CO adsorption energies . . . . .	105
8.3	Electron transfer on MNC catalysts . . . . .	107
8.4	Potential dependent reaction energies . . . . .	109
8.5	Kinetic modelling of CO <sub>2</sub> R . . . . .	113
8.5.1	FeNC catalysts . . . . .	114
8.5.2	Au, NiNC and CoPc catalysts . . . . .	115
8.5.3	Activity volcano of CO <sub>2</sub> R to CO . . . . .	117
8.6	Role of surface dipole moments . . . . .	119
8.7	Conclusion and outlook . . . . .	120
8.8	Computational methods . . . . .	121
<b>9</b>	<b>Final remarks</b>	<b>123</b>
	<b>Bibliography</b>	<b>125</b>
<b>10</b>	<b>Included publications</b>	<b>141</b>
10.1	Paper 1 . . . . .	141
10.2	Paper 2 . . . . .	149
10.3	Paper 3 . . . . .	156
10.4	Paper 4 . . . . .	167

# List of Figures

1.1	a) Observed increase in global temperatures across two centuries taken from Ref [1]. b) Cost of electricity based on solar and wind [3, 4]. . . . .	2
1.2	Schematic of an electrochemical cell; the negatively charged cathode is used to convert CO <sub>2</sub> to CO while the anode performs a counter reaction. . . . .	3
2.1	Potential energy surface for CO <sub>2</sub> adsorption on the ontop site of a Pt(111) surface. The $x$ -axis is the distance between the uppermost Pt atom and the C atom, while the O – C – O angle is shown on the $y$ -axis. All other degrees of freedom are kept fixed. . . . .	9
2.2	Schematic of the semi-infinite chain model, $a$ is the adsorbate with interacts with the metal through one metal atom $k_1$ , which is on one end of an infinitely long metal chain $k_1, k_2, \dots$ with coupling element $\beta$ . . . . .	12
2.3	Representative adsorbate density of states $\rho_{aa}$ , for weak coupling $\beta' = 0.5$ and strong coupling $\beta' = 1.5$ are shown in red; stars denote Dirac delta functions; $\Delta$ is shown as a dashed black line and $\Lambda$ as a solid line. All energies are in units of two times the width of the band (in this case, $\Delta$ ) . . . . .	14

2.4	Chemisorption energy from Equation 2.20 and occupancy of adsorbate state, $n_a$ from Equation 2.15 for $\epsilon_a = 0$ eV, $V_{ak}^2 = 1$ eV and different $\epsilon_d$ and $w_d$ values. . . . .	16
2.5	Energy contribution of the total and differential configurational entropy as a function of coverage, $\theta$ at 300 K . . . . .	20
4.1	Schematic of the TPD experiment; a molecule is dosed onto a given surface at low temperatures (say 80 K). Increasing the temperature causes the adsorbate to desorb (at say 220K). The rate of CO desorption is measured. . . . .	37
4.2	Fitted background of Temperature Programmed Desorption curves (solid line) for Au(211) and Au(310) based on the TPD curves from Ref [42] for Au(211) and Ref [39] for Au(310). <i>Reprinted from paper in Section 10.1 [29]</i> . . . . .	40
4.3	(a and d) Background corrected rates of CO desorption from TPD experiments in previous work for Au(211) from Ref [42] and Au(310) Ref [39] site motifs assigned to each peak are labelled directly in the figure; (b and e) $G_d$ as a function of the relative TPD coverage under vacuum conditions for the Au(100) step and Au(110) step; the dashed line indicates the best fit to the points (c and f) schematic of (211) and (310) surfaces. <i>Reprinted from paper in Section 10.1 [29]</i> . . . . .	41
4.4	Desorption energy corresponding to dilute coverages, $\Delta E_{\theta \rightarrow 0}$ of CO for (100) step and (110) step as a function of the initial exposure in Langmuir in the TPD experiment. Error bars show errors from the fit determined as the mean error of the residual; (b) contributions of the configurational entropy (solid lines) and CO-CO adsorbate-adsorbate interaction (dashed-lines) to the total desorption energy $G_d$ based on the fitting equation described in Equation 4.6. <i>Reprinted from paper in Section 10.1 [29]</i> . . . .	44

- 4.5 Equilibrium coverage of CO as a function of the temperature at 1 bar CO(g) pressure for both surface facets (211) and (310) for all considered initial exposures. The dashed black line shows the equilibrium coverage at 298.15 K. *Reprinted from paper in Section 10.1 [29]* . . . . . 45
- 4.6 DFT calculated adsorption energies as a function of the step coverage on (a) 211 (b) 310 (c) differential free energies for CO adsorption; all points at the different coverages are for the most stable adsorption site; in (a and b) the colored bands indicate  $\Delta E_{\theta \rightarrow 0}$  obtained from the TPD analysis for each facet, and the purple dashed line the value from Redhead analysis. *Reprinted from paper in Section 10.1 [29]* . . . . . 46
- 4.7 a) Water adsorption TPD experiments reproduced from Ref [40], where red points denote exposure greater than 1 L and green points have exposures lower than 1 L; (b-f) schematic illustrates the number of water molecules used for each coverage. (g) Average adsorption energy of H<sub>2</sub>O on Au(310) computed using ab initio molecular dynamics simulations; experimentally determined values of the adsorption energy from Ref [40] are indicated by the red and green dashed lines corresponding to high exposure (second peak) and low exposure (first peak). *Reprinted from paper in Section 10.2 [29]* . . . . . 49
- 4.8 Comparison of adsorption energies of CO on iron-doped vacancies as proposed in ref 20. Calculated with the GGA-RPBE functional (triangles) and the hybrid HSE06 functional (circles). Experimental estimate from TPD spectra from Ref [55] is marked by the blue band. The background fill indicates the coverage of CO predicted by the kinetic model using RPBE energetics. Fe(211) binding energies are shown with the dashed black line as a reference. *Reprinted from paper in Section 10.3 [56]* . . . . . 50

- 5.1 a) Total hybridisation energy as a function of the choice of  $\Delta_0$  for  $w_d = 2$  eV,  $V_{ak}^2 = 1$  eV,  $\epsilon_a = -5$  eV and  $\epsilon_d = -2$  eV b) Representative quantities from the Newns-Anderson model ( $\Delta$ ,  $\Lambda$ ,  $\epsilon - \epsilon_a$  and adsorbate projected density of states  $\rho_{aa}$ ) when  $\Delta_0 = 1$  eV. . . . . 58
- 5.2 a) Scatter plot of DFT chemisorption energies of O,  $\Delta E_O$  and C,  $\Delta E_C$  with the colour referring to the value of the  $d$ -band centre of the metal; note that there is no scaling between the adsorbates b) Deviation of the computed Pt point from that obtained from linear least squares fitting of the data-points in a. c-e) Same data as in a, split into  $3d$ ,  $4d$  and  $5d$  metals; f-h) Scaling of  $\Delta E_O$  and  $\Delta E_C$  with the upper edge of the  $d$ -band, determined through the maximum of the Hilbert transform of the  $d$ -projected density of states of the surface metal atoms. . . . . 63
- 5.3 a) Projected density of states from the Newns-Anderson model with  $\Delta_0 = 0.1$  eV,  $V_{ak} = 2.0$  eV and  $w_d = 3$  eV; the adsorbate density of states are shown in red for O ( $\epsilon_a = -5$  eV) and blue for C ( $\epsilon_a = -1$  eV). b-d) DFT projected density of states for the  $d$ -states of different transition metal surfaces and  $p$ -states of O (red) and C (blue). . . . . 66
- 5.4 Chemisorption energy from the model plotted against the DFT energies based on the parameters in 5.1. Colours indicate the row of the element in the periodic table; red for the  $3d$ , yellow for  $4d$  and green for  $5d$  transition metals. . . . . 69
- 5.5 Hybridisation energy (i.e. without orthogonalisation energy) plotted for a range of  $d$ -band centres for a) O\* with  $\epsilon_a = -5$  eV and b) C\* with  $\epsilon_a = -1$  eV; there is a saturation in the case of O\*, but no saturation for C\*. c) Total chemisorption energy of O\* vs. C\* from the model, the plot is analogous to the DFT energies in Figure 5.2. d)  $\epsilon_s$  (see text), a measure of the saturation in a-b for different adsorbates. . . . . 70



- 5.6 Interpolated parameters of  $V_{sd}^2$  and  $w_d$  plotted against the filling fraction. The points are values taken from Ref [10] for  $V_{sd}^2$  and from DFT calculations in the case of  $w_d$  . . . . . 73
- 6.1 Schematic of an electrochemical interface, consisting of an adsorbate A, electrons ( $e^-$ ), protons  $H^+$ , interfacial water molecules (in red and white) and electrolyte ions (in orange). . . . . 76
- 6.2 ATR-SEIRAS in the CO stretch region from a CV on an Au film in 0.1 M  $HClO_4$  purged with 1 bar CO. A spectral background was taken at +0.634 V in Ar-purged solution. (a) ATR-SEIRAS spectra before the addition of Pb. (b) ATR-SEIRAS spectra with 1 mM  $Pb(ClO_4)_2$ . Every eighth spectrum is shown. (c) Integrated intensities of the CO stretch peak as a function of potential and (d) corresponding 2 mV/s CV with and without Pb. *Reprinted from paper in Section 10.2 [30]* . . . . . 78
- 6.3 Computed surface Pourbaix diagrams on four prototype Au facets (111), (100), (110), and (211). The dashed black line indicates the potential at which the coverage has increased between the discrete intervals for which the DFT calculation was performed. To the right of each surface, the Pourbaix diagram is the associated Pb-UPD CVs taken from Ref [36]. The multiple broadened peaks observed in the (100) facet suggest substantial reconstruction. *Reprinted from paper in Section 10.2 [30]* . . . . . 82
- 6.4 Snapshots of CO on Au(211) and Au(100) in vacuum or with explicit water from an *ab initio* MD simulation, performed in periodic unit cell sizes of 3x3 for (211) at a coverage of 1/3 ML and 3x4 for (100) at a coverage of 1/16 ML. Internal ( $\Delta E_{CO}$ ) and free energies of adsorption ( $\Delta G_{CO}$ ) with their standard deviations based on different runs are given below the snapshots. *Reprinted from paper in Section 10.2 [30]* . . . . . 84

- 7.1 Variation of a) reaction energies b) barriers for  $C + H^+ + e^- \rightarrow CH$  with the mean workfunction. Atomic positions of the initial state and the transition state are shown within insets, the reacting proton is marked in blue. Colors indicate different cell sizes with different proton concentrations. Cell sizes annotated with a ' indicate multiple protons in the unit cell; the rest have a single proton in the unit cell. . . . . 90
- 7.2 Schematic showing the normalised reaction path for a proton electron transfer reaction,  $C + H^+ + e^- \rightarrow CH^*$  on a metal surface.  $\omega$  denotes the idealised reaction path; IS, TS and FS are the initial, transition and final state respectively. . . . . 93
- 7.3 Equivalence of the dipole derivative  $d\mu/dR$  and the force derivative  $dF/d\xi$  for a range of elementary electrode reactions . . . . . 96
- 7.4 a) Raw energies from images used in a nudged-elastic band calculation of  $C^* + H^+ + e^- \rightarrow CH^*$  b)  $(q_2 - q_1)$  obtained for all images for the reaction  $H^+ + e^- + C^* \rightarrow CH^*$  c) Energy vs. mean potential based on fitting (black line) and the predictions from finite difference for different cells (colors) . . . . . 98
- 7.5 Parity plot for  $q$  from fitting through Equation 7.4 for a series of increasingly larger unit cells and through the force-based method as in Equation 7.17; dashed line indicates exact fit and green band indicates  $\pm 0.1$  error with either methodology. Alternative  $\omega$  denotes an idealised reaction path where the proton descends directly to the surface along the direction of the surface normal. . . . . 99

- 8.1 Comparison of RPBE and RPBE+U adsorption energies for relevant CO<sub>2</sub>R intermediates for a) DV4N b) DV2N. Insets show the corresponding structures and mean absolute errors for both functionals. c) Projected density of states (DOS) of DV2N structure with three functionals RPBE, HSE06 and RPBE+U with U=2 eV ; color scheme: Blue: Carbon, Green: Nitrogen, Orange: Iron, Black: total DOS; states near the Fermi level have been magnified for clarity; horizontal line divides spin up and spin down states. *Reprinted from paper in Section 10.3 [56]* . . . . . 106
- 8.2 Rate of electron hopping (a) for the different idealized Lorentzian peaks shown in b. c-g, Densities of states projected onto CO<sub>2</sub> *s* and/or *p*-states for selected images of a CO<sub>2</sub> adsorption climbing image nudged elastic band run on FeNC show a short timescale of electron transfer. Insets: zoomed-in parts of the highlighted region; red bands indicate the estimated width of the states at the Fermi level,  $\epsilon_f$ ; a.u. is arbitrary units. *Reprinted from paper in Section 10.4 [106]* . . . . . 108
- 8.3 Schematic showing the multiple capacitances that have been used in this work;  $q_c$  denotes the charge for the capacitance for CO<sub>2</sub> adsorption, while  $q_i$  denotes the charge for the capacitance from continuum charging. *Reprinted from paper in Section 10.4 [106]* . 110
- 8.4 Free energy diagram at the theoretical equilibrium potential  $U_{eq} = -0.3$  V and at two other potentials:  $-0.75$  V and  $-1.2$  V vs SHE for DV4N and DV2N vacancies at a pH of 2. *Reprinted from paper in Section 10.3 [56]* . . . . . 113
- 8.5 a) TOF taken from two publications - Strasser et al. [110] and Hu et al. [60]; current densities were converted to TOF by assuming all iron sites were involved in catalytic activity b) TOF obtained from mean-field microkinetic modelling; TOFs are normalized to the activity at  $-0.6$  V vs. SHE, to emphasize relative trends. *Reprinted from paper in Section 10.3 [56]* . . . . . 114

- 8.6 Free energy diagram of  $\text{CO}_2$  to CO for a) Au(211) at  $U = -0.6, -0.8$  and  $-1.0$  V vs. SHE b) FeNC c) NiNC d) CoPc adsorbed on graphene at  $U = -0.8$  V vs. SHE with pH=2; schematics of the calculated surfaces are shown above their respective free energy diagrams, with the four double-vacancy MNC. Experimental current densities plotted against NHE potential for e) polycrystalline Au (from Ref [111]) f) FeNC (from Ref [59, 60]) g) NiNC (this work,[106]) h) CoPc on CNT (this work, [106]) *Reprinted from paper in Section 10.4* [106] . . . . . 116
- 8.7 a) Rate map at  $-0.8$  V vs SHE and pH 2 for  $\text{CO}_2$ R to CO obtained from the (211) transition metal scaling line. The annotated points show MNC catalysts either at single vacancies or double vacancies. b) Coverage map in monolayers (ML) with the same points showing which surfaces are poisoned by CO. *Reprinted from paper in Section 10.4* [106] . . . . . 118
- 8.8 Vacuum dipole moments for (211) and (100) Tm surfaces (blue) and Fe and Ni MNCs (red). The MNC materials (first index indicates the type of vacancy, 1 for single and 2 for double; second index indicates the number of substituting N atoms) have larger dipole moments as compared with those of the transition metals. b) Charge density difference plot for  $\text{CO}_2$  adsorbed on NiN4. c) Density of states projected onto the  $s$  and  $p$  states of  $\text{CO}_2^*$  (green) and the  $d$  states of the transition metals (purple) show that the adsorbate states are much narrower on MNC materials than they are on transition metals. *Reprinted from paper in Section 10.4* [106] . . . . . 119

# List of Tables

5.1	Fitting parameters for C* and O* from a least-squares error minimisation routine . . . . .	68
8.1	$q_c$ determined based on the method discussed in Chapter 7 for different transition metals and MNC materials. On average, it appears that $q_c$ determined for MNC materials is larger than those on transition metal surfaces. . . . .	111



# Chapter 1

## Introduction

### 1.1 Closing the carbon cycle

Anthropogenic CO<sub>2</sub> and other greenhouse gas emissions have increased the risk of climate change [1]. This increased risk has been linked to increasing likelihood of destructive rare weather events, hotter temperatures and rising sea water levels [2]. Figure 1.1a shows the observed increase in temperature from 1850 up to the present. It is clear that there has been a noticeable increase in temperature over the last 100 years, coinciding with the industrialisation of the global economy.

Significant contributors to greenhouse emissions are burning fossil fuels and other related industrial processes. The CO<sub>2</sub> released from these sources accounts for 65% of the global greenhouse gas produced from 2000-2010 [5]. An obvious solution to this problem is switching the global economy from fossil fuels to renewable sources of energy such as solar or wind based energies. Such a switch has the potential to be economically viable, with recent studies showing that the cost of renewable electricity has been steadily decreasing. For example, Figure 1.1b shows the cost of electricity steadily decreasing for solar (orange) and offshore wind sources (blue) [3, 4].

A major argument against the complete switch to renewable energy is that of

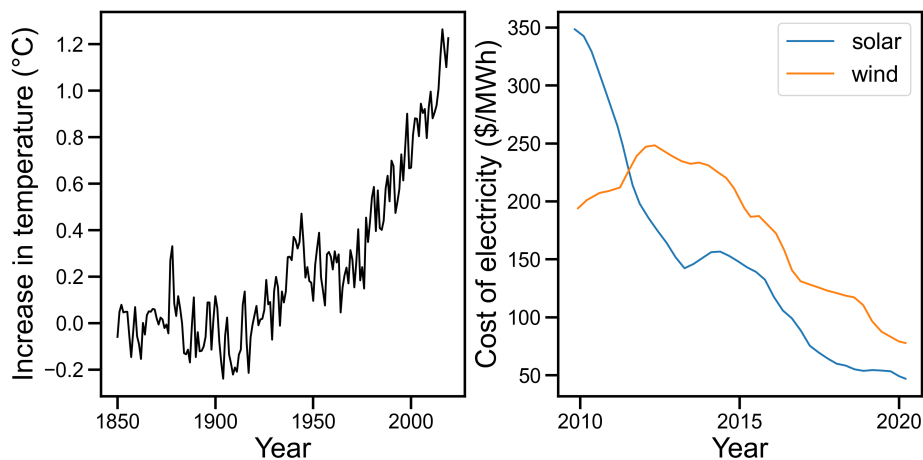


Figure 1.1: a) Observed increase in global temperatures across two centuries taken from Ref [1]. b) Cost of electricity based on solar and wind [3, 4].

seasonality. The sun shines during limited parts of the day and wind might not always be able to produce enough electricity throughout the year. This intermittent energy production is unacceptable for modern industry and households, which require constant access to electricity.

Thus, in the context of renewable energy, storage is key. Chemical bonds, particularly those with carbon, are particularly good at this task. The energy density of a substance, defined as the amount of energy stored per volume, is significant for carbon containing fossil fuels such as diesel and Gasoline (between 30-40 MJ/L [6]). However, it is exactly through burning of these substances that  $\text{CO}_2$  emissions have been driven up over the last century.

A potential solution to this problem is to find technologies that produce compounds such as diesel and gasoline, while using  $\text{CO}_2$  as an input along with (relatively) cheap electricity in the form of renewable energy. Specifically, we would have to break carbon-oxygen bonds (such as in  $\text{CO}_2$ ) and replace them with carbon-hydrogen bonds (such as in fossil fuels). In practice, performing this chemistry is challenging owing to the fact that  $\text{CO}_2$ , the most oxidised form of carbon, is extremely stable and inert.



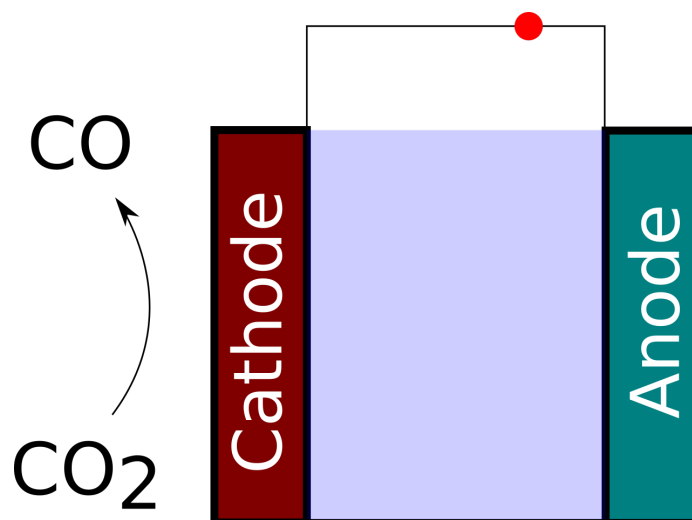


Figure 1.2: Schematic of an electrochemical cell; the negatively charged cathode is used to convert  $\text{CO}_2$  to  $\text{CO}$  while the anode performs a counter reaction.

## 1.2 Electrochemical reduction of $\text{CO}_2$

A promising approach to solve the problem of storage is that of electrochemical  $\text{CO}_2$  reduction ( $\text{CO}_2\text{R}$ ). Figure 1.2 shows an electrochemical cell, consisting of a negatively charged cathode and a positively charged anode.  $\text{CO}_2\text{R}$  involves the reduction of  $\text{CO}_2$  to species such as carbon mono-oxide ( $\text{CO}$ ), methane ( $\text{CH}_4$ ), ethanol ( $\text{C}_2\text{H}_4$ ), etc. and occurs at the cathode. A counter reaction, for example, oxidising  $\text{H}_2\text{O}$  to  $\text{O}_2$  occurs at the anode. Overall, this process satisfies the requirement that  $\text{CO}_2$  be used as an input and has the propensity to produce fuel as an output.

The amount of electricity used to convert  $\text{CO}_2$  to reduced products depends on the material used as the cathode. Transition metal electrodes such as gold ( $\text{Au}$ ) and silver ( $\text{Ag}$ ) are able to effectively convert  $\text{CO}_2$  to  $\text{CO}$ , the simplest of reactions in  $\text{CO}_2\text{R}$ . These so-called electrocatalysts facilitate (in acidic solutions)

the relatively simple reaction,



These catalysts convert  $\text{CO}_2$  to  $\text{CO}$ , by consuming two protons ( $\text{H}^+$ ) from the electrolyte solution and two electrons ( $e^-$ ) from the electrode surface. This reaction is the first  $\text{CO}_2\text{R}$  process to be realised commercially. Ag-based gas-diffusion electrodes can produce up to  $300 \text{ mAcm}^{-2}$  of  $\text{CO}$  from a  $\text{CO}_2$  input stream [7]. More reduced products such as ethanol, methanol, ethane, etc. are produced by Copper (Cu) electrodes [8, 9].

A competing reaction to  $\text{CO}_2\text{R}$  is the hydrogen evolution reaction (HER). This reaction typically occurs at the same potential range and conditions as  $\text{CO}_2\text{R}$  (approx.  $-0.6 \text{ V}$  vs. SHE, pH of 6.8). In the context of  $\text{CO}_2\text{R}$  it is considered a loss of efficiency. In this reaction, protons and electrons are consumed to give  $\text{H}_2(\text{g})$ ,



### 1.3 Outline of Thesis

In this thesis, we study the electrochemical conversion of  $\text{CO}_2$  to  $\text{CO}$ , one of the simplest reaction in the  $\text{CO}_2\text{R}$  network. We begin by highlighting the main methodologies and theories central to heterogeneous catalysis and electro catalysis in Chapter 2. In Chapter 3, we discuss how these quantities are obtained through *ab-initio* calculations. Chapters 2 and 3 are meant to serve as a brief summary of the theories and methods used in this thesis.

One of the central quantities in heterogeneous catalysis is the chemisorption energy, i.e. the binding strength of an adsorbate to the surface of a material. In Chapters 4 and 5 we focus on the effect of the electrode surface on the chemisorption energies. In Chapter 4 (based on the paper in Section 10.1), we develop a model that extracts the chemisorption energy from a popular

experimental technique, temperature programmed desorption (TPD). We apply our methodology to find the equilibrium coverage of CO on stepped gold surfaces at standard conditions. In Chapter 5, we build upon the Newns-Anderson and Hammer-Nørskov models to describe the variation of the chemisorption energies with the  $d$ -band centre of a metal. We describe the conditions under which the chemisorption energies of two adsorbates scale with each other. A significant achievement of our model is that it explains why two of the simplest adsorbates, carbon and oxygen, *do not* scale with each other.

In Chapters 6–8, we investigate variations in the chemisorption energy at the electrochemical interface caused by both the electrolyte and electrode. In Chapter 6 (based on paper in Section 10.2), we perform *ab-initio* molecular dynamics calculations to determine the effect of interfacial water on the chemisorption energies of adsorbates. As an example, we study CO adsorption on stepped and terrace gold surfaces and find that stepped surfaces are significantly destabilised in the presence of water, while terraces are largely unaffected. In Chapter 7, we describe the effect of the interfacial field on the chemisorption energies. We develop a model to quantify this effect through *ab-initio* calculations.

Finally, in Chapter 8 (based on papers in Sections 10.3 and 10.4) we apply all the methods and models of this thesis to understand the CO<sub>2</sub>R reaction on various materials. We accurately predict the rate limiting step at operating potentials on transition metal catalysts as well as doped-metal graphene catalysts. We find that CO<sub>2</sub> adsorption is the rate limiting step on transition metals, but the first protonation is likely rate-limiting on some doped-graphene materials. Our predictions are in excellent agreement with available experiments on a range of catalysts. We end by discussing possible design strategies to find improved catalysts for CO<sub>2</sub>R.



## Chapter 2

# Theory of heterogeneous catalysis

In this chapter, we discuss the main concepts in heterogeneous catalysis which we will apply in this thesis. A significant amount of heterogeneous catalysis and electrocatalysis involves studying the breaking and forming of chemical bonds [10]. It follows that a typical theme in the field centres around understanding how strongly molecules are bound to a surface, that is, determining the chemisorption energy of a given adsorbate on a chosen surface.

We begin by illustrating the molecular perspective of chemisorption through the potential energy surface. We then describe the Newns-Anderson model [11] to understand the atomistic nature of chemisorption. We follow this section by a discussion on the role the environment plays in altering the binding strength of an adsorbate on a surface. We defer discussion of how these chemisorption energies are obtained through *ab-initio* methods to Chapter 3.

## 2.1 Potential energy surface: An atomistic view of chemisorption

A potential energy surface (PES) for a reaction allows us to determine the chemisorption energy for a chosen molecule and surface. As an example, consider the process of CO<sub>2</sub> adsorption on a Pt(111) surface. The potential energy surface for this reaction is shown in Figure 2.1. The axes refer to quantities that are altered (the O – C – O internal angle and the Pt – C height) and the background denotes the energy,

$$E = E_{\text{CO}_2} - E_{\text{CO}_2(\text{g})} + * \quad (2.1)$$

where \* indicates the surface, in this case, Pt(111) and  $E_{\text{CO}_2}$  is the energy of CO<sub>2</sub> at different positions and O – C – O internal angles. The chemisorption energy is the energy to bring CO<sub>2</sub> from far away (CO<sub>2</sub>(g)) up to the point that it adsorbs on the surface of the catalyst (CO<sub>2</sub>\*). We ignore all other degrees of freedom in this example. This assumption will lead to an overestimation of the chemisorption energies.

Figure 2.1 highlights several features common to adsorbates other than just CO<sub>2</sub>. For example, at large Pt–C distances weak long-range van-der-Waal forces dominate, causing minor changes in the chemisorption energies. At closer distances ( $\approx 2 - 3\text{\AA}$ ), there is overlap between the electronic states of the adsorbate and the metallic surface causing the formation of a chemical bond [10]. If the adsorbate approaches the surface any further, it would be met with a steep increase in energy due to Pauli-repulsion. A more quantitative description of this process will be provided in Section 2.2.1 and built upon later in Chapter 5.

There are also features in Figure 2.1 that are unique to CO<sub>2</sub> adsorption. For example, at small Pt–C heights (less than  $\approx 2\text{\AA}$ ) it would appear that CO<sub>2</sub> can lower its chemisorption energy by changing its internal O – C – O angle. This additional degree of flexibility gives CO<sub>2</sub> distinctive electronic structure properties, which we will explore in Chapter 8.

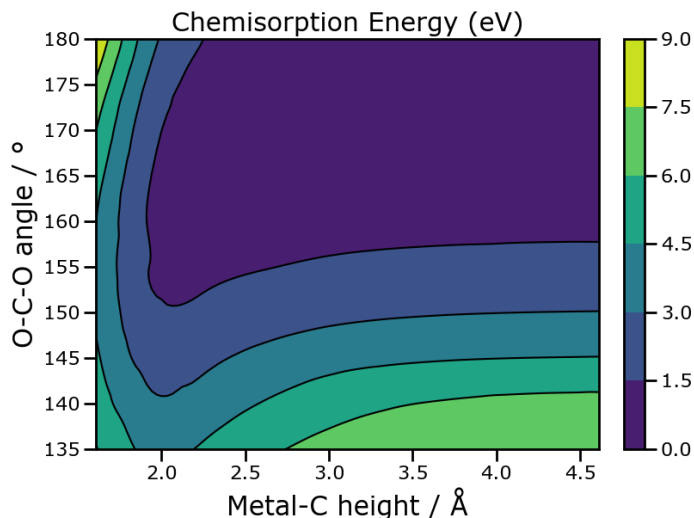


Figure 2.1: Potential energy surface for  $\text{CO}_2$  adsorption on the ontop site of a Pt(111) surface. The  $x$ -axis is the distance between the uppermost Pt atom and the C atom, while the  $\text{O}-\text{C}-\text{O}$  angle is shown on the  $y$ -axis. All other degrees of freedom are kept fixed.

## 2.2 Electronic structure view of the chemisorption energy

### 2.2.1 Newns-Anderson model of chemisorption

An early model of chemisorption was proposed by Newns [11] in 1969. Despite its simplicity, the model sheds light on some of the most fundamental characteristics of interaction between the metal  $d$ -states and an adsorbate. In this section, we present some important expressions developed in this model and explain their significance. We will modify these expressions to incorporate the effect of the  $sp$ -states of the metal and orthogonalisation in Chapter 5.

### Anderson Hamiltonian

Consider a system consisting of an adsorbate  $|a\rangle$  adsorbed on a (metallic) surface having a continuum of states  $|k\rangle$ . The overall Hamiltonian  $\hat{H}$  is split into a non-interacting Hamiltonian  $\hat{H}_0$ , and a Hamiltonian  $\hat{V}$ , consisting solely of coupling elements  $V_{ak}$  between  $|a\rangle$  and  $|k\rangle$ .

$$\hat{H} = \hat{H}_0 + \hat{V} \quad (2.2)$$

The interaction between  $|a\rangle$  and  $|k\rangle$  is most generally represented by the Anderson Hamiltonian [12] as,

$$\begin{aligned} \hat{H} = & \underbrace{\sum_{\sigma} \epsilon_a n_{a\sigma} + \sum_{k,\sigma} \epsilon_k n_{k\sigma}}_{\text{unperturbed metal and adsorbate}} \\ & + \underbrace{\sum_{k,\sigma} \left( V_{ak} c_{a,\sigma}^{\dagger} c_{k,\sigma} + V_{ak} c_{a,\sigma} c_{k,\sigma}^{\dagger} \right)}_{\text{Coupling between the eigenstates}} \\ & + \underbrace{U n_{a\sigma} n_{a-\sigma}}_{\text{Coulomb interaction}} \end{aligned} \quad (2.3)$$

where  $\sigma$  denotes spin,  $\langle a|H|a\rangle = \epsilon_a$  and  $\langle k|H|k\rangle = \epsilon_k$ . Note that the basis orbitals in Equation 2.3 are orthogonal. However, in the case of adsorption events effects of overlap between adsorbate and metal states cannot be completely neglected [13, 14]. We return to the inclusion of this effect in Chapter 5.

The term in the first bracket of Equation 2.3 indicates the contributions of the unperturbed  $|k\rangle$  and  $|a\rangle$  states. The second term indicates a coupling between  $|a\rangle$  and  $|k\rangle$  states through the hopping terms  $V_{ak} c_{a,\sigma}^{\dagger} c_{k,\sigma}$  (creation of a state in  $|a\rangle$  and deletion of a state in  $|k\rangle$ ) and  $V_{ak} c_{a,\sigma} c_{k,\sigma}^{\dagger}$  (creation of a state in  $|k\rangle$  and deletion of a state in  $|a\rangle$ ). For each  $\sigma$ , there is also a Coulomb interaction term,  $U n_{a\sigma} n_{a-\sigma}$ .



### Adsorbate projected density of states

In the context of surface catalysis, it is instructive to look at the projected density of states, particularly of those projected onto the adsorbate. To do so, Newns derived the Green operator for the Hamiltonian in Equation 2.3 in Ref [11]. The Green operator,  $G_{aa}(\epsilon)$  is given by,

$$G_{aa}(\epsilon) = \left[ \epsilon - \epsilon_a - \sum_k V_{ak}^2 / (\epsilon + i\alpha - \epsilon_k) \right]^{-1} \quad (2.4)$$

which can be expressed succinctly as the sum of two functions,

$$G_{aa} = [\epsilon - \epsilon_a - \Lambda(\epsilon) + i\Delta(\epsilon)]^{-1} \quad (2.5)$$

where  $\Delta$  (commonly called the chemisorption function) is defined as,

$$\Delta(\epsilon) = \pi \sum_k |V_{ak}|^2 \delta(\epsilon - \epsilon_k) \quad (2.6)$$

and  $\Lambda$  is the Hilbert transform of  $\Delta$ ,

$$\Lambda(\epsilon) = \frac{P}{\pi} \int_{-\infty}^{\infty} \frac{\Delta(\epsilon')}{\epsilon - \epsilon'} d\epsilon' \quad (2.7)$$

where  $P$  is the Cauchy principal value. Together,  $\Delta$  and  $\Lambda$  are used to compute the adsorbate projected density of states based on projections to the eigenfunctions,  $|m\rangle$ .

$$\rho_{aa}(\epsilon) = \sum_m |\langle m|a\rangle|^2 \delta(\epsilon - \epsilon_m) = \langle a| \delta(\epsilon - \hat{H}) |a\rangle \quad (2.8)$$

and the Green operator in Equation 2.5 can be expressed as,

$$G_{aa}(\epsilon) = \lim_{\alpha \rightarrow 0} \frac{1}{\epsilon - \hat{H} + i\alpha} = \frac{P}{\epsilon - \hat{H}} - i\pi \delta(\epsilon - \hat{H}) \quad (2.9)$$

which gives a convenient way to extract the adsorbate projected density of states from  $G_{aa}$ ,

$$\rho_{aa}^\sigma(\epsilon) = -\frac{1}{\pi} \text{Im} \langle a|G_{aa}(\epsilon)|a\rangle = -\frac{1}{\pi} \text{Im}(G_{aa}) \quad (2.10)$$

where  $\text{Im}$  stands for the imaginary part of the variable. Substituting Equation 2.5 into Equation 2.10,

$$\rho_{aa}(\epsilon) = \frac{1}{\pi} \frac{\Delta(\epsilon)}{[\epsilon - \epsilon_a - \Lambda(\epsilon)]^2 + \Delta(\epsilon)^2} \quad (2.11)$$

### Semi-infinite chain

To simplify the expression further, it is assumed that adsorbate-metal interactions occur through a semi-infinite chain. Figure 2.2 shows a schematic of such a semi-infinite chain, consisting of the adsorbate,  $|a\rangle$  interacting with the metal,  $|k\rangle$ . Within the model, the adsorbate interacts with the metal atoms with an interaction strength of  $V_{ak}$ . The metal atoms themselves interact with each other with a strength of  $\beta$ .

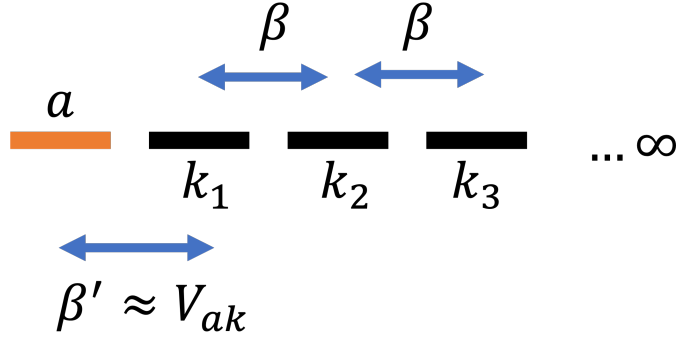


Figure 2.2: Schematic of the semi-infinite chain model,  $a$  is the adsorbate with interacts with the metal through one metal atom  $k_1$ , which is on one end of an infinitely long metal chain  $k_1, k_2, \dots$  with coupling element  $\beta$ .

The advantage of such an assumption is that we obtain a simplified version of  $\Delta$ , which comes from inserting the eigenvalues of the semi-infinite chain model into Equation 2.6 [15].

$$\Delta(\epsilon) = \pi V_{ak}^2 [1 - \epsilon^2]^{1/2} \quad (2.12)$$

and Equation 2.12 can be easily generalised to different band widths,  $w_d$  and band centres,  $\epsilon_d$  by setting,

$$\epsilon \rightarrow \frac{\epsilon - \epsilon_d}{w_d} \quad (2.13)$$

The density of states of the adsorbate is obtained by substituting Equation 2.12 into 2.11. An interesting feature of the semi-elliptical model is that Equation 2.11 can be visualised graphically in a relatively simple manner. We are particularly interested in the poles of Equation 2.11, that is, the  $\epsilon$  values at which the denominator in Equation 2.11 becomes 0. Thus, we need  $\epsilon$  for which,

$$\epsilon - \epsilon_a = \Lambda(\epsilon), \quad \Delta(\epsilon) = 0 \quad (2.14)$$

Graphically, Equation 2.14 implies that we need to find the point  $\epsilon$  for which the line  $\epsilon - \epsilon_a$  intersects  $\Lambda(\epsilon)$ , while ensuring that  $\Delta(\epsilon)$  is 0. Figure 2.3 shows a few representative scenarios. The dashed lines show the semi-ellipse  $\Delta$  and the solid back line shows its Hilbert transform  $\Lambda$ . In the case of weak coupling between  $|a\rangle$  and  $|k\rangle$ , the red line ( $\epsilon - \epsilon_a$ ) intersect  $\Delta$  only once (the red star shows the  $\epsilon$  corresponding to the intersection). In the case of strong coupling, two points meet the condition of Equation 2.14 (two red stars).

The presence of two points meeting the condition of 2.14 (sometimes referred to as localised states), presents an intuitive picture of chemical bonding at surfaces. The state lower in energy is the bonding state, while that of higher energy is the anti-bonding state. In the case of weak coupling, no such splitting takes places, and the adsorbate induced density of states is very similar to the original, unperturbed state.

Another quantity of interest is the occupancy of the adsorbate state upon chemisorption,  $n_a$ , which is obtained by integrating Equation 2.11 for all the occupied energy levels,

$$n_a = \int_{-\infty}^{\epsilon_f=0} \rho_{aa} d\epsilon \quad (2.15)$$

where  $\epsilon_f$  is the Fermi level (which we set to 0 throughout this thesis).

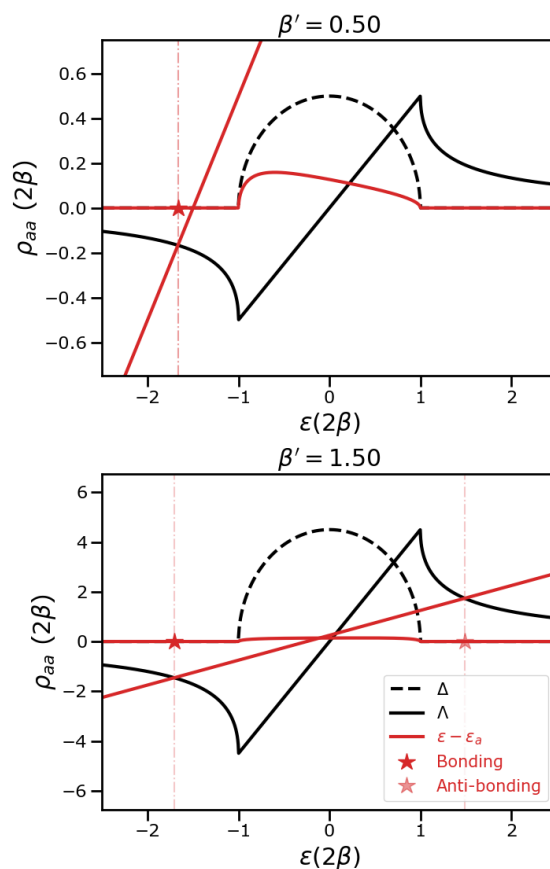


Figure 2.3: Representative adsorbate density of states  $\rho_{aa}$ , for weak coupling  $\beta' = 0.5$  and strong coupling  $\beta' = 1.5$  are shown in red; stars denote Dirac delta functions;  $\Delta$  is shown as a dashed black line and  $\Lambda$  as a solid line. All energies are in units of two times the width of the band (in this case,  $\Delta$ )

### Chemisorption energy

Once the density of states has been determined from Equation 2.11, it is straightforward to compute the chemisorption energy within the framework of this tight binding model. The chemisorption energy is given as the difference between all

the occupied states *after* chemisorption with the those *before* chemisorption,

$$E_{\text{chem}} = \left[ \sum_{m,\text{occ}} \epsilon_m \right] - \left[ \sum_{k,\text{occ}} \epsilon_k + \epsilon_a \right] \quad (2.16)$$

where the one-electron ( $1e$ ) term is written as,

$$\Delta E_{1e} = \sum_{m,\text{occ}} \epsilon_m - \sum_{k,\text{occ}} \epsilon_k \quad (2.17)$$

For a function  $f(z)$ , which is analytic within some contour  $\mathbf{C}$  and another function  $\psi$  which is analytic within  $\mathbf{C}$  except for some finite number of points (which are poles),

$$(2\pi i)^{-1} \int_{\mathbf{C}} f(z) \frac{\psi'(z)}{\psi(z)} dz = \sum_i f(a_i) - \sum_i f(b_i) \quad (2.18)$$

and using  $f(\epsilon) = \epsilon$ , we can write

$$\Delta E_{1e} = (2\pi i)^{-1} \int_{\mathbf{C}} \epsilon \frac{d}{d\epsilon} \ln \left( \epsilon - \epsilon_\sigma - \sum_k \frac{|V_{ak}|^2}{\epsilon - \epsilon_k} \right) d\epsilon \quad (2.19)$$

upon integrating by parts gives the following general expression for  $\Delta E_{1e}$ ,

$$\Delta E_{1e} = \pi^{-1} \int_{-\infty}^{\epsilon_f=0} \tan^{-1} \left( \frac{\Delta}{\epsilon - \epsilon_\sigma - \Lambda} \right) d\epsilon \quad (2.20)$$

It follows that the hybridisation energy is simply,

$$\Delta E = \pi^{-1} \int_{-\infty}^{\epsilon_f=0} \tan^{-1} \left( \frac{\Delta}{\epsilon - \epsilon_\sigma - \Lambda} \right) d\epsilon - \epsilon_a \quad (2.21)$$

where  $-\pi < \tan^{-1} < 0$ . An illustrative example of the variation of  $\Delta E$  for different  $\epsilon_d$  and  $w_d$  values is shown in Figure 2.4a. Corresponding  $n_a$  values are shown in Figure 2.4. In Chapter 5 we explore in detail the change in chemisorption energy with  $\epsilon_d$  and  $w_d$  for the different transition metals.

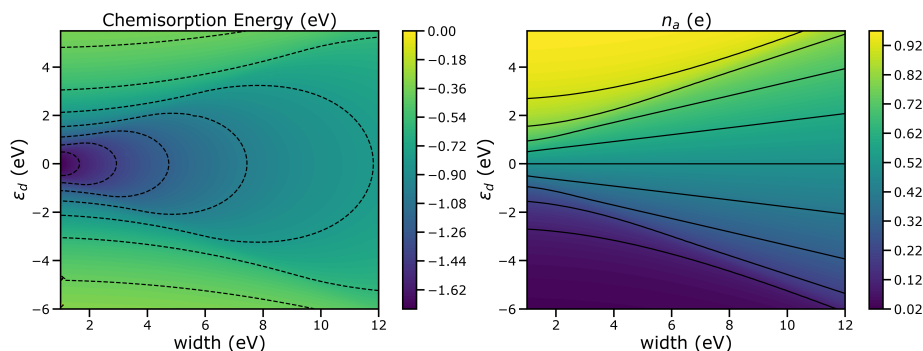


Figure 2.4: Chemisorption energy from Equation 2.20 and occupancy of adsorbate state,  $n_a$  from Equation 2.15 for  $\epsilon_a = 0$  eV,  $V_{ak}^2 = 1$  eV and different  $\epsilon_d$  and  $w_d$  values.

### 2.2.2 Hammer-Nørskov model

In this section, we review a simple, but effective model of chemisorption, first proposed in Ref [16]. In contrast to the chemisorption energy derived in Section 2.2.1, the Hammer-Nørskov  $d$ -band model uses the simple two-state problem to describe chemisorption. For an adsorbate with a re-normalised valence energy of  $\epsilon_a$ , the total chemisorption energy is written as the sum of the hybridisation energy and the orthogonalisation energy,

$$E_{\text{chem}} = \underbrace{-\text{sign}(\epsilon_a - \epsilon_d) |n_b - f| \frac{V_{ak}^2}{|\epsilon_a - \epsilon_d|}}_{\text{Hybridisation}} - \underbrace{V_{ak} S_{ak}}_{\text{Orthogonalisation}} \quad (2.22)$$

where sign refers to the sign function,  $n_b$  is to either 0 or 1 depending on if the state is above or below the Fermi level respectively,  $S_{ak}$  refers to the overlap between the metal states and the adsorbate states upon chemisorption. Note that the orthogonalisation term is not considered in the case of the Newns-Anderson model presented in Section 2.2.1.

The model was first applied to CO chemisorption on late transition metals and overlayers. It was able to successfully predict trends within and across rows of the periodic table. It was found that the main determinant of  $E_{\text{chem}}$  was  $\epsilon_d$ ,

that is, the  $d$ -band centre. Given its relative simplicity and success in predicting trends, the  $d$ -band centre has become a regular descriptor of the chemisorption energy for several adsorbates. In Chapter 5 we explore  $\epsilon_d$  as a descriptor within a model using the hybridisation energy from the Newns-Anderson model and the orthogonalisation energy of the Hammer-Nørskov model.

## 2.3 Impact of environment on adsorption energies

In Sections 2.2.1 and 2.2.2, we described the binding strength as if it were a single value for a given adsorbate and surface. In fact, the binding strength can be modified by a number of factors, such as temperature, pressure in a gas-phase environment; potential and pH in an electrochemical environment. It can also be altered by an increase or decrease of coverage or the presence of other species. In this section, we discuss the impact that these conditions have on the binding strength of an adsorbate to a surface. These concepts will be applied in Chapters 4, 6 and 8.

### 2.3.1 Coverage dependence of the chemisorption energy

The adsorbate coverage,  $\theta$ , is defined as the number of adsorbate species,  $n$  divided by the amount of surface sites,  $N$ , i.e.  $\theta = n/N$ . We would like to determine  $E_{\text{chem}}(\theta)$ , i.e. the chemisorption energy as a function of the coverage [17]. To do so, we would need to determine the *average* adsorption energy, given as

$$E_{\text{chem}}(\theta) = \frac{E_n - nE_{\text{gas}} - E_{\text{surface}}}{n} \quad (2.23)$$

where  $E_n$  is the chemisorption energy with  $n$  adsorbates on the surface,  $E_{\text{gas}}$  is the energy of the gas molecule and  $E_{\text{surface}}$  is the energy of the clean surface.

It is also instructive to determine the integral adsorption energy i.e. the total

energy for  $n$  adsorbates to be on a surface as,

$$E_{\text{int}}(\theta) = \theta E_{\text{avg}}(\theta) \quad (2.24)$$

and the differential adsorption energy, i.e. the energy to go from the  $i^{\text{th}}$  to the  $(i + 1)^{\text{th}}$  coverage.

$$E_{\text{diff}} = \frac{dE_{\text{int}}(\theta)}{d\theta} \quad (2.25)$$

### 2.3.2 Adsorption free energy

For a given temperature,  $T$ , the free energy of adsorption,  $\Delta G$ , of an adsorbate on a surface is given by the expression

$$\Delta G = \Delta H - T\Delta S \quad (2.26)$$

where  $\Delta H$  is the adsorption enthalpy and  $\Delta S$  is the adsorption entropy. In this section, we present a brief discussion on how the enthalpy and entropy are influenced by the environment in which adsorption is taking place. We neglect the  $pV$  term to convert the Helmholtz free energy (under constant volume conditions) to the Gibbs free energy (under constant pressure conditions). This assumption allows us to approximate the free energy as differences between adsorbed and gas-phases quantities in Equation 2.26.

#### Adsorption enthalpy

The enthalpy of a gas molecule is written as,

$$H(T) = H(T = 0) + \int_{T=0}^T C_p(T) dT \quad (2.27)$$

At 0 K, there would be two contributions to the enthalpy. The first is  $E_{\text{chem}}(\theta)$ , defined in Equation 2.23. The second is the zero-point energy, i.e. the energy at the lowest energy coming from a harmonic oscillator,  $h\omega_i/2$ , where  $\omega_i$  are the vibrational frequencies.



### Adsorption entropy

The adsorption entropy,  $\Delta S$  is the difference between the entropy of a molecule when it is adsorbed on the surface,  $S_{\text{ads}}$ , and when it is in gas phase,  $S_{\text{gas}}$ ,

$$\Delta S = S_{\text{ads}} - S_{\text{gas}} \quad (2.28)$$

$S_{\text{gas}}$  is often computed under the assumption that the molecule exhibits ideal gas behaviour. In order to determine  $S_{\text{gas}}$ , it is instructive to write the molecular partition function,  $q$ , for the different types of motion,

$$q = q_{\text{tr}} q_{\text{vib}} q_{\text{rot}} q_{\text{el}} \quad (2.29)$$

where  $q_{\text{tr}}$  is the translational partition function,  $q_{\text{vib}}$  is the vibrational partition function,  $q_{\text{rot}}$  is the rotational partition function and  $q_{\text{el}}$  is the electronic partition function. The entropy is determined from  $q$  as,

$$S_{\text{gas}} = k_B T \frac{\partial \ln q}{\partial T} + k_B \ln q \quad (2.30)$$

$q_{\text{tr}}$  is determined separately for each Cartesian coordinate,  $x, y, z$ . It is evaluated using the energies for a particle in one-dimensional box as  $\epsilon_n = h^2 n^2 / 8mL^2$ . Taking all dimensions together and setting the volume,  $V = L_x L_y L_z$ ,

$$\frac{q_{\text{tr}}}{V} = \frac{(2\pi m k_B T)^{3/2}}{h^3} \quad (2.31)$$

$q_{\text{rot}}$  for a poly-atomic molecule is given by,

$$q_{\text{rot}} = \frac{\sqrt{\pi}}{\sigma} \left( \frac{2\pi^2 k_B T}{h^2} \right)^{3/2} \sqrt{I_A I_B I_C} \quad (2.32)$$

where  $\sigma$  is the symmetry number of the molecule,  $I_A, I_B, I_C$  are the diagonal elements of the moment of inertia tensor.

$q_{\text{vib}}$  for a non-linear molecule, with  $3N - 6$  degrees of freedom, where  $N$  is the number of atoms is given by,

$$q_{\text{vib}} = \prod_{k=1}^{3N-6} \frac{\exp(-\beta h \omega_k / 2)}{1 - \exp(-\beta h \omega_k)} \quad (2.33)$$

where  $\beta = (k_B T)^{-1}$ . Note that the vibrational degrees of freedom for a linear molecule is  $3N - 5$ .

$q_{\text{el}}$  is composed of contributions from the different possible electronic states, each with a degeneracy of  $g$ ,

$$q_{\text{el}} = g_1 + g_2 \exp(-\beta \epsilon_2) + \dots \quad (2.34)$$

Determining the entropic contribution of an adsorbed molecule is a harder task. It is typically assumed that the adsorbate has no translational and rotational types of motion. The entire contribution to the partition function comes only from  $q_{\text{vib}}$ .

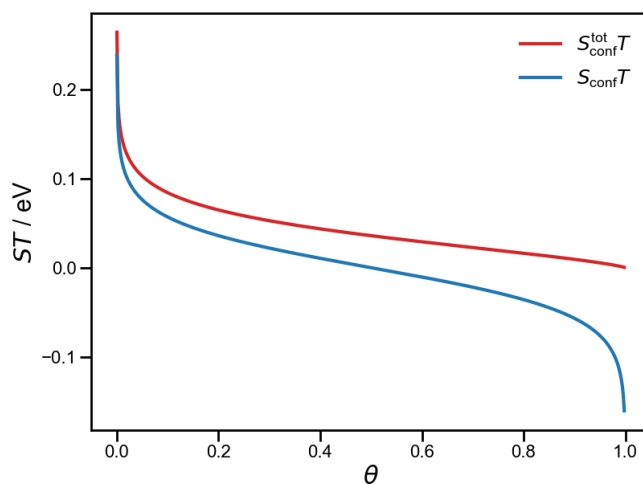


Figure 2.5: Energy contribution of the total and differential configurational entropy as a function of coverage,  $\theta$  at 300 K

There is an additional entropic contribution that needs to be included for an adsorbed molecule. It comes from different possible arrangements of  $N_a$  adsorbate molecules on  $N_s$  random sites. The number of such possibilities, assuming indistinguishably is given by,

$$N_{\text{conf}} = \frac{N_s!}{(N_s - N_a)! N_a!} \quad (2.35)$$

Substituting,  $\theta = N_a/N_s$  and using Sterling's approximation gives the total configurational entropy for the system,

$$S_{\text{conf}}^{\text{tot}} = -k_B \ln \left( \frac{\theta}{1-\theta} \right) - \frac{k_B}{\theta} \ln(1-\theta) \quad (2.36)$$

Since we are interested in per-adsorbate quantities, we often consider the *differential* configurational entropy,

$$S_{\text{conf}} = -k_B \ln \left( \frac{\theta}{1-\theta} \right) \quad (2.37)$$

Figure 2.5 shows the behaviour of the total and differential configurational entropy with coverage. The total gain in entropy asymptotically decreases in the case of  $S_{\text{conf}}^{\text{tot}}$ . In the case of  $S_{\text{conf}}$ , the energy contribution tends to  $\infty$  as  $\theta \rightarrow 0$  and  $-\infty$  as  $\theta \rightarrow 1$ , implying that we would never have a fully clean or fully covered surface. We utilise this idea in Chapter 4 to extract  $E_{\text{chem}}(\theta)$  by fitting this form of the configurational entropy to data from TPD experiments.

## 2.4 Adsorption free energy in electrocatalysis

The free energies determined in Equation 2.26 incorporates the effect of temperature, pressure and coverage, making it suitable for use in studying several reactions in heterogeneous catalysis. In addition to these variables, we would need the variation of the free energies with the potential, which is the driving force for reactions to occur in electrocatalysis. In this section we discuss the consequences of incorporating the potential, pH and interfacial field on the *thermodynamics* of a reaction. We defer a discussion of reaction kinetics to Section 2.5.

### 2.4.1 Dependence on the potential and pH

To understand the dependence of potential on pH on an electrochemical reaction [18], we consider the following test case,



where  $A^*$  is any adsorbate on the surface and  $AH^*$  is its protonated form.  $H^+$  is a proton and  $e^-$  is an electron. The free energy change for the reaction is,

$$\Delta G = \mu_{AH^*} - (\mu_{A^*} + \mu_{H^+} + \mu_{e^-}) \quad (2.39)$$

where  $\mu_{AH^*}$  is the chemical potential of the product,  $\mu_{A^*}$  is the chemical potential of the reactant,  $\mu_{H^+}$  is the chemical potential of the proton and  $\mu_{e^-}$  is the chemical potential of the electron. It is through the latter two chemical potentials that pH and potential are included in the free energy.

We split  $\mu_{e^-}$  as a sum of  $\mu_{e^-}^0$ , the chemical potential under standard conditions and  $e\Phi_{SHE}$ , the dependence on the potential referenced to the Standard Hydrogen Electrode (SHE),

$$\mu_{e^-} = \mu_{e^-}^0 + e\Phi_{SHE} \quad (2.40)$$

where the SHE scale is an absolute scale, i.e. changing in  $\Phi_{SHE}$  changes  $\mu_{e^-}$  and not on  $\mu_{H^+}$ .

The pH [19] is included through  $\mu_{H^+}$ . Specifically, it is included through the configurational entropy of the proton as,

$$\mu_{H^+} = -T\Delta S = k_B T \ln \left( \frac{c_{H^+}}{c_{H^+}^0} \right) = -2.3k_B T \text{pH} \quad (2.41)$$

where  $c_{H^+}$  is the concentration of the proton as a reactant and  $c_{H^+}^0$  is the concentration at standard conditions. Here we assume that the activity of the species is the same as its concentration.

### 2.4.2 Dependence on interfacial field

The chemical potentials of the reactant and product of Equation 2.39 are influenced by the potential as well. This dependence comes through the electrostatic interactions between the adsorbate and the field set up by the double-layer outside the electrode surface. In its most general form [20], this interaction can be represented through the multipole expansion,

$$G_{\text{field}} = G_0 + \mu\xi - \alpha\frac{\xi^2}{2} + \dots \quad (2.42)$$

where  $G_0$  is free energy at standard conditions,  $\mu$  is the surface dipole moment of the adsorbate,  $\xi$  is the strength of the interfacial field,  $\alpha$  is the polarisability of the adsorbate. A more detailed discussion on the inclusion of this effect can be found in Chapter 7 and is applied to CO<sub>2</sub>R in Chapter 8.

## 2.5 Micro-kinetic modelling

So far we have discussed the thermodynamics associated with chemisorption. The rate of a reaction, however, requires knowledge of the (electrochemical) activation energies. The rate of any elementary reaction is given by,

$$\text{rate} = k_+ \prod_i \theta_i \prod_j p_j - k_- \prod_i \theta_i \prod_j p_j \quad (2.43)$$

where + indicates the forward reaction and – indicates the reverse reaction,  $p$  denotes the pressure,  $\theta$  is the coverage and  $k$  is the rate constant. More generally, the rate constants are given as

$$k_+ = \exp\left(-\frac{G_{a,+}}{k_B T}\right) \quad (2.44)$$

$$k_- = \exp\left(-\frac{G_{a,-}}{k_B T}\right) \quad (2.45)$$

We discuss how  $G_a$  is determined in Chapter 7. The general strategy to solve the kinetic model in Equation 2.43. For a given reaction network having

$n$  species adsorbed on a surface with a certain coverage  $\theta_i$  for each species  $i$ , we can write,

$$\sum_{i=1}^N \theta_i = 1 \quad (2.46)$$

that is, sum of all coverages (including that of the clean slab, no adsorbate) sum to 1.

$$\frac{\partial \theta_i}{\partial t} = f_i(\theta_1, \theta_2 \dots \theta_i \dots \theta_n) \quad (2.47)$$

We assume steady state, i.e. the coverage of a species does not change with time.

$$0 = f_i(\theta_1, \theta_2 \dots \theta_i \dots \theta_n) \quad (2.48)$$

The coverages are obtained by solving Equation 2.48 with a multi-dimensional Newton root algorithm,

$$\mathbf{J}(\theta) \cdot \delta x = -f(\theta) \quad (2.49)$$

where  $\mathbf{J}$  is the Jacobian matrix of  $f(\theta)$ .

## Chapter 3

# Theory and methods

In Chapter 2 we described the role of the chemisorption energy, both to understand the nature of bonding between transition metals and adsorbates as well as its role in determining the activity of a catalyst. In this section, we briefly describe how these chemisorption energies are obtained through *ab-initio* methods. We will primarily use Density Functional Theory (DFT) to determine these chemisorption energies.

We begin by briefly describing the electronic structure problem, followed by a brief description of DFT. We focus on how energies and forces, quantities relevant for this thesis, are determined. We highlight some practical methods and provide a brief outline of the different simulation techniques that rely on outputs of DFT calculations.

### 3.1 The electronic structure problem

The time independent electronic structure problem is written as an eigenvalue problem through the Schrödinger equation,

$$\hat{H}\Psi = E\Psi \tag{3.1}$$

where  $\hat{H}$  is the Hamiltonian,  $\Psi$  is the wave function, and  $E$  is the energy. In its

most general form,  $\hat{H}$  is written as,

$$\hat{H} = \left( \underbrace{-\sum_i \frac{\hbar^2}{2m_e} \nabla_i^2}_{\hat{T}_e} + \underbrace{\frac{1}{2} \sum_{i \neq j} \frac{e^2}{|\mathbf{r}_i - \mathbf{r}_j|}}_{\hat{U}_{ee}} + \underbrace{\sum_{ij} \frac{Z_j e^2}{|\mathbf{r}_i - \mathbf{R}_j|}}_{\hat{V}_{en}} \right) + \left( \underbrace{-\sum_i \frac{\hbar^2}{2M_i} \nabla_i^2}_{\hat{T}_n} + \underbrace{\sum_{i \neq j} \frac{Z_i Z_j e^2}{|\mathbf{R}_i - \mathbf{R}_j|}}_{\hat{V}_{nn}} \right) \quad (3.2)$$

where the lower case variables,  $\mathbf{r}$ , denotes the position vector of the electron and the upper case,  $\mathbf{R}$ , denotes that of the nuclei.  $\hat{T}_e$  and  $\hat{T}_n$  are the kinetic energy operator for the electron and nuclei respectively.  $\hat{U}_{ee}$  is the Coulomb operator for electrons, while electron-nuclei and nuclei-nuclei interactions are captured via  $\hat{V}_{en}$  and  $\hat{V}_{nn}$  respectively.

A common approach to solving Equation 3.1 is to employ the Born - Oppenheimer approximation [21]. Within this framework, it is assumed that the motion of the nuclei is slow in comparison to that of the electron. Instead of  $\hat{H}$  in Equation 3.2, the Schrödinger equation is solved with  $\hat{H}_e$ ,

$$\hat{H}_e = \hat{T}_e + \hat{U}_{ee} + \hat{V}_{en} \quad (3.3)$$

Even after employing this approximation, it is still very expensive to solve the Schrödinger equation for any system with more than a few electrons.

## 3.2 Density functional theory

One of the most significant advancements in solving the electronic structure problem was the development of DFT through the work of Hohenberg, Kohn and Sham [22, 23]. In contrast to wave function based approaches relying on Equation 3.2, where the positions are the central quantity, DFT uses the electron



density  $n(\mathbf{r})$  as the central variable. This simplification effectively converts a problem with  $3N$  degrees of freedom to one of just 3 (as in  $n(\mathbf{r})$ ). In this section, we briefly describe the Hohenberg-Kohn theorems [22], which allow for the use of the ground state electron density. We then present an outline of the Kohn-Sham framework, which is used to compute the ground state density and energy in practice.

### 3.2.1 Hohenberg-Kohn theorems

**Theorem.** *External potential uniquely determines the ground state density*

For a ground state of  $|\Psi\rangle$  with an electron density of  $n(\mathbf{r})$ , the Hamiltonian is,

$$\hat{H} = \hat{T}_e + \hat{U}_{ee} + \hat{V}_{\text{ext}} \quad (3.4)$$

where the external potential,  $\hat{V}_{\text{ext}}$  is written as,  $\hat{V}_{\text{ext}} = v_{\text{ion}}(\mathbf{r})$ . Hohenberg and Kohn [22] proved that the system is uniquely determined by  $v_{\text{ion}}(\mathbf{r})$ , that is, the external potential is given by the ground state electron density.

**Theorem.** *The total energy can be considered as a functional of the density*

It follows from Equation 3.4 that the ground state energy functional for the ground state electron density,  $E[n]$  is given by,

$$E[n] = \langle \Psi[n] | \hat{T}_e + \hat{U}_{ee} + \hat{V}_{\text{ext}} | \Psi[n] \rangle \quad (3.5)$$

$$E[n] = \langle \Psi[n] | \hat{T}_e + \hat{U}_{ee} | \Psi[n] \rangle + \langle \Psi[n] | \hat{V}_{\text{ext}} | \Psi[n] \rangle \quad (3.6)$$

$$E[n] = F[n] + \int v_{\text{ion}}(r)n(r)dr \quad (3.7)$$

where  $F[n]$  is the “universal” electronic density functional, consisting of the kinetic energy and Coulomb terms.

### 3.2.2 Kohn-Sham framework

To obtain the ground state electron density, and hence the ground state energy, Kohn and Sham [23] considered a reference, non-interacting system with an external potential,  $v_r$  but with the same ground state density ( $n$ ) as the real system. The Hamiltonian  $\hat{H}_r$ , for such a system is,

$$\hat{H}_R = -\frac{\hbar^2}{2m}\nabla^2 + v_r(\mathbf{r}) = \hat{T}_s + v_r(\mathbf{r}) \quad (3.8)$$

where  $\hat{T}_s$  is the kinetic energy operator for the non-interacting system. The task is to find  $v_r(\mathbf{r})$  such that the eigenvalue problem,

$$\hat{H}_R\phi_i(\mathbf{r}) = \epsilon_i\phi_i(\mathbf{r}) \quad (3.9)$$

yields the actual ground state electron density,  $n(\mathbf{r})$  through

$$\sum_{i=1}^N |\phi_i(\mathbf{r})|^2 = n(\mathbf{r}) \quad (3.10)$$

To relate this reference system to the real system with the same  $n$ , the Hohnberg-Kohn energy functional from Equation 3.7 is rewritten as,

$$E[n] = \hat{T}[n] + \hat{U}_{ee}[n] + \int v_{\text{ion}}(r)n(\mathbf{r})dr \quad (3.11)$$

$\hat{T}$  is split into its non-interacting system contribution,  $\hat{T}_s$  and the extra correlation contributions are put into an addition energy term called  $E_{\text{xc}}$ . Similarly,  $\hat{U}_{ee}$  is split into a Hartree term and all exchange and correlation contributions are stored in  $E_{\text{xc}}$ .

$$E[n] = -\frac{\hbar^2}{2m} \sum_{i=1}^N \langle \phi_i | \nabla^2 | \phi_i \rangle + \frac{1}{2} \int \int \frac{n(r)n(r')}{|r-r'|} drdr' + \int v_{\text{ion}}(r)n(r)dr + E_{\text{xc}}[n] \quad (3.12)$$

and  $E[n]$  is similarly written for the reference system,

$$E[n] = T_s[n] + \int v_r(r)n(r)dr \quad (3.13)$$

The real and reference system are related through the variational principle, which is accounted for by taking functional derivative of  $n$ , i.e.  $\delta/\delta n$

$$\frac{\delta}{\delta n} \left[ E[n] - \mu \left( \int n(\mathbf{r})d\mathbf{r} - N \right) \right] = 0 \quad (3.14)$$

where  $N$  is the total number of electrons and  $\mu$  is the Lagrange multiplier. The derivative for the real system is,

$$\frac{\delta T_s[n]}{\delta n} + \int \frac{n(r')}{|r-r'|} dr' + v_{\text{ion}}(\mathbf{r}) + \frac{\delta E_{\text{xc}}}{\delta n} = \mu \quad (3.15)$$

which is rewritten as,

$$\frac{\delta T_s[n]}{\delta n} + v_{\text{Hartree}}(r) + v_{\text{ion}}(\mathbf{r}) + v_{\text{xc}}(r) = \mu \quad (3.16)$$

And for the reference system,

$$\frac{\delta T_s[n]}{\delta n} + v_r(\mathbf{r}) = \mu \quad (3.17)$$

Combining Equations 3.16 and 3.17 (and hence incorporating the variational nature of the problem),

$$v_r(\mathbf{r}) = v_{\text{Hartree}}(r) + v_{\text{ion}}(\mathbf{r}) + v_{\text{xc}}(\mathbf{r}) \quad (3.18)$$

The Kohn-Sham equations are typically solved self-consistently in the following four steps.

1. Choose  $n(\mathbf{r})$  as an initial guess
2. Generate  $v_r(\mathbf{r}) = v_{\text{Hartree}}(\mathbf{r}) + v_{\text{ion}}(\mathbf{r}) + v_{\text{xc}}(\mathbf{r})$
3. Solve the eigenvalue problem to get the Kohn-Sham eigenstates,  $\phi_i(\mathbf{r})$  and eigenvalues  $\epsilon_i$  from Equation 3.9

4. Solve for  $n(r)$  from Equation 3.10 and return to Step 2.

In general, the Kohn-Sham eigenvalues do not correspond to those of the real system. However, they can be used to look at trends as we shall do in Chapter 5. The Kohn-Sham approach is exact in principle. In practice, the exchange-correlation functional is not known. Therefore, an assumption needs to be made to approximate this functional to determine the ground-state energy.

### 3.2.3 Exchange-correlation energy

In this section we review the common assumptions used to determine the exchange-correlation energy in practice. It is clear from Equation 3.16 that the functional derivative of the exchange-correlation energy functional at the ground state electron density is needed to solve Kohn-Sham equations in practice. There are different possibilities to construct this energy functional, here we discuss a small selection that are pertinent to this thesis.

#### Local density approximation

The local density approximation (LDA) is the simplest of exchange-correlation functionals and is given by,

$$E_{xc}[n] = \int \epsilon_{xc}[n]n(\mathbf{r})d\mathbf{r} \quad (3.19)$$

The exchange energy is computed directly from the homogeneous electron gas (constant  $n$ ) while the correlation term is fit to Quantum Monte Carlo simulation results.

#### Generalised gradient approximation

In heterogeneous systems an improvement is seen by incorporating not just the value of  $n$  at  $\mathbf{r}$ , but also its derivative,  $\nabla n(\mathbf{r})$ . This approach is called the

generalised gradient approximation (GGA).

$$E_{\text{xc}}[n] = \int \epsilon_{\text{xc}}[n, \nabla n] n(\mathbf{r}) d\mathbf{r} \quad (3.20)$$

Most chapters in this thesis will use either the PBE [24] functional or revised versions of the PBE functional, such as the RPBE functional [25], all of which fall under the banner of the GGA.

### Hybrid functionals

Both LDA and GGA functionals suffer from self-interaction errors. These errors arise from the fact that the electron feels a slight repulsion from itself because of the lack of error cancellation between the self ( $i = j$ ) Hartree term and the exchange term constructed separately for each type of functional. One approach to circumvent this issue is to incorporate some amount of exchange from the single particle orbitals through,

$$E_{\text{x}}^{\phi} = -\frac{1}{2} \sum_{jk} \int \int \frac{\phi_j^*(\mathbf{r}') \phi_k^*(\mathbf{r}) \phi_j(\mathbf{r}) \phi_k(\mathbf{r})}{|\mathbf{r} - \mathbf{r}'|} \quad (3.21)$$

Typically only a fraction this exchange energy is incorporated, i.e. it is mixed with the exchange energy coming from an LDA or GGA functional. For example, when it is coupled to a GGA functional with a given fraction  $\alpha$ ,

$$E_{\text{xc}}^{\text{hyb}} = \alpha E_{\text{x}}^{\phi} + (1 - \alpha) E_{\text{x}}^{\text{GGA}} + E_{\text{c}}^{\text{GGA}} \quad (3.22)$$

We use the hybrid functional HSE06 in Chapter 4 to calculate chemisorption energies for systems where self-interaction errors are large with GGA functionals.

### 3.2.4 Atom-centred forces

Another quantity that is important to understand electronic structure of materials is the force on an atom. Within the framework of DFT, the forces are

obtained directly from Equation 3.8. This transformation is possible through the Hellmann-Feynman [26] theorem, which states that

$$\frac{dE_\lambda}{d\lambda} = \langle \phi_\lambda | dH_\lambda/d\lambda | \phi_\lambda \rangle \quad (3.23)$$

If  $\lambda$  is one of the coordinates  $(x, y, z)$  of one of the nuclei, then the atom-centered force,  $\mathbf{F}$  is nothing but the negative of the left hand side (lhs) of Equation 3.23. Substituting Equation 3.8 into Equation 3.23 gives,

$$\mathbf{F}_\lambda = - \int d\mathbf{r} \phi \phi^* \frac{dv_r}{d\lambda} = - \int n(\mathbf{r}) \frac{dv_r(\mathbf{r})}{d\lambda} d\mathbf{r} - \sum_i \frac{\partial E_{i-i}}{d\lambda} \quad (3.24)$$

where the first term denotes the contribution of the electrons and the second contribution is that of the ions (which is treated classically). Determining the forces directly from the ground state electron density and potential allows for the algorithmic relaxation of a given structure. Starting from an initial guess of nuclei positions and electron density, a structure can be relaxed to a state where  $\mathbf{F} = 0$ .

### 3.3 Nudged elastic band method

It is often desired to have more than just the ground state energy and density from DFT calculations. One such quantity is the transition state between two ground states. Typical examples include reactions, adsorption or diffusion of species on a surface. In this thesis, we use the nudged elastic band (NEB) method to determine these transition states and the minimum energy path joining them. We briefly describe the method in this section.

A so-called elastic band is constructed with  $N + 1$  images, with positions  $R_0, R_1, \dots, R_N$ . The total force, as determined from Equation 3.24, is projected onto two components, one acting along the local tangent,  $\mathbf{F}_{i,\parallel}$  and another perpendicular to this tangent,  $\mathbf{F}_{i,\perp}$ ,

$$\mathbf{F}_i = \mathbf{F}_{i,\parallel} + \mathbf{F}_{i,\perp} \quad (3.25)$$

where the index  $i$  is for each image.  $\mathbf{F}_{i,\parallel}$  is replaced by a spring-force between each image acting along the tangent as,

$$\mathbf{F}_{i,\parallel}^s = k(|R_{i+1} - R_i| - |R_i - R_{i-1}|) \quad (3.26)$$

while the force in the perpendicular direction is left free and determined by,

$$\mathbf{F}_{i,\perp} = \mathbf{F}_i - \mathbf{F}_{i,\parallel} = \mathbf{F}_i - \mathbf{F}_i \cdot \hat{\tau}_i \quad (3.27)$$

In some chapters of this thesis, the climbing-image nudged elastic band (ci-NEB) [27] is used. In this method, the image with the highest energy feels no force of the springs. Instead, the component of the force along the band is inverted which forces the image to reach the saddle point.

### 3.4 *ab-initio* molecular dynamics

*ab-initio* molecular dynamics (AIMD) calculations in this thesis are performed via the Born-Oppenheimer molecular dynamics simulation method. The evolution of the nuclei with time is governed by the classical (Newtonian) equations of motion,

$$m_I \ddot{\mathbf{r}} = \mathbf{F}_I \quad (3.28)$$

where  $I$  denotes the index of the nuclei and the dots denote the derivative with respect to time. Equation 3.28 is integrated via the Verlet integration scheme to obtain the positions of the nuclei after a certain (chosen) time step.

Most systems in heterogeneous catalysis are studied under constant temperature conditions. Thus, it is beneficial to simulate a canonical ensemble at a given temperature,  $T$  by using a thermostat in AIMD calculations. In this thesis, we will primarily employ the Nosé-Hoover thermostat [28]. Briefly, the equations of motion are generated based on a Hamiltonian of “virtual” variables

containing an additional degree of freedom  $s$ ,

$$H_{\text{NH}} = \sum_i \frac{p_i^2}{2ms^2} + E(\mathbf{r}) + \frac{p_s^2}{2Q} + gk_B T \ln s \quad (3.29)$$

where  $\mathbf{p}_i$  is the momentum,  $p_s$  is the momentum of  $s$ ,  $Q$  is the equivalent of the mass for  $p_s$ ,  $g$  is a constant  $= 3N$  where  $N$  is the number of particles and  $E(\mathbf{r})$  is the potential energy.



## Chapter 4

# Benchmark of DFT adsorption energies with temperature programmed desorption (TPD)

In this chapter, we discuss our method to extract chemisorption energies (interchangeably referred to as adsorption energies) from temperature programmed desorption (TPD) experiments. Much of the contents of this chapter is presented in the manuscript titled *How to extract adsorption energies, adsorbate-adsorbate interaction parameters and saturation coverages from temperature programmed desorption experiments* [29] (Paper enclosed in Section 10.1). We also present two other applications, illustrated for benchmarking water adsorption on gold surfaces, which is a part of *Interaction of CO with Gold in an Electrochemical Environment* [30] (enclosed in Section 10.2) and CO adsorption on metal-doped graphene catalysts, which is a part of *Dipole-Field Interactions Determine the CO<sub>2</sub> Reduction Activity of 2D Fe-N-C Single-Atom Catalysts* (enclosed in Sec-

tion 10.3).

## 4.1 Introduction

As discussed in Chapter 2, adsorption energies are crucial to understanding chemical reactions on surfaces. However, experiments are not available for all systems of interest and determining them accurately from DFT calculations can be challenging for some adsorbate-metal combinations [31, 32]. Given that a majority of high-throughput studies rely on DFT computations [33], it is important that computed adsorption energies are benchmarked against experimental estimates for systems where both sets of data are available. This benchmark allows us to investigate if the chosen computational setup is able to accurately predict chemisorption energies, and hence catalytic activity.

Including TPD, there are predominantly three experimental methods to determine adsorption energies, namely single crystal calorimetry (SCAC) and equilibrium adsorption isotherms (EAI). However, between these two techniques, there is little data available for adsorption energies on noble metal surfaces such as gold. There is also comparatively less data on stepped facets as compared to terraces [34, 35]. It is precisely these attributes, namely stepped surfaces and noble metals, that are active for reactions such as CO<sub>2</sub>R [36, 37]. Meanwhile, TPD experiments are more commonly available for these systems [38, 39, 40, 41, 42]. While they might be available for several intermediates and surfaces, they require fitting techniques and interpretation of the underlying kinetics to extract the adsorption energies from the experiment [43].

In the following section, we introduce the main features of the TPD experimental technique and discuss the governing expressions required to model it. We present our method to extract not just adsorption energies, but also adsorbate-adsorbate interaction parameters and adsorbate saturation coverages directly from fits to TPD spectra. In contrast to other methods [44, 45], our approach explicitly accounts for a temperature dependent pre-factor and a coverage dependent desorption energy term. The coverage dependence in the adsorption free

energy arises from both configurational entropy and linear adsorbate-adsorbate interactions. These effects are relevant at low and high coverages, respectively, and accounting for them allows us to fit the entire TPD peak, even in cases where it overlaps with other peaks. We illustrate the use of this method for reported TPD data for CO adsorbed on Au(211) and Au(310) stepped single crystal facets. We compare the adsorption energies and equilibrium coverages against five density functionals and find that RPBE-D3 and PBE are the closest to the TPD value, PBE-D3 overestimates the binding strength, while BEEF-vdW and RPBE slightly underestimates it.

## 4.2 Background on TPD

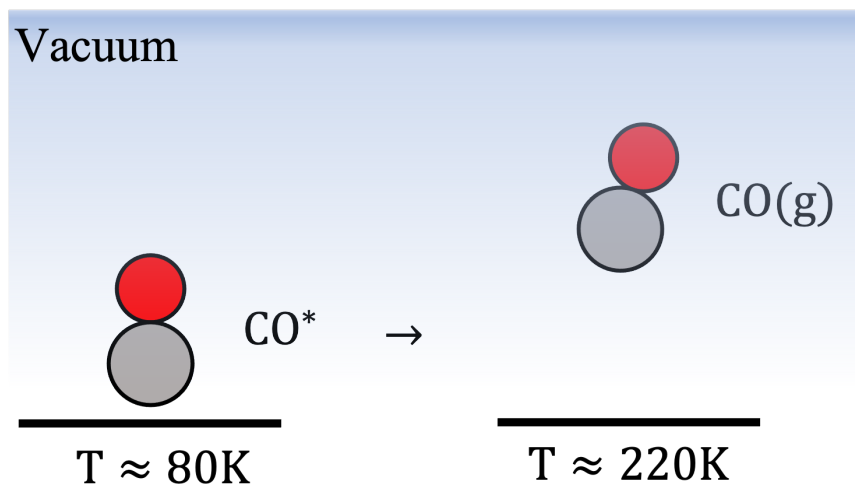


Figure 4.1: Schematic of the TPD experiment; a molecule is dosed onto a given surface at low temperatures (say 80 K). Increasing the temperature causes the adsorbate to desorb (at say 220K). The rate of CO desorption is measured.

In this section we briefly describe the TPD experiment. Figure 4.1 shows a schematic of a typical TPD experiment. A molecule, such as CO, is fed into the system, allowing it to adsorb onto the surface. This step is typically done at

very low temperatures, in order to allow for a large coverage of species to form on the surface. We denote this low temperature coverage as  $\theta_{\text{sat}}$ .

The experiment is carried out in vacuum. The temperature is slowly ramped up as a rate  $\beta$  (units of temperature per time,  $dT/dt$ ) while constantly measuring the amount of desorbed CO at every temperature. This measured quantity is proportional to the change in coverage with temperature,  $d\theta/dT$ , which is easily converted to a rate of change with time,  $d\theta/dt$  by multiplying  $d\theta/dT$  with  $\beta$ . Assuming that the reaction is first order (i.e. it depends on only  $\theta$  of the adsorbate),

$$\text{rate} = \frac{d\theta}{dt} = v(T) \exp\left(-\frac{G_d(\theta, T)}{k_B T}\right) \theta(T) \quad (4.1)$$

where  $v(T)$  is an empirical temperature dependent pre-factor,  $G_d$  is the desorption free energy,  $k_B$  is the Boltzmann constant. The objective is to extract the adsorption energy and interaction parameter between adsorbates from the right hand side of Equation 4.1 based on the knowledge of the rate (left hand side) as a function of  $T$  (independent variable).

The most commonly used methodology to extract the adsorption energy uses the Redhead equation in its linearised form [46, 47],

$$G_d = k_B T_p \ln\left(\frac{v T_p}{\beta} - 3.64\right) \quad (4.2)$$

to relate the free energy of desorption to the peak temperature of the TPD,  $T_p$ .

The two assumptions in the Redhead analysis are that the adsorption energy is independent of coverage and  $v$  is independent of temperature [44]. Another method, known as the Complete Analysis, linearizes Equation 4.1 by plotting  $\ln(\text{rate})$  vs  $1/T$  [44, 47]. Similar to the Redhead analysis, coverage dependence of the adsorption energies is missing from this analysis. More detailed methods to treat TPD experiments include temperature dependent  $v$  as a function of  $G_d$  which is fit to several TPD plots of differing initial dosage [45].

### 4.3 Summary of procedure

The sole input required to extract the adsorption energy is the data from the temperature programmed desorption experiment. Below we provide a step-by-step guide of the procedure.

1. Remove the background signal (typically due to pumping of CO or adsorption of CO on the walls of the container) by fitting an exponential tail to each TPD curve [48] as,

$$\frac{d\theta(T)}{dt} = A \exp(-kT) \quad (4.3)$$

where  $A, k$  are obtained from a least-squares fitting routine. In this work, we use the Python `scipy.optimize.minimize` routine [49].

2. Determine the relative coverage ( $\theta_{\text{rel}}$ ) by integrating the following expression,

$$\theta_{\text{rel}}(T) = \frac{\int_{T_{\text{min}}}^T (d\theta/dT) dT}{\int_{T_{\text{min}}}^{T_{\text{max}}} (d\theta/dT) dT} \quad (4.4)$$

Numerical integration is carried out by using the `numpy` [50] trapezoidal rule integration scheme.

3. Get the free energy of desorption by inverting Equation 4.1 as,

$$G_d = -k_B T \log \left( \frac{d\theta(T)/dt}{v\theta(T)} \right) \quad (4.5)$$

4. Perform the fit for  $G_d$  based on the following expression,

$$G_d(\theta, T) = \Delta E_{\theta \rightarrow 0} - b\theta_{\text{rel}}\theta_{\text{sat}} - k_B T \ln \left( \frac{\theta_{\text{rel}}\theta_{\text{sat}}}{1 - \theta_{\text{rel}}\theta_{\text{sat}}} \right) \quad (4.6)$$

where  $\theta_{\text{sat}}$  is the saturation coverage from the initial dosage,  $\theta_{\text{rel}}$  is the relative coverage based on setting  $\theta_{\text{sat}}$  as the maximum attainable value and  $b$  is the adsorbate-adsorbate interaction parameter.

5. Compare  $\Delta E_{\theta \rightarrow 0}$  against the adsorption enthalpy,  $\Delta H (\approx \Delta E + \Delta \text{ZPE})$  from DFT calculations and  $b$  from  $\Delta H$  obtained from a series of DFT calculations performed in different cell sizes [17, 29].

## 4.4 CO adsorption on gold

### 4.4.1 Illustration of fitting procedure

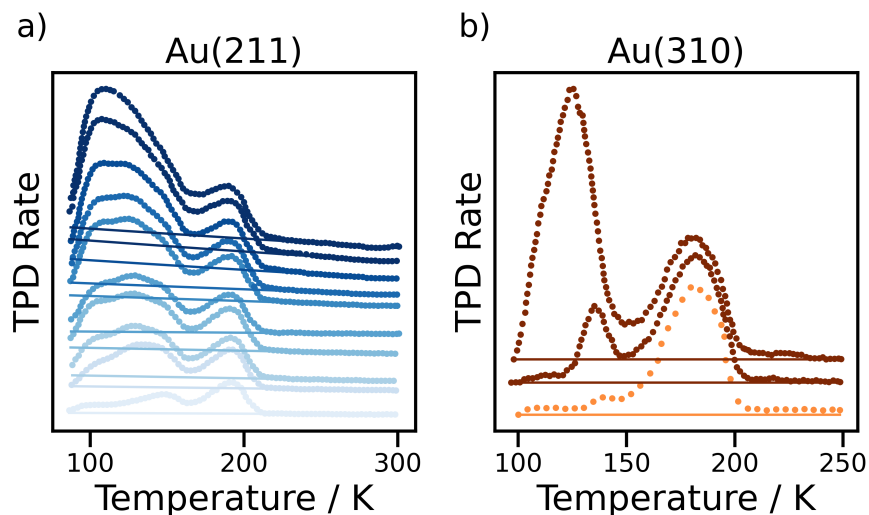


Figure 4.2: Fitted background of Temperature Programmed Desorption curves (solid line) for Au(211) and Au(310) based on the TPD curves from Ref [42] for Au(211) and Ref [39] for Au(310). *Reprinted from paper in Section 10.1* [29]

In this section, we apply the procedure described in Section 4.3 to the CO TPD experiments performed by Ref [42] for Au(211) and Ref [39] for Au(310). We investigate CO adsorption on these stepped gold surfaces as they are active facets for reaction such as  $\text{CO}_2\text{R}$  and CO oxidation [37, 51]. The binding strength of CO is challenging to obtain accurately, particularly for GGA DFT, due to the incorrect alignment of the  $2\pi^*$  state of  $\text{CO}^*$  [31, 32, 52]. This lack of accuracy in determining the adsorption energies leads to inaccuracies in mechanistic modelling of reactions involving CO (or similar reaction intermediates).

As a first step to the procedure, we correct the experimental TPD data by removing any background signal present during the experiment. Background signals can come from multiple sources, such as adsorption (and later desorp-

tion) of CO from the walls of the apparatus. Figure 4.2 shows the extracted experimental data (points) and the correction for the background signal from Equation 4.3 (line in Figure 4.2).

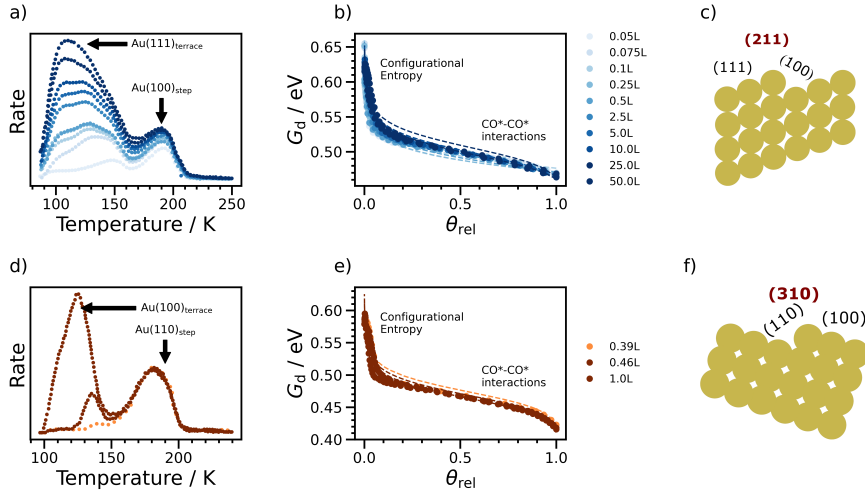


Figure 4.3: (a and d) Background corrected rates of CO desorption from TPD experiments in previous work for Au(211) from Ref [42] and Au(310) Ref [39] site motifs assigned to each peak are labelled directly in the figure; (b and e)  $G_d$  as a function of the relative TPD coverage under vacuum conditions for the Au(100) step and Au(110) step; the dashed line indicates the best fit to the points (c and f) schematic of (211) and (310) surfaces. *Reprinted from paper in Section 10.1 [29]*

Figure 4.3(a,d) shows the TPD curves post correction for Au(211) and Au(310) respectively. The different shades of blue and brown represent the initial exposure of CO (in Langmuir, L). The peaks at lower temperatures in Figure 4.3a correspond to (111) terrace sites and higher temperatures to stronger binding (100) step sites. Similarly, in Figure 4.3d, the low temperature peaks are (100) terrace sites, and the high temperature peaks are considered to be (110) step sites.

We perform the next step of the treatment in Section 4.3 to the TPD plots of

Figure 4.3(a,d). Assuming a first order reaction, we “invert” the rate equation in Equation 4.1 to express it as a function of the  $G_d(\theta, T)$  as in Equation 4.5. The *relative* coverage is determined from Equation 4.4 as a function of temperature. Note that the coverage is relative and not absolute because we do not know the low temperature saturation coverage,  $\theta_{\text{sat}}$ . Figure 4.3(b,e) shows the two extracted parameters,  $G_d$  and  $\theta_{\text{rel}}$  plotted against each other for Au(211) and Au(310) surfaces.

The variation of  $G_d$  with  $\theta_{\text{rel}}$  allows us to split  $G_d$  into its constituent components. At mid-to-large  $\theta_{\text{rel}}$ ,  $G_d$  decreases linearly. This decrease in  $G_d$  is due to the interaction of the adsorbate with other adsorbates on the surface. In this analysis, we assume that there is only one species on the surface (i.e. only CO\* is present). Given the linearity of  $G_d$ , we choose to model this adsorbate-adsorbate interaction energy as,

$$\Delta G_{\text{ads-ads}} = b\theta_{\text{rel}}\theta_{\text{sat}} = b\theta \quad (4.7)$$

where  $b$  is assumed to be a constant. This (repulsive) term dominates the variation of  $G_d$  when  $\theta$  is large. While we have chosen a comparatively simple functional form for the adsorbate-adsorbate interactions, more complex functions can be used in the subsequent fitting procedure by simply altering  $\Delta G_{\text{ads-ads}}$ .

At very low  $\theta_{\text{rel}}$  ( $< 0.1$ ) it appears that the  $G_d$  increases sharply. The cause of this increase is the configurational entropy, which diverges at very small or very large coverages (see Chapter 2 for a more detailed discussion of the configurational entropy). We model the differential configurational entropy based on the expression in Subsection 2.3.2 and plotted in Figure 2.5,

$$\Delta S_{\text{conf}} = -k_B \ln \left( \frac{\theta}{1-\theta} \right)$$

To simplify our analysis, we assume that  $G_d$  is expressed exclusively as the sum of the repulsive adsorbate-adsorbate interaction term and the configura-



tional entropy term as,

$$G_d = \Delta E_{\theta \rightarrow 0} - T\Delta S_{\text{conf}} + \Delta G_{\text{ads-ads}} \quad (4.8)$$

where  $\Delta E_{\theta \rightarrow 0}$  is the sum of the internal energy at the dilute coverage limit ( $\theta \rightarrow 0$ ) and  $\Delta \text{ZPE}$  is the difference in zero-point energy between the adsorbed and gas-phase states of CO. Written out explicitly, we obtain Equation 4.6. By considering only these three terms contribute to  $G_d$ , we have implicitly assumed the following,

1. The internal energy of the transition state for CO desorption is well approximated by that of CO(g). That is, the internal energies of the transition state is the sum of the gas-phase CO species and that of the surface,

$$E_{\text{CO}^{\text{TS}}} \approx E_{\text{CO}(\text{g})} + E_*$$

2. The entropic contributions of CO is similar to that of CO\* and both can be described harmonically.

$$S_{\text{CO}^{\text{TS}}} \approx S_{\text{CO}^*}$$

Figure 4.4 shows the different components of Equation 4.6 based on TPD data of Figure 4.3. Within error bounds from the least-squares error fitting procedure,  $\Delta E_{\theta \rightarrow 0}$ , shown in Figure 4.4a, does not vary with initial exposure. This result is consistent with the assumption that the internal energy obtained by splitting the contributions of  $G_d$  is independent of the coverage. As expected, the configurational entropy is significant only at very low coverages, while the adsorbate-adsorbate interactions are large at high coverages (Figure 4.4b).

#### 4.4.2 Equilibrium coverages from TPD

Having extracted  $G_d$  from the TPD experiment, we now convert it to the *equilibrium* coverage,  $\theta$ . To do so, we express the free energy of adsorption,  $\Delta G(\theta, T)$

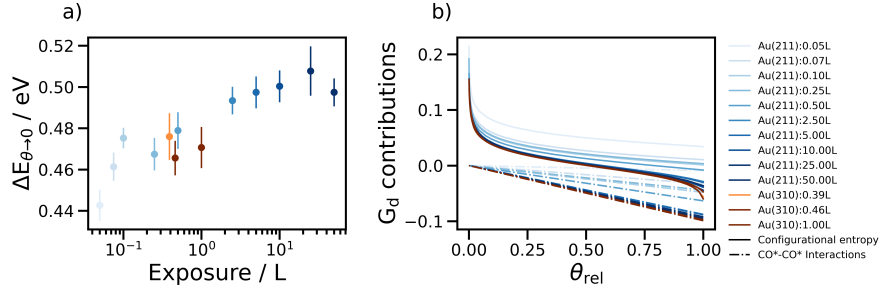


Figure 4.4: Desorption energy corresponding to dilute coverages,  $\Delta E_{\theta \rightarrow 0}$  of CO for (100) step and (110) step as a function of the initial exposure in Langmuir in the TPD experiment. Error bars show errors from the fit determined as the mean error of the residual; (b) contributions of the configurational entropy (solid lines) and CO-CO adsorbate-adsorbate interaction (dashed-lines) to the total desorption energy  $G_d$  based on the fitting equation described in Equation 4.6. *Reprinted from paper in Section 10.1 [29]*

as,

$$\Delta G(\theta, T) = -G_d(\theta, T) - T \left( S_{\text{CO}^*}^{\text{harm}} - S_{\text{CO}(g)}^{\text{ideal}} \right) - k_B T \ln(p_{\text{CO}}) \quad (4.9)$$

where  $p_{\text{CO}}$  is the pressure of CO referenced to 1 bar,  $S_{\text{CO}^*}^{\text{harm}}$  is the entropy of  $\text{CO}^*$  (under the harmonic approximation) and  $S_{\text{CO}(g)}^{\text{ideal}}$  is the entropy of the gas-phase CO molecule (under the ideal-gase approximation).

Note that the  $\theta$  and  $T$  dependence is implicit in Equation 4.9 and so the equation has to be solved numerically. To highlight this  $\theta$  dependence, we separate Equation 4.9 into the free energy at standard conditions,  $\Delta G_{\theta=\frac{1}{2}}$  under conditions of  $\theta = 1/2$  ML (monolayer),  $p_{\text{CO}} = 1$  bar and  $T = 298.15$  K

$$\Delta G_{\theta=\frac{1}{2}} = -\Delta E_{\theta=\frac{1}{2}} + \frac{b}{2} - T \left( S_{\text{CO}^*}^{\text{harm}} - S_{\text{CO}(g)}^{\text{ideal}} \right) \quad (4.10)$$

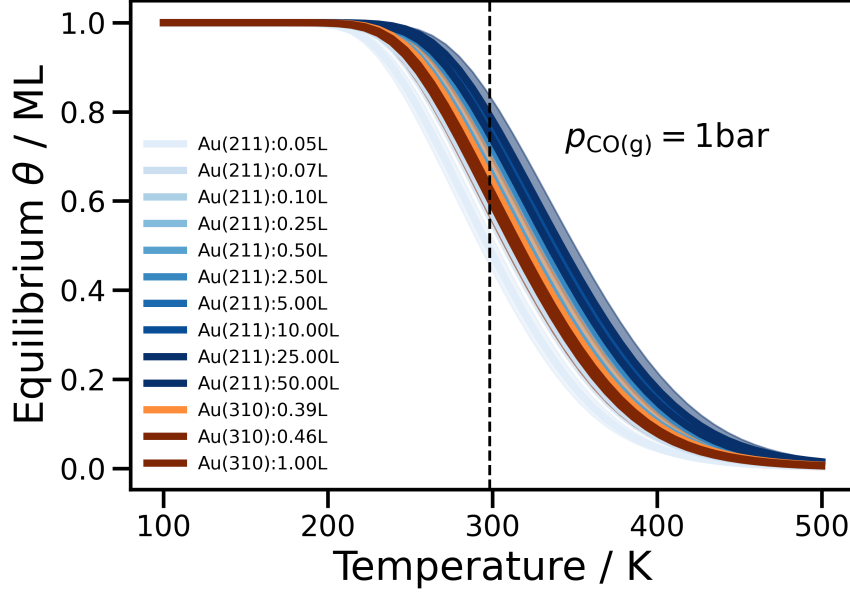


Figure 4.5: Equilibrium coverage of CO as a function of the temperature at 1 bar CO(g) pressure for both surface facets (211) and (310) for all considered initial exposures. The dashed black line shows the equilibrium coverage at 298.15 K. *Reprinted from paper in Section 10.1 [29]*

substituting Equation 4.10 into Equation 4.9 and rearranging gives,

$$\Delta G_{\text{CO}^*} = \Delta G_{\theta=\frac{1}{2}} + b \left( \theta - \frac{1}{2} \right) + k_B T \ln \left( \frac{\theta}{1-\theta} \right) - k_B T \ln(p_{\text{CO}}) \quad (4.11)$$

where we set the right hand side of Equation 4.11 to 0 as the equilibrium coverage would be at  $\Delta G(\theta, T) = 0$ ,

$$\theta(T, p_{\text{CO}}) = \frac{K(\theta, T)p_{\text{CO}}}{1 + K(\theta, T)p_{\text{CO}}} = \exp \left( - \frac{\Delta G_{\theta=\frac{1}{2}} + b \left( \theta - \frac{1}{2} \right)}{k_B T} \right) \quad (4.12)$$

Figure 4.5 shows the equilibrium coverage of CO,  $\theta$  which is the result of the numerical solution of Equation 4.12 at 1 bar CO(g). Given that 1 ML

corresponds to complete coverage of sites, all exposures on both (100) step and (110) step sites show approximately a coverage of between 0.4 to 0.9 ML present on both (211) and (110) surfaces at a temperature of 300 K and pressure of 1 bar CO(g).

#### 4.4.3 Benchmark of exchange correlation functionals

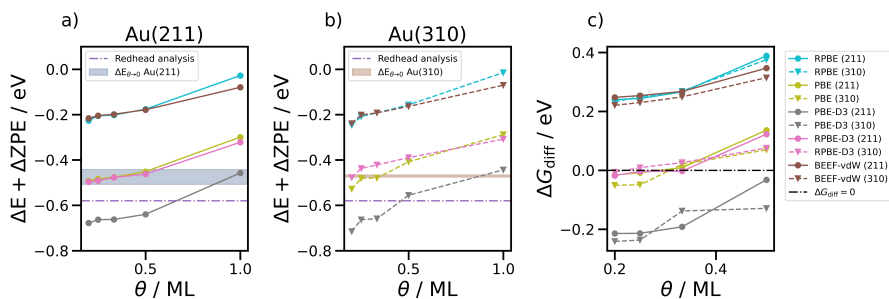


Figure 4.6: DFT calculated adsorption energies as a function of the step coverage on (a) 211 (b) 310 (c) differential free energies for CO adsorption; all points at the different coverages are for the most stable adsorption site; in (a and b) the colored bands indicate  $\Delta E_{\theta \rightarrow 0}$  obtained from the TPD analysis for each facet, and the purple dashed line the value from Redhead analysis. *Reprinted from paper in Section 10.1* [29]

In this section, we compare the adsorption energies and equilibrium coverages obtained through the TPD curves against DFT computed enthalpies. Three different exchange-correlation functionals are chosen based on their common usage in studies in the field of heterogeneous catalysis, namely PBE [24], RPBE [25] and BEEF-vdW [53]. We also compute the adsorption energies along with an empirical dispersion correction from Ref [54] for the PBE and RPBE functional.

Figure 4.6(a,b) shows the computed enthalpy (denoted as  $\Delta E + \Delta ZPE$ ) for the two stepped facets. For comparison, we indicate  $\Delta E_{\theta \rightarrow 0}$  as a blue and brown band for the (211) and (310) facet respectively. RPBE-D3 and PBE

are the closest to the TPD estimates in the low coverage region. RPBE and BEEF-vdW, underestimate binding of CO while PBE-D3 overestimates it.

We also compare the equilibrium coverage from the computations against those obtained from the TPD experiment (in Figure 4.5). To do so, we compute the differential adsorption free energy,  $\Delta G_{\text{diff}}$ , defined as,

$$\Delta G_{\text{diff}} = \frac{G_m - G_n - (m - n)G_{\text{CO(g)}}}{m - n} \quad (4.13)$$

where  $G_x$  is the free energy corresponding to a system with  $x$  adsorbed CO\* and  $G_{\text{CO(g)}}$  is the free energy of gas-phase CO(g). The DFT predicted free energy would then be the coverage at which

$$\Delta G_{\text{diff}} = 0 \quad (4.14)$$

Figure 4.6 shows  $\Delta G$  for the different functionals for Au(211) and Au(310). For RPBE-D3 and PBE functionals, the equilibrium coverage is close to 0.5 ML, determined as the coverage where the lines (dashed for 310 and solid for 211) meet the  $\Delta G_{\text{diff}} = 0$  line. This computed equilibrium coverage is close to the lower bound of the TPD extracted value ( $\approx 0.4$  ML).

In summary, we extract the adsorption energies and equilibrium coverages at standard conditions from TPD experiments. We do so by interpreting the underlying kinetics and fitting the experimental free energy to a model including repulsive adsorbate-adsorbate interactions and the configurational entropy. We compare the dilute coverage adsorption enthalpy estimated from TPD against the same quantity from DFT calculations with different exchange-correlation functionals. We hope that this approach provides a simple method to benchmark adsorption energies from DFT calculations for systems where only TPD data is available.

## 4.5 Water adsorption on gold

In the previous section, we described how to compare computed energies against TPD derived energies for first order reaction processes. In this section, we compare the computed water adsorption energies against TPD extracted values. Unlike CO adsorption, water adsorption is a zeroth order process, with a rate expression,

$$\text{rate} = v(T) \exp\left(-\frac{G_d}{k_B T}\right) \quad (4.15)$$

which is used to extract a value for  $G_d$  if  $v(T) = k_B T/h$  and Equation 4.15 is linearised (by applying  $\ln$  on both sides of the equation) [44]. Figure 4.7a shows the zeroth order TPD plots for water adsorption on Au(310) from Ref [40]. As a computational analogue, we use a single layer of water on an Au(310) surface (schematic shown in Figure 4.7b-f). We compute the *average* adsorption energy,  $\Delta \langle E \rangle$  as,

$$\Delta \langle E \rangle = \frac{E_n - E_* - nE_{\text{H}_2\text{O}}}{n} \quad (4.16)$$

where  $n$  is the number of water molecules considered in the calculation. At coverages greater than 0.5 ML,  $\Delta \langle E \rangle$  saturates at a constant value of  $\approx -0.4$  eV. This value is compared against the TPD adsorption energy, which is  $-0.49$  eV for the low temperature peak (present for low exposures in green) and  $-0.57$  eV for the high temperature peaks (present for both high and low exposures, red and green). In either case, the computed adsorption energy is underestimated by at least 0.1 eV.

An interesting feature of Figure 4.7g is that the (average) adsorption energy decreases with coverage. In contrast, the adsorption energy of CO (in Figure 4.6) increases with coverage. These contrasting coverage dependencies suggest that water is stabilised with increasing coverage, while CO is destabilised.

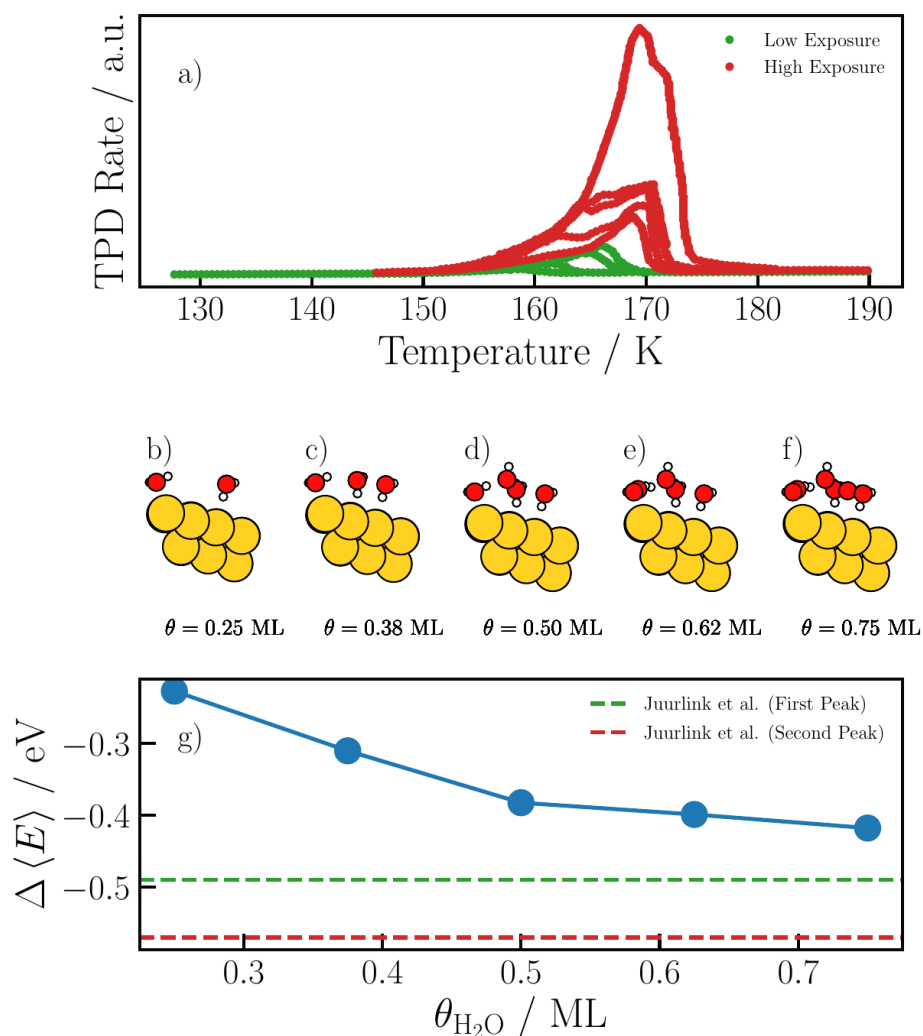


Figure 4.7: a) Water adsorption TPD experiments reproduced from Ref [40], where red points denote exposure greater than 1 L and green points have exposures lower than 1 L; (b-f) schematic illustrates the number of water molecules used for each coverage. (g) Average adsorption energy of  $\text{H}_2\text{O}$  on Au(310) computed using ab initio molecular dynamics simulations; experimentally determined values of the adsorption energy from Ref [40] are indicated by the red and green dashed lines corresponding to high exposure (second peak) and low exposure (first peak). *Reprinted from paper in Section 10.2 [29]*

## 4.6 CO adsorption on metal-doped graphene

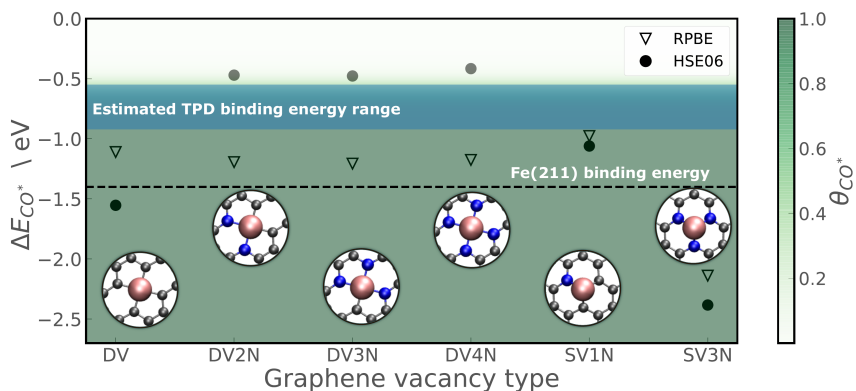


Figure 4.8: Comparison of adsorption energies of CO on iron-doped vacancies as proposed in ref 20. Calculated with the GGA-RPBE functional (triangles) and the hybrid HSE06 functional (circles). Experimental estimate from TPD spectra from Ref [55] is marked by the blue band. The background fill indicates the coverage of CO predicted by the kinetic model using RPBE energetics. Fe(211) binding energies are shown with the dashed black line as a reference. *Reprinted from paper in Section 10.3* [56]

In this section, we compare TPD adsorption energies against DFT energies for metal-doped graphene materials. These materials have attracted attention in the field of CO<sub>2</sub>R (commonly referred to as MNC for metal-nitrogen-carbon) [57, 58, 59]. They have been experimentally shown to give large current densities (geometric current densities exceed 100 mA cm<sup>-2</sup> at -0.4 V vs RHE for Fe-doped graphene [60]). Given their importance as a CO<sub>2</sub>R catalyst, it is critical that the adsorption energies are predicted accurately from computations.

Figure 4.8 shows the adsorption energy of CO on different site motifs of Fe doped graphene (nitrogen concentration is altered). We consider both spin-polarized RPBE (triangles) and HSE06 (circles) functionals, which are prototypes for GGA-DFT and hybrid-DFT, respectively. For most site motifs, we find that the adsorption energies from HSE06 is different from RPBE. How-



ever, HSE06 adsorption energies for DV2N, DV3N and DV4N are comparatively closer to the TPD estimated energies (blue band). We discuss the practical consequences for this disparity in prediction of adsorption energies in Chapter 8.

## 4.7 Conclusion and outlook

In this chapter, we presented a method to extract adsorption energies, adsorbate-adsorbate interaction parameters and equilibrium coverages from TPD experiments. We compared adsorption energies and equilibrium coverages with GGA DFT calculations performed with different exchange correlation functionals. As basis for comparison, we chose three systems relevant for heterogeneous catalysts, CO adsorption on stepped gold surfaces, water adsorption on Au(310) and CO adsorption on Fe doped graphene.

## 4.8 Computational methods

Density functional theory calculations were performed using Vienna Ab-initio Software Package (VASP) [61]. Core electrons were described using Projector Augmented Waves (PAW) potentials [62]. Valence electrons were described using plane-waves with kinetic energy up to 500 eV. Gaussian smearing with a width of 0.1 eV was used. The functionals used to benchmark CO adsorption on gold were BEEF-vdW [53], RPBE [25], PBE [24], RPBE-D3 [25, 54], PBE-D3 [24, 54]. Structures were prepared using the Atomic Simulation Environment (ASE) [63]. The lattice constant of gold was optimized using a 12x12x12 Monkhorst-Pack [64]  $k$ -point mesh grid. Slabs four layers thick were made (211) and (310) facets were constructed, with the bottom two layers kept fixed. For the (211) surface, (1x3), (2x3), (3x3), (4x3) and (5,3) cells were used with  $k$ -points (12,4,1), (6,4,1), (4,4,1), (3,4,1) and (3,4,1) respectively. For the (310) surface (1x4), (2x4), (3x4), (4x4) and (5,4) cells were used with  $k$ -points (12,6,1), (6,6,1), (4,6,1), (3,6,1) and (3,6,1) respectively. All calculations were run using AiiDA [65], which keeps track of the provenance of each result. Static adsorp-

tion energies for were calculated on all unique surface sites on each facet. Initial structures were generated using pymatgen [66]. All geometries were optimized until forces on all atoms was less than  $0.025 \text{ eV \AA}^{-1}$ . Vibrational frequencies were computed using a finite difference method as implemented in VASP [61].

For metal-doped graphene systems, the RPBE functional was used for GGA DFT calculations, while the HSE06 functional was used for hybrid calculations [67, 68]. Relaxation is not considered when performing calculations with hybrid functionals, the structure is kept fixed to that of the relaxed configuration from an RPBE+U calculation [69]. All calculations were performed with spin-polarization.

For all *ab-initio* molecular dynamics (AIMD) calculations, valence electrons were described using plane-waves with kinetic energy up 400 eV for ab-initio MD calculations (as opposed to 500 eV used for static calculations). Gaussian smearing with a width of 0.1 eV was used. The BEEF-vdW [53] functional was used for all AIMD calculations.

## Chapter 5

# Scaling relations with the Newns-Anderson and $d$ -band model

In Chapter 2, we illustrated the importance of the chemisorption energy in catalysis. We described how to obtain them in practice, both from DFT calculations and from TPD experiments in Chapter 4. In this section, we explore trends in these chemisorption energies along and across rows of the periodic table for different adsorbates.

### 5.1 Introduction

Understanding the formation of a bond between a metallic surface and an adsorbate is critical to the field of heterogeneous catalysis [33, 70]. The strength of this bond is quantified by the chemisorption energy, usually determined either

---

This chapter is being prepared for submission under the title: *Limits to scaling relations between adsorption energies?* [Sudarshan Vijay](#), Karen Chan and Jens K Nørskov (2022).

through surface science experiments or DFT calculations.

The chemisorption energy determines if a chosen (metallic) surface is an active catalyst for a given reaction [71]. If an adsorbate present in a chosen reaction network binds too strongly, it will poison the surface, preventing successive reaction steps from taking place. Conversely, if its binding strength is too weak, there would not be enough of it present on the surface for the subsequent reaction to occur. This idea, known as the Sabatier principle, suggests that the most active catalyst for a reaction has an optimum binding strength (and hence optimum chemisorption energy), neither too strong, nor too weak.

The Sabatier principle has been realised in practice for a variety of reactions in heterogeneous catalysis through so-called volcano relationships. Within this model, the chemisorption energies (and, if available, activation energies) of all reaction intermediates are linearly mapped onto the chemisorption energies of a smaller selection of adsorbates [34, 72, 73]. These chosen adsorbates are denoted as descriptors for the reaction. This mapping greatly simplifies the study of reaction networks. Instead of the cumbersome task of computing chemisorption energies for several intermediates on many surfaces, one computes the energies on a handful of transition metals and establishes linear “scaling-relations” for that reaction. This simplification has facilitated several high-throughput computational studies [33] to search for new catalysts, as only the chemisorption energies of the descriptors (usually one or two in number) needs to be determined to gauge the activity towards a given reaction.

The simplicity of this approach is predicated on linear scaling relations between the chemisorption energies of the adsorbates involved in the reaction network. Such a linear relationship is observed when two adsorbates bind to the metal through the same atom such as \*C, \*CH, \*CH<sub>2</sub> and \*CH<sub>3</sub>[74], where \* denotes the surface. However, it is not observed when the binding atom is different, such as in the case of \*C and \*O [34].

The lack of scaling between carbon and oxygen implies that reactions involving both of these species need at least two descriptors in order to fully describe their reaction network. Practically, this need for two descriptors leads to the

conclusion that materials that are too strong binding for one reaction might not be so for another. Consider platinum, which is considered too strong binding for carbon based reactions such as electrochemical reduction of  $\text{CO}_2$  [75]. Meanwhile, the same material is considered slightly weak binding for oxygen based reactions such as the oxygen reduction reaction [76]. Thus, it is essential that we understand the limits of linear scaling, while having an *a priori* estimate on whether two adsorbates will or will not scale with each other.

In this work, we develop a model for chemisorption of small molecule adsorbates on transition metal surfaces. Our model combines a modified form of the Newns-Anderson hybridisation energy accounting for both *sp* and *d* metal-adsorbate interactions with an effective expression for the orthogonalisation energy. We apply our model to investigate scaling relations (or lack thereof) between atomic carbon and oxygen adsorbed on late transition metal surfaces. Our model shows that the root cause of the deviation away from scaling lies in the differences in the re-normalised single particle reference energies of the lower lying O-*p* states as compared to the higher lying C-*p* states. We quantify the effect that this difference has on the chemisorption energy through the maximum *d*-band centre at which the *d*-band contributes net-zero to the Newns-Anderson hybridisation energy. Through this analysis, we identify the exact conditions under which carbon and oxygen do scale with each other; linear scaling is established by using late transition metals of the same row in the scaling line, without the noble metals.

## 5.2 Model development

There are primarily two effects that alter the electronic states of an atom when it is adsorbed on a surface as compared to when it is in vacuum. First, the states of the adsorbate upon chemisorption need to be orthogonal to that of the metal atom. This requirement is known as Pauli repulsion and is an energetic cost to chemical bonding. Second, the adsorbate states are shifted down in energy and broadened into resonances when interacting with the *sp*-states of the metal

surface. There is an additional interaction with the  $d$ -electrons of the metal, if it contains any. The hybridisation energy resulting from the  $sp$  and  $d$ -electrons of the metal is a net energy gain. Thus, chemical bonding on metallic surfaces is a competition between the net positive contributions of Pauli repulsion and the net negative contributions due to hybridisation.

$$E_{\text{chem}} = \underbrace{E_{\text{d-hyb}} + E_{\text{sp-hyb}}}_{\text{Hybridisation}} + \underbrace{E_{\text{ortho}}}_{\text{Orthogonalisation}} + \dots \quad (5.1)$$

Other factors that influence the chemisorption energy include electrostatic interactions, coverage of other species on the surface, etc. We explore these factors through DFT calculations separately in latter sections of this thesis. In this section we discuss a model that captures the hybridisation and orthogonalisation contributions.

### 5.2.1 Hybridisation with $sp$ and $d$ states of the metal

We begin by treating the hybridisation energy coming from the interaction of the adsorbate with the  $d$  and  $sp$  states of the metal. We use the Newns-Anderson model of chemisorption with a modified coupling parameter,  $\Delta$ , to treat both of these contributions simultaneously. We write  $\Delta$  as the sum of terms coming from the  $d$ -states,  $\Delta_d$  and the  $sp$ -states,  $\Delta_0$ .

$$\Delta = \Delta_d + \Delta_0 \quad (5.2)$$

where  $\Delta_d$  is treated in a similar fashion to that used in the work of Newns in semi-elliptical form,

$$\Delta_d(\epsilon) = \pi V_{ak}^2 \rho_d = \frac{\pi V_{ak}^2}{\pi w_d/2} \left[ 1 - \left( \frac{\epsilon - \epsilon_d}{w_d} \right)^2 \right]^{1/2} \quad (5.3)$$

where the  $\pi w_d/2$  normalisation comes from the fact that we set  $\int \rho_d d\epsilon = 1$ , i.e. the integral of the semi-elliptical  $d$ -density of states is set to 1. As a result,  $\int \Delta_d d\epsilon = \pi V_{ak}^2$ , i.e. the height of the semi-ellipse is dictated only by  $V_{ak}$  as

in Ref [11]. We represent the *sp*-states of the metal as a constant over a fixed energy range, i.e. we assume that it has a rectangular density of states.

$$\Delta_0(\epsilon) = b \quad \forall \quad \epsilon_{sp}^{\min} < \epsilon < \epsilon_{sp}^{\max} \quad (5.4)$$

The Hilbert transform of the combined metallic density of states function,  $\Delta$  is given by,

$$\Lambda(\epsilon) = \frac{P}{\pi} \int_{-\infty}^{\infty} \frac{\Delta_d(\epsilon') + \Delta_0(\epsilon')}{\epsilon - \epsilon'} d\epsilon' \quad (5.5)$$

where  $P$  denotes the Cauchy principal value.

Scaling all energies by the width of the metal *d*-band and translating such that the *d*-band centre is at 0,  $\epsilon_r = (\epsilon - \epsilon_d)/w_d$  and realizing that the Cauchy principal value of the function  $\Delta_0/(\epsilon - \epsilon')$  is 0,

$$\Lambda(\epsilon_r) = 2 \frac{V_{ak}^2}{w_d} P \int_{-1}^1 \frac{(1 - \epsilon_r'^2)^{1/2}}{\epsilon_r - \epsilon_r'} d\epsilon_r' \quad (5.6)$$

In line with the normalised eigenvalues of the semi-infinite chain, we set  $\epsilon_r' = -\cos \theta$ .

$$\Lambda(\epsilon_r) = 2 \frac{V_{ak}^2}{w_d} P \int_0^\pi \frac{\sin^2 \theta}{\epsilon_r + \cos \theta} d\theta \quad (5.7)$$

which can be simplified for the three different regions of energy,

$$\Lambda(\epsilon_r) = \begin{cases} 2\pi V_{ak}^2/w_d [\epsilon_r], & |\epsilon_r| < 1 \\ 2\pi V_{ak}^2/w_d [\epsilon_r + (\epsilon_r^2 - 1)^{1/2}], & \epsilon_r < -1 \\ 2\pi V_{ak}^2/w_d [\epsilon_r - (\epsilon_r^2 - 1)^{1/2}], & \epsilon_r > 1 \end{cases} \quad (5.8)$$

We now have all the quantities needed to determine the hybridisation energy from the Newns-Anderson model,

$$\Delta E_{d\text{-hyb}} + \Delta E_{sp\text{-hyb}} = \frac{2}{\pi} \int_{-\infty}^{\epsilon_f=0} \arctan \left( \frac{\Delta + \Delta_0}{\epsilon - \epsilon_a - \Lambda} \right) d\epsilon - 2\epsilon_a \quad (5.9)$$

where the range of arctan is between 0 to  $-\pi$ . The term  $\Delta E_{d\text{-hyb}} + \Delta E_{sp\text{-hyb}}$  represents the combined hybridisation energy coming from interaction of the adsorbate with the  $sp$  and  $d$  states of the metal. Figure 5.1a shows this combined hybridisation energy plotted for different values of  $\Delta_0$ . With an increase in  $sp$  contribution, the hybridisation energy becomes more negative.

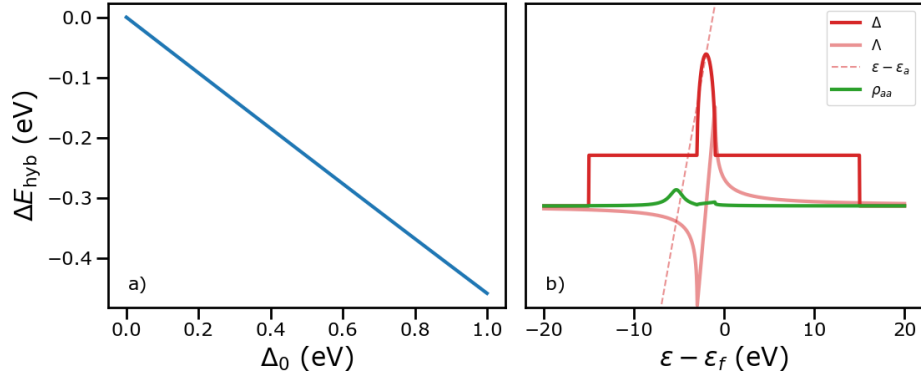


Figure 5.1: a) Total hybridisation energy as a function of the choice of  $\Delta_0$  for  $w_d = 2$  eV,  $V_{ak}^2 = 1$  eV,  $\epsilon_a = -5$  eV and  $\epsilon_d = -2$  eV b) Representative quantities from the Newns-Anderson model ( $\Delta, \Lambda, \epsilon - \epsilon_a$  and adsorbate projected density of states  $\rho_{aa}$ ) when  $\Delta_0 = 1$  eV.

The adsorbate projected density of states is computed similarly as in the Newns-Anderson model, just using  $\Delta$  from the above discussion,

$$\rho_{aa} = \pi^{-1} \frac{\Delta_d + \Delta_0}{[\epsilon - \epsilon_a - \Lambda]^2 + (\Delta_d + \Delta_0)^2} \quad (5.10)$$

Figure 5.1b shows a schematic of  $\rho_{aa}$  (in green) for some representative values of  $\Delta_0$ . Note that the localised states on either end of  $\Delta$  are broadened out due to the contribution of the  $sp$ -states. This broadening is in contrast to  $\delta$ -functions obtained from the Newns-Anderson model (Equation 2.11). A practically consequence of including  $\Delta_0$  is that  $\rho_{aa}$  needs to be integrated numerically throughout the entire  $\epsilon$  region going from  $-\infty$  to 0 in the process of determining  $n_a$  (see Section 5.5 for implementation details.)



### 5.2.2 Orthogonalisation energy

We now turn to determining the expression for the orthogonalisation energy. To do so, we explore the energies from the simple two-level energy problem including non-zero overlap between the two states. We then compare them with the Newns-Anderson energies for the same scenario and isolate extra terms. These extra terms correspond to the energetic consequence of overlap between the two states, a contribution missing from the Newns-Anderson model, but present in the two-level problem. As a consequence, these additional terms represents the orthogonalisation energy.

#### Two-level problem

Let the adsorbate state be represented by an energy of  $\epsilon_a$  and corresponding eigenstate  $\psi_a$  and the metal states given by  $\epsilon_k$  with the eigenstate  $\psi_k$ . Similar to Ref [10], we use the framework of linear combination of atomic orbitals (LCAO), the combined eigenstate is given by  $\psi = c_a\psi_a + c_k\psi_k$ .

Further, we write the off-diagonal terms such that  $\langle\psi_a|H|\psi_k\rangle = V_{ak} = \langle\psi_k|H|\psi_a\rangle = V_{ka}$  where  $V_{ak} = V_{ka}$  is constant coupling element. The overlap element  $S$  is given by  $\langle\psi_a|\psi_k\rangle$ . The eigenvalue problem is written as,

$$(\mathbf{H} - \mathbf{S}\epsilon) \mathbf{c} = 0 \quad (5.11)$$

where  $\mathbf{H}$  is the Hamiltonian written in matrix form,

$$\mathbf{H} = \begin{pmatrix} \epsilon_a & V_{ak} \\ V_{ak} & \epsilon_k \end{pmatrix} \quad (5.12)$$

and the overlap matrix,  $\mathbf{S}$  is given by,

$$\mathbf{S} = \begin{pmatrix} 1 & S \\ S & 1 \end{pmatrix} \quad (5.13)$$

For our chosen  $\mathbf{H}$ , we would need the following determinant to be 0,

$$\begin{vmatrix} \epsilon_a - \epsilon & V_{ak} - S\epsilon \\ V_{ak} - S\epsilon & \epsilon_k - \epsilon \end{vmatrix} = 0 \quad (5.14)$$

which upon simplification yields,

$$\epsilon_{\mp} = \frac{\epsilon_a + \epsilon_k - 2V_{ak}S_{ak} \pm \sqrt{(\epsilon_a - \epsilon_k)^2 - 4V_{ak}S(\epsilon_a + \epsilon_k) + 4V_{ak}^2 + 4S^2\epsilon_a\epsilon_k}}{2(1 - S^2)} \quad (5.15)$$

where  $\epsilon_{\mp}$  denotes the energies of the anti-bonding and bonding state. Similar to previous work, we assume that  $S \ll 1$  leading to all the terms multiplied by  $S$  in the square root being neglected and  $1 - S^2 \approx 1$  in the denominator.

$$\epsilon_{\mp} = \frac{\epsilon_a + \epsilon_k}{2} - V_{ak}S \pm \frac{1}{2}\sqrt{(\epsilon_a - \epsilon_k)^2 + 4V_{ak}^2} \quad (5.16)$$

### Narrow-band limit of the Newns-Anderson model

The two-level problem can also be represented within the Newns-Anderson model by using the following narrow-band limit of  $\Delta$ ,

$$\Delta = \pi V_{ak}^2 \rho_d = \pi V_{ak}^2 \delta(\epsilon - \epsilon_d) \quad (5.17)$$

that is, the  $d$ -states of the metal is just a  $\delta$  function at  $\epsilon = \epsilon_d$ . By solving the Newns-Anderson model with this  $\Delta$ , we will compare the obtained energies of the bonding and anti-bonding states with that of the two-level problem to isolate the contributions of  $S \neq 0$ . These contributions will represent the orthogonalisation penalty in our model.

For this  $\Delta$  function, the Hilbert transform is computed analogous to Equation 2.7 as,

$$\Lambda(\epsilon) = \pi V_{ak}^2 \frac{P}{\pi} \int_{-\infty}^{\infty} \frac{\delta(\epsilon - \epsilon_d)}{\epsilon - \epsilon'} d\epsilon' \quad (5.18)$$

which upon simplification gives the following expression for  $\Lambda$ ,

$$\Lambda(\epsilon) = \frac{V_{ak}^2}{\epsilon - \epsilon_d} \quad (5.19)$$

Finally, we are interested in determining the poles,  $\epsilon_p$  at which the term  $\epsilon_p - \epsilon_a - \Lambda(\epsilon_p) = 0$ . Solving the quadratic roots problem gives the following expression for the poles,  $\epsilon_p$ ,

$$\epsilon_p = \frac{\epsilon_a + \epsilon_d}{2} \pm \frac{1}{2} \sqrt{(\epsilon_a - \epsilon_d)^2 + 4V_{ak}^2} \quad (5.20)$$

Comparing the expression for  $\epsilon_{\pm}$  in Equation 5.16 with  $\epsilon_p$  from Equation 5.20 ( $\epsilon_k \equiv \epsilon_d$  for a  $\delta$  function distribution of  $\Delta$ ), it is clear that the extra term for each of the anti-bonding and bonding state is  $V_{ak}S$ . Thus, the orthogonalisation energy for a  $\delta$  function distribution of  $\Delta$  would be of the form,

$$E_{\text{ortho}}^{\delta} = -2V_{ak}S \quad (5.21)$$

Since the model of  $\Delta$  for the hybridisation energy is a semi-ellipse while the orthogonalisation term was derived for a  $\delta$  function, the coupling term in the orthogonalisation energy needs to incorporate non-integer occupancy. In our model, we simply replace  $S$  by  $(n_a + f)S$  where  $n_a$  is the occupancy of the single-particle adsorbate state upon adsorption given by Equation 2.15 and  $f$  is the filling of the metal atom. So, the final expression for the orthogonalisation energy is,

$$E_{\text{ortho}} = -2(n_a + f)V_{ak}S \quad (5.22)$$

### 5.2.3 Comparison with previous models of chemisorption

The  $d$ -band model assumes that trends in adsorption energies are given by the interaction of the adsorbate state with the  $d$ -bands of the metal. As described in Chapter 2, the Hammer-Nørskov  $d$ -band model [16] uses the two-level problem to describe the chemisorption energy of CO on late transition metal surfaces.

In this section we highlight the difference between our model and the simple two-level system to model the interaction between the  $d$ -states of the metal and the adsorbate.

The first and most obvious benefit to this modification is that it allows us to incorporate the width of the transition metals into the corresponding hybridisation energies. Another difference between the two models is based on the acceptable range of energy values that can be studied without a loss of accuracy. To demonstrate this difference, we truncate Equation 5.16 up to the first order binomial expansion  $(1+x)^n \approx 1+nx$ , where  $x \ll 1$ ,

$$\epsilon_{\mp} = \frac{\epsilon_a + \epsilon_k}{2} - V_{ak}S \pm \frac{\epsilon_a - \epsilon_k}{2} \sqrt{1 + \left( \frac{2V_{ak}}{\epsilon_a - \epsilon_k} \right)^2} \quad (5.23)$$

which when separated into the respective bonding and anti-bonding states,

$$\epsilon_- = \epsilon_a - V_{ak}S + \frac{V_{ak}^2}{\epsilon_a - \epsilon_k} \quad (5.24)$$

$$\epsilon_+ = \epsilon_k - V_{ak}S - \frac{V_{ak}^2}{\epsilon_a - \epsilon_k} \quad (5.25)$$

Within the two-level model, the term  $V_{ak}^2/\epsilon_a - \epsilon_k$  is used to describe hybridisation, while  $V_{ak}S$  is used to describe the orthogonalisation contribution. Note that the above binomial expansion can be carried out only if  $|\epsilon_a - \epsilon_k| \gg V_{ak}^2$ , i.e. the spacing between the adsorbate and metal states are much larger than the coupling between them. By using the Newns-Anderson model to describe the hybridisation component of the chemisorption energies, we effectively relax this approximation, allowing us to study systems such as C\* and O\* where the earlier assumption breaks down.

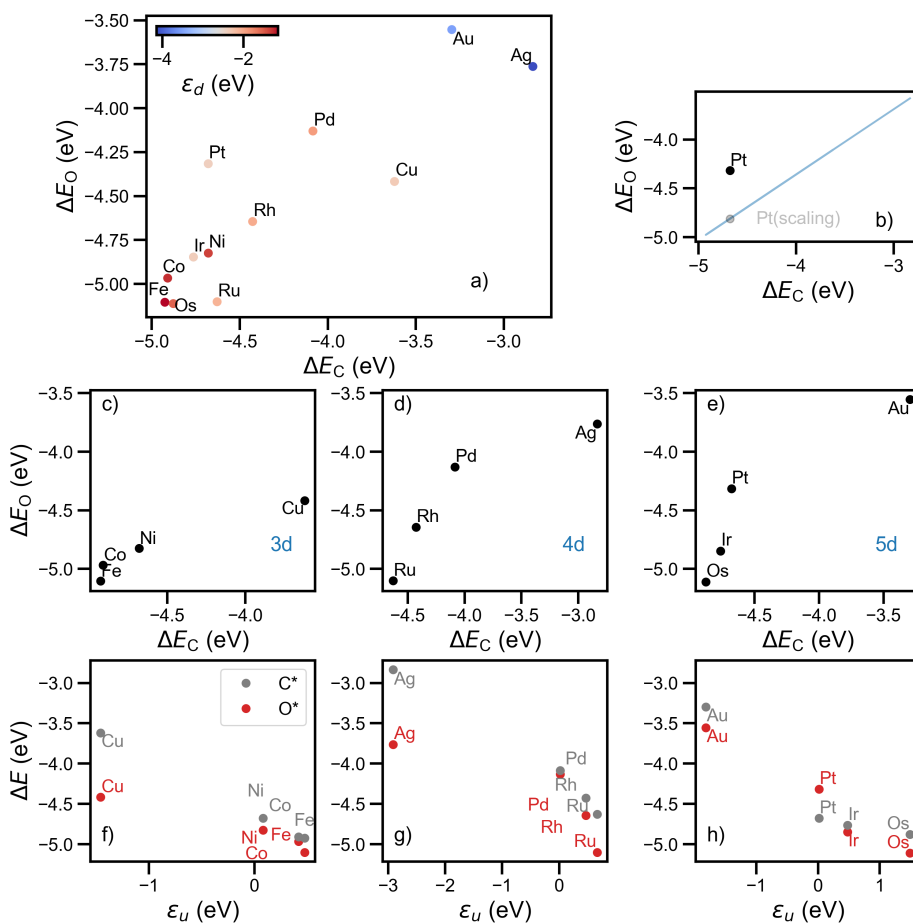


Figure 5.2: a) Scatter plot of DFT chemisorption energies of O,  $\Delta E_O$  and C,  $\Delta E_C$  with the colour referring to the value of the  $d$ -band centre of the metal; note that there is no scaling between the adsorbates b) Deviation of the computed Pt point from that obtained from linear least squares fitting of the data-points in a. c-e) Same data as in a, split into  $3d$ ,  $4d$  and  $5d$  metals; f-h) Scaling of  $\Delta E_O$  and  $\Delta E_C$  with the upper edge of the  $d$ -band, determined through the maximum of the Hilbert transform of the  $d$ -projected density of states of the surface metal atoms.

## 5.3 Results and discussion

### 5.3.1 Chemisorption energies of carbon and oxygen do not scale

In this section, we discuss computational results from DFT calculations showing scaling (or lack thereof) between the chemisorption energies of C\* and O\* energies. The chemisorption energy for an adsorbate  $A$  is defined as

$$\Delta E_A = E_{A^*} - E_* - E_A$$

where  $A^*$  is the atom adsorbed on the surface,  $*$  is the free surface and  $A$  is the atom in vacuum. Figure 5.2a shows the chemisorption energies of C\* plotted against that of O\*. It is clear that there is significant amount of scatter for it to be considered linear with  $R^2 = 0.77$  for a linear least-squares fit of the data. This poor correlation of data is in contrast to other scaling relation lines such as C\* vs.  $\text{CH}_x^*$  ( $x = 1, 2, 3$ ) [74],  $\text{COOH}^*$  vs  $\text{CO}^*$  [76] or  $\text{OOH}^*$  vs  $\text{OH}^*$  [18].

Despite the lack of linear scaling, there is broadly an increasing trend for both C\* and O\* energies in Figure 5.2a. Metals that bind C\* strongly (Fe, Os) bind O\* strongly and those that bind C\* weakly (Au, Ag) bind O\* weakly. However, due to the noticeable amount of scatter, this general “rule” does not always hold. Consider the example of platinum. Figure 5.2b shows the difference between the computed  $\Delta E_O$  point (in black) and that obtained from a linear least-squares fitting of all points in Figure 5.2a. The binding strength of O\* is about 0.5 eV weaker than what linear scaling would predict. This weaker than expected binding manifests in the catalytic activity of Pt, where it is considered weak binding for oxygen based reactions but has a lot of interesting carbon chemistry.

The scatter in scaling is markedly reduced when each row of transition metals are plotted separately as in Figure 5.2(c-e). Mid-row transition metals for each series show linear behaviour, with the final element of each row (Au, Ag and Cu) falling off a linear fit. For 3d it appears that Ni falls off as well.

Similar trends are seen when the energies are plotted against the upper edge of the  $d$ -band centre. As in previous work, the upper-band edge ( $\epsilon_u$ ) is determined as the energy ( $\epsilon$ ) value at which the Hilbert transform of the  $d$ -projected density of states reaches a maximum. This tailing-off behaviour of the energies at higher  $\epsilon_u$  values is symptomatic of increased repulsive interactions that predominate in noble metals. This leveling off would suggest that it is not just hybridisation between adsorbate and metal atoms that dictate the scaling of C\* and O\* on transition metals. We would need to account for the competition between the hybridisation and repulsive interactions in our description of C\* and O\* binding, which we do by applying the model presented in Section 5.2.

### 5.3.2 Parameterisation of model

In this section we parameterise the model for chemisorption of small molecule adsorbates on transition metal surfaces developed in Section 5.2. We use the DFT chemisorption energies presented in Figure 5.2 as input data for this parameterisation.

By performing this parameterisation, we effectively split the total energy into contributions coming from hybridisation of the adsorbate with the  $sp$  and  $d$  metallic states and the repulsive orthogonalisation accompanying adsorption. We will then use the relative contributions of these two terms to explain the lack of scaling of chemisorption energies of C\* and O\*.

By combining the Newns-Anderson hybridisation energy with an *effective* repulsive orthogonalisation energy from the two-state system (Section 5.2), the total chemisorption energy within our model,  $E_{\text{chem}}$ , is given by

$$E_{\text{chem}} = \underbrace{E_{\text{d-hyb}} + E_{\text{sp-hyb}}}_{\text{Hybridisation}} - \underbrace{2(n_a + f)SV_{ak}}_{\text{Orthogonalisation}} + \text{constant} \quad (5.26)$$

where the combined  $sp$  and  $d$  hybridisation term is given by Equation 5.9,

$$\Delta E_{\text{d-hyb}} + \Delta E_{\text{sp-hyb}} = \frac{2}{\pi} \int_{-\infty}^{\epsilon_f=0} \arctan \left( \frac{\Delta + \Delta_0}{\epsilon - \epsilon_a - \Lambda} \right) d\epsilon - 2\epsilon_a$$

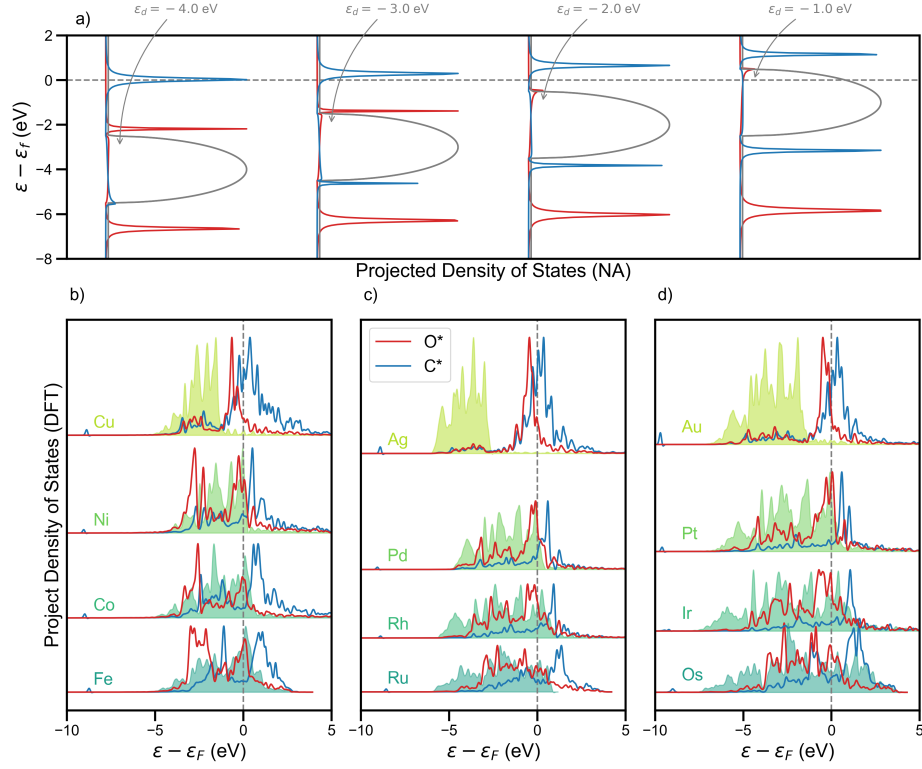


Figure 5.3: a) Projected density of states from the Newns-Anderson model with  $\Delta_0 = 0.1$  eV,  $V_{ak} = 2.0$  eV and  $w_d = 3$  eV; the adsorbate density of states are shown in red for O ( $\epsilon_a = -5$  eV) and blue for C ( $\epsilon_a = -1$  eV). b-d) DFT projected density of states for the  $d$ -states of different transition metal surfaces and  $p$ -states of O (red) and C (blue).

To visualise the input quantities into the model (such as  $\Delta$ ,  $\epsilon_a$ ) we plot the adsorbate projected density of states from both the Newns-Anderson model and from DFT calculations in Figure 5.3. The adsorbate projected density of states from the model is given by Equation 5.10 as,

$$\rho_{aa} = \frac{\Delta_d + \Delta_0}{[\epsilon - \epsilon_a - \Lambda]^2 + (\Delta_d + \Delta_0)^2}$$

and is shown in red for O\* and blue for C\* in Figure 5.3a. The semi-elliptical



$\Delta$  (in grey) is shown moving up in energy from  $\epsilon_d = -4$  eV to  $-1$  eV, which is the typical range of  $d$ -band centre values of late transition metals (Fe to Au in Figure 5.3b-d). The  $p$ -projected density of states are shown in Figure 5.3b-d for both O\* (in red) and C\* (in blue) along with the  $d$ -projected density of states of the different metal surfaces.

There are several similarities between the DFT density of states and the Newns-Anderson density of states. First, the  $d$ -projected density of states of the metal resemble a semi-ellipse, which is the shape of  $\Delta$  that was used in the Newns-Anderson model. The  $p$ -projected density of states also show localised states above and below the  $d$ -band (red and blue), similar to that of the red and blue curves of the Newns-Anderson adsorbate projected density of states in Figure 5.3. Further, the Newns-Anderson density of states show that as the metallic states move down in energy (for example, Ru  $\rightarrow$  Ag), the anti-bonding state gradually become occupied. The increased occupancy in the anti-bonding state eventually causes weakening of the bond between the adsorbate and the metal.

We now parameterise Equation 5.26 in order to deconstruct the energy into its constituent contributions. As in Ref [77] and due to its ability to reproduce the density of states from DFT, we choose the O- $p$  states to have  $\epsilon_a = -5$  eV. Similarly, we choose  $\epsilon_a = -1$  eV for the C- $p$  states. We also note that the adsorbate projected density of states of both C\* and O\* are similar to experimental X-ray photoemission spectra from Ref [78] for Cu and Ni, further validating the approach of using a single renormalised energy for C\* and O\*.

As in Ref [16], we assume that the coupling elements are proportional to the coupling elements from the linear muffin tin orbital (LMTO) framework (coupling elements referenced as  $V_{sd}$ ) [10].

$$V_{ak}^2 = \beta V_{sd}^2 \quad (5.27)$$

where  $\beta$  is a constant for all metals we consider in this work. To simplify the expression further, we assume that the overlap matrix element is proportional

to the coupling element,

$$S = -\alpha V_{ak} \quad (5.28)$$

where  $\alpha$  is another constant which is identical for all metals.

Adsorbate	$\alpha$ (eV <sup>-1</sup> )	$\beta$ (eV <sup>2</sup> )	$\Delta_0$ (eV)
C* ( $\epsilon_a = -1$ eV)	0.117	1.645	0.1
O* ( $\epsilon_a = -5$ eV)	0.041	2.962	0.1

Table 5.1: Fitting parameters for C\* and O\* from a least-squares error minimisation routine

The filling,  $f$ , of the metal states comes directly in our model from  $\Delta_d + \Delta_0$ ,

$$f = \frac{\int_{-\infty}^0 (\Delta_d + \Delta_0) d\epsilon}{\int_{-\infty}^{\infty} (\Delta_d + \Delta_0) d\epsilon}, \quad s.t. \quad 0 < f < 1 \quad (5.29)$$

Finally  $n_a$  is obtained by directly integrating the adsorbate projected density of states up to the Fermi level ( $\epsilon_f$ , set to 0).

$$n_a = \pi^{-1} \int_{-\infty}^{\epsilon_f=0} \frac{\Delta_d + \Delta_0}{[\epsilon - \epsilon_a - \Lambda]^2 + (\Delta_d + \Delta_0)^2} d\epsilon, \quad s.t. \quad 0 < n_a < 1 \quad (5.30)$$

The only free parameters within the model are  $\alpha$  and  $\beta$ , which are constant for all the metals. We obtain these parameters by fitting Equation 5.26 to the DFT energies in Figure 5.2. Table 5.1 shows the fitted parameters for each of the adsorbates and Figure 5.4 shows the fitted chemisorption energies from the model compared against the DFT energies. Given the simplicity of our parameterised model, the fit across and along rows of the periodic table is reasonable.

### 5.3.3 Saturation of energy causes scatter in scaling relations

In this section, we describe the reason behind the lack of scaling of C\* and O\* as seen in the DFT calculations (Figure 5.2) based on the model developed in the previous section.

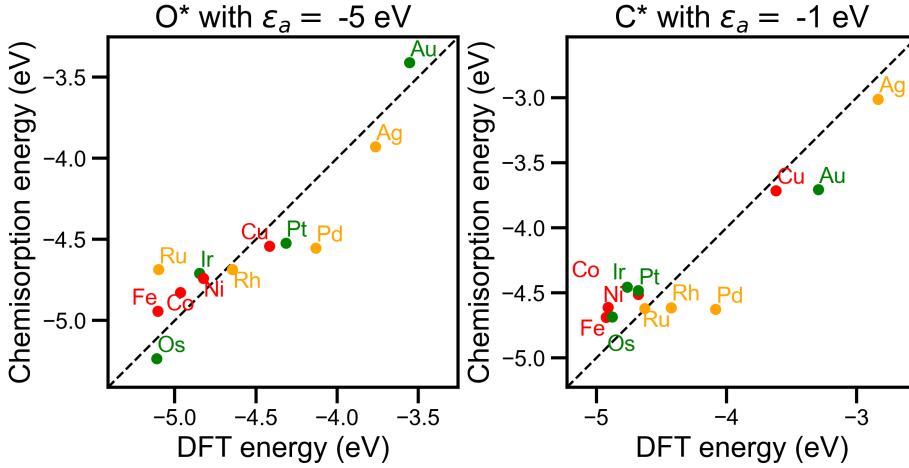


Figure 5.4: Chemisorption energy from the model plotted against the DFT energies based on the parameters in 5.1. Colours indicate the row of the element in the periodic table; red for the 3d, yellow for 4d and green for 5d transition metals.

The hybridisation energy ( $\Delta E_{d\text{-hyb}} + \Delta E_{sp\text{-hyb}}$ ), saturates at negative  $\epsilon_d$  values for O\*, but does not saturate for C\*. That is, the Newns-Anderson  $d$ -hybridisation energy is 0 for the noble metals (Cu, Ag and Au) and  $\rightarrow 0$  for some late transition metals as seen in Figure 5.5a, but not for C\* in Figure 5.5b.

Saturation of the hybridisation energies implies that the repulsive contributions are dominant for late transition metals in the case of O\*, while not being as dominant for C\*. This lopsided dependence of the repulsive contribution can be seen through the upward spike in the weak binding energies in Figure 5.5c, a gradual increase starting at  $\Delta E_O \approx -4.5$  eV in O\* energies.

Another feature of Figure 5.5c is the scaling between the each row of transition metals at  $\Delta E_O < -4.5$  eV. The metals that are below this value are the late transition metals except for the noble metals. Thus, in the case of C\* vs. O\* scaling it would be acceptable to generate linear scaling relationships by separately fitting each row of transition metals and skipping the noble metals.

We now generalise our findings beyond C\* vs O\* scaling by proposing a

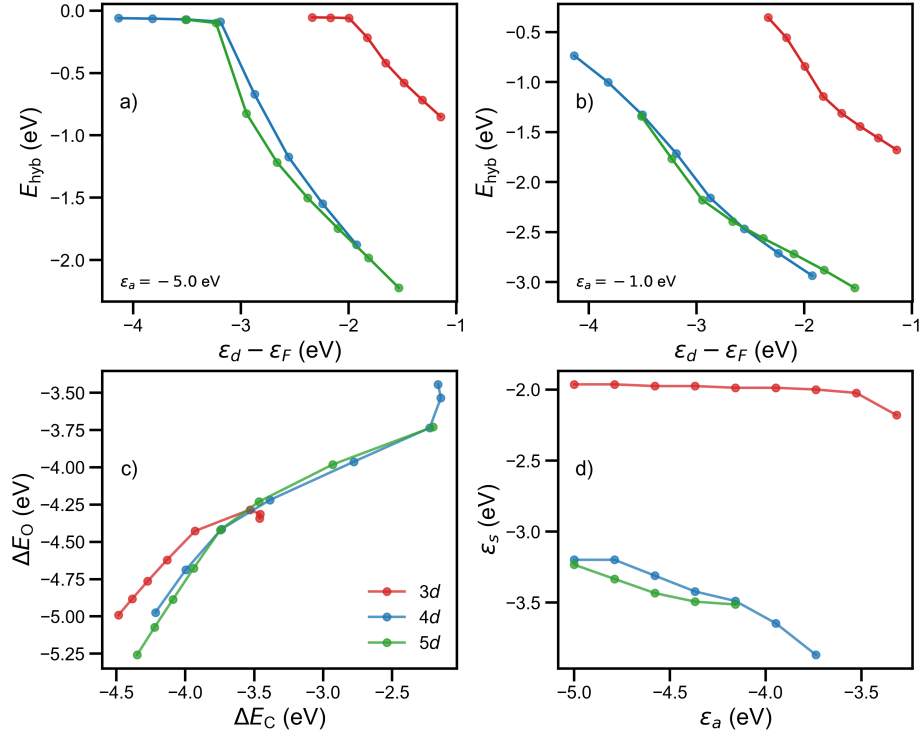


Figure 5.5: Hybridisation energy (i.e. without orthogonalisation energy) plotted for a range of  $d$ -band centres for a) O\* with  $\epsilon_a = -5$  eV and b) C\* with  $\epsilon_a = -1$  eV; there is a saturation in the case of O\*, but no saturation for C\*. c) Total chemisorption energy of O\* vs. C\* from the model, the plot is analogous to the DFT energies in Figure 5.2. d)  $\epsilon_s$  (see text), a measure of the saturation in a-b for different adsorbates.

descriptor to determine the limit of  $\epsilon_d$  value up to which scaling is expected. To do so, we estimate the  $\epsilon_d$  at which the curves in Figure 5.5(a,b) saturate. The curves would saturate only when  $\Delta E_{\text{d-hyb}} \rightarrow 0$  and the entire contribution to the energy comes from  $\Delta E_{\text{sp-hyb}}$ . We denote the  $\epsilon_d$  from which saturation is expected as  $\epsilon_s$  and it can be found by using the following rule,

$$\epsilon_s = \operatorname{argmin}(\epsilon_d) \quad \text{for} \quad E_{\text{hyb}} - \Delta_0 = 0 \quad (5.31)$$

that is, the  $\epsilon_d$  at which the entire hybridisation energy contribution comes from interaction of the adsorbate with the  $sp$ -states and the *net* contribution with the  $d$ -states is 0. Figure 5.5 shows  $\epsilon_s$  for a range of renormalised energy levels. For  $-5 \text{ eV} < \epsilon_a < -3.5 \text{ eV}$ , different rows of the transition metals have different  $\epsilon_s$  values, implying that each row must be fit separately (just as in Figure 5.2b-d). The  $3d$  row appears to saturate at less negative  $\epsilon_d$  values, thus explaining the curvature of points in Figure 5.2b.

We note that in practice there could be several reasons for lack of scaling between two adsorbates. Relaxation of the surface and site dependence of the adsorbate might cause scatter on simple transition metal surfaces. Complex materials such as metal oxides, alloys and doped materials might also cause scatter by having vastly different coupling elements from what is considered in this work. Electrostatics and coverage based effects can also cause deviations in scaling. However, the adsorbates and surfaces we describe in this chapter are transition metals with the simplest of mono-atomic adsorbates, with chemisorption energies in the dilute coverage limit. The fact that these simple systems do not scale in an obvious manner shows the complexity associated with surface chemical bond formation. Thus, care must be taken while fitting linear scaling relations for transition metals for more complex reactions and intermediates.

## 5.4 Conclusion

In this work, we developed a model to understand why the chemisorption energies of  $\text{C}^*$  and  $\text{O}^*$  do not scale in the conventional sense of linear-scaling relations. Our model combines a modified version of the Newns-Anderson hybridisation energy, including interaction with both  $sp$  and  $d$  states of the metal along with the an effective terms for the orthogonalisation repulsion. We show that the root cause of the lack of scaling lies in the saturation of the hybridisation energy of  $\text{O}^*$  for lower lying  $d$ -band centres, while the hybridisation energy for  $\text{C}^*$  experiences no such saturation. This imbalanced saturation in hybridisation energy comes from the fact that oxygen, due to the presence of one extra

electron has a lower lying renormalised energy state as compared to  $C^*$ . We suggest a measure for the lowest  $\epsilon_d$  value at which saturation is expected and show how linear scaling relations can be recovered in the case of  $C^*$  and  $O^*$  by simply fitting lines across metals of the same row of the transition metal series, bar the noble metals.

## 5.5 Computational methods

Density functional theory calculations were carried out using Quantum ESPRESSO [79]. Core electrons were treated using pseudopotentials from the SSSP Efficiency pseudopotential database [80]. Valence electrons were described using plane-waves with kinetic energy and density cutoffs of at least 60 Ry and 480 Ry respectively. In cases where the recommended cutoffs are greater than these values, the larger value is used. Cold smearing of width 0.0075 Ry ( $\approx 0.1$  eV) was used for all calculations. A  $k$ -point mesh of (4, 4, 1) was used for all surface calculations. The PBE [24] functional was used to describe exchange and correlation effects. The self-consistent field cycle was considered converged if the energy difference between two successive steps was less than at least  $10^{-8}$  Ry. All calculations were performed *without* spin polarisation. Structures were prepared using the Atomic Simulation Environment [63]. The adsorbate is fixed at the ontop site at a distance equal to the sum of the covalent radii of the metal atom and the adsorbate atom. Provenance of each calculation in this work was stored using AiiDA [65] and performed using the AiiDA quantumpresso plugin.

The Newns-Anderson expressions were implemented using trigonometric functions from the Python *numpy* library. Multi-precision C-library *arb* was used to integrate the projected density of states using the *acb\_calc\_integrate* function. Decimal precision of 50 was used throughout this work. Least-squares error fitting were performed using the Python *scipy* library.

## 5.A Appendix: Continuous variation of parameters

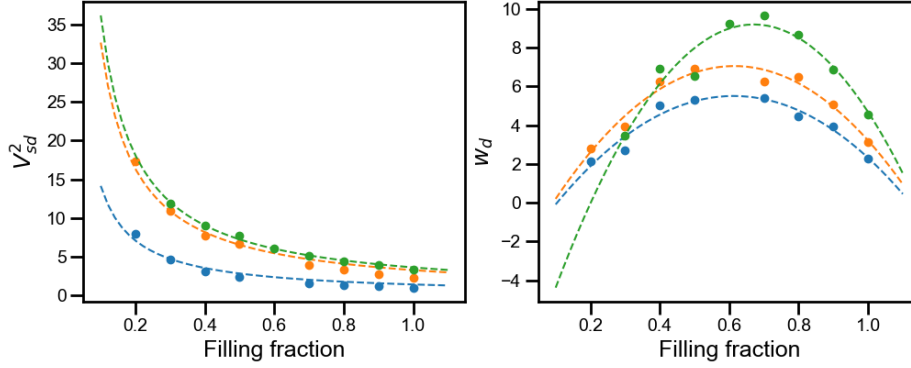


Figure 5.6: Interpolated parameters of  $V_{sd}^2$  and  $w_d$  plotted against the filling fraction. The points are values taken from Ref [10] for  $V_{sd}^2$  and from DFT calculations in the case of  $w_d$

In this Appendix, we describe how a continuous variation of all parameters is constructed so as to make Figure 5.5.

**Adsorbate specific parameters:**  $\alpha$  and  $\beta$  are linearly interpolated from Table 5.1 for  $-5 \text{ eV} < \epsilon_a < -1 \text{ eV}$ .

**Metal specific parameters:**  $V_{sd}^2$  is obtained using a  $1/r$  fit to all the metals and  $w_d$  is fit to a quadratic expression  $b - a(r - c)^2$ . The results of least squares fit for these expressions are shown in Figure 5.6. The filling fraction is determined based as  $(v - 1)/10$  where  $v$  valence of the metal atom.





## Chapter 6

# Impact of interfacial water on adsorption energies

In Chapters 4 and 5 we studied the chemisorption of a single adsorbate on transition metal surfaces. In this chapter, we investigate the simultaneous chemisorption of two adsorbates on a surface. Such a scenario of competition between two (or more) species for sites on a surface is common in electrocatalysis, where catalytic reactions occur in the presence of interfacial water, electrolytes, etc.

To investigate chemisorption of two species on a surface, we use a combination of surface Pourbaix diagrams constructed through DFT calculations and *ab-initio* molecular dynamics calculations. We continue to explore these effects through the system of CO adsorption on gold (as in Chapter 4). This choice of system allows us to compare our results for adsorption in an electrochemical environment to those in vacuum or in gas-phase. The contents of this chapter are taken from the manuscript *Interaction of CO with Gold in an Electrochemical Environment* [30] (enclosed in Section 10.2).

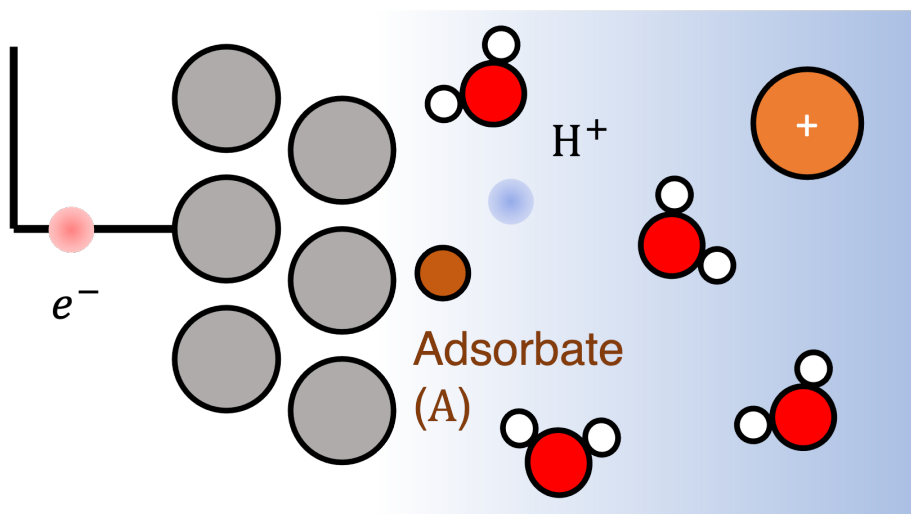


Figure 6.1: Schematic of an electrochemical interface, consisting of an adsorbate A, electrons ( $e^-$ ), protons  $H^+$ , interfacial water molecules (in red and white) and electrolyte ions (in orange).

## 6.1 Introduction

The electrochemical interface is complex. Figure 6.1 shows a typical interface, consisting of an adsorbate A at a certain coverage  $\theta$ , electrons ( $e^-$ ), protons  $H^+$ . A typical reactions with these species would be a so-called proton-electron transfer reaction,



where species such as interfacial water molecules and electrolyte ions could also play a role.

To understand the influence of different components of Equation 6.1, we write the the free energy change ( $\Delta G$ ) as a difference between the sum of chemical potentials of all species on the products and reactants (as discussed in

Chapter 2),

$$\Delta G = \mu_{\text{AH}^*} - (\mu_{\text{A}^*} + \mu_{\text{e}^-} + \mu_{\text{H}^+}) \quad (6.2)$$

where  $\mu_X$  is the chemical potential of species  $X$ . Equation 6.2 presents a clear way to incorporate the effect of potential (on an absolute scale, such as an SHE/NHE scale) through  $\mu_{\text{e}^-} = \mu_{\text{e}^-}^0 + e\Phi_{\text{SHE}}$ , ( $\mu^0$  is the chemical potential of the electron at standard conditions, pH of 0). Meanwhile, the effect of the pH is incorporated through the configurational entropy of the proton [81],  $\mu_{\text{H}^+} = -2.3k_B T \text{pH}$ .

Treating  $\mu_{\text{AH}^*}$  and  $\mu_{\text{A}^*}$  in a complete manner (as shown in Figure 6.1) is less straightforward. A common assumption is to neglect the influence of water, ions and other possible species. Under this assumption,  $\mu$  for an adsorbed species would be computed similar to the free energies of adsorption in vacuum as done in Chapters 4 and 5. This approach has been successful in predicting trends of reactivity on different metals for a variety of electrochemical reactions such as  $\text{CO}_2\text{R}$  [75], the oxygen reduction reaction [76], the hydrogen evolution reaction [82], among others.

In this chapter we test the assumption of using the computed gas-phase free energies of reaction intermediates as an alias of the true electrochemical energetics. We do so by revisiting the example of CO adsorption on gold surfaces. Unlike in gas-phase, we find that CO is destabilised on steps of gold, which dramatically lowers its coverage. We postulate that the decreased binding strength of CO to the step sites of gold in an electrochemical environment is due to the competition for binding sites with interfacial water, which also binds strongly to step sites of Gold. We model this interaction through *ab-initio* molecular dynamics and show that the adsorption energy of CO on gold is weakened on steps, but remains roughly the same on terraces.

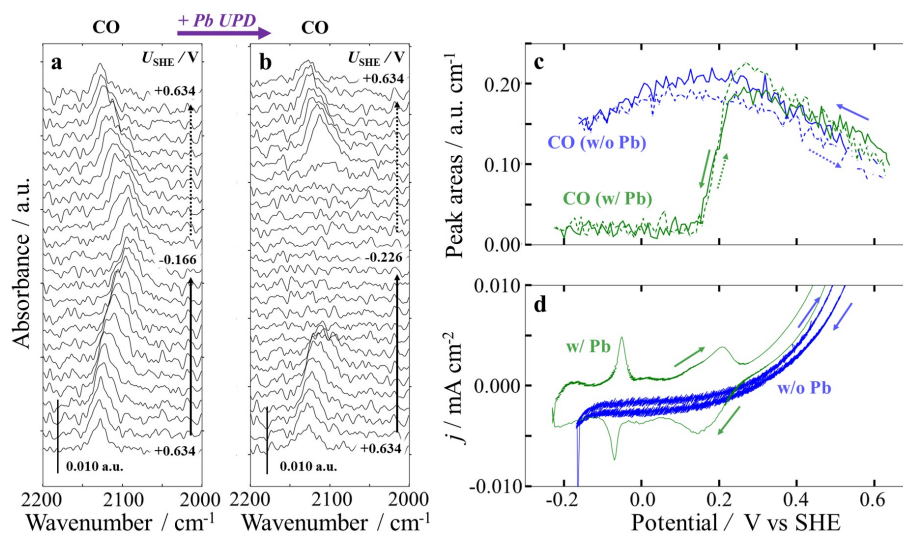


Figure 6.2: ATR-SEIRAS in the CO stretch region from a CV on an Au film in 0.1 M  $\text{HClO}_4$  purged with 1 bar CO. A spectral background was taken at +0.634 V in Ar-purged solution. (a) ATR-SEIRAS spectra before the addition of Pb. (b) ATR-SEIRAS spectra with 1 mM  $\text{Pb}(\text{ClO}_4)_2$ . Every eighth spectrum is shown. (c) Integrated intensities of the CO stretch peak as a function of potential and (d) corresponding 2 mV/s CV with and without Pb. *Reprinted from paper in Section 10.2* [30]

## 6.2 Revisiting CO adsorption on gold

In Section 4.4, we determined the equilibrium coverage of CO on stepped gold surfaces (211) and (310) to be between 0.4 – 0.9 ML at a temperature of 300K and pressure of CO of 1 bar. Under the assumption that water and ions do not alter the binding strength of CO, we would expect there to be a similar coverage under electrochemical conditions. In this section, we test this assumption based on lead-underpotential deposition experiments and surface Pourbaix diagrams.

We begin by briefly describing the experiment which we model later in this chapter (detailed discussion on the experimental procedure can be found in Ref [30]). Figure 6.2a shows the vibrational band of the C–O stretch frequency

on poly-crystalline Au over a potential window of  $-0.166$  to  $0.634$  V vs SHE, determined through the surface-enhanced Infrared spectroscopy (ATR-SEIRAS) technique. Figure 6.2b shows the vibrational band of CO at roughly the same potential region, however the experiment is run with Pb in the electrolyte. The presence of Pb would lead to its deposition on the gold surface at some potential (referred to as the underpotential deposition of Pb). Due to the adsorbed Pb, the vibrational band of CO starts to disappear at approximately  $0.25$  V vs. SHE and does not appear at lower (more cathodic) potentials. However, the cycle is reversible, with the vibrational band reappearing as the potential is increased from  $-0.226$  V vs SHE.

The results of this ATR-SEIRAS experiment are summarised by the peak areas shown in Figure 6.2c. In the absence of Pb in the electrolyte, the peak area of the vibrational band reaches a maximum at approximately  $0.2$  V vs. SHE. However, in the presence of Pb, the peak areas fall to zero at approximately  $0.2$  V vs. SHE. We attribute this effect to the replacement of CO on the surface with Pb. Furthermore, Figure 6.2d shows there is a coverage of CO on the surface at positive potentials ( $> 0.2$  V vs SHE) due to the onset of CO-oxidation.

To summarise the results of the experiments, it appears that CO is replaced by Pb as the potentials become more cathodic (where Pb adsorption is more favourable). Given that the experiment was conducted on a poly-crystalline gold surface, it is not immediately clear which surface facet is responsible for adsorbing CO. However, we know from Figure 6.2c that Pb must adsorb on gold at potentials of about  $0.2$  V vs. SHE (or higher). If Pb adsorbs on a particular gold facet at potentials more cathodic than  $0.2$  V vs. SHE, it will not be able to replace CO at  $0.2$  V vs. SHE. Thus, the problem changes from finding which surface facet adsorbs CO to one of where we must determine the potential at which Pb adsorbs on the surface.

### 6.3 Pb adsorption on gold

To determine the potential at which Pb is deposited on the surface, we perform a computational surface Pourbaix analysis [83] and compare our results with experimental cyclic voltammograms (CV). We study four different facets, (111) and (100) terraces and (211) and (110) steps.

The half-reaction for Pb deposition is given by,



with the following potential dependent free energy,  $\Delta G_{\text{Pb}}$ ,

$$\Delta G_{\text{Pb}} = \Delta G_{\text{Pb}}^0 + 2e (U_{\text{SHE}} - U_{\text{Pb}^{2+}/\text{Pb}}) \quad (6.4)$$

where  $U_{\text{Pb}^{2+}/\text{Pb}}$  is the standard redox potential of  $\text{Pb}^{2+}/\text{Pb}$  half cell reaction and  $U_{\text{SHE}}$  is the potential referenced to the SHE scale and  $\Delta G_{\text{Pb}}^0$  is the free energy change for the reaction at 0 V vs.  $\text{Pb}^{2+}/\text{Pb}$ .

By computing  $\Delta G_{\text{Pb}}$  as a function of coverage of Pb,  $\theta$ , we determine the most stable coverage of Pb at a given potential. Figure 6.3(a-d; left) shows the computed  $\Delta E$  for different  $\theta$  values. Throughout this analysis, we assume that  $\Delta E \approx \Delta G$ , i.e. the entropic contributions of Pb are set to 0.

The color of each line in Figure 6.3(a-d;left) corresponds to  $\Delta G$  at certain value of  $\theta$ . For terrace surfaces we consider three discrete surfaces,  $\theta = 1/9, 1/4, 1$  ML as shown in Figure 6.3e. For step sites, we consider  $\theta = 1/3, 2/3, 1$  ML coverages as shown in Figure 6.3f. The black line corresponds to  $\theta \rightarrow 0$ , negligible surface coverage of Pb. Intersections between lines of different colours indicate a change in the surface coverage. In reality, we would expect a continuous variation of coverage. However, since we can compute only a discrete number of points we choose to compare intersections between discrete coverage  $\Delta G$  lines against experiments (dashed black lines). The lowest lying  $\Delta G$  curve at any potential denotes the most stable coverage at that potential.

Figure 6.3(a-d;right) shows the experimental CVs for the same facets. The dashed lines (identical on both right and left plots) indicate the transition from

one coverage to another, as suggested by the computational Pourbaix diagram in Figure 6.3(a-d;left).

For both (211) and (110) surface facets, at 0.2 V vs. SHE, we would anticipate  $\approx 1/4$ ML and  $\approx 2/3$  ML coverage of Pb respectively. In the case of (100) surface facets, we would anticipate  $\approx 1/4$  ML coverage as well. However, the presence of multiple broadened peaks suggests surface reconstruction in the case of the (100) surface facet. Hence, from this analysis, we cannot exclude the possibility that (100), (211) and (110) surface facets adsorb CO under electrochemical conditions.

The (111) surface facet is expected to have a significant coverage of Pb only at  $\approx 0$  V vs. SHE, lower than the potential at which CO desorbs from the experiments (at 0.2 V vs. SHE). Thus, based on this combined surface Pourbaix and CV analysis, we can exclude (111) as a possibility for a surface facet that adsorbs CO under electrochemical conditions.

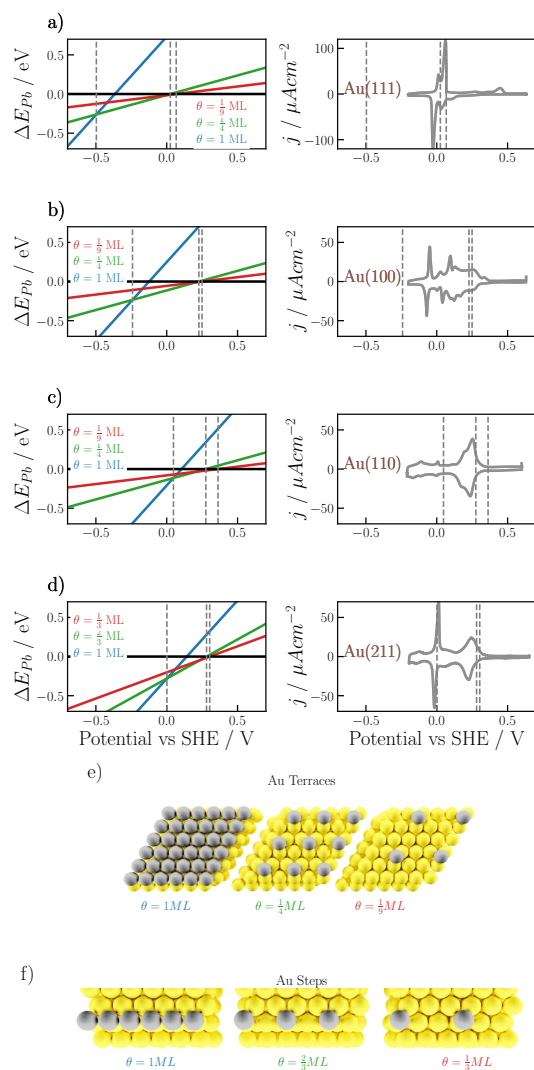


Figure 6.3: Computed surface Pourbaix diagrams on four prototype Au facets (111), (100), (110), and (211). The dashed black line indicates the potential at which the coverage has increased between the discrete intervals for which the DFT calculation was performed. To the right of each surface, the Pourbaix diagram is the associated Pb-UPD CVs taken from Ref [36]. The multiple broadened peaks observed in the (100) facet suggest substantial reconstruction. *Reprinted from paper in Section 10.2 [30]*



## 6.4 Simultaneous water and CO adsorption

In this section, we narrow the possible surface facets for CO adsorption on gold under electrochemical conditions further. To do so, we perform *ab-initio* molecular dynamics calculations of CO adsorbed in the presence of water on (211) and (100) surface. We choose the (211) surface facet as it represents a prototype step surface while (100) represents a prototype terrace surface.

Figure 6.4 shows the internal energies  $\Delta E$  and the free energies  $\Delta G$  for the adsorption of CO in the presence and absence of water.  $\Delta E$  is determined by choosing the lowest energy out of at least three separate trajectories.  $\Delta G$  is determined by using the harmonic approximation (for the adsorbate) and ideal gas for CO(g),

$$\Delta G = \Delta E - T(S_{\text{harm}} - S_{\text{ideal}}) - T\Delta S_{\text{config}} \quad (6.5)$$

In gas phase, it is clear that stepped facets bind CO stronger, as illustrated by the 0.12 eV stronger binding of (211) vs. (100) surfaces in vacuum. However, under electrochemical conditions the effect is reversed. Instead, the terrace site binds 0.75 eV stronger than the terrace site. This significant destabilisation of an adsorbed intermediate has been seen even in the case of Cu in Ref [84] and Pt in Ref [85].

This large difference in adsorption energies computed under vacuum and electrochemical conditions suggests that the (100) is expected to bind CO, while the (211) facet (and perhaps other step facets) do not. The contrast in adsorption energies stem from the competition between water and the adsorbate. This competition is present under electrochemical conditions but absent in vacuum.

There are a few uncertainties in the calculated adsorption energies. The choice of functional in this work under-binds both H<sub>2</sub>O and CO by roughly 0.1 eV (see Figure 4.7 and Figure 4.6 respectively), and the standard deviation between the three trajectories is large. Despite these errors, the computed adsorption energies compare well against the measured enthalpy for CO on polycrystalline gold surfaces, which was estimated to be -0.35 eV for CO(aq) → CO\*

[86]. Adding the contribution of  $\text{CO}(\text{g}) \rightarrow \text{CO}(\text{aq})$  which is  $-0.1$  eV gives a total enthalpy of  $-0.45$  eV, which is close to the computed value of  $-0.52$  eV on Au(100).

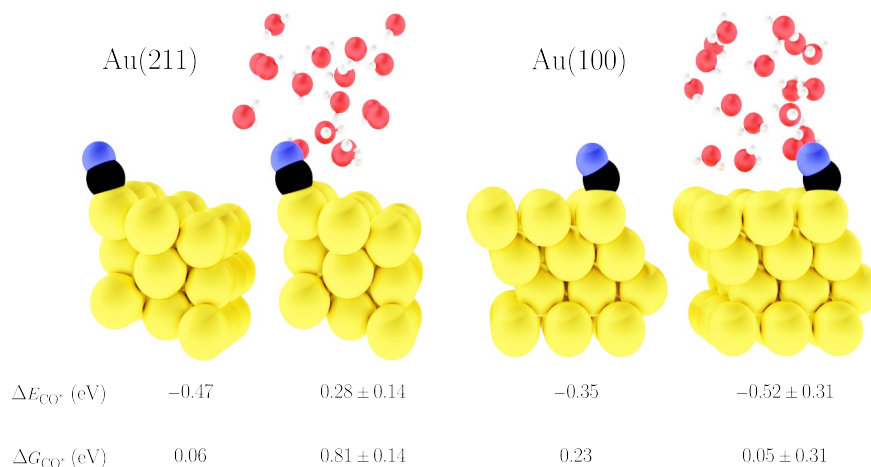


Figure 6.4: Snapshots of CO on Au(211) and Au(100) in vacuum or with explicit water from an *ab initio* MD simulation, performed in periodic unit cell sizes of  $3 \times 3$  for (211) at a coverage of  $1/3$  ML and  $3 \times 4$  for (100) at a coverage of  $1/16$  ML. Internal ( $\Delta E_{\text{CO}}$ ) and free energies of adsorption ( $\Delta G_{\text{CO}}$ ) with their standard deviations based on different runs are given below the snapshots. Reprinted from paper in Section 10.2 [30]

## 6.5 Conclusion

In this chapter we studied the adsorption of two species adsorbing on the surface through a combination of computational surface Pourbaix diagrams and *ab-initio* molecular dynamics calculations. Computations and experimental CVs of lead underpotential deposition experiments suggest that open facets such as

(100) and stepped facets are likely to bind CO. However, *ab-initio* molecular dynamics simulations suggest that the adsorption of CO on step sites is weakened in the presence of interfacial water.

## 6.6 Computational methods

Density functional theory calculations were performed using Vienna Ab-initio Software Package (VASP) [61]. Core electrons were described using Projector Augmented Waves (PAW) potentials [62]. Valence electrons were described using plane-waves with kinetic energy up to 500 eV for static calculations and 400eV for ab-initio MD calculations. Gaussian smearing with a width of 0.1 eV was used. The BEEF-vdW [35] functional was used for all calculations. All calculations were run without spin-polarization.

Structures were prepared using the Atomic Simulation Environment (ASE) [63]. The lattice constant of gold was optimized using a 12x12x12 Monkhorst-Pack [64]  $k$ -point mesh grid and was determined to be 4.205Å. Slabs four layers thick were made for (111), (100), (110) and (211) facets were constructed, with the bottom two layers kept fixed to mimic bulk metal. Static adsorption energies for CO and Pb were calculated on all unique surface sites on each facet. Initial adsorbate geometries were generated using CatKit [87]. All geometries were optimized until forces on all atoms was less than 0.025 eV Å<sup>-1</sup>. Vibrational frequencies were computed using a finite difference method as implemented in VASP (IBRION = 5) and calculated only for the surface adsorbate. *ab-initio* MD calculations are performed using a Nosé-Hoover [28] thermostat that keeps the temperature at approximately 300K.



## Chapter 7

# Charge transfer coefficients from atom-centered forces

Having discussed the importance of the chemisorption energy in catalysis, we now turn to activation energies. We described how to obtain them in practice from DFT calculations in both gas-phase conditions (Chapter 4) and in an electrochemical environment (Chapter 6). In this chapter, we discuss our methodology to obtain the activation energy for electrocatalytic systems, as well as their dependence on potential. Our approach builds on extrapolation based approaches [81, 88, 89, 90, 91] to determine the activation energy from a single DFT computation.

### 7.1 Introduction

Computational *ab-initio* investigations with Density Functional Theory (DFT) have provided the basis for the mechanistic understanding of several electro-

---

This chapter is being prepared for submission under the title: *Force-based method to determine the potential dependence in electrochemical barriers*, [Sudarshan Vijay](#), Georg Kastlunger, Joseph A. Gauthier, Anjali Patel and Karen Chan.

chemical reactions, such as the oxygen reduction reaction (ORR) [18], electrochemical CO<sub>2</sub> reduction (CO<sub>2</sub>R) [92], hydrogen evolution reaction (HER) [82], amongst others. While reaction thermodynamics are readily captured by the computational hydrogen electrode [18], accurately determining activation energies remains a challenge.

The main challenge to modelling *ab-initio* electrochemical barriers in periodic simulation cells of feasible size is that the workfunction (often used as an alias for the electrode potential) changes by about 1–2 eV [89, 93] during the course of a reaction involving an ion-electron pair or adsorption of a polar intermediate. This change is an artifact of the finite nature of a super cell, containing a fixed number of electrons. At the hypothetical infinitely sized cell there would be no change in the workfunction accompanying a reaction, guaranteeing that the simulated electrochemical reaction proceeds without a change in the potential.

In the past decade, a variety of methods to address this challenge have been developed [88, 89, 90, 91, 93, 94, 95, 96, 97, 98]. These methods can be broadly grouped into two categories, extrapolation and grand-canonical schemes. Extrapolation methods seek to determine the reaction energies at the limit of infinite cell size by correcting DFT energies for finite cell size effects. For example, in Refs [88, 89], the infinite cell limit is reached by extrapolating energies from DFT calculations done at successively larger cell sizes, through so-called cell extrapolation. Another approach is to *a priori* assume that the electrochemical interface can be modelled as a parallel plate capacitor [90, 91], where the ion (or adsorbate) forms one end and the metal surface the other. The charge stored in the parallel plate capacitor is determined through a charge partitioning approach and the potential is estimated through the workfunction. In this charge extrapolation scheme the DFT energies are corrected with a purely electrostatic model, to obtain energies at the infinite cell size. Alternatively, grand-canonical (GC) methods keep the workfunction constant by adding or subtracting excess electrons within the simulation cell, along with a corresponding counter-charge in different possible continuum models of the electrolyte [94, 95].

In theory, it has been shown that both GC and extrapolation methodology are equivalent in specific limiting cases, such as adsorption reactions of polar species. For example, Ref [93] showed that for  $\text{CO}_2 \rightarrow \text{CO}_2^*$ , both GC and extrapolation procedures provide the same potential dependent energies. However, in practice, challenges still remain. Cell extrapolation is computationally expensive to implement, while charge extrapolation necessitates charge partitioning, which has short-comings in cases of significant hybridisation between atoms. For example, charge transfer coefficients for protonation to oxygen and nitrogen intermediates show sharp changes along the reaction path [99]. This behaviour is likely a failure of charge partitioning as a consequence of increasing hybridisation between the reacting species. Furthermore, rotation of water present in the simulation cell along a reaction path leads to abrupt changes in workfunction. Grand-canonical methods require an accurate capacitance in order to avoid cell-size dependence of reaction energetics. Finally, all of the above methods are typically applied with static water structures, while dynamic simulations under constant potential are only recently emerging [85, 100].

In this chapter, we propose a method to determine potential dependent energetics of electrochemical reactions by building upon the framework of extrapolation methodologies. The strength of our approach is that we determine the charge transfer coefficient directly from atomic positions and atom-centered forces, without the need for explicit partitioning of the charge density or performing multiple DFT calculations. We begin by illustrating the current extrapolation based procedure to determine charge transfer coefficients and potential dependent energies for a prototype reaction of a proton-electron transfer to C adsorbed on Pt(111). We then develop a model which relates the atom centred forces to the charge transfer coefficient. The computational overhead associated with implementing our approach is equivalent to a typical finite difference Hessian calculation. We show that the force-based method is able to provide consistent charge transfer coefficients for a range of reactions, irrespective of how strongly the reacting species are hybridised. We benchmark this methodology against calculations done at different cell sizes, i.e. through cell extrapolation

and discuss possible limitations.

## 7.2 Extrapolation procedures in practice

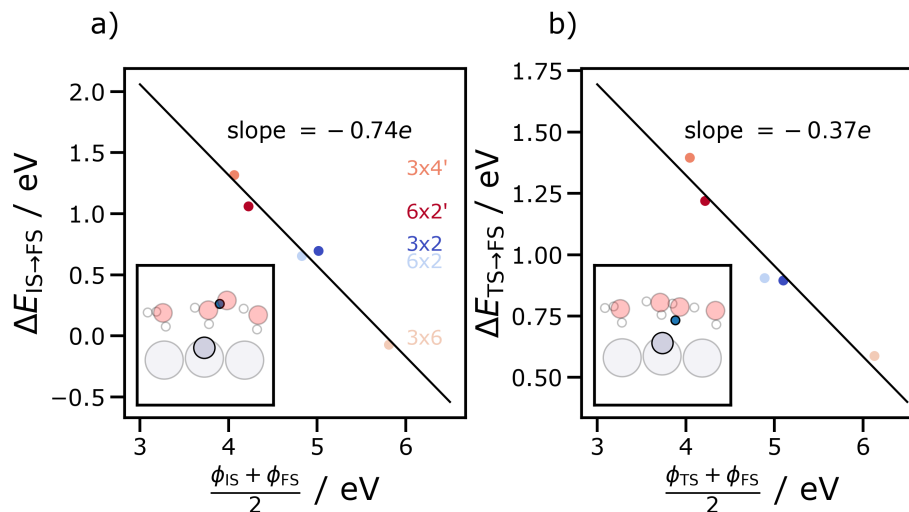


Figure 7.1: Variation of a) reaction energies b) barriers for  $C + H^+ + e^- \rightarrow CH$  with the mean workfunction. Atomic positions of the initial state and the transition state are shown within insets, the reacting proton is marked in blue. Colors indicate different cell sizes with different proton concentrations. Cell sizes annotated with a ' indicate multiple protons in the unit cell; the rest have a single proton in the unit cell.

In this section we review how to obtain the charge transfer coefficient and the potential dependent energies of an elementary reaction, based on the framework of extrapolating to the infinite cell size. As in previous work [88, 89, 90, 91, 93], we assume that the electrochemical interface is represented by a capacitor of constant capacitance,  $C$  and is invariant with respect to the electrode potential and the reaction geometry [93]. We expect this assumption to hold for small changes in potential far from the potential of zero charge (pzc) where water structures are relatively ordered [101]. In such a purely electrostatic view of



the electrochemical interface, a reaction event such as protonation would be equivalent to altering the charge stored in this capacitor.

By treating the metal-water interface from our DFT computations as a parallel plate capacitor, we explicitly determine the different energy contributions associated with a reaction. We write the energies of a given state (corresponding to a particular number of atoms and geometry)  $E$ , as a function of the charge stored in the capacitor  $q$  in the form of a Taylor series expansion,[93, 98]

$$E = E_0 + q \left. \frac{\partial E}{\partial q} \right|_{q=0} + \frac{q^2}{2} \left. \frac{d^2 E}{dq^2} \right|_{q=0} + \mathcal{O}(q^3), \quad (7.1)$$

$$E = E_0 + q\phi_0 + \frac{q^2}{2C} \quad (7.2)$$

where  $E_0$  corresponds to a purely chemical, non-electrostatic energy, the first derivative of energy with charge,  $\frac{\partial E}{\partial q}$  corresponds to the workfunction at  $q = 0$ ,  $\phi_0$ , and the second derivative of energy with  $q$  corresponds to the inverse of the capacitance,  $1/C$ . To account for reaction energies, we calculate the energy to go from state 1 to state 2,  $\Delta E_{1 \rightarrow 2}$ . This term corresponds to the reaction energy from a DFT calculation (the y-axis of either plot in Figure 7.1). Taking the difference between single state energies for 1 and 2 from Equation 7.2 gives,

$$\Delta E_{1 \rightarrow 2} = \Delta E_0 + (q_2 - q_1) \phi_0 + \frac{1}{2C} (q_2^2 - q_1^2), \quad (7.3)$$

which can be simplified using the parallel-plate capacitor relationship  $C = q_2 / (\phi_2 - \phi_0) = q_1 / (\phi_1 - \phi_0)$

$$\Delta E_{1 \rightarrow 2} = \Delta E_0 + (q_2 - q_1) \left[ \frac{\phi_1 + \phi_2}{2} \right] \quad (7.4)$$

Note that as described in Ref [93], we write the infinite cell size energy,  $\Delta E_\infty$  in the limit that the potential does not change during the reaction, i.e.  $\phi_1 = \phi_2 = \phi$  as,

$$\Delta E_\infty = \Delta E_0 + (q_2 - q_1) \phi \quad (7.5)$$

Comparing Equation 7.4 and Equation 7.5,  $\Delta E_\infty = \Delta E_{1 \rightarrow 2}$  when  $\phi = (\phi_1 + \phi_2)/2$ .

Figure 7.1 shows  $\Delta E_{1 \rightarrow 2}$  for two reaction steps, initial state (IS) to final state (FS),  $\Delta E_{\text{IS} \rightarrow \text{FS}}$  and transition state (TS) to final state (FS),  $\Delta E_{\text{TS} \rightarrow \text{FS}}$ . Here, we vary the hydrogen atom concentration in the water layer, which by spontaneously donating their electron to the electrode change the electrode potential and become protons [81]. The greater the number of protons per unit area, the lower the overall potential. At lower potentials, the reaction is more likely to occur and, hence,  $E_{\text{IS}} > E_{\text{FS}}$  and  $E_{\text{TS}} > E_{\text{FS}}$ .

The slopes of the lines in Figure 7.1(a,b) correspond to differences in charges stored in the capacitor,  $q_{\text{TS} \rightarrow \text{FS}} = -0.37e$  and  $q_{\text{IS} \rightarrow \text{FS}} = -0.74e$ . Physically,  $q_{\text{TS} \rightarrow \text{FS}}$  represents the charge transferred going from TS to FS. Thus, Equation 7.4 allows for a clear determination of the charge transfer coefficient from DFT energies and workfunctions. Note that  $q_{\text{IS} \rightarrow \text{FS}} \neq 1$ , which is in line with previous findings [90, 91]. This lower than expected value of the charge transfer coefficient is likely caused by hybridisation of the metal with the proton in the IS [102].

To summarise, there are three critical quantities to obtain potential dependent energies from DFT calculations, as seen from Equation 7.4. Two of these quantities, the reaction energy  $\Delta E_{1 \rightarrow 2}$  and the mean workfunction  $(\phi_1 + \phi_2)/2$  are outputs of DFT calculations performed in a single cell size. The charge transfer coefficient,  $(q_2 - q_1)$ , however, requires DFT calculations in several different cell sizes or the use of charge partitioning schemes.

### 7.3 Model development

In this section we develop a model to obtain the charge transfer coefficient,  $q_2 - q_1$ , from a single DFT calculation. We start by defining a normalised reaction coordinate between two states,  $\omega$ , a reaction length  $l_e$  and the reaction coordinate  $\mathbf{Q}$  (bold symbols denote vectors; standard typeface indicates norm

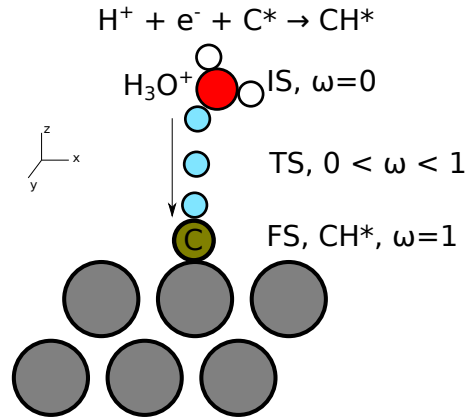


Figure 7.2: Schematic showing the normalised reaction path for a proton electron transfer reaction,  $C + H^+ + e^- \rightarrow CH^*$  on a metal surface.  $\omega$  denotes the idealised reaction path; IS, TS and FS are the initial, transition and final state respectively.

of the vectors). These three quantities are related as,

$$Q = l_e \omega \quad (7.6)$$

Figure 7.2 shows a schematic of the reaction,  $H^+ + e^- + C^* \rightarrow CH^*$ , where we have marked  $\omega$  as it changes from the IS through the TS to the FS. Throughout this work we define the TS as the state corresponding to the energy maximum along a reaction path. In the IS, the proton is bound to  $H_2O$  forming a hydronium ion. As the reaction proceeds, the proton reaches the TS and finally protonates  $C^*$  to form  $CH^*$  in the FS. Within this picture,  $\omega$  is 0 at the IS, 1 at the FS and any value in between 0 and 1 at the TS.

To begin, we illustrate the reaction coordinate consisting of moving just the proton (shown in cyan in Figure 7.2) to the surface. We will later generalise this coordinate to any number of atoms. We Taylor expand the variation of charge transfer coefficient with respect to  $\omega$ . In general, between two states 1 and 2,

where  $\omega = 0$  at state 1 and  $\omega = 1$  at state 2, for each dimension,

$$\mathbf{q}_2 = \mathbf{q}_1 + \left( \frac{d\mathbf{q}}{d\omega} \Big|_{\omega=0} \omega \right) + \mathcal{O}(\omega^2) \quad (7.7)$$

The quantity in the brackets in Equation 7.7 is rewritten as a function of the dipole moment measured along the corresponding dimension,  $\boldsymbol{\mu}$ , and  $\mathbf{Q}$  by realising that the poles of the dipole are at a distance  $l_e$  such that,

$$\boldsymbol{\mu} = l_e \mathbf{q} \quad (7.8)$$

leading to,

$$\frac{d\mathbf{q}}{d\omega} = \frac{d\boldsymbol{\mu}}{d\mathbf{Q}} \quad (7.9)$$

Note that in the limit of  $l_e \rightarrow 0$ ,  $\boldsymbol{\mu} \rightarrow 0$  such that  $q$  is always finite.

In typical periodic surface computational setups  $\boldsymbol{\mu}$  for a given computational cell may be determined by integrating the charge density  $\boldsymbol{\rho}$ , as  $\boldsymbol{\mu} = \int \boldsymbol{\rho} d\mathbf{R}$  where  $\mathbf{R}$  are the Cartesian coordinates. Additionally, most modern *ab-initio* codes provide  $\boldsymbol{\mu}$  as an output.

Finally, we obtain the quantity  $d\boldsymbol{\mu}/d\mathbf{Q}$  by finding the dipole derivative along  $\mathbf{R}$  and then projecting onto the reaction mode  $\boldsymbol{\omega}$  (represented in Cartesian coordinates)[103]

$$\frac{d\boldsymbol{\mu}}{d\mathbf{Q}} = \frac{d\boldsymbol{\mu}}{d\mathbf{R}} \cdot \boldsymbol{\omega} \quad (7.10)$$

where  $\boldsymbol{\mu}$  is the dipole moment vector in Cartesian coordinates. Equation 7.10 can be generalised to include any number of atoms by writing the dot product of the right-hand side as a sum over  $i = 1, \dots, N$  atoms,

$$\frac{d\boldsymbol{\mu}}{d\mathbf{Q}} = \sum_{i=1}^N \frac{d\boldsymbol{\mu}}{d\mathbf{R}_i} \cdot \boldsymbol{\omega}_i, \quad (7.11)$$

where  $N$  is the number of atoms involved in the reaction. Note that  $N$  does not have to be all atoms in the unit cell. The overall equation for the differences in

charges between two states 1 and 2 from Equation 7.7 reduces to,

$$\mathbf{q}_2 - \mathbf{q}_1 = \sum_{i=1}^N \frac{d\boldsymbol{\mu}}{d\mathbf{R}_i} \cdot \boldsymbol{\omega}_i \quad (7.12)$$

Electrochemical barriers are conventionally computed in quasi-2D surface setups, where we are usually concerned with the dipole moment only in the out-of-plane direction. Henceforth, we will refer to  $d\mu/dR$ , the derivative in Equation 7.12 as that along the direction of the surface normal. We obtain the dipole derivative in two ways [103]:

1. Moving atoms by small displacements  $\Delta z$ , in the Cartesian coordinates  $R$  and then computing the derivative through finite differences

$$\frac{d\mu}{dR} = \frac{\mu^{j+1} - \mu^{j-1}}{2\Delta z} \quad (7.13)$$

where we have dropped the subscript (1,2 in Equation 7.12 ) on  $\mu$ , since this finite difference operation is valid at any state.  $\mu^{j+1}$  is the dipole moment at  $+\Delta z$  and  $\mu^{j-1}$  is the dipole moment at  $-\Delta z$  from the equilibrium positions

2. Making use of the following equivalence between the dipole derivative and the first derivative of the force,  $F$  the applied field,  $\xi$  (through, for example, a saw-tooth potential) and using  $\mu = dE/d\xi$  and  $F = dE/dR$ ,

$$\frac{d\mu}{dR} = \frac{d}{d\xi} \frac{dE}{dR} = \frac{dF}{d\xi} \quad (7.14)$$

We compute the force based derivative through finite differences by applying saw-tooth potentials of different magnitude with a spacing of  $\Delta\xi$

$$\frac{dF}{d\xi} = \frac{-F^{j+2} + 8F^{j+1} - 8F^{j-1} + F^{j-2}}{12\Delta\xi} \quad (7.15)$$

where we use a four point finite difference stencil of  $\xi$  to reduce the requirements for accurate forces from the SCF cycle. Superscripts of  $F$  denote the order of the applied field, such that  $F^{j+2}$  are the forces at  $\xi + 2\Delta\xi$ ,  $F^{j+1}$  are the forces at  $\xi + \Delta\xi$  and so on.

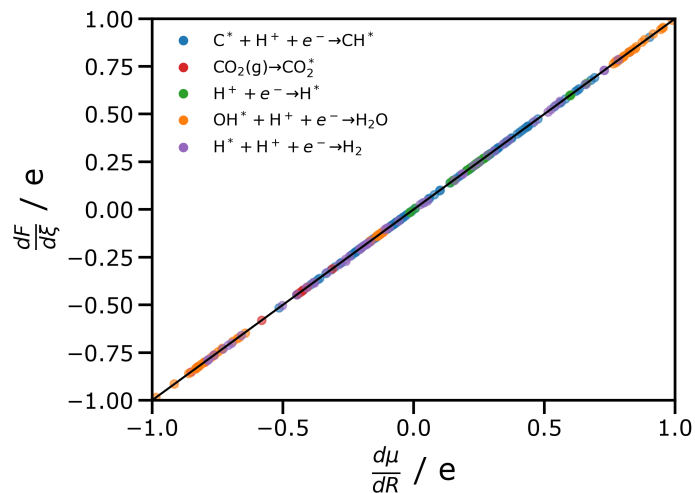


Figure 7.3: Equivalence of the dipole derivative  $d\mu/dR$  and the force derivative  $dF/d\xi$  for a range of elementary electrode reactions

In practice, we obtain  $\omega_i$  by simply normalising the atomic positions of state 1 and 2,

$$\omega_i \approx \frac{\text{positions}_{i,2} - \text{positions}_{i,1}}{|\text{positions}_{i,2} - \text{positions}_{i,1}|} \quad (7.16)$$

Finally, the differences in charge stored between two states 1 and 2 is obtained by substituting Equation 7.14 into Equation 7.12,

$$q_2 - q_1 = \sum_{i=1}^N \left( \frac{dF}{d\xi_i} \cdot X_i \right)_i \quad (7.17)$$

Figure 7.3 shows that obtaining the derivatives from either displacement through dipole (Equation 7.14) or through forces (Equation 7.15) leads to the same value. This equivalence between the two approaches implies that we prefer to use the atom-centered forces from a DFT-calculation at a chosen structure (as in  $dF/d\xi$ ) instead of displacing atoms (as in  $d\mu/dR$ ). Note that this equivalence is only seen when the forces are properly converged.

## 7.4 Application to electrocatalytic reactions

In this section, we apply the force-based methodology to several electrochemical reactions, including protonation and adsorption of polar intermediates. The latter class of reactions will be studied in detail in Chapter 8 when we investigate CO<sub>2</sub> adsorption as a reaction step of CO<sub>2</sub>R. We compare the value of the transfer coefficient,  $q = (q_2 - q_1)$  from Equation 7.17 with that obtained by fitting multiple cell sizes through Equation 7.4.

We start by investigating the prototype reaction discussed in Figure 7.1, i.e.  $\text{H}^+ + \text{e}^- + \text{C}^* \rightarrow \text{CH}^*$ . Figure 7.4a shows the variation of the energy and Figure 7.4b shows  $q$  from Equation 7.17 along the reaction path considering just the proton and the adsorbed C atom. The charge goes through a maximum at the TS falling to zero when the CH\* species is formed, mirroring the change in energy with reaction path. Different cell sizes, spanning a potential range of 2V in potential, are consistent in their force-based prediction of  $q \approx 0.3e$ , which is similar to the value of  $q = 0.37e$  from fitting over the varying cell sizes in Figure 7.1. Note that in contrast to the slope in Figure 7.1, the predicted  $q$  is much lower in the case of the IS (first point in Figure 7.4a and Figure 7.4b). The reason for this lower prediction is that in the IS the reacting proton does not exist as a single entity. Rather the charge is spread out over the hydronium ion (bottom left inset Figure 7.4b). This spreading out of the charge explains why the predicted  $q$  for a single proton is roughly 1/3<sup>rd</sup> that determined in Figure 7.1a (see below for discussion on treating FS  $\rightarrow$  IS).

The central quantity of interest for the purposes of reaction kinetics studies is the charge transfer coefficient, i.e.  $q$  at the TS with respect to a thermodynamically stable state (such as IS or FS). Specifically, the variation of the TS energy with potential is typically an input into micro-kinetic models. Figure 7.4b shows the variation of  $\Delta E^{\text{TS}}$  with the mean potential,  $(\phi_{\text{TS}} + \phi_{\text{FS}})/2$  for different cell sizes (and hence different proton concentrations). The black line indicates the least squares fit to the cell sizes and lines of other colours indicate the predicted variation of the  $\Delta E^{\text{TS}}$  through the  $q$  obtained in Figure

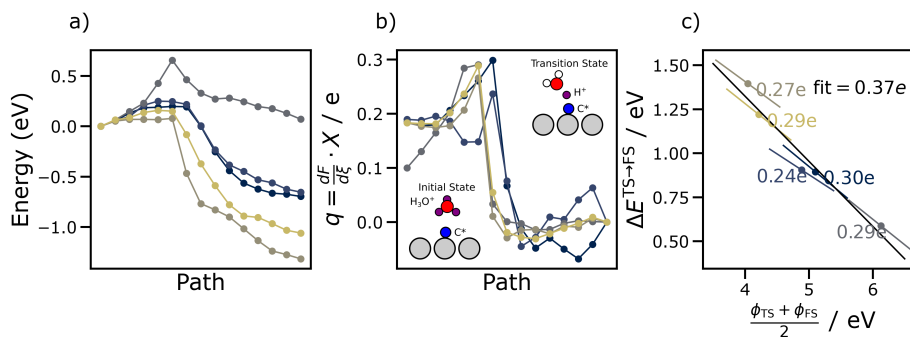


Figure 7.4: a) Raw energies from images used in a nudged-elastic band calculation of  $\text{C}^* + \text{H}^+ + \text{e}^- \rightarrow \text{CH}^*$  b)  $(q_2 - q_1)$  obtained for all images for the reaction  $\text{H}^+ + \text{e}^- + \text{C}^* \rightarrow \text{CH}^*$  c) Energy vs. mean potential based on fitting (black line) and the predictions from finite difference for different cells (colors)

7.4b. Thus, for transition states, the force-based method is able to predict the variation of energies with potential.

We now compare the charge transfer coefficient for our force-based method with the cell extrapolated value. To do so, we perform electrochemical barrier calculations for three reactions,  $\text{C}^* + \text{H}^+ + \text{e}^- \rightarrow \text{CH}^*$  (this work),  $\text{OH}^* + \text{H}^+ + \text{e}^- \rightarrow \text{H}_2\text{O}$  and  $\text{H}^* + \text{H}^+ + \text{e}^- \rightarrow \text{H}_2$  (from Ref.[90, 91]). Figure 7.5 shows a parity plot between the  $q$  obtained from Equation 7.17 and from fitting (Equation 7.4), the dashed line indicates an exact match. For these three reactions, the obtained values for both methods are within  $\pm 0.1e$  for all cells.

As in Ref [93], we suggest that adsorption processes can be considered within the framework of the capacitor model. While an *ab-initio* reaction path would then be missing, we choose a simplified reaction path, where all atoms participating in the reaction move simultaneously along the axis perpendicular to the surface. For example, in the case of the  $\text{CO}_2$  adsorption reaction,  $\omega$  would correspond to a transition from a bent  $\text{CO}_2^*$  molecule to a linear  $\text{CO}_2$ . Figure 7.5 shows that this approximation leads to  $q$  which is slightly underestimated from the corresponding value obtained by fitting, likely a consequence of assuming an idealised reaction path.



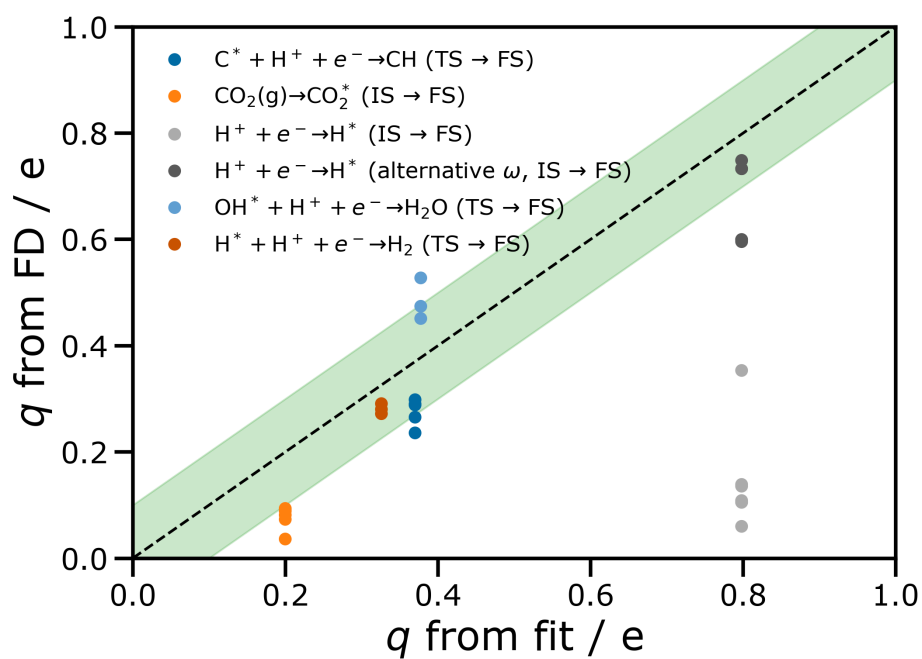


Figure 7.5: Parity plot for  $q$  from fitting through Equation 7.4 for a series of increasingly larger unit cells and through the force-based method as in Equation 7.17; dashed line indicates exact fit and green band indicates  $\pm 0.1$  error with either methodology. Alternative  $\omega$  denotes an idealised reaction path where the proton descends directly to the surface along the direction of the surface normal.

In the case of IS  $\rightarrow$  FS reaction paths, such as in  $\text{H}^+ + \text{e}^- \rightarrow \text{H}^*$ , we again see that the predicted  $q$  from finite differences is roughly a third of the value predicted by fitting (due to the hybridised nature of the proton in the IS). An idealised reaction coordinate  $\omega = (0, 0, 1)$  corresponding to a proton dropping linearly along the surface-normal axis, leads to a closer match between the two methodologies (denoted as alternative  $\omega$  in Figure 7.5). This improvement by simplification suggests that the two term Taylor series expansion in Equation 7.12 breaks down in the limit of large reaction coordinates, which is unlikely to occur when extrapolating from TS to FS.

To summarise, the overall strength of this methodology lies in its ability to determine the charge transfer coefficient,  $q$  using a simple model of the interface and the atom centered forces. Besides treating ion-electron transfers, it can also be used to determine the electrode potential dependence of polar adsorbates like  $\text{CO}_2^*$  and other intermediates that are critical to mechanistic understanding in reactions such as  $\text{CO}_2\text{R}$ .

## 7.5 Conclusion

Activation energies are critical to a mechanistic understanding of electrochemical reaction processes. However, significant challenges such as cell-size dependence remain to determining accurate *ab-initio* electrochemical barriers. In this work, we suggest a simple model to compute the charge transfer coefficients, and hence the activation energies, with just a single DFT calculation. Our method builds upon previous extrapolation procedures and removes the short-comings of explicit partitioning of the charge density, which give rise to ambiguous or unphysical jumps in charge transfer along the reaction pathway. We show that the charge transfer coefficient is related to the derivative of the atom centered forces with applied field. We perform a series of electrochemical barrier calculations and show that the charge transfer coefficient computed with our method is in good agreement with the value obtained by performing traditional cell-extrapolation procedures, which require multiple cell sizes. We show that our

methodology can be successfully used for transition states as well as polar adsorbates, both critical species in electrochemical reactions.

## 7.6 Computational Methods

Density functional theory calculations were carried out using the Vienna Ab Initio Software Package [61]. Core electrons were described using projector augmented wave (PAW) potentials. Valence electrons were described as plane waves with kinetic energy up to 500 eV. All calculations were performed using the RPBE functional [25]. The lattice constant of Pt was calculated using a  $12 \times 12 \times 1$   $k$ -point sampling and the ISIF=3 algorithm implemented in VASP and the obtained value was 3.99 Å. Gaussian smearing with a width of 0.1 eV was used. Pt(111) slabs were prepared using the Atomic Simulation Environment [63]. Cells of sizes (3x2), (3x4), (3x6) and (6x2) were used with  $k$ -point sampling of (4,6,1), (4,3,1), (4,2,1), (2,6,1) respectively. A dipole correction was applied in the axis perpendicular to the surface. Transition states for  $C^* \rightarrow CH^*$  was determined using the AIDNEB [104]. 15 images were used for each calculation.

$H^* \rightarrow H_2$  and  $OH^* \rightarrow H_2O$  were taken from previous work and were calculated using GPAW [105] as the DFT code [90, 91]. Calculations were done in (3x2), (3x4), (3x6) and (6x4) with a  $k$ -point sampling of (4,6,1), (4,3,1), (4,2,1) and (2,3,1) respectively. FermiDirac smearing was used with a width of 0.1 eV.

Finite difference calculations for all reactions considered in this work were performed using the same computational setup as for relaxations except for a smaller EDIFF =  $10^{-7}$  eV in order to ensure convergence of atom centered forces (for VASP). In the case of GPAW, energies were converged to up to  $10^{-9}$  eV. Atom displacements were 0.01 Å unless mentioned otherwise, saw-tooth potentials were added using the EFIELD option in VASP and the Constant-ElectricField option in GPAW with a strength of  $-0.2, -0.1, 0.1, 0.2$  V/Å.



## Chapter 8

# Dipole-field interactions in CO<sub>2</sub>R

In this chapter we apply the models developed in this thesis to the CO<sub>2</sub>R reaction. We find that dipole-field interactions play a crucial role in determining the activity of a material towards this reaction. We highlight this effect by studying CO<sub>2</sub>R on transition metal surfaces as well as on doped graphene materials. The contents of this chapter overlap with two publications, *Dipole-Field Interactions Determine the CO<sub>2</sub> Reduction Activity of 2D Fe-N-C Single Atom Catalysts* [56] (enclosed in Section 10.3) and *Unified mechanistic understanding of CO<sub>2</sub> reduction to CO on transition metal and single atom catalysts* [106] (enclosed in Section 10.4).

### 8.1 Introduction

Electrochemical reduction of CO<sub>2</sub> is one of the most promising approaches to store renewable energy into valuable fuels and chemicals. The simplest reaction within CO<sub>2</sub>R reaction network is the reduction of CO<sub>2</sub> to CO. Noble metals such as gold and silver are good electro catalysts for this reaction. At lab scale,

gold produces as much as  $10 \text{ mA cm}^{-2}$  of CO at upto 100% Faradaic efficiency [107]. The process is also one of the first to be realised commercially with Ag gas diffusion electrodes producing up to  $300 \text{ mA cm}^{-2}$  of CO [7].

The major obstacles to commercial realisation of  $\text{CO}_2\text{R}$  is activity and cost. Recently, iron doped graphene materials (shortened to FeNC, iron nitrogen carbon) have been shown to produce impressive geometric current densities (up to  $100 \text{ mA cm}^2$ ). These catalysts have high Faradaic efficiencies to CO, while being less selective towards the hydrogen evolution reaction (HER) at typical operating conditions of  $-0.6 \text{ V vs RHE}$  [60].

From a computational perspective, mechanistic study of metal-nitrogen-carbon (MNC) systems present several challenges. There are a plethora of possible active sites caused by the mode of synthesis of defected graphene, which makes computational prediction of chemisorption energies and activation energies of reaction intermediates challenging. For selected active sites of FeNC that have been studied with DFT [57, 58, 59], the chemisorption energy of CO is predicted to be in the range of  $-0.6$  to  $-1.2 \text{ eV}$ . These values correspond to a strong-binding CO surface ( $\Delta G < 0$ ,  $\theta \gg 0$ ), which is contrary to experimental evidence which suggests FeNC is a good  $\text{CO}_2\text{R}$  catalyst to CO (implying weak CO binding). Further, there is controversy regarding the nature of the  $\text{CO}_2$  adsorption step, written as,



This step is often considered to produce a unit-charged  $\text{CO}_2$  intermediate [8, 108] (such as  $\text{CO}_2^-$ ). This suggestion might arise from the aqueous reduction of  $\text{CO}_2$  to  $\text{CO}_2^-$ , which occurs at very negative reduction potentials of  $-1.9 \text{ V vs. SHE}$ . Another hypothesis centers around solvent reorganisation which has been considered through Marcus theory [108]. In this chapter and corresponding manuscripts [56, 106], we propose that this reaction is driven by the interaction of the dipole created by an adsorbed  $\text{CO}_2$  with an interfacial field. Given that near-electrode field strengths can reach up to  $10^9 \text{ Vm}^{-1}$  at reducing potentials

on metal electrodes, a surface dipole moment created by an adsorbate would be (de)stabilised by this environment. With this approach, there is no need for a unit charged  $\text{CO}_2$ , but instead only a polarised  $\text{CO}_2^*$  species, similar to other adsorbed intermediates such as  $\text{CO}^*$ .

In this chapter, we overcome the above-mentioned challenges related to modelling MNC materials through a rigorous computational study. Through a combination of Hybrid DFT calculations and interpreting temperature programmed desorption experiments we show that GGA functionals are inadequate to accurately describe the binding of the reaction intermediates of  $\text{CO}_2\text{R}$  on FeNC. We parameterise a Hubbard-U value to be used in conjunction with GGA functionals to obtain reasonably accurate adsorption energies at lower computational cost than hybrid-DFT calculations. By considering the width of the *sp*-projected density of states of  $\text{CO}_2^*$  along with the Newns-Anderson model of chemisorption, we find that electron transfer to MNC materials are facile, just like in transition metals. We combine DFT calculations with consideration of dipole-field interactions to micro-kinetic models of  $\text{CO}_2\text{R}$  to  $\text{CO}$  to find that transition metals are limited by the first step of the reaction, i.e.  $\text{CO}_2$  adsorption. Likewise, FeNC is limited by  $\text{CO}_2$  adsorption, while NiNC (Nickel doped graphene) and CoPc (Cobalt Phthalocyanine) appear to be limited by the second reaction step, i.e. the protonation of  $\text{CO}_2^*$  to form  $\text{COOH}^*$ . These computational findings are in agreement with experimental pH dependent experiments. We show that this difference in rate limiting step is caused by the large surface dipole moment of  $\text{CO}_2$  on MNC materials as compared to transition metals. We discuss implications of this finding for the design of novel  $\text{CO}_2\text{R}$  catalysts.

## 8.2 CO adsorption energies

In this section we discuss the computational setup that we choose to describe MNC catalysts. In Figure 4.8 (Chapter 4) we showed that for a range of FeNC motifs, GGA DFT calculations with RPBE led to strong CO binding ( $\approx -1$  eV), resulting in a large coverage of CO on FeNC. This prediction is inconsistent with

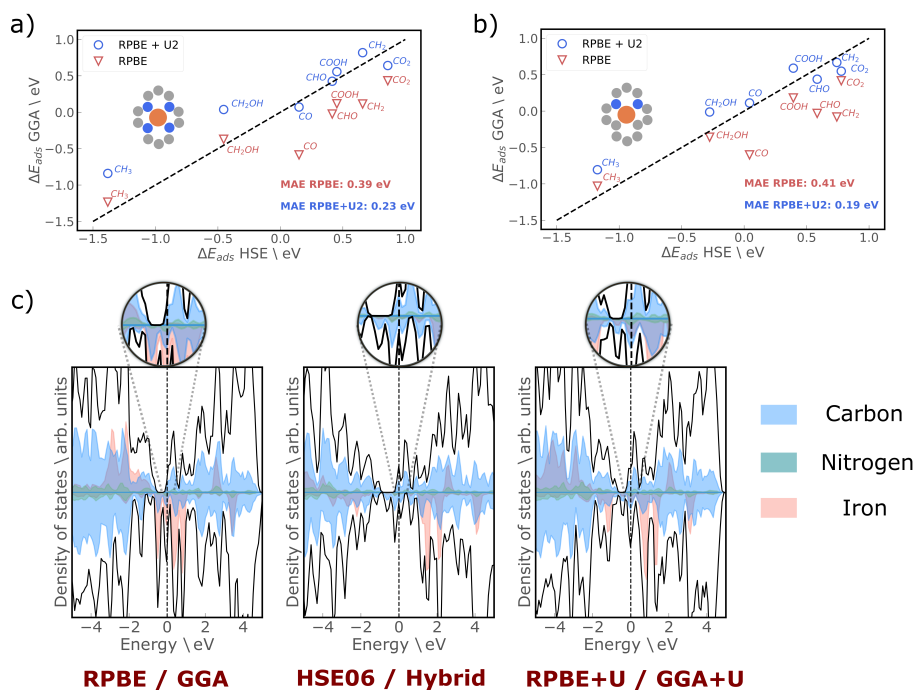


Figure 8.1: Comparison of RPBE and RPBE+U adsorption energies for relevant  $\text{CO}_2\text{R}$  intermediates for a) DV4N b) DV2N. Insets show the corresponding structures and mean absolute errors for both functionals. c) Projected density of states (DOS) of DV2N structure with three functionals RPBE, HSE06 and RPBE+U with  $U=2$  eV ; color scheme: Blue: Carbon, Green: Nitrogen, Orange: Iron, Black: total DOS; states near the Fermi level have been magnified for clarity; horizontal line divides spin up and spin down states. *Reprinted from paper in Section 10.3* [56]

two sets of experimental evidence,

1. FeNC has been shown to be a good  $\text{CO}_2\text{R}$  to CO catalysts, implying that it has weak to moderate CO binding strength.
2. The adsorption energy (i.e. the internal energy) of CO extracted from TPD experiments is between  $-0.6$  eV to  $-0.8$  eV.



The binding strength of CO is considerably weaker for hybrid DFT functional HSE06, which predicts CO binding to be approximately  $-0.5$  eV for three different site motifs. Note that the predicted energies for most of the FeNC motifs are weaker than those on Fe(211), suggesting that the active site for the CO<sub>2</sub>R reaction on FeNC materials is not an Fe surface (as CO would bind too strongly).

Performing hybrid DFT calculations is infeasible for a large scale computational study. To allow for computations at reduced cost, we determine a Hubbard-U parameters for the  $d$ -states of Fe. We find that  $U = 2$  eV approximates well the energies of different reaction intermediates in CO<sub>2</sub>R, shown in blue in Figure 8.1(a,b) for two different site motifs; double vacancy with four and two nitrogen atoms surrounding the metal (DV4N, DV2N respectively). The mean absolute error for this choice of Hubbard-U parameter is 0.16 eV lower than that from RPBE calculations (shown in red).

The reason for the improved prediction of adsorption energies by adding a Hubbard-U to the  $d$ -states of Fe is seen in the projected density of states in Figure 8.1c. The  $d$ -density of states in the case of RPBE are close to the Fermi level, while the gap between the  $d$ -states for the HSE06 functional is larger (about 4 eV). Adding a Hubbard-U shifts the  $d$ -states and mitigates the self-interaction error present in the RPBE calculation. We note that this Hubbard U parameter was determined specifically for FeNC systems and tested for a selection of motifs considered in this work. Careful parameterisation is needed for other MNC systems.

### 8.3 Electron transfer on MNC catalysts

In this section, we show that the electron transfer to the adsorbate is adiabatic for MNC materials under reducing conditions, as in transition metals. A consequence of this result is that we would not have to consider separate CO<sub>2</sub>\* (adsorbed) and CO<sub>2</sub><sup>-</sup> (unit charged) states in our computations. Instead, we would only need to compute CO<sub>2</sub>\* using conventional DFT setups (as described

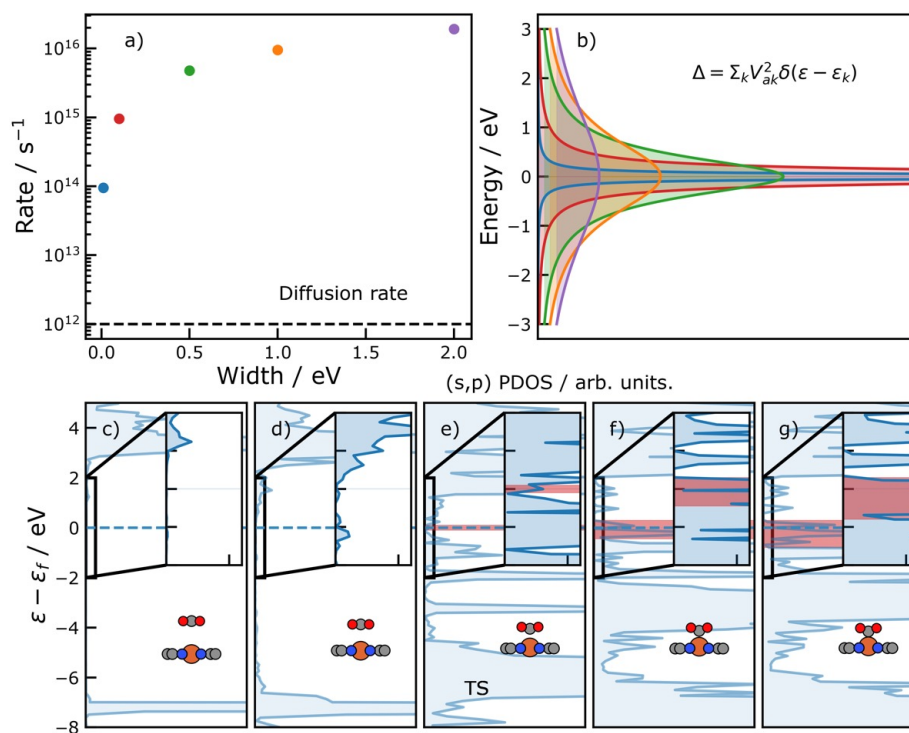


Figure 8.2: Rate of electron hopping (a) for the different idealized Lorentzian peaks shown in b. c-g, Densities of states projected onto CO<sub>2</sub> *s* and/or *p*-states for selected images of a CO<sub>2</sub> adsorption climbing image nudged elastic band run on FeNC show a short timescale of electron transfer. Insets: zoomed-in parts of the highlighted region; red bands indicate the estimated width of the states at the Fermi level,  $\epsilon_f$ ; a.u. is arbitrary units. *Reprinted from paper in Section 10.4* [106]

in Section 8.4).

Similar to Ref [109], we consider the rate of electron transfer to the adsorbate based on Fermi's Golden Rule,

$$\text{rate} = \frac{2\pi}{\hbar} \Delta \quad (8.2)$$

where the continuous coupling element,  $\Delta$ , is taken directly from the Newns-

Anderson model in Equation 2.6. Figure 8.2a show the rate as a function of the width of different Lorentzian functions, shown in Figure 8.2b. Even for a small width of 0.1 eV, the rate of electron transfer is greater than  $10^{14} \text{ s}^{-1}$ . This rate is at least two orders of magnitude larger than other competing processes, such as ion diffusion ( $\approx 10^{12} \text{ s}^{-1}$ ).

In practice, we obtain  $\Delta$  directly from the *sp* projected density of states of  $\text{CO}_2$  at the transition state of the reaction process in Reaction 8.1. Figure 8.2(c-g) shows the *sp* projected density of states of  $\text{CO}_2$  along the reaction path. As the  $\text{CO}_2$  molecule approaches the surface, its *sp* states broaden into resonances [25]. At the transition state, we determine the width of the peak at the Fermi level (denoted by the red bar) to be greater than 0.1 eV, which implies a timescale of  $10^{-14} \text{ s}$  (timescale is inverse of rate). Through this analysis, we conclude that the adsorption of  $\text{CO}_2$  is not limited by an electron transfer step on MNC materials.

## 8.4 Potential dependent reaction energies

In this section we describe how we compute potential dependent energetics for the reaction intermediates in  $\text{CO}_2\text{R}$  to  $\text{CO}$ . We use the method of Ref [93] and the charge transfer coefficients from Chapter 7 to determine the potential dependence of polar intermediate  $\text{CO}_2$ .

When an intermediate such as  $\text{CO}_2$  adsorbs in a bent configuration in a finite-sized unit cell, it changes the workfunction dramatically, as large as 1-2 eV in small unit cells [93]. This alteration to the workfunction is problematic because it prevents the computation from being done at a constant driving force. To alleviate this problem, constant workfunction methods have been developed, which introduces excess electrons into a DFT calculation, while preserving charge neutrality by adding positive charge into a continuum placed a suitable height above the adsorbate. However, the mismatch in capacitance of the different charging components give rise to variations in energies amongst different calculation setups or cell sizes, which are sometimes as large as 1 eV

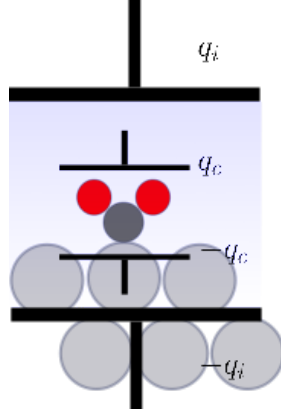


Figure 8.3: Schematic showing the multiple capacitances that have been used in this work;  $q_c$  denotes the charge for the capacitance for  $\text{CO}_2$  adsorption, while  $q_i$  denotes the charge for the capacitance from continuum charging. *Reprinted from paper in Section 10.4* [106]

[93]. One way to solve this problem is to use the effective surface charge as the descriptor of the driving force, instead of the workfunction, since it reflects the local interfacial field and potential drop. Here we describe these terms mathematically as well as illustrate how they are used to describe  $\text{CO}_2$  adsorption.

We employ two parallel plate capacitors to describe the charge separation arising from adsorbed  $\text{CO}_2$  ( $q_c$ ) and from the excess continuum charge ( $q_i$ ), as shown in Figure 8.3. The integral energy,  $E$ , for this system is expressed as a Taylor series expansion over  $q_c$  and  $q_i$  is written as,

$$\begin{aligned}
 E = E_0 + q_c \left. \frac{\partial E}{\partial q_c} \right|_{q_c=0, q_i=0} + q_i \left. \frac{\partial E}{\partial q_i} \right|_{q_c=0, q_i=0} + \\
 \frac{q_c^2}{2} \left. \frac{\partial^2 E}{\partial q_c^2} \right|_{q_c=0, q_i=0} + \frac{q_i^2}{2} \left. \frac{\partial^2 E}{\partial q_i^2} \right|_{q_c=0, q_i=0} \\
 + q_i q_c \left. \frac{\partial^2 E}{\partial q_i \partial q_c} \right|_{q_i=0, q_c=0} + \mathcal{O}(q_i^3, q_c^3) \quad (8.3)
 \end{aligned}$$

Note that there has been no *a priori* assumption of the configuration of the capacitors, i.e. it is not necessary that the capacitors are in series or parallel.

Table 8.1:  $q_c$  determined based on the method discussed in Chapter 7 for different transition metals and MNC materials. On average, it appears that  $q_c$  determined for MNC materials is larger than those on transition metal surfaces.

Transition metal	$q_c$ (e)	Metal-Nitrogen Carbon	$q_c$ (e)
Ag(100)	0.37	Fe(1,1)	0.35
Au(100)	0.21	Ni(1,1)	0.21
Cu(100)	0.25	Ni(1,2)	0.31
Pd(100)	0.14	Fe(1,3)	0.10
Pt(100)	0.13	Fe(2,1)	0.38
Ag(211)	0.35	Ni(2,1)	0.42
Au(211)	0.30	Fe(2,2)	0.49
Cu(211)	0.22	Ni(2,2)	0.47
Pd(211)	0.13	Fe(2,3)	0.1
Pt(211)	0.09	Ni(2,3)	0.49
		Fe(2,4)	0.29
		Ni(2,4)	0.49

The resultant differential energy,  $\Delta E$  between the two states  $\text{CO}_2(\text{g})$  and  $\text{CO}_2^*$  is obtained by taking the difference in energy between  $E(q_i, q_c = 0)$  and  $E(q_i, q_c = q_c)$  from Equation 8.3,

$$\Delta E = \Delta E_0 + q_c \left( \phi_0 + \frac{q_c + q_i}{2AC} \right) \quad (8.4)$$

where  $\Delta E_0$  is the energy of a hypothetical reference state consisting of all the non-electrostatic “chemisorption” based contributions having a workfunction  $\phi_0$ ,  $A$  is the surface area of the cell and  $C$  is the capacitance of the capacitor with charge  $q_c$  (in Figure 8.3). In order to determine  $q_c$ , we use the method described in Chapter 7. Table 8.1 shows the values for a few representative transition metals for (100) and (211) surface facets and Fe and Ni MNC materials.

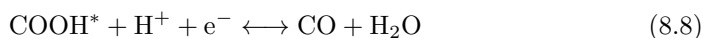
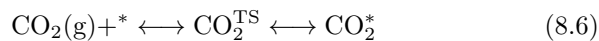
Having determined  $q_c$ , we use Equation 8.4 to plot the energy difference from a DFT calculation performed with a certain  $q_i$  against  $\sigma = (q_i + q_c)/2AC$ .  $\sigma$  is

converted to potential using the simple capacitor relationship,

$$\sigma = C_{\text{exp}} (\phi - \phi_0) \quad (8.5)$$

where  $C_{\text{exp}}$  is the experimental capacitance, assumed throughout this work to be  $25\mu\text{Fcm}^{-2}$ .  $\phi_0$  is the potential of zero charge of the material.

Having determined the energies as a function of potential, we now turn to  $\text{CO}_2\text{R}$ , which is a reaction network consisting of multiple proton-electron transfers as well as adsorption of polar species. The mechanism that we choose to describe this reaction is,



where the potential dependence of the proton-electron pair is included through the computational hydrogen electrode (CHE) [18]. The chemical potential of the proton and electron is related to that of  $\text{H}_2$  at 0 V vs RHE though,

$$\mu_{\text{H}^+} + \mu_{\text{e}^-} = \frac{1}{2}\mu_{\text{H}_2(\text{g})} \quad (8.10)$$

Figure 8.4 shows the free energy diagram for two motifs of FeNC at three different potentials including the equilibrium potential ( $-0.3$  V vs SHE) and two more representative potentials at which the reaction is expected to occur (at  $-0.75$  V vs SHE and  $-1.2$  V vs. SHE). The field dependence of the polar  $\text{CO}_2^*$  intermediate is captured by its decreasing  $\Delta G$  with potential. In the case of  $\text{COOH}^*$  and  $\text{CO}^*$ , the free energies decrease with potential due to the increased chemical potential of the electron as well as a (minor) field dependence.

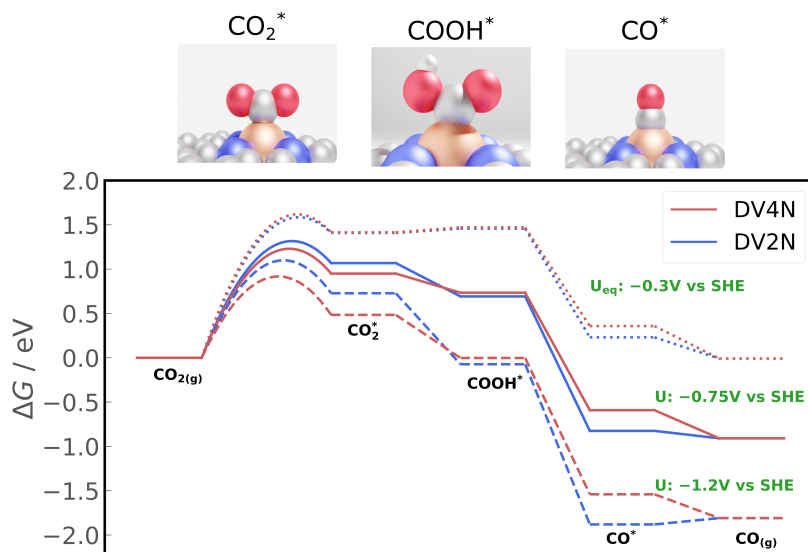


Figure 8.4: Free energy diagram at the theoretical equilibrium potential  $U_{\text{eq}} = -0.3$  V and at two other potentials:  $-0.75$  V and  $-1.2$  V vs SHE for DV4N and DV2N vacancies at a pH of 2. *Reprinted from paper in Section 10.3* [56]

## 8.5 Kinetic modelling of CO<sub>2</sub>R

In this section we utilise the potential dependent free energies computed in Section 8.4 to construct a kinetic model for the CO<sub>2</sub>R reaction. We use the reaction network in Reaction 8.6 to 8.9. Throughout this section, the turn-over frequencies (TOF) are determined from the rates obtained from a micro-kinetic model with rates (on a per-site basis, which is equivalent to the TOF) from Equation 2.43,

$$\text{TOF} = k_+ \prod_i \theta_i \prod_j p_j - k_- \prod_i \theta_i \prod_j p_j \quad (8.11)$$

We begin by developing a kinetic model for FeNC materials and comparing our results with available experiments. We then broaden the analysis to include transition metals and other MNC materials through a potential dependent vol-

cano for  $\text{CO}_2\text{R}$ .

### 8.5.1 FeNC catalysts

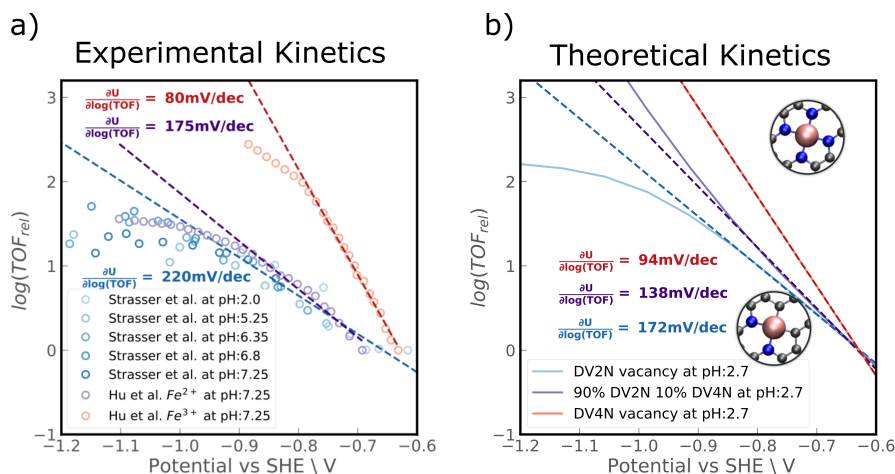


Figure 8.5: a) TOF taken from two publications - Strasser et al. [110] and Hu et al. [60]; current densities were converted to TOF by assuming all iron sites were involved in catalytic activity b) TOF obtained from mean-field microkinetic modelling; TOFs are normalized to the activity at  $-0.6$  V vs. SHE, to emphasize relative trends. *Reprinted from paper in Section 10.3* [56]

Experimentally determined pH-dependent rate measurements strongly suggest that proton-electron transfer is not involved in the rate limiting step for FeNC catalysts [60, 110]. Plotted on an SHE scale, Figure 8.5a, taken from Ref [110], shows that the experimental rates (converted to TOF assuming all sites are exposed on the surface) are independent of pH. If the rates of reaction are dependent only on an absolute scale, it would imply that the rate limiting step does *not* include a proton. This condition is reflected only in Reaction 8.6 for  $\text{CO}_2$  adsorption. Note that this condition does not hold for CO desorption in Reaction 8.9 as the coverage of CO is dependent on the previous proton electron transfers. This finding is consistent with the free energy diagram in Figure 8.4, where the reaction intermediate of  $\text{CO}_2$  has the highest free energy for all the



relevant potentials.

Based on the free energies in Figure 8.5 and the TOF expression in Equation 8.11, we compute the potential dependent TOF in Figure 8.5b. We compute the Tafel slope (dashed line in Figure 8.5b) and compare it with those obtained from the experimental TOF in Figure 8.5a. Hu et al. [60] observe Tafel slopes of 80 mV/dec for the more active sample and 126 mV/dec for the less active one. This difference is captured in our simple two-site model, with DV4N being significantly more active than DV2N. Strasser et al. also observe Tafel slopes of close to 200 mV / dec, which is similar to that obtained for DV2N.

Since CO<sub>2</sub> adsorption is the rate limiting step, the Tafel slope corresponding to activity from a given site is determined by the corresponding adsorbate dipole as follows [37]

$$\text{Tafel slope}^{-1} = \frac{\partial \log(\text{TOF})}{\partial \Phi} = \frac{\partial \log(\text{TOF})}{\partial \Delta G_{\text{CO}_2}} \frac{d \Delta G_{\text{CO}_2}}{d \Phi} \quad (8.12)$$

$$= -\frac{1}{k_B T} \frac{d \Delta G_{\text{CO}_2}}{d \sigma} \frac{d \sigma}{d \Phi} = -\frac{1}{k_B T} \frac{d \Delta G_{\text{CO}_2}}{d \sigma} C \quad (8.13)$$

$$= \frac{1}{k_B T} \frac{C}{\epsilon} \mu \quad (8.14)$$

where  $\epsilon$  is the permittivity of free space and  $\Delta G_{\text{CO}_2}$  is the free energy of CO<sub>2</sub> adsorption. Thus, larger the dipole moment, smaller the Tafel slope.

CO<sub>2</sub>\* at DV4N has a larger dipole moment as compared to that at DV2N. This is consistent with the lower Tafel slope obtained in the case of DV4N over DV2N as shown in Figure 8.5b. Since pyrolysis is the experimental method of choice to generate these catalysts, it is not yet possible to obtain atomic precision over the active site. To show how the slope shifts when multiple sites are contributing to the activity, we show the case of 10% DV4N and 90% DV2N sites, which gives an intermediate Tafel slope.

### 8.5.2 Au, NiNC and CoPc catalysts

We now present a few more examples of pH dependent rates from our computations and compare them against pH-dependent experiments. To simplify our

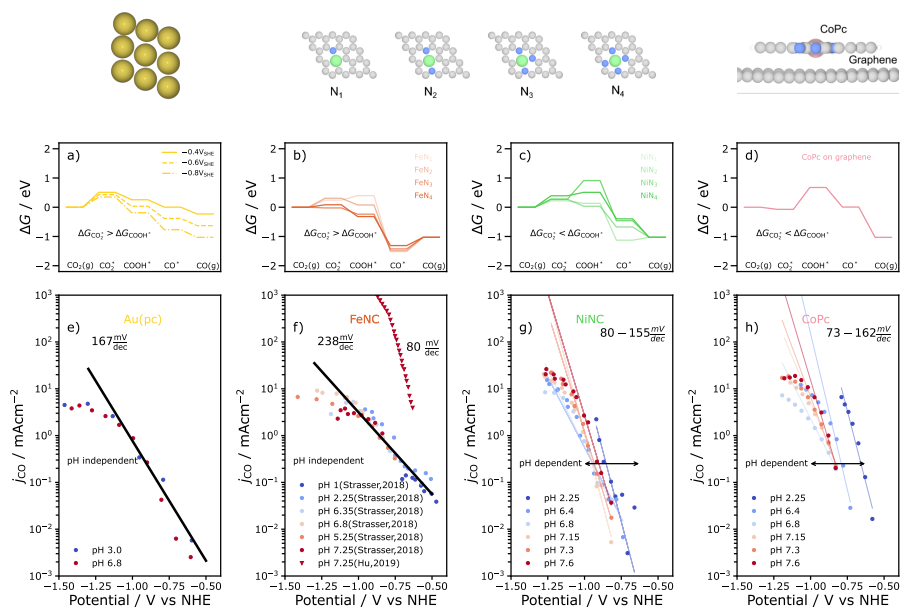


Figure 8.6: Free energy diagram of CO<sub>2</sub> to CO for a) Au(211) at  $U = -0.6, -0.8$  and  $-1.0$  V vs. SHE b) FeNC c) NiNC d) CoPc adsorbed on graphene at  $U = -0.8$  V vs. SHE with pH=2; schematics of the calculated surfaces are shown above their respective free energy diagrams, with the four double-vacancy MNC. Experimental current densities plotted against NHE potential for e) poly-crystalline Au (from Ref [111]) f) FeNC (from Ref [59, 60]) g) NiNC (this work,[106]) h) CoPc on CNT (this work, [106]) *Reprinted from paper in Section 10.4 [106]*

analysis, we assume that the barriers for each step are approximated by the free energies of the different reaction intermediates.

With the same arguments as in Section 8.5.1, where we showed that the FeNC catalysts were limited by the CO<sub>2</sub>\* adsorption step, NiNC catalysts and supported CoPc catalysts are limited by the CO<sub>2</sub>\* → COOH\* step. Figure 8.6c shows the free energy diagram for NiNC catalysts computed at  $-0.8$  V vs. SHE and a pH of 2 for various nitrogen coordination vs around the metal centre

for double vacancies (DVs). All the NiNC catalysts investigated, except for  $\text{NiN}_2$ , are limited by  $\text{COOH}^*$  formation, consistent with the pH dependence of experimental rates, as shown in Figure 8.6g. Similarly, supported CoPc catalysts also have  $\text{COOH}^*$  formation as the rate-limiting step, as shown in Figure 8.6d, which are also seen in the pH-dependent experiments shown in Figure 8.6h. Finally, analogous to FeNC catalysts, Au(211) is limited by  $\text{CO}_2$  adsorption (seen in the pH independence of rates in Figure 8.6e).

In summary, through a combination of pH and potential dependent computations, we predict the rate limiting step of  $\text{CO}_2\text{R}$  to CO on Au, FeNC, NiNC and CoPc catalysts. These predictions are in line with pH dependent experiments on the same catalysts.

### 8.5.3 Activity volcano of $\text{CO}_2\text{R}$ to CO

In order to generalise the findings of pH dependence and potential dependent rates in the previous section, we consolidate all our findings in the form of an activity volcano shown in Figure 8.7. The rate map is defined based on the scaling line of the transition metal (211) surface facet. The CO adsorption energies are incorporated in Figure 8.7 through the scaling of  $\text{COOH}^*$  and  $\text{CO}^*$  intermediates.

Figure 8.7 presents a simple scheme to determine the rate limiting step using computed  $\text{CO}_2^*$ ,  $\text{COOH}^*$  and  $\text{CO}^*$  free energies. If the point lies below the parity line, then the  $\text{COOH}^*$  formation step is rate-limiting. Meanwhile, if it is above the parity line,  $\text{CO}_2^*$  adsorption is rate limiting. At very negative adsorption energies, the surface is poisoned by CO, as shown in Figure 8.7b, which leads to  $\text{CO}^*$  desorption being rate limiting on TMs, such as Pd and Pt. All the transition metal (211) facets lie above the parity line, which indicates that  $\text{CO}_2$  adsorption or CO desorption is rate limiting at the studied potentials.

The activity volcano in Figure 8.7 serves as a template for computational screening studies using two descriptors,  $\Delta G_{\text{CO}_2}$  (which incorporates the dipole of  $\text{CO}_2^*$ ) and  $\Delta G_{\text{COOH}}$ .

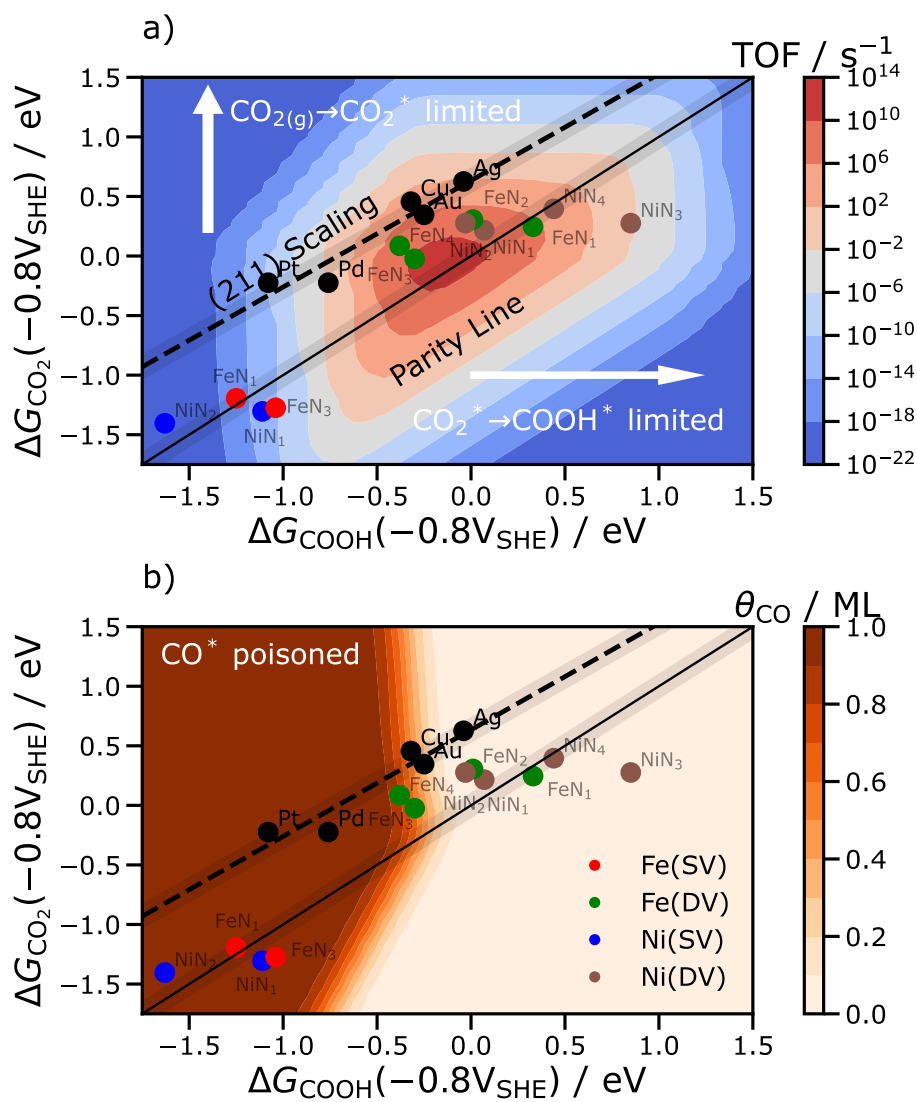


Figure 8.7: a) Rate map at  $-0.8 \text{ V}$  vs SHE and pH 2 for  $\text{CO}_2\text{R}$  to CO obtained from the (211) transition metal scaling line. The annotated points show MNC catalysts either at single vacancies or double vacancies. b) Coverage map in monolayers (ML) with the same points showing which surfaces are poisoned by CO. Reprinted from paper in Section 10.4 [106]

## 8.6 Role of surface dipole moments

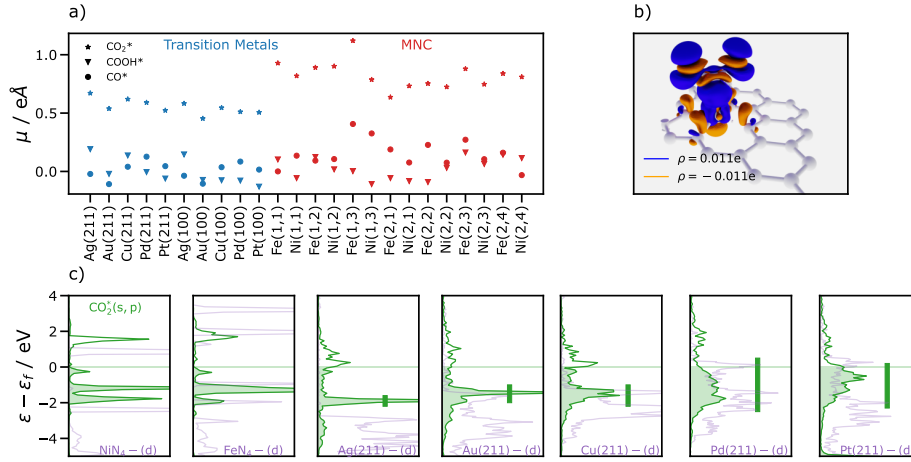


Figure 8.8: Vacuum dipole moments for (211) and (100) Tm surfaces (blue) and Fe and Ni MNCs (red). The MNC materials (first index indicates the type of vacancy, 1 for single and 2 for double; second index indicates the number of substituting N atoms) have larger dipole moments as compared with those of the transition metals. b) Charge density difference plot for CO<sub>2</sub> adsorbed on NiN<sub>4</sub>. c) Density of states projected onto the *s* and *p* states of CO<sub>2</sub><sup>\*</sup> (green) and the *d* states of the transition metals (purple) show that the adsorbate states are much narrower on MNC materials than they are on transition metals. *Reprinted from paper in Section 10.4* [106]

MNC catalysts deviate from the transition metal (211) scaling line (Figure 8.7a). In this section we show that this deviation originates from the large surface dipole moments of CO<sub>2</sub> on MNC materials.

Figure 8.8b shows the charge density difference of CO<sub>2</sub><sup>\*</sup>. The dipole moment caused by such a charge density distribution is given by,

$$\mu = \int \rho dz$$

where  $\mu$  is the dipole moment and  $\rho$  is the charge density and  $z$  is the axis

of integration. Figure 8.8a shows the computed dipole moment for transition metals and MNC materials. MNC catalysts (red) have substantially larger CO<sub>2</sub> dipole moments as compared to those on transition metals (blue).

We rationalise this difference in dipole moments of CO<sub>2</sub>\* based on differences in its computed *sp* projected density of states. The interactions between an adsorbate and a surface is determined by both the position and shape of the *d* states, and is reflected in the width of the *sp* adsorbate states (shown in Figure 8.8c).

In FeN4 and NiN4 catalysts, the narrow *sp* states of CO<sub>2</sub>\* mean they resemble those of their molecular counterpart, which indicates poor hybridization with the surface. Poor overlap between the *s, p* states close to the Fermi level of CO<sub>2</sub> and the *d* states of the surface means that there is a greater charge polarization between the two poles, i.e. a larger dipole. The same effect is present to a lesser extent on the weakly binding metals, Ag and Au, which, in comparison with the strongly binding ones, have slightly narrower *d* states and correspondingly slightly larger dipole moments. In the strongly binding Pt and Pd catalysts, the broadened states indicate a large interaction, and a lower charge polarization results from the mixing of adsorbate states with those of the surface and a lower resultant surface dipole. Overall, the trends in the width of the *sp* projected density of states of CO<sub>2</sub>\* are consistent with the larger dipole moments of MNC catalysts.

## 8.7 Conclusion and outlook

In this chapter we studied the role of dipole-field interactions in the CO<sub>2</sub>R reaction on transition metal and MNC catalysts. We benchmark our computational setup against available TPD experiments and proposed a Hubbard-U parameter for FeNC systems. We described how the methodology in Chapter 7 is applied to obtain potential dependent reaction energies. Through a combination of pH and potential dependent kinetic modelling and DFT calculations, we propose that the rate limiting step of CO<sub>2</sub>R is CO<sub>2</sub> adsorption for transition metals and

FeNC catalysts and COOH formation for NiNC and supported CoPc catalysts. Our computational rate limiting step predictions are in line with available experiments for Au, FeNC, NiNC and CoPc catalysts. Finally, we suggest that the large surface dipole moments created by CO<sub>2</sub> adsorption on MNC materials are responsible for their increased activity. We rationalise this finding based on the narrow *d*-states of MNC catalysts as compared to the broader *d*-states of transition metals. Our results suggest that materials with similarly narrow *d*-states could also have large dipole moments, such as molecules and clusters, other 2d materials and ionic compounds.

## 8.8 Computational methods

Density functional theory calculations were carried out using the Vienna Ab-Initio Software Package (VASP) [61]. Implicit solvation and counter charge was added to calculations by using VASPsol [112]. Core electrons were described using Projector Augmented Waves (PAW) potentials [62]. Valence electrons were described by plane waves with kinetic energy up to 500 eV. Gaussian smearing with a width of 0.1 eV is used. The RPBE [25] functional was used for GGA-DFT calculations, while the HSE06 [67, 68] functional was used for hybrid calculations. Single-point energies with HSE06 functional on RPBE+U geometries are reported throughout the text. Hubbard-U corrections were added to the *d*-orbitals of iron using the implementation of Dudarev [69].

Single layer 3x3 graphene was used as a model system [57]. Structures were prepared using the Atomic Simulation Environment [63]. The lattice for undoped graphene was optimized using a 12x12x1 Monkhorst-Pack [64] *k*-point mesh. The 3x3 single layer graphene structures were made with the obtained lattice parameter. All structures were then treated with 4x4x1 Monkhorst-Pack [64] *k*-point mesh with at least 16 Å of vacuum. Depending on the vacancy type, carbon atoms in the graphene structure were replaced by nitrogen and iron atoms. The structure obtained after creating vacancies and doping was subjected to an optimization of both position and lattice constants ( VASP [61]

keyword `ISIF = 3` ) before adding an adsorbate to the unit cell. All geometries are optimized until forces are less than  $0.025 \text{ eV}\text{\AA}^{-1}$ . Transition state geometries and energies were obtained by using the Climbing Image Nudged Elastic Band (CI-NEB) [27] implemented within VASP. Forces on the climbing image were considered as converged if they are lower than  $0.05 \text{ eV}\text{\AA}^{-1}$ . The density of states for transition states were obtained by carrying out a single-point with HSE06 at the image associated with the transition state with an  $8 \times 8 \times 1$  k-point mesh and Gaussian smearing of  $0.1 \text{ eV}$ .



## Chapter 9

# Final remarks

In this PhD thesis, we presented a series of theoretical and computational studies on the CO<sub>2</sub>R reaction to CO. The central theme linking all chapters of this thesis is the chemisorption of small molecule adsorbates on different surfaces in various environments.

In Chapter 4 we studied the chemisorption of CO on gold surfaces. We developed a method to determine the chemisorption energy from TPD experiments and compared the result with DFT calculations. In Chapter 5 we developed a general model of chemisorption of small molecules on transition metal surfaces, combining the Newns-Anderson model of hybridisation contributions with an effective term for repulsive orthogonalisation contributions. We applied our model to understand scaling relations between carbon and oxygen adsorbed on late transition metals. In Chapter 6, we studied how the chemisorption of species is affected by the presence of another, competing species. As an example of this effect we studied competition of water and CO for surface sites of stepped and terrace gold surfaces. We found that interfacial water weakens CO binding on steps, while leaving terrace binding strength relatively unchanged.

We then moved on to processes occurring in electrochemistry. In Chapter 7 we developed a method to obtain charge transfer coefficients from DFT calculations, without the need for multiple cell size computations. We applied

this method in Chapter 8 to study CO<sub>2</sub>R to CO on transition metals and single atom, graphene doped catalysts. We found that large dipoles of CO<sub>2</sub> on graphene doped catalysts are stabilised by the presence of an interfacial field near the electrode surface, leading to more active catalysts for the CO<sub>2</sub>R reaction. We presented two simple descriptors to gauge the activity towards CO<sub>2</sub>R to CO, namely  $\Delta G_{\text{CO}_2}$  and  $\Delta G_{\text{COOH}}$  which can be used as a basis to computationally screen for new catalysts.

# Bibliography

- [1] Valérie Masson-Delmotte, Panmao Zhai, Yang Chen, Leah Goldfarb, Melissa I Gomis, J B Robin Matthews, Sophie Berger, Mengtian Huang, Ozge Yelekçi, Rong Yu, Baiquan Zhou, Elisabeth Lonnoy, Thomas K Maycock, Tim Waterfield, Katherine Leitzell, and Nada Caud. *Working Group I Contribution to the Sixth Assessment Report of the Intergovernmental Panel on Climate Change Edited by.* 2021.
- [2] IPCC. Climate Change 2021 Working Group I contribution to the Sixth Assessment Report of the Intergovernmental Panel on Climate Change Summary for Policymakers. Technical report, 2021.
- [3] BP. Consumption by Fuel 1965-2008 - Statistical Review of World Energy Full Report 2009. Technical report, 2009.
- [4] BP. Statistical Review of World Energy - 2020 at a glance. Technical report, 2021.
- [5] Ottmar Edenhofer, Ramón Pichs-Madruga, Youba Sokona Mali, Susanne Kadner, Jan C Minx, Steffen Brunner, Shardul Agrawala, Giovanni UK Baiocchi, Igor Alexeyevich Bashmakov, Gabriel Blanco, and John Broome. TS Technical Summary Coordinating Lead Authors: Lead Authors. Technical report.
- [6] Wikimedia Commons. File:Energy density.svg — Wikimedia Commons, the free media repository, 2021.

- [7] Thomas Haas, Ralf Krause, Rainer Weber, Martin Demler, and Guenter Schmid. Technical photosynthesis involving CO<sub>2</sub> electrolysis and fermentation. *Nat. Catal.*, 1(1):32–39, 2018.
- [8] Yoshio Hori, Akira Murata, and Ryutaro Takahashi. Formation of hydrocarbons in the electrochemical reduction of carbon dioxide at a copper electrode in aqueous solution. Technical Report 8, 1989.
- [9] Stephanie Nitopi, Erlend Bertheussen, Soren B. Scott, Xinyan Liu, Albert K. Engstfeld, Sebastian Horch, Brian Seger, Ifan E.L. Stephens, Karen Chan, Christopher Hahn, Jens K. Nørskov, Thomas F. Jaramillo, and Ib Chorkendorff. Progress and Perspectives of Electrochemical CO<sub>2</sub> Reduction on Copper in Aqueous Electrolyte. *Chem. Rev.*, 119(12):7610–7672, 2019.
- [10] Jens K. Nørskov, Felix Studt, Frank Abild-Pedersen, and Thomas Bligaard. *Fundamental Concepts in Heterogeneous Catalysis*, volume 9781118888. Wiley Blackwell, oct 2014.
- [11] D. M. Newns. Self-consistent model of hydrogen chemisorption. *Phys. Rev.*, 178(3):1123–1135, feb 1969.
- [12] P. W. Anderson. Localized magnetic states in metals. *Phys. Rev.*, 124(1):41–53, oct 1961.
- [13] T. B. Grimley. Overlap effects in the theory of adsorption using Anderson’s Hamiltonian. *J. Phys. C Solid State Phys.*, 3(9):1934–1942, 1970.
- [14] A. H. Larsen, J. Kleis, K. S. Thygesen, J. K. Nørskov, and K. W. Jacobsen. Electronic shell structure and chemisorption on gold nanoparticles. *Phys. Rev. B - Condens. Matter Mater. Phys.*, 84(24):1–13, 2011.
- [15] R A Marcus. Tight-binding approximation for semi-infinite solids. Application of a transform method and of delta function normalization. *J. Chem. Phys.*, 98(7):5604–5611, 1993.

- [16] B. Hammer, Y. Morikawa, and J K Nørskov. CO Chemisorption at Metal Surfaces and Overlayers. *Phys. Rev. Lett.*, 76(12):2141–2144, mar 1996.
- [17] Lars C. Grabow, Britt Hvolbæk, and Jens K. Nørskov. Understanding Trends in Catalytic Activity: The Effect of Adsorbate–Adsorbate Interactions for CO Oxidation Over Transition Metals. *Top. Catal.*, 53(5-6):298–310, may 2010.
- [18] J. K. Nørskov, J. Rossmeisl, A. Logadottir, L. Lindqvist, J. R. Kitchin, T. Bligaard, and H. Jónsson. Origin of the Overpotential for Oxygen Reduction at a Fuel-cell Cathode. *J. Phys. Chem. B*, 108(46):17886–17892, 2004.
- [19] Jan Rossmeisl, Karen Chan, Egill Skúlason, Márten E. Björketun, and Vladimir Tripkovic. On the pH dependence of electrochemical proton transfer barriers. *Catal. Today*, 262:36–40, 2016.
- [20] J. J. Mortensen, B. Hammer, and J. K. Nørskov. Alkali promotion of N<sub>2</sub> dissociation over Ru(0001). *Phys. Rev. Lett.*, 80(19):4333–4336, may 1998.
- [21] M. Born and R. Oppenheimer. Zur Quantentheorie der Molekeln. *Ann. Phys.*, 389(20):457–484, 1927.
- [22] P. Hohenberg and W. Kohn. Inhomogeneous electron gas. *Phys. Rev.*, 136(8):809–811, nov 1964.
- [23] W. Kohn and L. J. Sham. Self-consistent equations including exchange and correlation effects. *Phys. Rev.*, 140(4A):A1133, nov 1965.
- [24] John P Perdew, Kieron Burke, and Matthias Ernzerhof. Generalized gradient approximation made simple. *Phys. Rev. Lett.*, 77(18):3865–3868, 1996.
- [25] B. Hammer, L. B. Hansen, and J. K. Nørskov. Improved Adsorption Energetics Within Density-functional Theory Using Revised Perdew-Burke-Ernzerhof Functionals. *Phys. Rev. B - Condens. Matter Mater. Phys.*, 59(11):7413–7421, mar 1999.

- [26] R. P. Feynman. Forces in Molecules. *Phys. Rev.*, 56(4):340–343, aug 1939.
- [27] Graeme Henkelman, Blas P. Uberuaga, and Hannes Jónsson. Climbing Image Nudged Elastic Band Method for Finding Saddle Points and Minimum Energy Paths. *J. Chem. Phys.*, 113(22):9901–9904, dec 2000.
- [28] Shuichi Nosé. A unified formulation of the constant temperature molecular dynamics methods. *J. Chem. Phys.*, 81(1):511–519, 1984.
- [29] Sudarshan Vijay, Henrik H. Kristoffersen, Yu Katayama, Yang Shao-Horn, Ib Chorkendorff, Brian Seger, and Karen Chan. How to extract adsorption energies, adsorbate-adsorbate interaction parameters and saturation coverages from temperature programmed desorption experiments. *Phys. Chem. Chem. Phys.*, 23(42):24396–24402, nov 2021.
- [30] Sudarshan Vijay, Thomas V. Hogg, Johan Ehlers, Henrik H. Kristoffersen, Yu Katayama, Yang Shao Horn, Ib Chorkendorff, Karen Chan, and Brian Seger. Interaction of CO with Gold in an Electrochemical Environment. *J. Phys. Chem. C*, 125(32):17684–17689, aug 2021.
- [31] L Schimka, J Harl, A Stroppa, A Grüneis, M Marsman, F Mittendorfer, and G Kresse. Accurate surface and adsorption energies from many-body perturbation theory. *Nat. Mater.*, 9(9):741–744, 2010.
- [32] Peter J Feibelman, B. Hammer, J K Nørskov, F. Wagner, M. Scheffler, R. Stumpf, R. Watwe, and J Dumesic. The CO/Pt(111) Puzzle. *J. Phys. Chem. B*, 105(18):4018–4025, may 2001.
- [33] J. K. Nørskov, T. Bligaard, J. Rossmeisl, and C. H. Christensen. Towards the computational design of solid catalysts, apr 2009.
- [34] Andrew J. Medford, Aleksandra Vojvodic, Jens S. Hummelshøj, Johannes Voss, Frank Abild-Pedersen, Felix Studt, Thomas Bligaard, Anders Nilsson, and Jens K. Nørskov. From the Sabatier principle to a predictive theory of transition-metal heterogeneous catalysis. *J. Catal.*, 328:36–42, jul 2015.

- [35] Jess Wellendorff, Trent L. Silbaugh, Delfina Garcia-Pintos, Jens K. Nørskov, Thomas Bligaard, Felix Studt, and Charles T. Campbell. A benchmark database for adsorption bond energies to transition metal surfaces and comparison to selected DFT functionals. *Surf. Sci.*, 640:36–44, 2015.
- [36] Stefano Mezzavilla, Sebastian Horch, Ifan E. L. Stephens, Brian Seger, and Ib Chorkendorff. Structure Sensitivity in the Electrocatalytic Reduction of CO<sub>2</sub> with Gold Catalysts. *Angew. Chemie*, 131(12):3814–3818, 2019.
- [37] Stefan Ringe, Carlos G Morales-Guio, Leanne D Chen, Meredith Fields, Thomas F Jaramillo, Christopher Hahn, and Karen Chan. Double Layer Charging Driven Carbon dioxide Adsorption Limits the Rate of Electrochemical Carbon dioxide Reduction on Gold. *Nat. Commun.*, 11(1), 2020.
- [38] Manuel J. Kolb, Federico Calle-Vallejo, Ludo B.F. Juurlink, and Marc T.M. Koper. Density functional theory study of adsorption of H<sub>2</sub>O, H, O, and OH on stepped platinum surfaces. *J. Chem. Phys.*, 140(13), 2014.
- [39] M. E. Van Reijzen, M. A. Van Spronsen, J. C. Docter, and L. B.F. Juurlink. CO and H<sub>2</sub>O adsorption and reaction on Au(310). *Surf. Sci.*, 605(17-18):1726–1731, sep 2011.
- [40] Matthijs A Van Spronsen, Kees Jan Weststrate, Angela Den Dunnen, Maarten E Van Reijzen, Christine Hahn, and Ludo B.F. Juurlink. Hydrophilic Interaction between Low-Coordinated Au and Water: H<sub>2</sub>O/Au(310) Studied with TPD and XPS. *J. Phys. Chem. C*, 120(16):8693–8703, 2016.
- [41] Cansin Badan, Marc T.M. Koper, and L. B.F. Juurlink. How well does Pt(211) represent Pt[n (111) × (100)] surfaces in adsorption/desorption? *J. Phys. Chem. C*, 119(24):13551–13560, 2015.

- [42] Jooho Kim, Enrique Samano, and Bruce E Koel. CO Adsorption and Reaction on Clean and Oxygen-Covered Au(211) Surfaces. *J. Phys. Chem. B*, 110(35):17512–17517, sep 2006.
- [43] Charles T Campbell and Jason R.V. Sellers. Enthalpies and entropies of adsorption on well-defined oxide surfaces: Experimental measurements, 2013.
- [44] A. M. de Jong and J W Niemantsverdriet. Thermal Desorption Analysis: Comparative Test of Ten Commonly Applied Procedures. *Surf. Sci.*, 233(3):355–365, 1990.
- [45] Steven L Tait, Zdenek Dohnálek, Charles T Campbell, and Bruce D Kay. n-alkanes on MgO(100). II. Chain length dependence of kinetic desorption parameters for small n-alkanes. *J. Chem. Phys.*, 122(16):164708, apr 2005.
- [46] Spencer D Miller, Vladimir V Pushkarev, Andrew J Gellman, and John R Kitchin. Simulating Temperature Programmed Desorption of Oxygen on Pt(111) Using DFT Derived Coverage Dependent Desorption Barriers. *Top. Catal.*, 57(1-4):106–117, 2014.
- [47] Charles T Campbell and Jason R.V. Sellers. Enthalpies and entropies of adsorption on well-defined oxide surfaces: Experimental measurements, 2013.
- [48] I. Chorkendorff and S. Tougaard. Background subtraction in electron spectroscopy by use of reflection electron energy loss spectra. *Appl. Surf. Sci.*, 29(1):101–112, 1987.
- [49] Pauli Virtanen, Ralf Gommers, Travis E. Oliphant, Matt Haberland, Tyler Reddy, David Cournapeau, Evgeni Burovski, Pearu Peterson, Warren Weckesser, Jonathan Bright, Stéfan J. van der Walt, Matthew Brett, Joshua Wilson, K. Jarrod Millman, Nikolay Mayorov, Andrew R.J. Nelson, Eric Jones, Robert Kern, Eric Larson, C. J. Carey, İlhan Polat,



- Yu Feng, Eric W. Moore, Jake VanderPlas, Denis Laxalde, Josef Perktold, Robert Cimrman, Ian Henriksen, E. A. Quintero, Charles R. Harris, Anne M. Archibald, Antônio H. Ribeiro, Fabian Pedregosa, Paul van Mulbregt, Aditya Vijaykumar, Alessandro Pietro Bardelli, Alex Rothberg, Andreas Hilboll, Andreas Kloeckner, Anthony Scopatz, Antony Lee, Ariel Rokem, C. Nathan Woods, Chad Fulton, Charles Masson, Christian Häggström, Clark Fitzgerald, David A. Nicholson, David R. Hagen, Dmitrii V. Pasechnik, Emanuele Olivetti, Eric Martin, Eric Wieser, Fabrice Silva, Felix Lenders, Florian Wilhelm, G. Young, Gavin A. Price, Gert Ludwig Ingold, Gregory E. Allen, Gregory R. Lee, Hervé Audren, Irvin Probst, Jörg P. Dietrich, Jacob Silterra, James T. Webber, Janko Slavič, Joel Nothman, Johannes Buchner, Johannes Kulick, Johannes L. Schönberger, José Vinícius de Miranda Cardoso, Joscha Reimer, Joseph Harrington, Juan Luis Cano Rodríguez, Juan Nunez-Iglesias, Justin Kuczynski, Kevin Tritz, Martin Thoma, Matthew Newville, Matthias Kümmerer, Maximilian Bolingbroke, Michael Tartre, Mikhail Pak, Nathaniel J. Smith, Nikolai Nowaczyk, Nikolay Shebanov, Oleksandr Pavlyk, Per A. Brodtkorb, Perry Lee, Robert T. McGibbon, Roman Feldbauer, Sam Lewis, Sam Tygier, Scott Sievert, Sebastiano Vigna, Stefan Peterson, Surhud More, Tadeusz Pudlik, Takuya Oshima, Thomas J. Pingel, Thomas P. Robitaille, Thomas Spura, Thouis R. Jones, Tim Cera, Tim Leslie, Tiziano Zito, Tom Krauss, Utkarsh Upadhyay, Yaroslav O. Halchenko, and Yoshiki Vázquez-Baeza. SciPy 1.0: fundamental algorithms for scientific computing in Python. *Nat. Methods*, 17(3):261–272, 2020.
- [50] Stéfan Van Der Walt, S. Chris Colbert, and Gaël Varoquaux. The NumPy array: A structure for efficient numerical computation. *Comput. Sci. Eng.*, 13(2):22–30, mar 2011.
- [51] Paramaconi Rodriguez and Marc T.M. Koper. Electrocatalysis on gold, 2014.
- [52] G Kresse, A Gil, and P Sautet. Significance of single-electron energies for

- the description of CO on Pt(111). *Phys. Rev. B - Condens. Matter Mater. Phys.*, 68(7), 2003.
- [53] Jess Wellendorff, Keld T Lundgaard, Andreas Møgelhøj, Vivien Petzold, David D Landis, Jens K Nørskov, Thomas Bligaard, and Karsten W Jacobsen. Density functionals for surface science: Exchange-correlation model development with Bayesian error estimation. *Phys. Rev. B - Condens. Matter Mater. Phys.*, 85(23):235149, 2012.
- [54] Stefan Grimme. Semiempirical GGA-type Density Functional Constructed with a Long-range Dispersion Correction. *J. Comput. Chem.*, 27(15):1787–1799, nov 2006.
- [55] Fang Luo, Chang Hyuck Choi, Mathias J.M. Primbs, Wen Ju, Shuang Li, Nathaniel D. Leonard, Arne Thomas, Frédéric Jaouen, and Peter Strasser. Accurate Evaluation of Active-Site Density (SD) and Turnover Frequency (TOF) of PGM-Free Metal-Nitrogen-Doped Carbon (MNC) Electrocatalysts using CO Cryo Adsorption. *ACS Catal.*, 9(6):4841–4852, jun 2019.
- [56] Sudarshan Vijay, Joseph A Gauthier, Hendrik H. Heenen, Vanessa Jane Bukas, Henrik H. Kristoffersen, and Karen Chan. Dipole-field interactions determine the CO<sub>2</sub> reduction activity of 2D Fe-N-C single atom catalysts. *ACS Catal.*, 57:13, 2020.
- [57] Vladimir Tripkovic, Marco Vanin, Mohammedreza Karamad, Mårten E. Björketun, Karsten W. Jacobsen, Kristian S. Thygesen, and Jan Rossmeisl. Electrochemical CO<sub>2</sub> and CO Reduction on Metal-functionalized Porphyrin-like Graphene. *J. Phys. Chem. C*, 117(18):9187–9195, 2013.
- [58] Alexander Bagger, Wen Ju, Ana Sofia Varela, Peter Strasser, and Jan Rossmeisl. Single Site Porphyrine-like Structures Advantages over Metals for Selective Electrochemical CO<sub>2</sub> Reduction. *Catal. Today*, 288:74–78, 2017.

- [59] Wen Ju, Alexander Bagger, Xingli Wang, Yulin Tsai, Fang Luo, Tim Möller, Huan Wang, Jan Rossmeisl, Ana Sofia Varela, and Peter Strasser. Unraveling Mechanistic Reaction Pathways of the Electrochemical CO<sub>2</sub> Reduction on Fe-N-C Single-Site Catalysts. *ACS Energy Lett.*, 4(7):1663–1671, 2019.
- [60] Jun Gu, Chia Shuo Hsu, Lichen Bai, Hao Ming Chen, and Xile Hu. Atomically Dispersed Fe<sup>3+</sup> Sites Catalyze Efficient CO<sub>2</sub> Electroreduction to CO. *Science (80-. )*, 364(6445):1091–1094, 2019.
- [61] G Kresse and J. Furthmüller. Efficient Iterative Schemes for ab initio Total-energy Calculations using a Plane-wave Basis Set. *Phys. Rev. B - Condens. Matter Mater. Phys.*, 54(16):11169–11186, 1996.
- [62] D Joubert. From ultrasoft pseudopotentials to the projector augmented-wave method. *Phys. Rev. B - Condens. Matter Mater. Phys.*, 59(3):1758–1775, 1999.
- [63] Ask Hjorth Larsen, Jens Jørgen Mortensen, Jakob Blomqvist, Ivano E. Castelli, Rune Christensen, Marcin Dułak, Jesper Friis, Michael N. Groves, Bjørk Hammer, Cory Hargus, Eric D. Hermes, Paul C. Jennings, Peter Bjerre Jensen, James Kermode, John R. Kitchin, Esben Leonhard Kolsbjerg, Joseph Kubal, Kristen Kaasbjerg, Steen Lysgaard, Jón Bergmann Maronsson, Tristan Maxson, Thomas Olsen, Lars Pastewka, Andrew Peterson, Carsten Rostgaard, Jakob Schiøtz, Ole Schütt, Mikkel Strange, Kristian S. Thygesen, Tejs Vegge, Lasse Vilhelmsen, Michael Walter, Zhenhua Zeng, and Karsten W. Jacobsen. The atomic simulation environment - A Python library for working with atoms. *J. Phys. Condens. Matter*, 29(27):273002, jul 2017.
- [64] Hendrik J Monkhorst and James D Pack. Special points for Brillouin-zone integrations. *Phys. Rev. B*, 13(12):5188–5192, jun 1976.
- [65] Sebastiaan P. Huber, Spyros Zoupanos, Martin Uhrin, Leopold Talirz,

- Leonid Kahle, Rico Häuselmann, Dominik Gresch, Tiziano Müller, Aliaksandr V. Yakutovich, Casper W. Andersen, Francisco F. Ramirez, Carl S. Adorf, Fernando Gargiulo, Snehal Kumbhar, Elsa Passaro, Conrad Johnston, Andrius Merkys, Andrea Cepellotti, Nicolas Mounet, Nicola Marzari, Boris Kozinsky, and Giovanni Pizzi. AiiDA 1.0, a scalable computational infrastructure for automated reproducible workflows and data provenance. *Sci. Data*, 7(1), dec 2020.
- [66] Shyue Ping Ong, William Davidson Richards, Anubhav Jain, Geoffrey Hautier, Michael Kocher, Shreyas Cholia, Dan Gunter, Vincent L. Chevrier, Kristin A. Persson, and Gerbrand Ceder. Python Materials Genomics (pymatgen): A robust, open-source python library for materials analysis. *Comput. Mater. Sci.*, 68:314–319, feb 2013.
- [67] Jochen Heyd, Gustavo E Scuseria, and Matthias Ernzerhof. Hybrid functionals based on a Screened Coulomb Potential. *J. Chem. Phys.*, 118(18):8207–8215, 2003.
- [68] Jochen Heyd, Gustavo E Scuseria, and Matthias Ernzerhof. Erratum: Hybrid functionals based on a screened Coulomb potential. *J. Chem. Phys.*, 124(21):9901, 2006.
- [69] S. Dudarev and G. Botton. Electron-energy-loss Spectra and the Structural Stability of Nickel Oxide: An LSDA+U study. *Phys. Rev. B - Condens. Matter Mater. Phys.*, 57(3):1505–1509, 1998.
- [70] A. Vojvodic, J. K. Nørskov, and F. Abild-Pedersen. Electronic structure effects in transition metal surface chemistry. *Top. Catal.*, 57(1-4):25–32, 2014.
- [71] Zhi Wei Seh, Jakob Kibsgaard, Colin F. Dickens, Ib Chorkendorff, Jens K. Nørskov, and Thomas F. Jaramillo. Combining Theory and Experiment in Electrocatalysis: Insights into Materials Design. *Science (80-. )*, 355(6321), 2017.

- [72] Andrew J. Medford, Jess Wellendorff, Aleksandra Vojvodic, Felix Studt, Frank Abild-Pedersen, Karsten W. Jacobsen, Thomas Bligaard, and Jens K. Nørskov. Assessing the reliability of calculated catalytic ammonia synthesis rates. *Science (80-. )*, 345(6193):197–200, jul 2014.
- [73] Andrew J. Medford, Chuan Shi, Max J. Hoffmann, Adam C. Lausche, Sean R. Fitzgibbon, Thomas Bligaard, and Jens K. Nørskov. CatMAP: A Software Package for Descriptor-Based Microkinetic Mapping of Catalytic Trends. *Catal. Letters*, 145(3):794–807, mar 2015.
- [74] F Abild-Pedersen, J Greeley, F Studt, J Rossmeisl, T R Munter, P G Moses, E Skúlason, T Bligaard, and J K Nørskov. Scaling properties of adsorption energies for hydrogen-containing molecules on transition-metal surfaces. *Phys. Rev. Lett.*, 99(1), 2007.
- [75] Heine A Hansen, Joel B Varley, Andrew A Peterson, and Jens K Nørskov. Understanding trends in the electrocatalytic activity of metals and enzymes for CO<sub>2</sub> reduction to CO. *J. Phys. Chem. Lett.*, 4(3):388–392, 2013.
- [76] Heine A Hansen, Venkatasubramanian Viswanathan, and Jens K. Nørskov. Unifying kinetic and thermodynamic analysis of 2 e<sup>-</sup> and 4 e<sup>-</sup> reduction of oxygen on metal surfaces. *J. Phys. Chem. C*, 118(13):6706–6718, 2014.
- [77] J Hammer, B. Norskov. Theory of adsorption and surface reactions. *J. Phys. A Math. Theor.*, 1997.
- [78] Anders Nilsson and Lars G M Pettersson. Adsorbate Electronic Structure and Bonding on Metal Surfaces BT - Chemical Bonding at Surfaces and Interfaces. Technical report, 2008.
- [79] Paolo Giannozzi, Stefano Baroni, Nicola Bonini, Matteo Calandra, Roberto Car, Carlo Cavazzoni, Davide Ceresoli, Guido L. Chiarotti, Matteo Cococcioni, Ismaila Dabo, Andrea Dal Corso, Stefano De Gironcoli,

- Stefano Fabris, Guido Fratesi, Ralph Gebauer, Uwe Gerstmann, Christos Gougoussis, Anton Kokalj, Michele Lazzeri, Layla Martin-Samos, Nicola Marzari, Francesco Mauri, Riccardo Mazzarello, Stefano Paolini, Alfredo Pasquarello, Lorenzo Paulatto, Carlo Sbraccia, Sandro Scandolo, Gabriele Sclauzero, Ari P. Seitsonen, Alexander Smogunov, Paolo Umari, and Renata M. Wentzcovitch. QUANTUM ESPRESSO: A modular and open-source software project for quantum simulations of materials. *J. Phys. Condens. Matter*, 21(39):395502, 2009.
- [80] Gianluca Prandini, Antimo Marrazzo, Ivano E. Castelli, Nicolas Mounet, and Nicola Marzari. Precision and efficiency in solid-state pseudopotential calculations. *npj Comput. Mater.*, 4(1), dec 2018.
- [81] Jan Rossmeisl, Egill Skúlason, Márten E. Björketun, Vladimir Tripkovic, and Jens K. Nørskov. Modeling the electrified solid-liquid interface. *Chem. Phys. Lett.*, 466(1-3):68–71, 2008.
- [82] J. K. Nørskov, T. Bligaard, A. Logadottir, J. R. Kitchin, J. G. Chen, S. Pandelov, and U. Stimming. Trends in the Exchange Current for Hydrogen Evolution. *J. Electrochem. Soc.*, 152(3):J23, 2005.
- [83] Heine A. Hansen, Jan Rossmeisl, and Jens K. Nørskov. Surface Pourbaix diagrams and oxygen reduction activity of Pt, Ag and Ni(111) surfaces studied by DFT. *Phys. Chem. Chem. Phys.*, 10(25):3722–3730, 2008.
- [84] Henrik H. Kristoffersen and Jin Hyun Chang. Effect of Competitive Adsorption at the Interface between Aqueous Electrolyte and Solid Electrode. *ACS Symp. Ser.*, 1331:225–238, 2019.
- [85] Henrik H. Kristoffersen and Karen Chan. Towards constant potential modeling of CO-CO coupling at liquid water-Cu(1 0 0) interfaces. *J. Catal.*, 396:251–260, apr 2021.
- [86] Anna Wuttig, Jaeyune Ryu, and Yogesh Surendranath. Electrolyte Com-

- petition Controls Surface Binding of CO Intermediates to CO<sub>2</sub> Reduction Catalysts. (2):1–12, 2019.
- [87] Jacob R Boes, Osman Mamun, Kirsten Winther, and Thomas Bligaard. Graph Theory Approach to High-Throughput Surface Adsorption Structure Generation. *J. Phys. Chem. A*, 123(11):2281–2285, 2019.
- [88] Egill Skúlason, Gustav S. Karlberg, Jan Rossmeisl, Thomas Bligaard, Jeff Greeley, Hannes Jónsson, and Jens K. Nørskov. Density functional theory calculations for the hydrogen evolution reaction in an electrochemical double layer on the Pt(111) electrode. *Phys. Chem. Chem. Phys.*, 9(25):3241–3250, 2007.
- [89] Egill Skúlason, Vladimir Tripkovic, Mårten E. Björketun, Sigríður Guðmundsdóttir, Gustav Karlberg, Jan Rossmeisl, Thomas Bligaard, Hannes Jónsson, and Jens K. Nørskov. Modeling the electrochemical hydrogen oxidation and evolution reactions on the basis of density functional theory calculations. *J. Phys. Chem. C*, 114(42):18182–18197, 2010.
- [90] Karen Chan and Jens K Nørskov. Electrochemical barriers made simple. *J. Phys. Chem. Lett.*, 6(14):2663–2668, 2015.
- [91] Karen Chan and Jens K. Nørskov. Potential Dependence of Electrochemical Barriers from ab Initio Calculations. *J. Phys. Chem. Lett.*, 7(9):1686–1690, 2016.
- [92] Andrew A. Peterson, Frank Abild-Pedersen, Felix Studt, Jan Rossmeisl, and Jens K. Nørskov. How copper catalyzes the electroreduction of carbon dioxide into hydrocarbon fuels. *Energy Environ. Sci.*, 3(9):1311–1315, 2010.
- [93] Joseph Gauthier, Colin Dickens, Hendrik Heenen, Stefan Ringe, and Karen Chan. Unified Approach to Implicit and Explicit Solvent Simulations of Electrochemical Reaction Energetics. *Chemrxiv*, pages 1–41, 2019.

- [94] Georg Kastlunger, Per Lindgren, and Andrew A Peterson. Controlled-Potential Simulation of Elementary Electrochemical Reactions: Proton Discharge on Metal Surfaces. *J. Phys. Chem. C*, 122(24):12771–12781, jun 2018.
- [95] Francesco Nattino, Matthew Truscott, Nicola Marzari, and Oliviero Andreussi. Continuum models of the electrochemical diffuse layer in electronic-structure calculations. *J. Chem. Phys.*, 150(4):1–41, 2019.
- [96] Tamio Ikeshoji, Minoru Otani, Ikutaro Hamada, Osamu Sugino, Yoshitada Morikawa, Yasuharu Okamoto, Yumin Qian, and Ichizo Yagi. The charged interface between Pt and water: First principles molecular dynamics simulations. *AIP Adv.*, 2(3), 2012.
- [97] Sneha A. Akhade, Nicole J. Bernstein, Monica R. Esopi, Michael J. Regula, and Michael J. Janik. A simple method to approximate electrode potential-dependent activation energies using density functional theory. *Catal. Today*, 288:63–73, jun 2017.
- [98] M. Mamatkulov and J.-S. Filhol. An abinitio study of electrochemical vs. electromechanical properties: the case of CO adsorbed on a Pt(111) surface. *Phys. Chem. Chem. Phys.*, 13(17):7675, 2011.
- [99] Anjali M Patel, Sudarshan Vijay, Georg Kastlunger, Jens Kehlet Nørskov, and Karen Chan. Generalizable Trends in Electrochemical Protonation Barriers. *J. Phys. Chem. Lett.*, 12:5193–5200, 2021.
- [100] Zachary K. Goldsmith, Marcos F. Calegari Andrade, and Annabella Selloni. Effects of applied voltage on water at a gold electrode interface from ab initio molecular dynamics. *Chem. Sci.*, 12(16):5865–5873, apr 2021.
- [101] Jia Bo Le, Qi Yuan Fan, Jie Qiong Li, and Jun Cheng. Molecular origin of negative component of Helmholtz capacitance at electrified Pt(111)/water interface. *Sci. Adv.*, 6(41), 2020.



- [102] Joseph A. Gauthier, Alan C. Luntz, Jens K. Nørskov, Emily A. Carter, Leanne D. Chen, Karen Chan, J. Mark P. Martinez, Caroline M. Krauter, and Michal Bajdich. Understanding the apparent fractional charge of protons in the aqueous electrochemical double layer. *Nat. Commun.*, 9(1):1–8, 2018.
- [103] Dirk Porezag and Mark R Pederson. Infrared intensities and Raman-scattering activities within density-functional theory. *Phys. Rev. B - Condens. Matter Mater. Phys.*, 54(11):7830–7836, 1996.
- [104] José A. Garrido Torres, Paul C Jennings, Martin H Hansen, Jacob R Boes, and Thomas Bligaard. Low-Scaling Algorithm for Nudged Elastic Band Calculations Using a Surrogate Machine Learning Model. *Phys. Rev. Lett.*, 122(15), 2019.
- [105] J. Enkovaara, C. Rostgaard, J. J. Mortensen, J. Chen, M. Dulak, L. Ferrighi, J. Gavnholt, C. Glinsvad, V. Haikola, H. A. Hansen, H. H. Kristofersen, M. Kuisma, A. H. Larsen, L. Lehtovaara, M. Ljungberg, O. Lopez-Acevedo, P. G. Moses, J. Ojanen, T. Olsen, V. Petzold, N. A. Romero, J. Stausholm-Møller, M. Strange, G. A. Tritsaridis, M. Vanin, M. Walter, B. Hammer, H. Häkkinen, G. K.H. Madsen, R. M. Nieminen, J. K. Nørskov, M. Puska, T. T. Rantala, J. Schiøtz, K. S. Thygesen, and K. W. Jacobsen. Electronic structure calculations with GPAW: A real-space implementation of the projector augmented-wave method, jun 2010.
- [106] Sudarshan Vijay, Wen Ju, Sven Brückner, Sze Chun Tsang, Peter Strasser, and Karen Chan. Unified mechanistic understanding of CO<sub>2</sub> reduction to CO on transition metal and single atom catalysts. *Nat. Catal.*, 4(12):1024–1031, dec 2021.
- [107] Yihong Chen, Christina W. Li, and Matthew W. Kanan. Aqueous CO<sub>2</sub> Reduction at very Low Overpotential on Oxide-derived Au Nanoparticles. *J. Am. Chem. Soc.*, 134(49):19969–19972, 2012.

- [108] Steven M. Brown, Michael J. Orella, Yung Wei Hsiao, Yuriy Roman-Leshkov, Yogesh Surendranath, Martin Z. Bazant, and Fikile Brushett. Electron Transfer Limitation in Carbon Dioxide Reduction Revealed by Data-Driven Tafel Analysis. *ChemRxiv*, 2020.
- [109] Joseph A. Gauthier, Meredith Fields, Michal Bajdich, Leanne D. Chen, Robert B. Sandberg, Karen Chan, and Jens K. Nørskov. Facile Electron Transfer to CO<sub>2</sub> during Adsorption at the Metal|Solution Interface. *J. Phys. Chem. C*, 123(48):29278–29283, 2019.
- [110] Ana Sofia Varela, Matthias Kroschel, Nathaniel D. Leonard, Wen Ju, Julian Steinberg, Alexander Bagger, Jan Rossmeisl, and Peter Strasser. PH Effects on the Selectivity of the Electrocatalytic CO<sub>2</sub> Reduction on Graphene-Embedded Fe-N-C Motifs: Bridging Concepts between Molecular Homogeneous and Solid-State Heterogeneous Catalysis. *ACS Energy Lett.*, 3(4):812–817, 2018.
- [111] Stefan Ringe, Ezra L Clark, Joaquin Resasco, Amber Walton, Brian Seger, Alexis T Bell, and Karen Chan. Understanding Cation Effects in Electrochemical CO<sub>2</sub> Reduction. *Energy Environ. Sci.*, 12:3001, 2019.
- [112] Kiran Mathew, V. S. Chaitanya Kolluru, Srinidhi Mula, Stephan N. Steinmann, and Richard G Hennig. Implicit Self-consistent Electrolyte Model in Plane-wave Density-functional Theory. *J. Chem. Phys.*, 151(23), 2019.

# Chapter 10

## Included publications

### 10.1 Paper 1

**How to extract adsorption energies, adsorbate-adsorbate interaction parameters, and saturation coverages from temperature programmed desorption experiments**

Sudarshan Vijay, Henrik H. Kristoffersen, Yu Katayama, Yang Shao-Horn, Ib Chorkendorff, Brian Seger and Karen Chan

Reproduced from Phys. Chem. Chem. Phys., **2021**, 23, 24396-24402 with permission from the Royal Society of Chemistry.



# How to extract adsorption energies, adsorbate–adsorbate interaction parameters and saturation coverages from temperature programmed desorption experiments†

Cite this: *Phys. Chem. Chem. Phys.*, 2021, 23, 24396

Sudarshan Vijay, <sup>a</sup> Henrik H. Kristoffersen, <sup>a</sup> Yu Katayama, <sup>bc</sup> Yang Shao-Horn, <sup>bde</sup> Ib Chorkendorff, <sup>f</sup> Brian Seger <sup>f</sup> and Karen Chan \*<sup>a</sup>

We present a scheme to extract the adsorption energy, adsorbate interaction parameter and the saturation coverage from temperature programmed desorption (TPD) experiments. We propose that the coverage dependent adsorption energy can be fit using a functional form including the configurational entropy and linear adsorbate–adsorbate interaction terms. As one example of this scheme, we analyze TPD of CO desorption on Au(211) and Au(310) surfaces. We determine that under atmospheric CO pressure, the steps of both facets adsorb between 0.4–0.9 ML coverage of CO\*. We compare this result against energies obtained from five density functionals, RPBE, PBE, PBE-D3, RPBE-D3 and BEEF-vdW. We find that the energies and equilibrium coverages from RPBE-D3 and PBE are closest to the values determined from the TPD.

Received 5th May 2021,  
 Accepted 27th September 2021

DOI: 10.1039/d1cp01992a

[rsc.li/pccp](http://rsc.li/pccp)

In the past two decades, heterogeneous catalysis has seen tremendous growth in the use of density functional theory (DFT) for mechanistic analysis and computational catalyst discovery.<sup>1</sup> These efforts require accurate descriptions of adsorption energies of key reaction intermediates. DFT functionals have been benchmarked against experiments and, in general, DFT-predicted adsorption energies with workhorse GGA-level functionals are accurate to 0.2 eV.<sup>2</sup> However, benchmark datasets do not typically include noble metals such as gold, which are good catalysts for a variety of thermal and electrochemical catalytic reactions.<sup>3</sup>

Benchmark DFT datasets are generally determined from three experimental techniques: single-crystal adsorption calorimetry (SCAC), equilibrium adsorption isotherms (EAI) and temperature programmed desorption (TPD) experiments.<sup>2–6</sup>

SCAC measurements have been shown to be reliable, precise and are an unambiguous way of determining adsorption energies.<sup>7</sup> EAI requires reversible adsorption–desorption but experiments can be fit in a comparatively straightforward manner by using the Clausius–Clapeyron expression.<sup>6</sup> In comparison, TPD provides more features, but requires fitting techniques and interpretation of the underlying kinetics to extract adsorption energies. While TPD requires more analysis than the other two methods, its use is widespread and certain systems relevant to heterogeneous catalysis are characterized only by this methodology.<sup>8,9</sup> Thus, simple and precise methods to obtain quantities from TPD to benchmark against computations are valuable.

The central fitting equation for first order desorption TPD is an Arrhenius type relationship,  $\text{rate} = \nu(T)\exp\left(-\frac{G_d}{k_B T}\right)\theta$ , which relates the rate to an empirical pre-factor,  $\nu(T)$ , the desorption energy,  $G_d$  and the coverage  $\theta$ . The most commonly used, and simplest method, applies the Redhead equation<sup>10</sup> in its linearized form,  $G_d = k_B T_p \ln\left(\frac{\nu T_p}{\beta} - 3.64\right)$ , to relate peak(s) in the TPD,  $T_p$ , to the adsorption energies on various sites for a given rate of heating,  $\beta$ . The Redhead equation is derived with the assumption that  $G_d$  is independent of coverage and assumes a constant, temperature-independent  $\nu$ . Alternative techniques, such as Complete Analysis, fit a line to  $\ln(\text{rate})$  vs.  $1/T$ . However, the obtained energies from the analysis have no coverage dependence.<sup>11</sup> A more detailed method was provided

<sup>a</sup> *CatTheory*, Department of Physics, Technical University of Denmark, 2800 Kgs. Lyngby, Denmark. E-mail: [kchan@fysik.dtu.dk](mailto:kchan@fysik.dtu.dk)

<sup>b</sup> *Research Laboratory of Electronics*, Massachusetts Institute of Technology, Cambridge, MA 02139, USA

<sup>c</sup> *Department of Applied Chemistry*, Graduate School of Sciences and Technology for Innovation, Yamaguchi University, Tokiwadai, Ube, 755-8611, Japan

<sup>d</sup> *Department of Mechanical Engineering*, Massachusetts Institute of Technology, Cambridge, MA 02139, USA

<sup>e</sup> *Department of Materials Science and Engineering*, Massachusetts Institute of Technology, Cambridge, MA 02139, USA

<sup>f</sup> *SurfCat*, Department of Physics, Technical University of Denmark, 2800 Kgs. Lyngby, Denmark

† Electronic supplementary information (ESI) available. See DOI: 10.1039/d1cp01992a

by ref. 12, where a temperature-independent  $\nu$  and a function  $G_d(\theta)$  is fitted to all points from a series of TPD plots. Another approach is to generate TPD curves by the kinetic Monte Carlo methodology, which simulates the TPD experiment based on an idealized rate expression.<sup>13–15</sup> This rate expression can include adsorption energies, adsorbate–adsorbate interaction parameters, diffusion of adsorbates on the surface, amongst others. If the parameters used in the rate expression are obtained from DFT, the simulated TPD curves can be benchmarked against experimental TPD. Other models might assume a variable reaction order to fit adsorption isotherms (such as the Temkin isotherm), however that might lead to misinterpretation of the underlying kinetics.

In this work, we present a method to extract not just adsorption energies, but also adsorbate–adsorbate interaction parameters and adsorbate saturation coverages directly from fits to TPD. In contrast to other methods, in this approach we explicitly account for a temperature dependent pre-factor and a coverage dependent desorption energy term. The coverage dependence in the adsorption free energy of binding arises from both configurational entropy and linear adsorbate–adsorbate interactions. These effects are relevant at low and high coverages, respectively, and accounting for them allows us to fit the entire TPD peak, even in cases where it overlaps with other peaks. We benchmark the resultant adsorbate–adsorbate interaction parameters against computations. We illustrate the use of this method for reported TPD data for CO adsorbed on Au(211) and Au(310) stepped single crystal facets. We find an adsorption energy of 0.45 eV for on stepped sites at zero coverage, which differs from that of a Redhead analysis by approximately 0.1 eV,

which is the accuracy that is expected from density functionals commonly used to study CO adsorption.<sup>16,17</sup> Furthermore, we determine that the equilibrium coverage is between 0.4 to 0.9 ML of CO on step sites. We compare the adsorption energies and equilibrium coverages against five density functionals and find that RPBE-D3 and PBE are the closest to the TPD value, PBE-D3 overestimates the binding strength, while BEEF-vdW and RPBE underestimate it.

## CO on Au

To illustrate the application of our fitting method, we investigate CO adsorption on Au(211) and Au(310) steps. In this system the adsorbate–adsorbate interactions and configurational entropy are particularly important because large CO coverages may be present at the low temperature range of the TPD, while a very small coverage is expected at the high temperature range. Furthermore, CO binding on metals is a known challenge for DFT due to incorrect alignment of the  $2\pi^*$  state.<sup>18</sup> Fig. 1(a) and (d) show previously reported CO TPD data on Au(211)<sup>9</sup> and Au(310).<sup>19</sup> Note that we subtracted the baseline signal of CO desorption using an exponential decay function to the tail of this the curves<sup>20</sup> (see Fig. S1, ESI†). This background signal can arise from, for example, the desorption of CO from the walls of the apparatus.

As Fig. 1(c) and (f) illustrate, Au(211) consists of a three-atom-wide (111) terrace and a (100) step, which we will refer to as the (111)<sub>terrace</sub> and (100)<sub>step</sub>. Au(310) consists of a three-atom-wide (100) terrace and a (110) step, which we refer to as (100)<sub>terrace</sub> and (110)<sub>step</sub>, respectively.

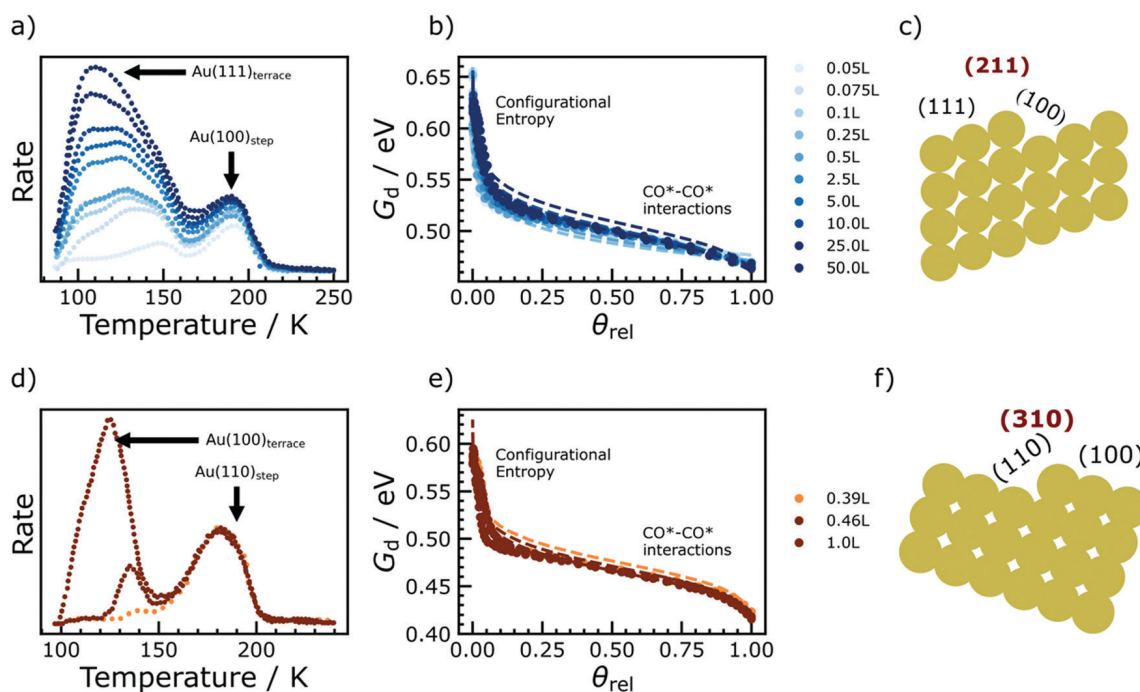


Fig. 1 (a and d) Background corrected rates of CO desorption from TPD experiments in previous work for Au(211) from ref. 9 and Au(310) ref. 19 site motifs assigned to each peak are labelled directly in the figure; (b and e)  $G_d$  as a function of the relative TPD coverage under vacuum conditions for the Au(100)<sub>step</sub> and Au(110)<sub>step</sub>; the dashed line indicates the best fit to the points (c and f) schematic of (211) and (310) surfaces.

## Peak assignments in TPD curves

In Fig. 1a we assign the peaks at lower temperatures to  $(111)_{\text{terrace}}$  and higher temperatures to the less coordinated, stronger binding  $(100)_{\text{step}}$  sites. Similarly, in Fig. 1d we assign the low temperature peaks to  $(100)_{\text{terrace}}$  sites, and the high temperature peaks to the  $(110)_{\text{step}}$ .

## How to extract adsorption energies and equilibrium coverages from fits of TPD curves

In what follows, we detail how we extract the free energy of CO adsorption,  $\Delta G_{\text{CO}^*}$ , from fitting kinetic parameters to TPD corresponding to different sites. Broadly, the strategy is to decompose  $G_{\text{d}}$ , the free energy of desorption, into its individual components. We then translate  $\Delta G_{\text{CO}^*}$  into an equilibrium coverage, on each of these sites under atmospheric pressure and a temperature of 300 K. We do so to compare results from DFT calculations with the quantities obtained from the TPD. In line with commonly used notation, we denote variables with a  $G$  as free energies and variables with  $E$  as internal energies.

We assume desorption to be a first order kinetic process with no readsorption (*i.e.* it is irreversible), which has the following rate:

$$\frac{d\theta_{\text{rel}}(T)}{dt} = \frac{k_{\text{B}}T}{h} \exp\left(-\frac{G_{\text{d}}(\theta_{\text{rel}}, T)}{k_{\text{B}}T}\right) \theta_{\text{rel}}(T) \quad (1)$$

where  $G_{\text{d}}(\theta_{\text{rel}}, T) = G_{\text{CO}^{\text{TS}}} - G_{\text{CO}^*}$  is the free energy barrier for CO desorption, and is the relative coverage of CO at temperature  $T$ , obtained by

$$\theta_{\text{rel}}(T) = \frac{\int_{T_{\text{min}}}^T \frac{d\theta}{dT} dT}{\int_{T_{\text{min}}}^{T_{\text{max}}} \frac{d\theta}{dT} dT} = \frac{\theta}{\theta_{\text{sat}}} \quad (2)$$

We obtain relative coverages here from TPD, since the coverage determined through integrating under a TPD rate curve provides a value relative to a maximum coverage  $\theta_{\text{sat}}$  for the given initial exposure,  $\theta_{\text{rel}} = \theta/\theta_{\text{sat}}$ , where  $\theta$  is the real coverage in monolayers (ML). Note that here we are considering a temperature-dependent prefactor,  $k_{\text{B}}T/h$ , from transition state theory,<sup>21</sup> and a coverage-dependent  $G_{\text{d}}$ . One approach is to take out the entropic terms from the exponential in eqn (1), which leads to the  $G_{\text{d}}(\theta_{\text{rel}}, T)$  being replaced by  $E_{\text{d}}(\theta_{\text{rel}})$ , the internal energy plus the zero-point energy. However, we will keep  $G_{\text{d}}(\theta_{\text{rel}}, T)$  within the exponential so that we can then expand it into its constituents.

By fitting eqn (1) and (2) to the rates in Fig. 1(a) and (d) we obtain  $G_{\text{d}}(\theta, T)$ . Fig. 1(b) and (e) shows the resultant  $G_{\text{d}}(\theta, T)$  vs.  $\theta_{\text{rel}}$  for  $(100)_{\text{step}}$  and  $(110)_{\text{step}}$  sites, under vacuum conditions (we discuss  $(111)_{\text{terrace}}$  and  $(100)_{\text{terraces}}$  in ESI† Note 1; briefly, adsorbates on terraces interact with those on step sites, which hinders accurate determination of adsorption energies on terraces from the TPD). At very low coverages, the divergent

configurational entropy (detailed below) causes a sharp increase in desorption free energy. As the coverage increases, the binding strength weakens slightly due to adsorbate–adsorbate interactions, which decreases the desorption energy.

The  $G_{\text{d}}$ , in terms of internal energies and entropies, is as follows:

$$G_{\text{d}} = G_{\text{CO}^{\text{TS}}} - G_{\text{CO}^*} = (E_{\text{CO}^{\text{TS}}} - TS_{\text{CO}^{\text{TS}}}^{\text{harm}}) - (E_{\text{CO}^*} + b\theta - TS_{\text{CO}^*}^{\text{harm}}) + \Delta\text{ZPE} - T\Delta S^{\text{config}} \quad (3)$$

where is the internal energy of the surface with CO at the transition state,  $E_{\text{CO}^*}$  is the internal energy of the adsorbed state at dilute coverage with  $\theta \rightarrow 0$ ,  $S_x^{\text{harm}}$  the vibrational contributions to entropy for state  $x$  as determined using the harmonic approximation,  $b$  is a CO–CO interaction parameter which accounts for the decrease in desorption energy with increasing  $\theta$ ,  $\Delta\text{ZPE}$  and  $\Delta S^{\text{config}}$  are the difference in zero point energy and configurational entropy between  $\text{CO}^{\text{TS}}$  and  $\text{CO}^*$ , respectively. While we use a simple linear model (see ESI,† Note 1) for adsorbate–adsorbate interactions through  $b\theta$ , more complex models can be used if needed by appropriately changing the functional form of eqn (3). We note that adsorbate–adsorbate interaction parameters can also be introduced into the Redhead analysis framework. Furthermore, all the interactions in eqn (3) can be included into a kinetic Monte Carlo setup. In this work, we use the presented mean-field framework to fit the TPD directly, which we compare directly to coverage-dependent adsorption energies computed with DFT.

In order to obtain  $\Delta G_{\text{CO}^*}$  from  $G_{\text{d}}$ , we assume the following:

- (1) The internal energy of the transition state ( $E_{\text{CO}^{\text{TS}}}$ ) is well approximated by that of  $\text{CO}_{(\text{g})}$ ,  $E_{\text{CO}^{\text{TS}}} \approx E_{\text{CO}_{(\text{g})}} + E^*$ , where  $E^*$  is the internal energy of the clean slab (evaluated in ESI,† Note 2).
- (2) The vibrational and rotational entropic contributions associated with the transition state of CO desorption,  $S_{\text{CO}^{\text{TS}}}^{\text{harm}}$  are approximated by those of  $\text{CO}^*$ ,  $S_{\text{CO}^*}^{\text{harm}}$ , since  $\text{CO}^{\text{TS}}$  lies very close to the surface, *i.e.*,  $S_{\text{CO}^{\text{TS}}}^{\text{harm}} \approx S_{\text{CO}^*}^{\text{harm}}$ .

These two assumptions simplify eqn (3) to a function only of thermodynamic parameters:

$$G_{\text{d}} \approx E_{\text{CO}_{(\text{g})}} + E^* - E_{\text{CO}^*} - b\theta + \Delta\text{ZPE} - T\Delta S^{\text{config}} \quad (4)$$

We define  $\Delta E_{\theta \rightarrow 0} = E_{\text{CO}_{(\text{g})}} + E^* - E_{\text{CO}^*} + \Delta\text{ZPE}$ ,  $\Delta E_{\theta \rightarrow 0}$  is the desorption energy of CO at the limit of  $\theta \rightarrow 0$ , which is independent of  $\theta$ . Along with the  $\theta$ -dependence of  $\Delta S^{\text{config}}$ ,  $G_{\text{d}}$  from eqn (4) becomes a function only of  $\theta$  (the true coverage) or  $\theta_{\text{rel}}$  (the relative coverage) and  $T$ :

$$G_{\text{d}}(\theta, T) \approx \Delta E_{\theta \rightarrow 0} - b\theta - k_{\text{B}}T \ln\left(\frac{\theta}{1-\theta}\right) = \Delta E_{\theta \rightarrow 0} - b\theta_{\text{rel}}\theta_{\text{sat}} - k_{\text{B}}T \ln\left(\frac{\theta_{\text{rel}}\theta_{\text{sat}}}{1-\theta_{\text{rel}}\theta_{\text{sat}}}\right) \quad (5)$$

We apply the right hand side of eqn (5) to fit the curves in Fig. 1(b) and (e). The resultant  $\Delta E_{\theta \rightarrow 0}$  are shown in Fig. 2a as a

function of initial exposures. Within error bounds,  $\Delta E_{\theta \rightarrow 0}$  does not vary with exposure, which is consistent with  $\Delta E_{\theta \rightarrow 0}$  having no dependence on coverage. Another parameter that can be changed in experiments to show the invariance of  $\Delta E_{\theta \rightarrow 0}$  is the ramp rate,  $dT/dt$ . The other two contributions to  $G_d(\theta, T)$  are shown in Fig. 2b. The configurational entropy term shows a large contribution only at very low coverages, while the interaction term contributes at higher coverages. The fit parameters,  $b$  and  $\theta_{\text{sat}}$ , are tabulated in ESI† Note 3. We note that while eqn (5) might work well for most surfaces, it does not account for dissociation of reactants on the surface. This additional reaction can be added to eqn (5) in the form of an additional  $k_n \theta_n$ , where  $n$  is the order of the surface reaction and might be particularly relevant for high temperature TPD.

To obtain the equilibrium  $\theta(T, p_{\text{CO}})$ , we translate  $G_d(\theta, T)$  into the free energy of adsorption,  $\Delta G_{\text{CO}^*}(\theta, T)$ , by adding the difference in the entropic contributions arising from  $\text{CO}^*$ ,  $S_{\text{CO}^*}^{\text{harm}}$ , and  $\text{CO}_{(\text{g})}$ ,  $S_{\text{CO}_{(\text{g})}}^{\text{ideal}}$ , as well as the pressure of  $\text{CO}_{(\text{g})}$ ,  $p_{\text{CO}}$ :

$$\Delta G_{\text{CO}^*}(\theta, T) \approx -G_d(\theta, T) - T(S_{\text{CO}^*}^{\text{harm}} - S_{\text{CO}_{(\text{g})}}^{\text{ideal}}) - k_b T \ln(p_{\text{CO}}) \quad (6)$$

We obtain  $S_{\text{CO}^*}^{\text{harm}}$  and  $S_{\text{CO}_{(\text{g})}}^{\text{ideal}}$  with calculations of vibrational frequencies from DFT (tabulated in the Table S1, ESI†). Combining eqn (5) and (6), we obtain  $\Delta G_{\text{CO}^*}(\theta, T)$  in terms of fitted parameters from  $G_d(\theta, T)$ :

$$\Delta G_{\text{CO}^*}(\theta, T) \approx -\Delta E_{\theta \rightarrow 0} + b\theta + k_b T \ln\left(\frac{\theta}{1-\theta}\right) - T(S_{\text{CO}^*}^{\text{harm}} - S_{\text{CO}_{(\text{g})}}^{\text{ideal}}) - k_b T \ln(p_{\text{CO}}) \quad (7)$$

We solve eqn (7) numerically for the equilibrium  $\theta(T)$ , under the equilibrium condition  $\Delta G_{\text{CO}^*}(\theta, T) = 0$ . Fig. 3 shows the equilibrium  $\theta(T)$  for  $p_{\text{CO}_{(\text{g})}} = 1$  bar as a function of  $T$  for all exposures. Given that 1 ML (monolayer) corresponds to complete coverage of sites, all exposures on both (100)<sub>step</sub> and (110)<sub>step</sub> sites show approximately a coverage of between 0.4 to 0.9 ML present on

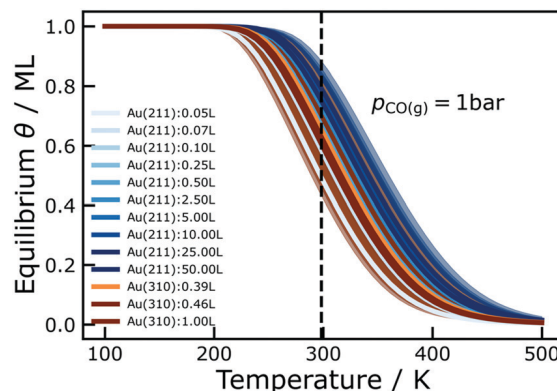


Fig. 3 Equilibrium coverage of CO as a function of the temperature at 1 bar  $\text{CO}_{(\text{g})}$  pressure for both surface facets (211) and (310) for all considered initial exposures. The dashed black line shows the equilibrium coverage at 298.15 K.

both (211) and (110) surfaces at a temperature of 300 K and pressure of 1 bar  $\text{CO}_{(\text{g})}$ .

As a side note: the  $\Delta G_{\text{CO}^*}(\theta, T) = 0$  condition gives rise to a physically intuitive adsorption isotherm expression.<sup>22</sup> At standard conditions,  $\theta = \frac{1}{2}$  and  $p_{\text{CO}} = 1$  bar, we define  $\Delta G_{\theta=\frac{1}{2}} = -\Delta E_{\theta \rightarrow 0} + \frac{b}{2} - T(S_{\text{CO}^*}^{\text{harm}} - S_{\text{CO}_{(\text{g})}}^{\text{total}})$  and write eqn (7) in terms of  $\Delta G_{\theta=\frac{1}{2}}$ :

$$\Delta G_{\text{CO}^*}(\theta, T) = \Delta G_{\theta=\frac{1}{2}} + b\left(\theta - \frac{1}{2}\right) + k_b T \ln\left(\frac{\theta}{1-\theta}\right) - k_b T \ln(p_{\text{CO}}) \quad (8)$$

With  $\Delta G_{\text{CO}^*}(\theta, T) = 0$  in eqn (8), the equilibrium  $\theta$  can be expressed implicitly in terms of the equilibrium constant,  $K(\theta, T)$ , in the form of an adsorption isotherm:

$$\theta(T, p_{\text{CO}}) = \frac{K(\theta, T)p_{\text{CO}}}{1 + K(\theta, T)p_{\text{CO}}}, \quad K(\theta, T) = \exp\left(-\frac{\Delta G_{\theta=\frac{1}{2}} + b\left(\theta - \frac{1}{2}\right)}{k_b T}\right) \quad (9)$$

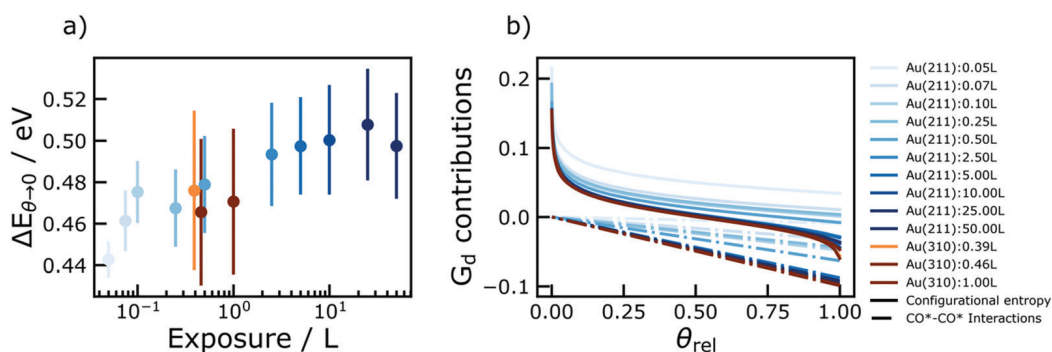


Fig. 2 (a) Desorption energy corresponding to dilute coverages,  $\Delta E_{\theta \rightarrow 0}$  of CO for (100)<sub>step</sub> and (110)<sub>step</sub> as a function of the initial exposure in Langmuir in the TPD experiment. Error bars show errors from the fit determined as the mean error of the residual; (b) contributions of the configurational entropy (solid lines) and CO–CO adsorbate–adsorbate interaction (dashed-lines) to the total desorption energy  $G_d$  based on the fitting equation described in eqn (5).



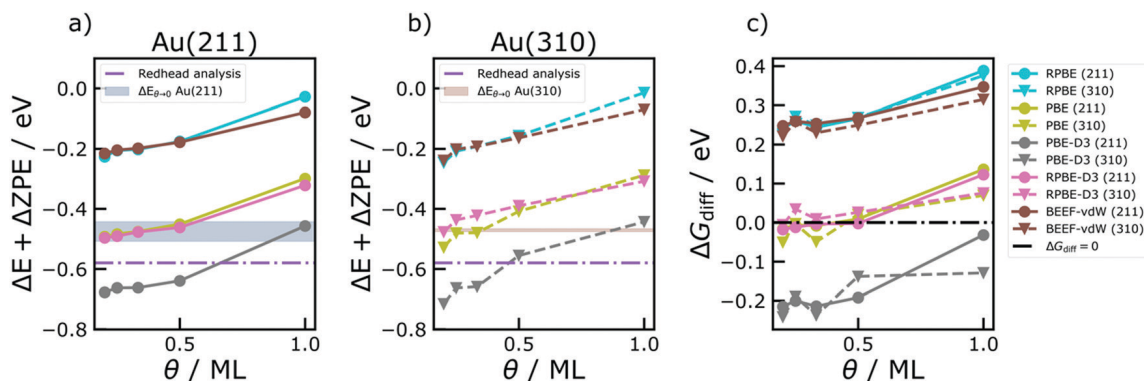


Fig. 4 DFT calculated adsorption energies as a function of the step coverage on (a) 211 (b) 310 (c) differential free energies for CO adsorption; all points at the different coverages are for the most stable adsorption site; in (a and b) the colored bands indicate  $\Delta E_{\theta \rightarrow 0}$  obtained from the TPD analysis for each facet, and the purple dashed line the value from Redhead analysis.

## Comparison of TPD-derived and DFT adsorption energies

We evaluate the  $\Delta E_{\theta \rightarrow 0}$  and equilibrium  $\theta$  from TPD against GGA-DFT calculations of adsorbed CO on Au(111), Au(100) terraces and Au(110), Au(211), Au(310) stepped facets (see ESI,† Note 2). By varying the number of CO\* within the periodic unit cells in our simulations, we calculate two quantities – 1)  $\Delta E + \Delta ZPE$ , which can be directly compared with  $\Delta E_{\theta \rightarrow 0}$  2)  $\Delta G_{\text{diff}}$ , the differential CO adsorption free energy at various coverages:

$$\Delta G_{\text{diff}} = \frac{G_{m_{\text{CO}^*}} - G_{n_{\text{CO}^*}} - (m_{\text{CO}} - n_{\text{CO}})G_{\text{CO}(\text{g})}}{m_{\text{CO}} - n_{\text{CO}}}, \quad (10)$$

where  $G_{x_{\text{CO}}}$  is the free energy corresponding to a state with  $x$  adsorbed CO\* and  $G_{\text{CO}(\text{g})}$  is the free energy of CO(g). Analogous to how it was defined for the TPD experiment in eqn (2), we define the coverage  $\theta$  as the number of CO\* per step atom for the (211) and (310) facet. We report both  $\Delta E + \Delta ZPE$  and  $\Delta G_{\text{diff}}$  as a function of  $\theta$  in Fig. 4a and b for all facets considered and for five density functionals, namely RPBE (cyan), PBE (grey), RPBE-D3 (pink), PBE-D3 (grey) and BEEF-vdW (brown); overall, we see the increase in  $\Delta G_{\text{diff}}$  with increasing  $\theta$ , which arises from increasing adsorbate–adsorbate interactions.

We indicate the  $\Delta E_{\theta \rightarrow 0}$  obtained from TPD for (100)<sub>step</sub> and (110)<sub>step</sub> facets in Fig. 4a and b by the light blue and red bands (the width indicates the uncertainty arising from fits to different exposures). In the low coverage regime, all the functionals are within 0.2 eV of  $\Delta E_{\theta \rightarrow 0}$ . RPBE-D3 and PBE are the closest to the TPD estimates in the low coverage region. RPBE and BEEF-vdW, underestimate binding of CO while PBE-D3 overestimates it. In comparison, the Redhead analysis (see ESI,† Note 1), gives a  $\Delta E_{\theta \rightarrow 0} = 0.58$  eV, which differs from  $\Delta E + \Delta ZPE$  obtained from our analysis by 0.1 eV in the stronger binding direction. The difference between the values obtained from our approach as compared to that from a standard Redhead analysis is small and our analysis suggests that using the latter for simple estimation of the adsorption energies might be reasonable. We note however, that using the adsorption energy from a Redhead analysis would predict complete saturation of the

surface (since it predicts stronger binding than our approach). Thus, for cases where it is critical to determine the equilibrium coverage, we believe that methodologies that account for coverage and configurational effects, such as the one presented in this work, should be used.

We also determine a GGA-DFT predicted equilibrium  $\theta$  from the data in Fig. 4b. The equilibrium  $\theta$  is highest coverage reached where the differential free energy of adsorption is zero:

$$\Delta G_{\text{diff}} = 0, \quad (11)$$

and is shown in Fig. 4c as a black line. The free energy includes the entropy of gas phase and adsorbed CO as well as its configurational entropy. The computed equilibrium  $\theta$  is about 0.5 ML for RPBE-D3 and PBE, which is very close to the lower bound of the estimate determined from the TPD. RPBE and BEEF-vdW show almost no coverage of CO (given by their very positive  $\Delta G_{\text{diff}}$ ), while PBE-D3 shows a coverage of greater than 0.5 ML.

Overall, the energies obtained from the above TPD analysis and some of the DFT functionals suggest that CO binds to the *step* sites of Au(211) and (310)/(110) at standard temperature, 298.15 K and pressure of 1 bar CO(g).

## Conclusions

CO adsorption on Au(211) and Au(310) surfaces are investigated using TPD and DFT calculations. We establish a methodology to extract adsorption energies and equilibrium coverages using TPD and benchmark the obtained values with DFT calculations. The approach involves fitting the desorption energy from experimental TPD to a functional form that includes the adsorption energy as a function of the entire range in coverage, through the configurational entropy and a linear adsorbate–adsorbate interaction term. This treatment is in contrast to the Redhead analysis which assumes coverage independent adsorption energies. We find under standard conditions with 1 bar CO and 298.15 K, 0.4–0.9 ML of CO may be present on the Au steps. Furthermore, we show that for Au step sites, computed adsorption energy and equilibrium coverages from



the RPBE-D3 and PBE functionals are in good agreement with TPD extracted values.

from PRACE (project ID: prpa85) and the Juelich Supercomputing Centre.

## Computational methods

Density functional theory calculations were performed using Vienna *ab initio* Software Package (VASP).<sup>23</sup> Core electrons were described using Projector Augmented Waves (PAW)<sup>24</sup> potentials. Valence electrons were described using plane-waves with kinetic energy up to 500 eV. Gaussian smearing with a width of 0.1 eV was used. The functionals used in this work were BEEF-vdW,<sup>4</sup> RPBE,<sup>25</sup> PBE,<sup>26</sup> RPBE-D3,<sup>27</sup> PBE-D3.<sup>27</sup>

Structures were prepared using the Atomic Simulation Environment (ASE).<sup>28</sup> The lattice constant of gold was optimized using a  $12 \times 12 \times 12$  Monkhorst–Pack<sup>29</sup> *k*-point mesh grid. Slabs four layers thick were made (211) and (310) facets were constructed, with the bottom two layers kept fixed. For the (211) surface, (1 × 3), (2 × 3), (3 × 3), (4 × 3) and (5,3) cells were used with *k*-points (12,4,1), (6,4,1), (4,4,1), (3,4,1) and (3,4,1) respectively. For the (310) surface (1 × 4), (2 × 4), (3 × 4), (4 × 4) and (5,4) cells were used with *k*-points (12,6,1), (6,6,1), (4,6,1), (3,6,1) and (3,6,1) respectively. All calculations were run using AiiDA, which keeps track of the provenance of each result.<sup>30</sup>

Static adsorption energies for CO were calculated on all unique surface sites on each facet. Initial structures were generated using pymatgen.<sup>31</sup> All geometries were optimized until forces on all atoms was less than 0.025 eV Å<sup>-1</sup>. Vibrational frequencies were computed using a finite difference method as implemented in VASP (IBRION = 5).

## Code availability

- (1) Python code to fit TPD: <https://github.com/CatTheoryDTU/tpd-analyse/tree/develop>.
- (2) Python code used to prepare figures: [https://github.com/sudarshanv01/CO\\_on\\_gold\\_papers](https://github.com/sudarshanv01/CO_on_gold_papers).
- (3) AiiDA archive files: 10.24435/materialscloud:b9-sq.

## Conflicts of interest

The authors have no conflicts of interest to declare.

## Acknowledgements

The authors would like to acknowledge funding from the European Union's Horizon 2020 research and innovation programme under grant agreement No. 85144, (SELECTCO2) and the Villum Fonden through the VSUSTAIN project (9455). The authors thank Jens K. Nørskov for the discussion regarding TPD. YK would like to acknowledge financial support from the Japan Society for the Promotion of Science (JSPS) KAKENHI Grant-in-Aid for Early-Career Scientists (19 K15360) and JSPS Open Partnership Joint Research Projects/Seminars (JPJSBP 120209925). SV and KC acknowledge computational resources

## References

- 1 J. K. Nørskov, T. Bligaard, J. Rossmeisl and C. H. Christensen, Towards the computational design of solid catalysts, *Nat. Chem.*, 2009, **1**(1), 37–46.
- 2 S. Mallikarjun Sharada, R. K. B. Karlsson, Y. Maimaiti, J. Voss and T. Bligaard, Adsorption on transition metal surfaces: Transferability and accuracy of DFT using the ADS41 dataset, *Phys. Rev. B*, 2019, **100**(3), 35439.
- 3 J. Wellendorff, T. L. Silbaugh, D. Garcia-Pintos, J. K. Nørskov, T. Bligaard and F. Studt, *et al.*, A benchmark database for adsorption bond energies to transition metal surfaces and comparison to selected DFT functionals, *Surf. Sci.*, 2015, **640**, 36–44, DOI: 10.1016/j.susc.2015.03.023.
- 4 J. Wellendorff, K. T. Lundgaard, A. Møgelhøj, V. Petzold, D. D. Landis and J. K. Nørskov, *et al.*, Density functionals for surface science: Exchange-correlation model development with Bayesian error estimation, *Phys. Rev. B: Condens. Matter Mater. Phys.*, 2012, **85**(23), 235149.
- 5 T. Bligaard, R. M. Bullock, C. T. Campbell, J. G. Chen, B. C. Gates, R. J. Gorte, *et al.*, *Toward Benchmarking in Catalysis Science: Best Practices, Challenges, and Opportunities*, ACS Catalysis, 2016, vol. 6, pp. 2590–2602. Available from: <https://pubs.acs.org/sharingguidelines>.
- 6 C. T. Campbell and J. R. V. Sellers, *Enthalpies and entropies of adsorption on well-defined oxide surfaces: Experimental measurements*, Chemical Reviews, 2013, vol. 113, pp. 4106–4135. Available from: <https://pubs.acs.org/sharingguidelines>.
- 7 C. T. Campbell, Energies of Adsorbed Catalytic Intermediates on Transition Metal Surfaces: Calorimetric Measurements and Benchmarks for Theory, *Acc. Chem. Res.*, 2019, **52**(4), 984–993. Available from: <https://pubs.acs.org/sharingguidelines>.
- 8 M. E. Van Reijzen, M. A. Van Spronsen, J. C. Docter and L. B. F. Juurlink, CO and H<sub>2</sub>O adsorption and reaction on Au(310), *Surf. Sci.*, 2011, **605**(17–18), 1726–1731.
- 9 J. Kim, E. Samano and B. E. Koel, CO Adsorption and Reaction on Clean and Oxygen-Covered Au(211) Surfaces, *J. Phys. Chem. B*, 2006, **110**(35), 17512–17517. Available from: <https://pubs.acs.org/sharingguidelines>.
- 10 P. A. Redhead, Thermal desorption of gases, *Vacuum*, 1962, **12**(5), 274.
- 11 A. M. de Jong and J. W. Niemantsverdriet, Thermal Desorption Analysis: Comparative Test of Ten Commonly Applied Procedures, *Surf. Sci.*, 1990, **233**(3), 355–365.
- 12 S. L. Tait, Z. Dohnálek, C. T. Campbell and B. D. Kay, N-alkanes on MgO(100). I. Coverage-dependent desorption kinetics of n-butane, *J. Chem. Phys.*, 2005, **122**(16), 164708. Available from: <https://aip-scitation-org.proxy.findit.dtu.dk/doi/pdf/10.1063/1.1883629?class=pdf>.
- 13 B. Lehner, M. Hohage and P. Zeppenfeld, Kinetic Monte Carlo simulation scheme for studying desorption processes, *Surf. Sci.*, 2000, **454**(1), 251–255.

- 14 C. Sendner and A. Groß, Kinetic Monte Carlo simulations of the interaction of oxygen with Pt(111), *J. Chem. Phys.*, 2007, **127**(1), 014704, DOI: 10.1063/1.2748379.
- 15 C. Sendner, S. Sakong and A. Groß, Kinetic Monte Carlo simulations of the partial oxidation of methanol on oxygen-covered Cu(1 1 0), *Surf. Sci.*, 2006, **600**(16), 3258–3265.
- 16 L. Schimka, J. Harl, A. Stroppa, A. Grüneis, M. Marsman and F. Mittendorfer, *et al.*, Accurate surface and adsorption energies from many-body perturbation theory, *Nat. Mater.*, 2010, **9**(9), 741–744. Available from: [www.nature.com/naturematerials](http://www.nature.com/naturematerials).
- 17 A. J. Medford, J. Wellendorff, A. Vojvodic, F. Studt, F. Abild-Pedersen and K. W. Jacobsen, *et al.*, Assessing the reliability of calculated catalytic ammonia synthesis rates, *Science*, 2014, **345**(6193), 197–200.
- 18 P. J. Feibelman, B. Hammer, J. K. Nørskov, F. Wagner, M. Scheffler and R. Stumpf, *et al.*, The CO/Pt(111) Puzzle, *J. Phys. Chem. B*, 2001, **105**(18), 4018–4025. Available from: <http://citeseerx.ist.psu.edu/viewdoc/download?doi=10.1.1.485.4397&rep=rep1&type=pdf>.
- 19 C. J. Weststrate, E. Lundgren, J. N. Andersen, E. D. L. Rienks, A. C. Gluhoi and J. W. Bakker, *et al.*, CO adsorption on Au(3 1 0) and Au(3 2 1): 6-Fold coordinated gold atoms, *Surf. Sci.*, 2009, **603**(13), 2152–2157.
- 20 I. Chorkendorff and S. Tougaard, Background subtraction in electron spectroscopy by use of reflection electron energy loss spectra, *Appl. Surf. Sci.*, 1987, **29**(1), 101–112.
- 21 J. K. Nørskov, F. Studt, F. Abild-Pedersen and T. Bligaard, Fundamental Concepts in Heterogeneous Catalysis, *Fundamental Concepts in Heterogeneous Catalysis*, Wiley Blackwell, 2014, vol. 9781118888, pp. 1–196.
- 22 C. J. Pursell, H. Hartshorn, T. Ward, B. D. Chandler and F. Boccuzzi, Application of the Temkin model to the adsorption of CO on gold, *J. Phys. Chem. C*, 2011, **115**(48), 23880–23892. Available from: <https://pubs.acs.org/sharingguidelines>.
- 23 G. Kresse and J. Furthmüller, Efficient iterative schemes for ab initio total-energy calculations using a plane-wave basis set, *Phys. Rev. B: Condens. Matter Mater. Phys.*, 1996, **54**(16), 11169–11186, DOI: 10.1103/PhysRevB.54.11169.
- 24 D. Joubert, From Ultrasoft Pseudopotentials to the Projector Augmented-wave Method, *Phys. Rev. B: Condens. Matter Mater. Phys.*, 1999, **59**(3), 1758–1775, DOI: 10.1103/PhysRevB.59.1758.
- 25 B. Hammer, L. B. Hansen and J. K. Nørskov, Improved Adsorption Energetics Within Density-functional Theory Using Revised Perdew-Burke-Ernzerhof Functionals, *Phys. Rev. B: Condens. Matter Mater. Phys.*, 1999, **59**(11), 7413–7421, DOI: 10.1103/PhysRevB.59.7413.
- 26 J. P. Perdew, K. Burke and M. Ernzerhof, Generalized gradient approximation made simple, *Phys. Rev. Lett.*, 1996, **77**(18), 3865–3868.
- 27 S. Grimme, J. Antony, S. Ehrlich and H. Krieg, A consistent and accurate ab initio parametrization of density functional dispersion correction (DFT-D) for the 94 elements H-Pu, *J. Chem. Phys.*, 2010, **132**(15), 164117, DOI: 10.1063/1.3382344.
- 28 A. Hjorth Larsen, J. Jürgen Mortensen, J. Blomqvist, I. E. Castelli, R. Christensen and M. Dułak, *et al.*, The atomic simulation environment—a Python library for working with atoms, *J. Phys.: Condens. Matter*, 2017, **29**(27), 273002, DOI: 10.1088/1361-648X/aa680e.
- 29 H. J. Monkhorst and J. D. Pack, Special points for Brillouin-zone integrations, *Phys. Rev. B: Solid State*, 1976, **13**(12), 5188–5192, DOI: 10.1103/PhysRevB.13.5188.
- 30 S. P. Huber, S. Zoupanos, M. Uhrin, L. Talirz, L. Kahle and R. Häuselmann, *et al.*, AiiDA 1.0, a scalable computational infrastructure for automated reproducible workflows and data provenance, *Sci. Data*, 2020, **7**(1), 1–18.
- 31 S. P. Ong, W. D. Richards, A. Jain, G. Hautier, M. Kocher and S. Cholia, *et al.*, Python Materials Genomics (pymatgen): A robust, open-source python library for materials analysis, *Comput. Mater. Sci.*, 2013, **68**, 314–319.


## 10.2 Paper 2

### **Interaction of CO with Gold in an Electrochemical Environment**

Sudarshan Vijay, Thomas V. Hogg, Johan Ehlers, Henrik H. Kristoffersen, Yu Katayama, Yang Shao Horn, Ib Chorkendorff, Karen Chan and Brian Seger  
Reprinted with permission from J. Phys. Chem. C **2021**, 125, 32, 17684-17689.  
Copyright 2021 American Chemical Society

# Interaction of CO with Gold in an Electrochemical Environment

Sudarshan Vijay, Thomas V. Hogg, Johan Ehlers, Henrik H. Kristoffersen, Yu Katayama, Yang Shao Horn, Ib Chorkendorff, Karen Chan,\* and Brian Seger\*

 Cite This: *J. Phys. Chem. C* 2021, 125, 17684–17689

 Read Online

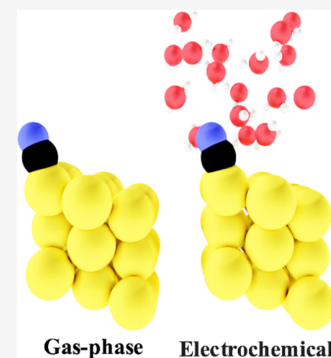
ACCESS |

 Metrics & More

 Article Recommendations

 Supporting Information

**ABSTRACT:** We present a joint theoretical–experimental study of CO coverage and facet selectivity on Au under electrochemical conditions. With in situ attenuated total reflection surface-enhanced IR spectroscopy, we investigate the CO binding in an electrochemical environment. At 0.2 V versus SHE, we detect a CO band that disappears upon facet-selective partial Pb underpotential deposition (UPD), suggesting that Pb blocks certain CO adsorption sites. With Pb UPD on single crystals and theoretical surface Pourbaix analysis, we eliminate (111) terraces as a possible adsorption site of CO. Ab initio molecular dynamics simulations of explicit water on the Au surface show the adsorption of CO on (211) steps to be significantly weakened relative to the (100) terrace due to competitive water adsorption. This result suggests that CO is more likely to bind to the (100) terrace than (211) steps in an electrochemical environment, even though Au steps under gas-phase conditions bind CO\* more strongly. The competition between water and CO adsorption can result in different binding sites for CO\* on Au in the gas phase and electrochemical environments.



## INTRODUCTION

Gold nanoparticles are highly active catalysts for a variety of thermal and electrocatalytic reactions. As a thermal catalyst, Au is excellent for CO oxidation,<sup>1</sup> whereas under electrochemical conditions, Au is the most active catalyst for CO<sub>2</sub> reduction (CO<sub>2</sub>R) to CO and is among the most active catalysts for CO and alcohol electro-oxidation.<sup>2</sup> Despite the apparent simplicity of many of these reaction processes, their mechanisms remain contentious.<sup>3–7</sup> The determination of relevant adsorbate coverages in situ, especially under electrochemical conditions, remains an open challenge. Computational mechanistic investigations have recently begun to include the impact of solvation and field, which can have a critical impact on reaction energetics.<sup>8–11</sup>

This work presents a combined theoretical and experimental investigation of the binding characteristics of CO on Au under electrochemical conditions. To investigate the adsorption sites in an electrochemical environment, we performed surface-enhanced IR spectroscopy on polycrystalline gold and detected a CO band with a signal maximum at 0.2 V versus SHE. This band disappears in the presence of lead, which we attribute to the disappearance of the signal to cause blocking of the CO adsorption sites. Using cyclic voltammograms (CVs) of lead underpotential deposition (UPD) on single crystals along with computational Pourbaix analysis, we narrow the adsorption site possibilities to open motifs such as (100) terraces or (211) and (110) steps. To gain further insights into which sites could adsorb CO in an electrochemical environment, we perform density functional theory (DFT) calculations in the gas phase and in the presence of an explicit solvent. In vacuum, DFT calculations and temperature-programmed desorption spec-

tra<sup>12</sup> show CO to bind more strongly on steps. In contrast, ab initio molecular dynamics simulations on (100) and (211) surfaces with explicit water suggest that competitive adsorption of water significantly destabilizes CO on the (211) step, making it more likely to bind to the (100) terrace instead of the (211) step. This analysis demonstrates the need to consider the effect of competitive adsorption of water since Au and other transition metals may not bind CO on the same sites in the gas phase and electrochemical environments.

## RESULTS AND DISCUSSION

**CO Adsorption with Lead UPD.** To probe the adsorption of CO under an electrochemical environment, we performed in situ attenuated total reflection surface-enhanced IR spectroscopy (ATR-SEIRAS) in conjunction with Pb UPD on an electroless-deposited polycrystalline Au film in a 0.1 M HClO<sub>4</sub> electrolyte (see details in Supporting Information Note 1). The spectro-electrochemical cell was initially purged with 1 bar of Ar, and a spectral background was acquired. The cell was then purged with 1 bar of CO. This procedure resulted in a single vibrational band for CO adsorbed on Au at 2128 cm<sup>-1</sup> (at +0.634 V vs SHE). We note that CO is well known to form Ni and Fe carbonyls when transferring through stainless-steel

Received: May 5, 2021

Revised: July 20, 2021

Published: August 9, 2021



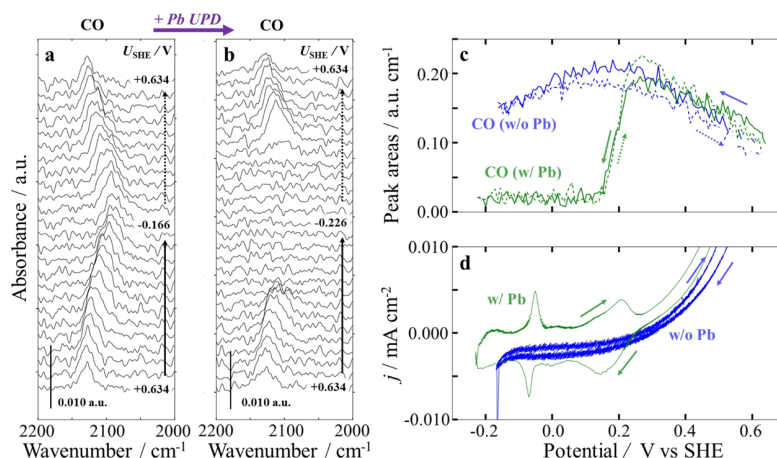


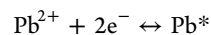
**Figure 1.** ATR-SEIRAS in the CO stretch region from a CV on an Au film in 0.1 M HClO<sub>4</sub> purged with 1 bar CO. A spectral background was taken at +0.634 V in Ar-purged solution. (a) ATR-SEIRAS spectra before the addition of Pb. (b) ATR-SEIRAS spectra with 1 mM Pb(ClO<sub>4</sub>)<sub>2</sub>. Every eighth spectrum is shown. (c) Integrated intensities of the CO stretch peak as a function of potential and (d) corresponding 2 mV/s CV with and without Pb.

pipes as was carried out in this work. However, the CO adsorption peak on Au at  $\sim 2100\text{ cm}^{-1}$  has been shown to be present even in the absence of bubbled CO (CO was produced via electroreduction of CO<sub>2</sub>).<sup>13</sup> Because of this observation, we attribute the CO adsorption peak to its adsorption on Au rather than on a Ni or Fe contaminant.

The vibrational band of CO adsorbed on Au was tracked while performing a CV in the Pb UPD region, first without Pb and then in the presence of Pb, as shown in Figure 1a,b, respectively. The observed peak position is in good agreement with the first reports of CO on vacuum and electroless-deposited Au films in HClO<sub>4</sub>.<sup>14,15</sup> Computed CO coverage-dependent IR spectra for the (111), (100), (110), and (211) surface facets (see Figure S5) show peaks between 1900 and 2100  $\text{cm}^{-1}$ ,<sup>16,17</sup> which is slightly smaller than the peak positions in Figure 1a,b. The linear shift in peak position with potential (i.e., the Stark shift) is measured to be 50  $\text{cm}^{-1}/\text{V}$ , in good agreement with previous reports. The effect of adding Pb is observed as a disappearance of the CO vibration band at more cathodic potentials and the reappearance on the returning, positive-going scan. We attribute this observation to Pb deposition blocking the sites that adsorb CO. The integrated band intensities for the two cases have been coplotted in Figure 1c, illustrating the difference. Without Pb, the CO band is present in the entire potential window (+0.634 to  $-0.166\text{ V}$ ) and has a maximum intensity of around 0.2 V versus SHE. In the presence of Pb, the CO band disappears over an approximately 100 mV range between 0.25 and 0.15 V vs SHE and then reappears in the same potential range on the return scan with this being a reversible process. Comparing the integrated band intensities to the UPD current in Figure 1d, we find that the disappearance of the CO band coincides with the broad and most anodic UPD waves centered around 0.2 V versus SHE. As shown in Figure 1d, the positive current which is more anodic than 0.3 V vs SHE corresponds to CO oxidation in both cases. The delayed hydrogen evolution onset in the solution with Pb allows for a slightly more cathodic potential window (+0.634 to  $-0.226\text{ V}$  vs SHE) compared to the solution without Pb.

Previously, ref 18 reported experimental Pb UPD CVs, which are reproduced in Figure 2a–d. These curves suggest that (211), (110), and (100) facets show Pb adsorption peaks

at more positive potentials than the (111) surface. This trend is consistent with our computational investigations of Pb adsorption on the same facets. Pb adsorption energies were calculated on all possible adsorption sites to determine the configuration with the most stable adsorption energy (Figure S4). The half reaction for the adsorption of lead is



The free energy for this reaction as a function of potential at a given surface coverage is

$$\Delta G_{\text{Pb}} = \Delta G_{\text{Pb}}^0 + 2e(U_{\text{SHE}} - U_{\text{Pb}^{2+}|\text{Pb}}) \quad (1)$$

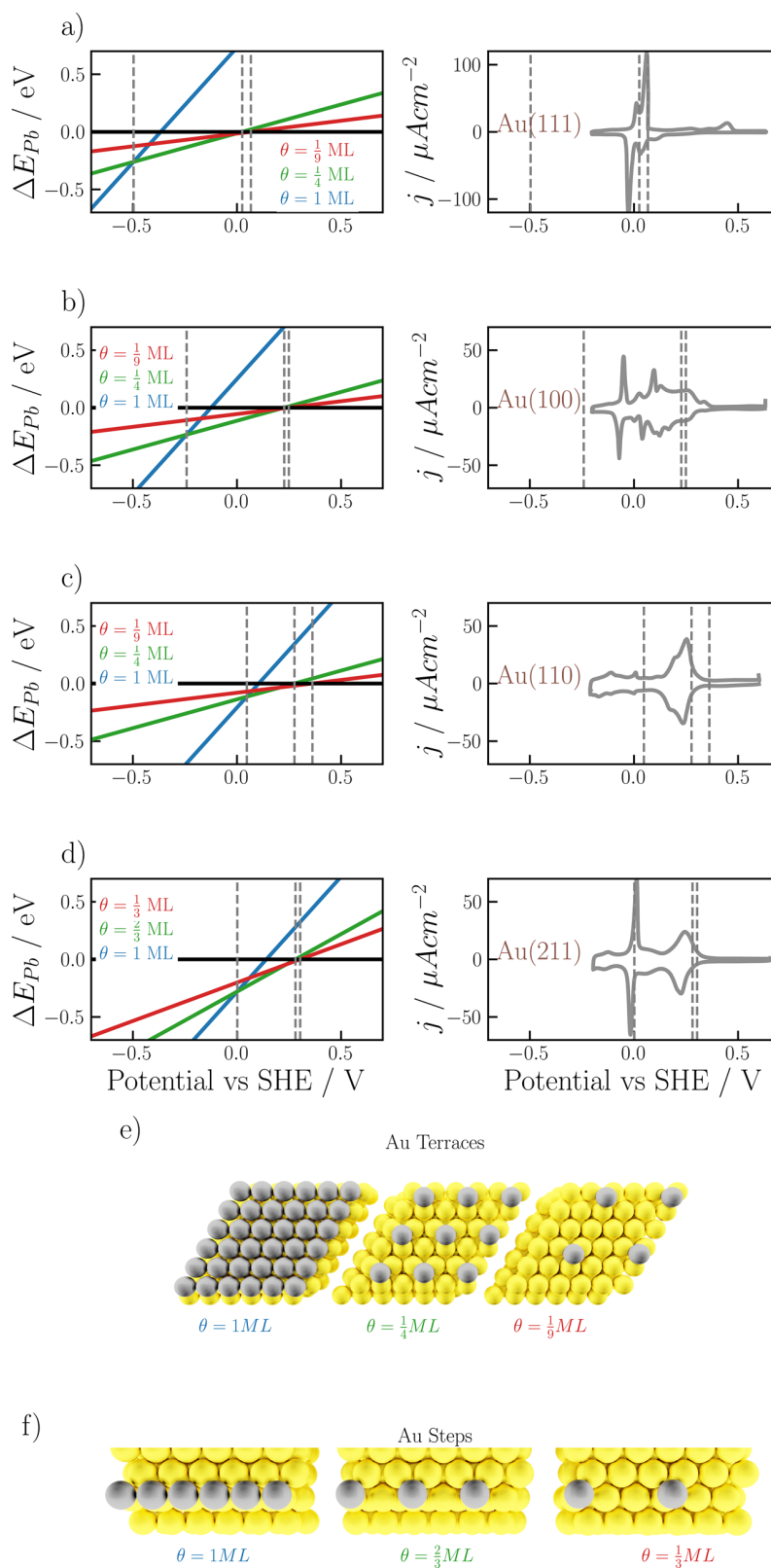
where  $\Delta G_{\text{Pb}}^0$  is the free energy referenced to 0 V versus  $U_{\text{Pb}|\text{Pb}^{2+}}$ ,  $U_{\text{SHE}}$  is the potential referenced to the standard hydrogen electrode, and  $U_{\text{Pb}^{2+}|\text{Pb}}$  is the standard redox potential of  $\text{Pb}^{2+}|\text{Pb}$ .

Figure 2a–d shows the surface Pourbaix diagrams for different coverages of Pb adsorbed on the four different surface facets of Au. Here, we assume that the entropic contribution of Pb adsorbed on Au is small, thus  $\Delta G_{\text{Pb}} = \Delta E_{\text{Pb}}$ . Each line corresponds to a certain coverage of Pb. On terraces, we consider coverages of 1/4, 1/9, and 1 ML (Figure 2e), and on steps, we consider coverages of 1/3, 2/3, and 1 ML (Figure 2f). Intersections between these lines are marked by the dashed black line and correspond to a change in the estimated Pb coverage on the surface and the generation of a current. The line with the lowest energy at a given potential corresponds to the estimated coverage of Pb on the Au surface.

To facilitate comparison with the experimental CVs from ref 18, we also show the computed “onsets” of the coverages considered directly on them as dashed black lines. These onsets are within the DFT error (about 0.15 eV)<sup>19</sup> consistent with onsets of the experimentally observed peaks. In the case of the Au(100) experiments, the multiple broadened peaks observed experimentally suggest reconstruction and the possible presence of surface defects.

With the displacement of CO\* with Pb\* in the CV (Figure 1d) at 0.2 V versus SHE, the surface facet(s) on which CO adsorbs must have onset potentials for Pb adsorption more positive than 0.2 V versus SHE. Both computational Pourbaix analysis and Pb UPD experiments show the onset of Pb





**Figure 2.** Computed surface Pourbaix diagrams on four prototype Au facets—(111), (100), (110), and (211). The dashed black line indicates the potential at which the coverage has increased between the discrete intervals for which the DFT calculation was performed. To the right of each surface, the Pourbaix diagram is the associated Pb-UPD CVs taken from ref 18. The multiple broadened peaks observed in the (100) facet suggest substantial reconstruction.

adsorption on the (111) facet to be at about 0 V versus SHE and above 0.25 V versus SHE for all other facets considered. Therefore, the combination of Pb UPD,<sup>18</sup> Pb adsorption calculations, and SEIRAS experiments together exclude the possibility of CO adsorption on the (111) terrace site and suggests that it adsorbs on a more open facet such as the (100) terrace and/or stepped sites.

We note that in a previous in situ STM work involving CO adsorption on Au,<sup>20</sup> full CO monolayer coverage on Au(111) was observed after 30 min, which is in contrast to what our work concludes. However, the authors of ref 20 saw CO depress into Au, which is highly unusual and led them to hypothesize that they were seeing physisorbed CO rather than chemisorbed CO. Thus, there could be an extra layer of complexity of CO adsorption beyond what this current work has focused on.

**Electrochemical Reaction Energetics.** Since steps or (100) is suggested by Pb UPD to be possible binding sites of CO\* in an electrochemical environment, we now investigate the energetics of CO adsorption with ab initio molecular dynamics (AIMD) simulations with liquid water on (100) and (211), as a prototypical stepped facet.

**Metal–Water Interface in Vacuum.** Water has been shown to competitively adsorb to metallic surfaces, which alters the adsorption energy of small molecules.<sup>21,22</sup> Since an accurate description of water binding is needed to capture facet selectivity on Au in an electrochemical environment, we first evaluate the accuracy of our simulations in capturing the metal–water interaction against previously published experimental temperature-programmed desorption (TPD) of water on Au(310).<sup>23</sup> As a computational analogue, we consider a single layer of water on a Au(310) stepped surface with different coverages of water, as shown in Figure 3b–f, and report energies based on AIMD calculations.

Figure 3g reports the average adsorption energy of water  $\Delta\langle E\rangle$ , defined as

$$\Delta\langle E\rangle = \frac{E_{n_{\text{H}_2\text{O}^*}} - E_* - n_{\text{H}_2\text{O}}E_{\text{H}_2\text{O}}}{n_{\text{H}_2\text{O}^*}}$$

where  $E_{n_{\text{H}_2\text{O}^*}}$  is the internal energy for a system consisting of  $n_{\text{H}_2\text{O}}$  water molecules on a surface and  $E_*$  is the internal energy of just the slab. At coverages greater than 0.5 ML,  $\Delta\langle E\rangle$  is roughly constant at a value of  $-0.4$  eV. As a basis for comparison, we use TPD experiments in ref 23, which have been analyzed using zero-order desorption kinetics. The data are reproduced in Figure 3a, where the green and red points refer to low ( $<1$  Langmuir) and high ( $>1$  Langmuir) exposures, respectively, and Langmuir refers to the pressure of gas (Torr) multiplied by the time of exposure (s). Two overlapping peaks were observed in the experiment between a temperature range of 158–170 K (first peak) and 161–168 K (second peak). The first peak, which we attribute to a step site, was visible at all exposures (both green and red curves in Figure 3a), while the second peak, which we attribute to a terrace site, was observed at high exposures (shown in red in Figure 3a).<sup>23</sup> Using leading edge analysis, where the log of the rate from a TPD spectra is fit to  $1/T$ , the averaged adsorption energy of water was determined to be  $-0.49$  eV for the first peak and  $-0.57$  eV for the second.<sup>23</sup> The free energies obtained from the simulations shown in Figure 3g for water coverages between 0.25 and 0.75 ML (depicted schematically

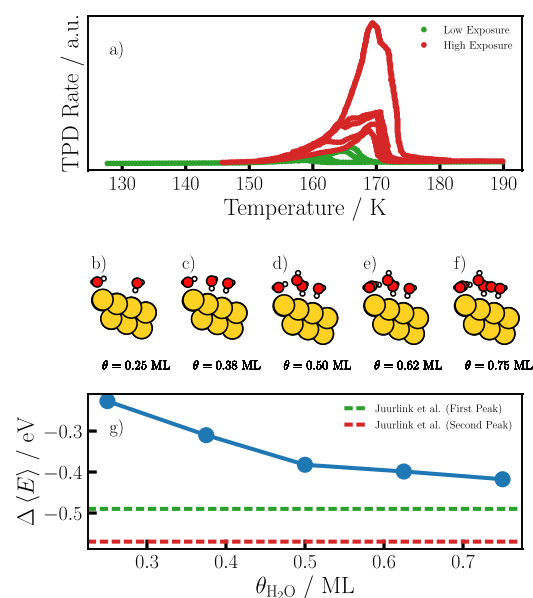


**Figure 3.** (a) Water adsorption TPD experiments reproduced from ref 23, where red points denote exposure greater than 1 L and green points have exposures lower than 1 L; (b–f) schematic illustrates the number of water molecules used for each coverage. (g) Average adsorption energy of H<sub>2</sub>O on Au(310) computed using ab initio molecular dynamics simulations; experimentally determined values of the adsorption energy from ref 23 are indicated by the red and green dashed lines corresponding to high exposure (second peak) and low exposure (first peak).

in Figure 3b–f) are within 0.1 eV from the energy of the first peak, which suggests that our chosen computational setup accurately models water–Au interactions (within the typical DFT error of 0.15 eV).<sup>19</sup>

**Metal–Water–CO Interface under Electrochemical Conditions.** We now compare the computed binding strengths of CO in vacuum against those from AIMD simulations that include explicit consideration of the water, which represents the electrochemical environment. We examine the (100) and (211) surface facets as prototype open facets suggested by Pb UPD experiments to be possible binding sites of CO\*. The potential range of the SEIRAS experiments (Figure 1c) is close to the potential of zero charge (pzc) of Au (0.4 V vs SHE, see Supporting Information Note 5) where electric fields and excess ion concentrations are the smallest.<sup>9,24,25</sup> We examined the impact of the electric field within this potential range in Figure S9, and, as expected, found it to be negligible ( $\sim 0.1$  eV in a 0.5 V range). Therefore, we did not consider the impact of ions in this study.

Figure 4 shows both the adsorption energies of CO in vacuum versus AIMD calculations with explicit water. Electronic energies ( $\Delta E$ ) correspond to the cumulative average from AIMD trajectories, while free energies include entropic contributions from CO\* and CO<sub>(g)</sub> using the harmonic approximation.

$$\Delta G_{\text{CO}^*} = \Delta E_{\text{CO}^*} - T(S_{\text{CO}^*}^{\text{harm}} - S_{\text{CO}(\text{g})}^{\text{ideal}}) - T\Delta S^{\text{config}} \quad (2)$$

The standard deviation associated with AIMD trajectories on the surface facets is about 0.1–0.3 eV, which compounds the errors associated with GGA functionals. We report standard deviations based on different calculation trajectories.

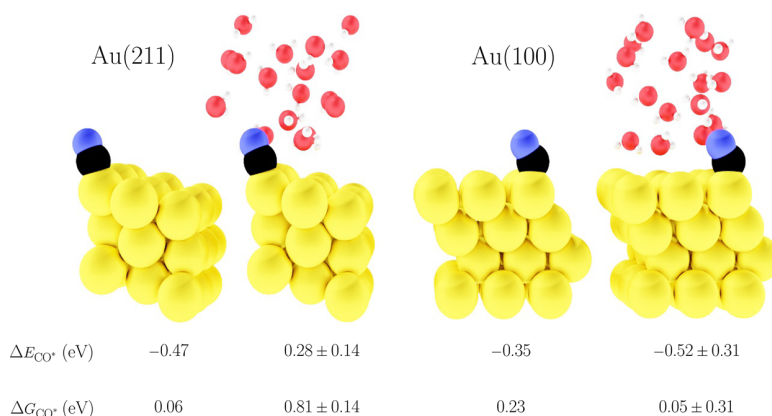


**Figure 4.** Snapshots of CO on Au(211) and Au(100) in vacuum or with explicit water from an ab initio MD simulation, performed in periodic unit cell sizes of  $3 \times 3$  for (211) at a coverage of 1/3 ML and  $3 \times 4$  for (100) at a coverage of 1/16 ML. Internal ( $\Delta E_{\text{CO}^*}$ ) and free energies of adsorption ( $\Delta G_{\text{CO}^*}$ ) with their standard deviations based on different runs are given below the snapshots.

In the gas phase, less-coordinated surfaces bind CO stronger,<sup>26</sup> as illustrated with the 0.17 eV smaller DFT-computed  $\Delta G_{\text{CO}^*}$  for the stepped (211) and terrace (100) in vacuum, in Figure 4. The solvation energy of CO captures the difference between the energies in vacuum and in AIMD with explicit water. In the case of (211), the calculated solvation energy is large and destabilizing (0.75 eV) due to competitive water adsorption. On a flat surface like (100), there is less competition from water, which is reflected in a stabilizing solvation energy of  $-0.18$  eV, which could arise from a stabilizing interaction of CO with the solvent (Figure S11). The significant destabilization of the adsorbed CO in water versus vacuum environments has also been observed on Cu(211)<sup>21</sup> and Pt(111)<sup>22,27</sup> (see Supporting Information Note 5).

The large difference in solvation energy between Au(211) and Au(100) gives rise to Au(100) having an  $\sim 0.8$  eV smaller  $\Delta G_{\text{CO}^*}$  of  $0.05 \pm 0.31$  eV, which suggests that Au(100) is more likely to bind CO in an electrochemical environment, although the uncertainties with the computed  $\Delta G_{\text{CO}^*}$  are large. These results suggest that the competitive adsorption of water affects the adsorption energies of CO on different facets of Au differently, such that CO binds to different sites in an electrochemical environment than in vacuum. Beyond these uncertainties, GGA-DFTs may be underestimating CO\* binding by about 0.1 eV on this surface, as was shown for the (211)<sub>step</sub> in ref 12. Despite these possible errors,  $\Delta E_{\text{CO}^*} = -0.52$  eV on Au(100) from the AIMD calculations compares well against measured enthalpy of CO adsorption on polycrystalline Au in an electrochemical environment, which was estimated to be  $-0.35$  eV<sup>16</sup> for CO(aq)  $\rightarrow$  CO\* and  $-0.1$  eV for CO(g)  $\rightarrow$  CO(aq).<sup>28</sup>

## CONCLUSIONS

CO adsorption on Au is a particularly important reaction for several electrochemical processes and more broadly for heterogeneous catalysis. However, there is still controversy regarding the adsorption of CO in electrochemical environments. In this study, we use a joint experimental and theoretical approach to elucidate binding characteristics of CO on Au with SEIRAS in conjunction with Pb UPD and ab initio molecular dynamics. Lead UPD in conjunction with SEIRAS suggests that open facets such as (100) and stepped sites are more likely to bind CO than (111) terraces. While Au

steps bind CO\* stronger than terraces in vacuum, ab initio MD simulations suggest that competitive water adsorption leads to a much larger destabilizing effect on the adsorption energies of CO on a (211) step versus a (100) terrace, making CO more likely to bind to the latter. Thus, CO can bind to different sites in the gas phase and electrochemical environments.

## ASSOCIATED CONTENT

### Supporting Information

The Supporting Information is available free of charge at <https://pubs.acs.org/doi/10.1021/acs.jpcc.1c04013>.

Computational and experimental methods, analysis of sampling of site dependence for CO with DFT calculations, IR spectra for CO, potential of zero charge computations, and details about AIMD convergence (PDF)

## AUTHOR INFORMATION

### Corresponding Authors

**Karen Chan** – *CatTheory, Department of Physics, Technical University of Denmark, 2800 Kongens Lyngby, Denmark;* [orcid.org/0000-0002-6897-1108](https://orcid.org/0000-0002-6897-1108); Email: [kchan@fysik.dtu.dk](mailto:kchan@fysik.dtu.dk)

**Brian Seger** – *SurfCat, Department of Physics, Technical University of Denmark, 2800 Kongens Lyngby, Denmark;* [orcid.org/0000-0002-0036-095X](https://orcid.org/0000-0002-0036-095X); Email: [brse@fysik.dtu.dk](mailto:brse@fysik.dtu.dk)

### Authors

**Sudarshan Vijay** – *CatTheory, Department of Physics, Technical University of Denmark, 2800 Kongens Lyngby, Denmark;* [orcid.org/0000-0001-8242-0161](https://orcid.org/0000-0001-8242-0161)

**Thomas V. Hogg** – *SurfCat, Department of Physics, Technical University of Denmark, 2800 Kongens Lyngby, Denmark*

**Johan Ehlers** – *SurfCat, Department of Physics, Technical University of Denmark, 2800 Kongens Lyngby, Denmark*

**Henrik H. Kristoffersen** – *CatTheory, Department of Physics, Technical University of Denmark, 2800 Kongens Lyngby, Denmark*

**Yu Katayama** – *Research Laboratory of Electronics, Massachusetts Institute of Technology, Cambridge, Massachusetts 02139, United States; Department of Applied Chemistry, Graduate School of Sciences and Technology for*



Innovation, Yamaguchi University, Tokiwadai, Ube 755-8611, Japan; [orcid.org/0000-0002-7842-2938](https://orcid.org/0000-0002-7842-2938)

**Yang Shao Horn** – Research Laboratory of Electronics, Massachusetts Institute of Technology, Cambridge, Massachusetts 02139, United States; Department of Mechanical Engineering and Department of Materials Science and Engineering, Massachusetts Institute of Technology, Cambridge, Massachusetts 02139, United States;

[orcid.org/0000-0001-8714-2121](https://orcid.org/0000-0001-8714-2121)

**Ib Chorkendorff** – SurfCat, Department of Physics, Technical University of Denmark, 2800 Kongens Lyngby, Denmark;

[orcid.org/0000-0003-2738-0325](https://orcid.org/0000-0003-2738-0325)

Complete contact information is available at:  
<https://pubs.acs.org/10.1021/acs.jpcc.1c04013>

## Notes

The authors declare no competing financial interest.

## ACKNOWLEDGMENTS

The authors would like to acknowledge funding from the European Union's Horizon 2020 research and innovation programme under grant agreement no. 85144 (SELECTCO2) and funding from the Villum Fonden through the VSUSTAIN project (9455). Y.K. would like to acknowledge financial support from the Japan Society for the Promotion of Science (JSPS) KAKENHI Grant-in-Aid for Early-Career Scientists (19K15360) and JSPS Open Partnership Joint Research Projects/Seminars (JPJSBP 120209925).

## REFERENCES

- (1) Lopez, N.; Janssens, T. V. W.; Clausen, B. S.; Xu, Y.; Mavrikakis, M.; Bligaard, T.; Nørskov, J. K. On the Origin of the Catalytic Activity of Gold Nanoparticles for Low-Temperature CO Oxidation. *J. Catal.* **2004**, *223*, 232–235.
- (2) Chen, Y.; Li, C. W.; Kanan, M. W. Aqueous CO<sub>2</sub> Reduction at Very Low Overpotential on Oxide-Derived Au Nanoparticles. *J. Am. Chem. Soc.* **2012**, *134*, 19969–19972.
- (3) Rodriguez, P.; Koper, M. T. M. Electrocatalysis on Gold. *Phys. Chem. Chem. Phys.* **2014**, *16*, 13583–13594.
- (4) Kwon, Y.; Lai, S. C. S.; Rodriguez, P.; Koper, M. T. M. Electrocatalytic Oxidation of Alcohols on Gold in Alkaline Media: Base or Gold Catalysis? *J. Am. Chem. Soc.* **2011**, *133*, 6914–6917.
- (5) Li, J.; Li, X.; Gunathunge, C. M.; Waegle, M. M. Hydrogen Bonding Steers the Product Selectivity of Electrocatalytic CO Reduction. *Proc. Natl. Acad. Sci. U.S.A.* **2019**, *116*, 9220.
- (6) Rodriguez, P.; Feliu, J. M.; Koper, M. T. M. Unusual Adsorption State of Carbon Monoxide on Single-Crystalline Gold Electrodes in Alkaline Media. *Electrochem. Commun.* **2009**, *11*, 1105–1108.
- (7) Duan, Z.; Henkelman, G. Calculations of the PH-Dependent Onset Potential for CO Electrooxidation on Au(111). *Langmuir* **2018**, *34*, 15268–15275.
- (8) Gauthier, J. A.; Ringe, S.; Dickens, C. F.; Garza, A. J.; Bell, A. T.; Head-Gordon, M.; Nørskov, J. K.; Chan, K. Challenges in Modeling Electrochemical Reaction Energetics with Polarizable Continuum Models. *ACS Catal.* **2019**, *9*, 920–931.
- (9) Ringe, S.; Clark, E. L.; Resasco, J.; Walton, A.; Seger, B.; Bell, A. T.; Chan, K. Understanding Cation Effects in Electrochemical CO<sub>2</sub> Reduction. *Energy Environ. Sci.* **2019**, *12*, 3001–3014.
- (10) Patel, A. M.; Ringe, S.; Siahrostami, S.; Bajdich, M.; Nørskov, J. K.; Kulkarni, A. R. Theoretical Approaches to Describing the Oxygen Reduction Reaction Activity of Single-Atom Catalysts. *J. Phys. Chem. C* **2018**, *122*, 29307–29318.
- (11) Kelly, S. R.; Kirk, C.; Chan, K.; Nørskov, J. K. Electric Field Effects in Oxygen Reduction Kinetics: Rationalizing PH Dependence

at the Pt(111), Au(111), and Au(100) Electrodes. *J. Phys. Chem. C* **2020**, *124*, 14581–14591.

(12) Vijay, S.; Kristoffersen, H. H.; Katayama, Y.; Shao-Horn, Y.; Chorkendorff, I.; Seger, B.; Chan, K. How to Extract Adsorption Energies, Adsorbate-adsorbate Interaction Parameters, and Saturation Coverages from Temperature Programmed Desorption Experiments. **2021**, ChemRxiv:10.26434/chemrxiv.14525496.

(13) Dunwell, M.; Lu, Q.; Heyes, J. M.; Rosen, J.; Chen, J. G.; Yan, Y.; Jiao, F.; Xu, B. The Central Role of Bicarbonate in the Electrochemical Reduction of Carbon Dioxide on Gold. *J. Am. Chem. Soc.* **2017**, *139*, 3774–3783.

(14) Miyake, H.; Ye, S.; Osawa, M. Electroless Deposition of Gold Thin Films on Silicon for Surface-Enhanced Infrared Spectroelectrochemistry. *Electrochem. Commun.* **2002**, *4*, 973–977.

(15) Sun, S.-G.; Cai, W.-B.; Wan, L.-J.; Osawa, M. Infrared Absorption Enhancement for CO Adsorbed on Au Films in Perchloric Acid Solutions and Effects of Surface Structure Studied by Cyclic Voltammetry, Scanning Tunneling Microscopy, and Surface-Enhanced IR Spectroscopy. *J. Phys. Chem. B* **1999**, *103*, 2460–2466.

(16) Wuttig, A.; Ryu, J.; Surendranath, Y. Electrolyte Competition Controls Surface Binding of CO Intermediates to CO<sub>2</sub> Reduction Catalysts. **2019**, ChemRxiv:10.26434/chemrxiv.7929038.

(17) Wuttig, A.; Yaguchi, M.; Motobayashi, K.; Osawa, M.; Surendranath, Y. Inhibited proton transfer enhances Au-catalyzed CO<sub>2</sub>-to-fuels selectivity. *Proc. Natl. Acad. Sci. U.S.A.* **2016**, *113*, E4585–E4593.

(18) Mezzavilla, S.; Horch, S.; Stephens, I. E. L.; Seger, B.; Chorkendorff, I. Structure Sensitivity in the Electrocatalytic Reduction of CO<sub>2</sub> with Gold Catalysts. *Angew. Chem.* **2019**, *131*, 3814–3818.

(19) Medford, A. J.; Wellendorff, J.; Vojvodic, A.; Studt, F.; Abild-Pedersen, F.; Jacobsen, K. W.; Bligaard, T.; Nørskov, J. K. Assessing the Reliability of Calculated Catalytic Ammonia Synthesis Rates. *Science* **2014**, *345*, 197–200.

(20) Shue, C.-H.; Ou Yang, L.-Y.; Yau, S.-L.; Itaya, K. In-Situ Scanning Tunneling Microscopy of Carbon Monoxide Adsorbed on Au(111) Electrode. *Langmuir* **2005**, *21*, 1942–1948.

(21) Heenen, H. H.; Gauthier, J. A.; Kristoffersen, H. H.; Ludwig, T.; Chan, K. Solvation at Metal/Water Interfaces: An *Ab Initio* Molecular Dynamics Benchmark of Common Computational Approaches. *J. Chem. Phys.* **2020**, *152*, 144703.

(22) Kristoffersen, H. H.; Chang, J. H. Effect of Competitive Adsorption at the Interface between Aqueous Electrolyte and Solid Electrode. *ACS Symp. Ser.* **2019**, *1331*, 225–238.

(23) Van Spronsen, M. A.; Weststrate, K.-J.; Den Dunnen, A.; Van Reijzen, M. E.; Hahn, C.; Juurlink, L. B. F. Hydrophilic Interaction between Low-Coordinated Au and Water: H<sub>2</sub>O/Au(310) Studied with TPD and XPS. *J. Phys. Chem. C* **2016**, *120*, 8693–8703.

(24) Resasco, J.; Chen, L. D.; Clark, E.; Tsai, C.; Hahn, C.; Jaramillo, T. F.; Chan, K.; Bell, A. T. Promoter Effects of Alkali Metal Cations on the Electrochemical Reduction of Carbon Dioxide. *J. Am. Chem. Soc.* **2017**, *139*, 11277–11287.

(25) Hori, Y.; Wakebe, H.; Tsukamoto, T.; Koga, O. Electrocatalytic Process of CO Selectivity in Electrochemical Reduction of CO<sub>2</sub> at Metal Electrodes in Aqueous Media. *Electrochim. Acta* **1994**, *39*, 1833–1839.

(26) Lopez, N.; Nørskov, J. K. Catalytic CO Oxidation by a Gold Nanoparticle: A Density Functional Study. *J. Am. Chem. Soc.* **2002**, *124*, 11262–11263.

(27) Kristoffersen, H. H.; Vegge, T.; Hansen, H. A. OH Formation and H<sub>2</sub> Adsorption at the Liquid Water-Pt(111) Interface. *Chem. Sci.* **2018**, *9*, 6912–6921.

(28) Reed, J. J.; Evans, W. H.; Parker, V. B.; Schumm, R. H.; Halow, I. Digitizing “The NBS Tables of Chemical Thermodynamic Properties: Selected Values for Inorganic and C1 and C2 Organic Substances in SI Units”. *J. Res. Natl. Inst. Stand. Technol.* **2020**, *125*, 1.

### 10.3 Paper 3

#### **Dipole-Field Interactions Determine the CO<sub>2</sub> Reduction Activity of 2D Fe-N-C Single-Atom Catalysts**

Sudarshan Vijay, Joseph A. Gauthier, Hendrik H. Heenen, Vanessa J. Bukas, Henrik H. Kristoffersen, and Karen Chan

Reprinted with permission from ACS Catal. **2020**, 10, 7826-7835. Copyright 2020 American Chemical Society

# Dipole-Field Interactions Determine the CO<sub>2</sub> Reduction Activity of 2D Fe–N–C Single-Atom Catalysts

Sudarshan Vijay, Joseph A. Gauthier, Hendrik H. Heenen, Vanessa J. Bukas, Henrik H. Kristoffersen, and Karen Chan\*



Cite This: *ACS Catal.* 2020, 10, 7826–7835



Read Online

ACCESS |



Metrics & More



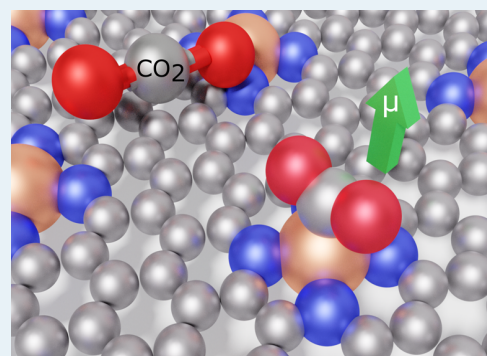
Article Recommendations



Supporting Information

**ABSTRACT:** Iron–nitrogen-doped graphene (FeNC) has emerged as an exciting earth-abundant catalyst for electrochemical CO<sub>2</sub> reduction (CO<sub>2</sub>R). However, standard theoretical approaches based on density functional theory (DFT) suggest complete poisoning of the active sites and are unable to rationalize the experimentally observed dramatic pH dependence and Tafel slopes, which have a critical impact on the electrocatalytic activity. In this work, we overcome these challenges through a rigorous theoretical investigation of FeNC single-atom catalysts using a combination of several state-of-the-art methods: hybrid functionals, continuum solvation, and potential-dependent electrochemical reaction energetics. Our model shows dipole-field interactions in CO<sub>2</sub> adsorption to determine the overall activity, which resolves the contentious origin of experimentally observed pH dependence and rationalizes differences in activity and Tafel slopes among different samples in experimental work. A critical conclusion of our study is that single-atom catalysts can be tuned for electrocatalytic activity not only through the traditionally considered binding energies but also through the corresponding surface dipole moment of rate-determining surface intermediates. Our presented methodology paves the way for accurate mechanistic studies as well as the computational catalyst design of general single-atom catalysts.

**KEYWORDS:** electrocatalysis, FeNC, single-atom catalysts, CO<sub>2</sub> reduction, dipole



## INTRODUCTION

The electrochemical reduction of CO<sub>2</sub> is a promising approach to store the energy from intermittent renewable sources such as wind and solar in the form of valuable fuels and chemicals.<sup>1,2</sup> From the catalysis perspective, the primary barriers to commercialization are activity, selectivity, stability, and cost.<sup>1,3</sup> To date, the most active and selective transition metal catalyst for CO<sub>2</sub> reduction (CO<sub>2</sub>R) to CO is Au, which shows current densities up to 10 mA/cm<sup>2</sup> at −0.4 V vs reversible hydrogen electrode (RHE) with nearly 100% Faradaic efficiency in two-compartment cell configurations.<sup>4</sup> Single-atom catalysts, which consist of earth-abundant elements such as Fe, Co, and Ni doped on a support material such as graphene, have emerged as promising alternatives to Au.<sup>5–7</sup> Very recently, FeNC catalysts, fabricated through pyrolysis on defected graphene and characterized within a gas-diffusion electrode, showed an impressive geometric current density of 100 mA/cm<sup>2</sup> with Faradaic efficiency toward CO greater than 90% at −0.4 V vs RHE. This high activity was suggested to arise from tailored Fe sites with a +3 oxidation state.<sup>8</sup>

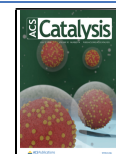
From the theoretical perspective, the mechanistic study of metal–nitrogen–carbon (M–N–C) single-atom catalysts presents several critical challenges. The graphene support is

highly defected, which gives rise to a plethora of possible active site configurations with varying coordination to N and C, with functionalization shown to be beneficial to activity.<sup>9</sup> Additionally, the impact of the electrolyte and the charging of the electric double layer in modeling the CO<sub>2</sub>R activity are unclear for M–N–C but have been demonstrated to be critical on transition metals in recent studies,<sup>10</sup> which echo thermal catalytic studies on the promoting effects of dipole-field interactions.<sup>11</sup> While computational studies of model systems such as molecular porphyrin systems have included effects such as solvation and Hubbard-U corrections,<sup>12–14</sup> studies using extended systems of M–N–C catalysts have generally omitted solvation and were restricted to charge-neutral thermodynamic approximations, which do not consider these phenomena. Reported adsorption energies for CO on a variety of different sites range from −0.6 to −1.2 eV.<sup>15–17</sup> Such large negative adsorption energies suggest CO would poison the surface with

Received: March 24, 2020

Revised: June 5, 2020

Published: June 5, 2020



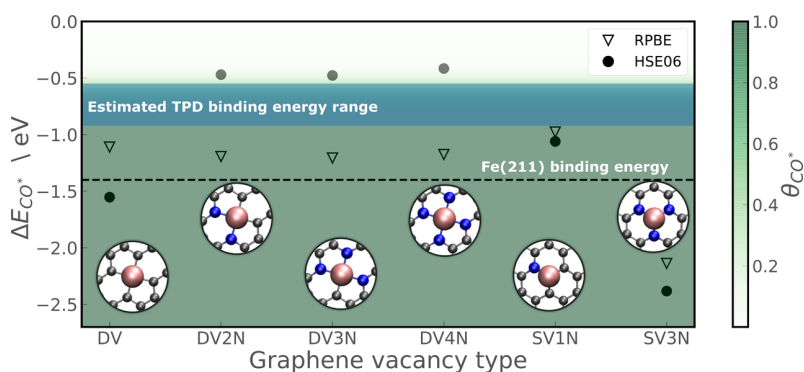


**Figure 1.** Comparison of adsorption energies of CO on iron-doped vacancies as proposed in ref 20. Calculated with the GGA-RPBE functional (triangles) and the hybrid HSE06 functional (circles). Experimental estimate from TPD spectra<sup>22</sup> is marked by the blue band. The background fill indicates the coverage of CO predicted by the kinetic model using RPBE energetics. Fe(211) binding energies are shown with the dashed black line as a reference.

negligible CO production rates, contrary to experimental findings. As a result, the active site of these materials remains a contentious issue. Furthermore, such computational models have been unable to explain why the electrolyte pH has no impact on the CO<sub>2</sub>R activity of FeNC catalysts on a standard hydrogen electrode (SHE) scale.<sup>18</sup> This has been suggested to be evidence of diabatic electron transfer to CO<sub>2</sub>, or a so-called “decoupled” proton–electron transfer that cannot be treated using a standard computational hydrogen electrode approach.<sup>18</sup>

In this work, we overcome the aforementioned challenges through a rigorous theoretical investigation of FeNC single-atom catalysts using a combination of several state-of-the-art methods: hybrid functionals, implicit electrolyte, potential-dependent reaction energetics,<sup>19</sup> and mean-field kinetic modeling. Through combination of hybrid calculations, analysis of temperature-programmed desorption (TPD) spectra, as well as microkinetic modeling, we show that standard generalized gradient approximation (GGA) functionals are inadequate to accurately describe the binding energies of essential intermediates. We furthermore show that reasonably accurate energetics can be obtained with GGA functionals by including a Hubbard-U correction, which circumvents the need for costly hybrid-level simulations. Through explicit consideration of the interaction between the interfacial electric field with dipolar adsorbates, we show the experimentally observed pH independence arises from a *field-dependent* CO<sub>2</sub> adsorption. Our results suggest double-vacancy four-nitrogen-doped (DV4N) vacancies to be generally more active than a two-nitrogen-doped vacancy (DV2N) site motif, and the associated simulated Tafel slopes are in line with experimental observations. A critical conclusion is that single-atom catalysts should be designed not only for optimal binding energies but also for their surface dipole moments. This may be achieved, for example, by doping with other p-block elements. These findings are critical from the perspective of fundamental mechanistic understanding and pave the way toward computation-guided design of general single-atom catalysts.

## RESULTS AND DISCUSSION

**Comparing Binding Energies of CO\*.** Given the aforementioned controversy surrounding the binding energies of CO\* and other intermediates, we first compare the energies of typical GGA-level simulations of CO binding on FeN<sub>x</sub> sites

against hybrid functionals. We consider both spin-polarized RPBE and HSE06 functionals, which are prototypes for GGA-DFT and hybrid-DFT, respectively. Figure 1 shows the computed binding energy of CO on possible active sites that were identified as most stable in ref 20. Redhead analysis of TPD spectra<sup>21</sup> was also used to ascertain a plausible range of energies based on reasonable prefactors, shown in further detail in the Supporting Information (SI) Note 2. Since it is likely that an ensemble of active sites bind CO, we include the entire spectra (as opposed to only considering the peak) in the estimation of the experimental binding energy, which results in a 0.4 eV range of estimated adsorption energies, as illustrated by the blue band.

A kinetic model consisting of just thermodynamic quantities was constructed based on RPBE energetics and an assumed mechanism (see SI Note 1). Coverages of CO from this model are used to detect whether the predicted energy leads to CO poisoning the surface. In the case of RPBE, all sites considered are covered by CO. This is consistent with previous reports on these materials.<sup>5,16</sup> However, in the case of HSE06 results, sites corresponding to a single vacancy doped with nitrogen atoms (SV1N, SV3N) and undoped double vacancies (DV) bind CO very strongly and are expected to be poisoned under CO<sub>2</sub> reducing conditions. Therefore, sites that can bind CO\* weakly enough to be able to produce CO are DV2N, DV3N, and DV4N (double vacancies doped with two, three, and four nitrogen atoms, respectively). Ref 20 indicates that DV2N and DV4N have formation energies of greater than −7 eV with respect to graphene. Due to the noted activity and stability, we examine DV2N and DV4N as model systems in the remainder of the work. However, different experimental synthesis methods have different vacancy types on the surface. Thus, it is possible that several active sites, apart from the ones considered in this work, might contribute to CO<sub>2</sub>R activity. We note that there is no need for additional gas-phase corrections to the CO(g) reference used in Figure 1, as the reaction CO<sub>2</sub> + H<sub>2</sub> → CO + H<sub>2</sub>O is well described by HSE06 (see SI Note 14). Further, the effect of using a dispersion correction is discussed in SI Note 3.

While hybrid functional calculations provide the needed accuracy for these systems, they are prohibitively expensive for computational screening studies. We find that we can mitigate the GGA error by adding a Hubbard-U<sup>23,24</sup> correction to the RPBE functional, which gives rise to essentially no additional computational cost relative to standard GGA calculations. The



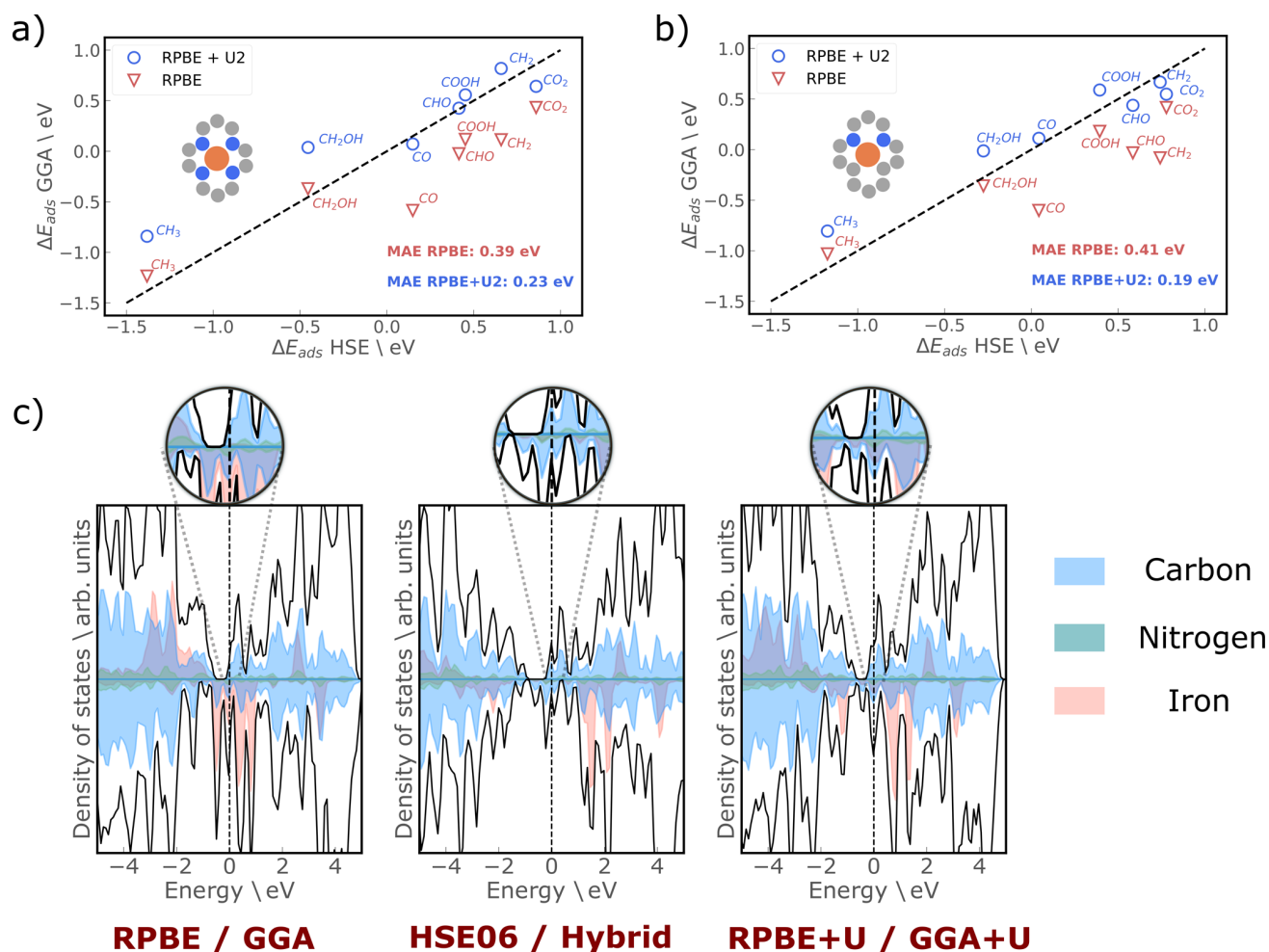


**Figure 2.** Comparison of RPBE and RPBE+U adsorption energies for relevant CO<sub>2</sub>R intermediates for (a) DV4N and (b) DV2N. Insets show the corresponding structures and mean absolute errors for both functionals. (c) Projected density of states (DOS) of DV2N structure with three functionals: RPBE, HSE06, and RPBE+U with  $U = 2$  eV; color scheme: blue: carbon, green: nitrogen, orange: iron, black: total DOS, States near the Fermi level have been magnified for clarity. Horizontal line divides spin up and spin down states.

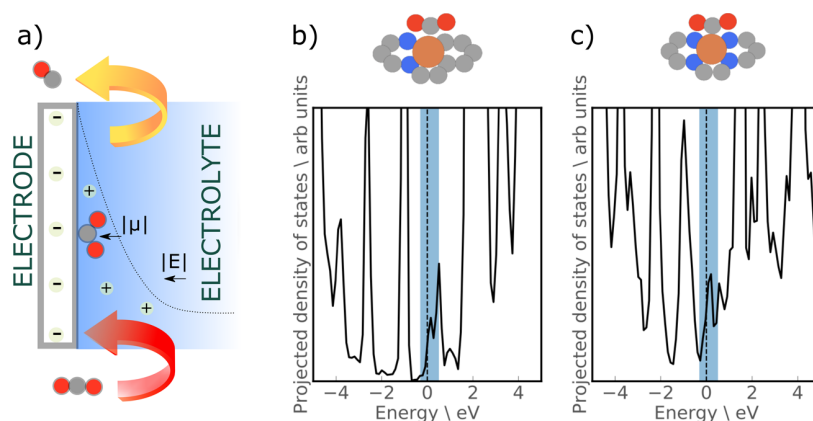


**Figure 3.** (a) Dipole-field stabilization model of CO<sub>2</sub> adsorbed on FeNC electrode. The dashed line is a schematic of the electrostatic potential profile from near the electrode surface to the bulk of the solvent density of states projected onto the s and p orbitals of the CO<sub>2</sub> molecule at the adsorption transition state for (b) DV4N and (c) DV2N vacancies at  $-0.5$  V vs SHE using the HSE06 functional based on transition states obtained from RPBE+U. The DOS was obtained by varying the surface charge and converting to potential using eq 2.

Hubbard-U value was varied systematically until the adsorption energies of CO on selected graphene vacancies are close to the value obtained using HSE06 (see SI Note 5). Figure 2(a,b)

shows the comparison between RPBE and RPBE+U against HSE06 binding energies. Adding a Hubbard- $U^{23}$  of 2eV to the d-states of Fe leads to a much better description of binding

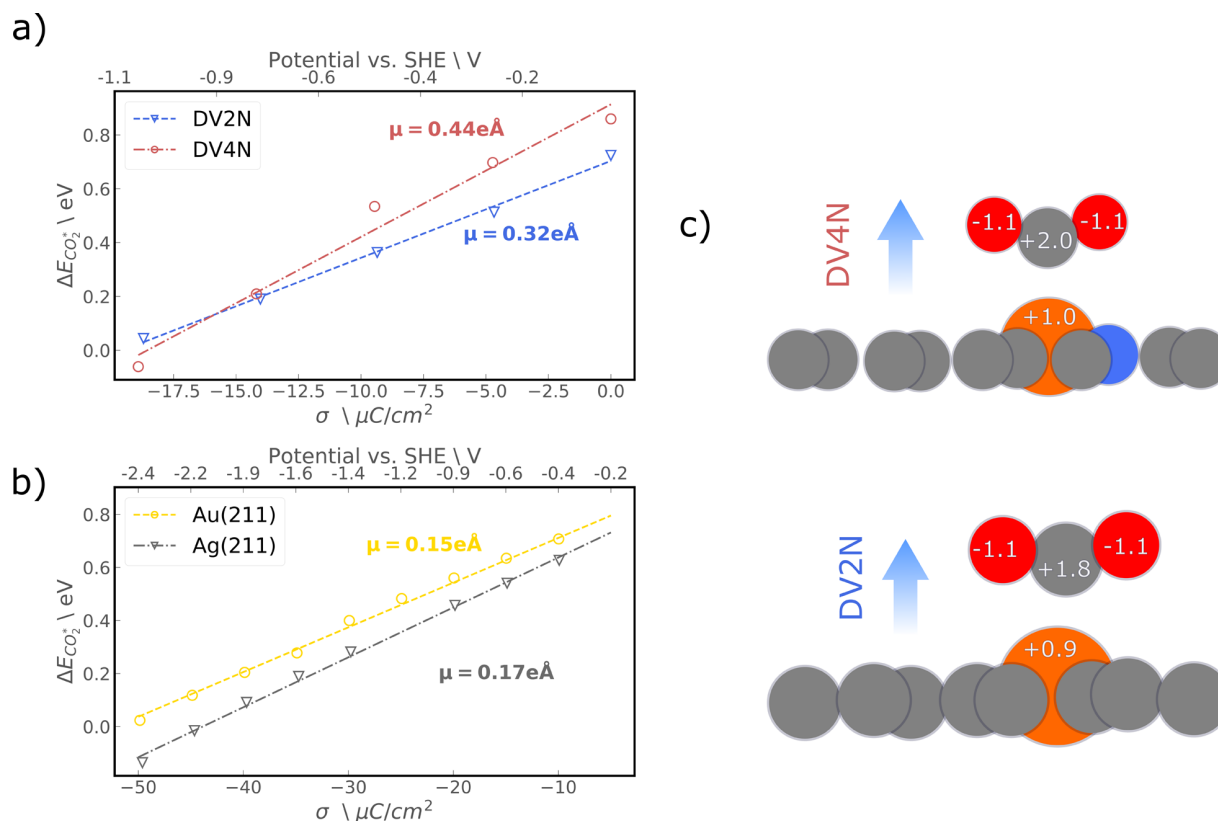


**Figure 4.** Change in adsorption energy of  $\text{CO}_2$  as a function of surface-charge density ( $\sigma$ ) for (a) doped vacancies DV2N ( $\Delta E = 0.036\sigma + 0.70$ , with  $R^2 = 0.99$ ) and DV4N ( $\Delta E = 0.04926\sigma + 0.91$ , with  $R^2 = 0.97$ ) as well as (b) Au(211) ( $\Delta E = 0.0168\sigma + 0.88$ , with  $R^2 = 0.99$ ) and Ag(211) ( $\Delta E = 0.0188\sigma + 0.83$ , with  $R^2 = 0.99$ ). The surface charge is defined as the number of excess electrons per unit area. (c) Calculated Bader charge for both DV4N (top) and DV2N (bottom) vacancies. Values annotated over atoms show the Bader charge. Negative values of charge densities indicate electrode reduction. Points in (a,b) denote the results from DFT calculations, while lines represent the corresponding best fit lines. Any scatter of points associated with (a,b) arises from the change in geometry following a relaxation at each discrete surface charge.

energies for intermediates such as CO and  $\text{CH}_2$  for both DV2N and DV4N vacancies. Mean absolute errors (MAE) as compared to HSE06 binding energies decrease from 0.4 to 0.2 eV.

Both the carefully chosen Hubbard-U and HSE06 mitigate self-interaction error and open an energy gap between d-states of Fe, as illustrated in Figure 2c. In the case of RPBE, the self-interaction error leads to d-states at the Fermi level. The relative energy of the narrow d-states has implications not only for binding energies but also for determining energetics as a function of potential. In the case of DV2N and DV4N vacancies, the potential dependence determined by the HSE06 calculations (dipole moments shown in SI Figure S14) is also captured by the current choice of Hubbard-U. However, we emphasize that this parameter holds only for the FeNC (see SI Note 5 for a detailed sensitivity analysis of different Hubbard-U values), and careful parametrization to experiment or higher levels of theory may be needed for other systems. Moreover, since potential dependencies can be sensitive to states around the Fermi level, HSE06 energies are used to describe potential-dependent energetics.

**Field-Driven  $\text{CO}_2$  Adsorption.** Recent experimental literature has shown that the partial current density to CO is invariant with pH on an SHE voltage scale in acidic media.<sup>18</sup> This effect has been associated with protons *not* being involved in the potential-limiting step, similar to other nonmetallic carbon catalysts.<sup>25,26</sup> For this particular system, this has led to

the rate-limiting step being assigned as the electron transfer to  $\text{CO}_2$ <sup>16,18</sup>



Since this step does not involve proton transfer, it would satisfy the experimentally observed independence of rate on pH. However, the width of adsorbate-induced states at the Fermi level of the transition state of  $\text{CO}_2$  adsorption on the electrode at potentials of interest precludes rate-limiting electron transfer from metal to the bent  $\text{CO}_2$  molecule. Figure 3(b,c) shows the s and p bands of  $\text{CO}_2$  at the transition state for  $\text{CO}_2$  adsorbing at the DV4N and DV2N vacancy structures. As the  $\text{CO}_2$  molecule approaches the surface, the adsorbate-induced molecular states broaden due to hybridization with the metal continuum of electronic states around the Fermi level. This broadening implies that the electron is delocalized between the bands of the metal and the  $\text{CO}_2$  molecule. We can estimate a time scale for electron transfer ( $\Delta t$ ) using the uncertainty relationship  $\Delta E \Delta t \geq \frac{\hbar}{2}$ .  $\Delta E$  is given by the width of adsorbate density of states ( $n_a$ ) at the Fermi level using Fermi's golden rule, which gives the rate of electron transfer as  $\frac{2\pi}{\hbar} n_a$ .<sup>27,28</sup> For this system, the width is about 0.8 eV (shaded in Figure 3) for both vacancies, which would correspond to a rate of  $10^{15} \text{ s}^{-1}$  and, hence, an electron lifetime of about  $10^{-15} \text{ s}$ . Since the motion of atoms occur on a time scale of

picoseconds, electron transfer is facile in comparison to the adsorption of CO<sub>2</sub>.

Our analysis suggests that the rate-limiting step is not so much a slow electron transfer to \*CO<sub>2</sub><sup>-</sup> but a field-stabilized CO<sub>2</sub> adsorption (cf., Figure 3a, showing electrostatic interaction between a dipolar, bent \*CO<sub>2</sub> adsorbate and the electric field at the electrochemical interface). Since the interfacial field depends on the absolute potential, this step also shows an absolute potential dependence, i.e., the corresponding rate depends on an SHE, not RHE scale. The schematic shown in Figure 3a illustrates this by showing the dipole for bent CO<sub>2</sub> adsorbed on the surface and its interaction with the electrical double layer.

In the past few years, hybrid continuum/*ab initio* models of the electrochemical interface<sup>29–32</sup> have been developed to capture the impact of double layer charging on reaction energetics. We have recently shown the surface-charge density to be the most appropriate descriptor for the electrostatic effects of the double layer on reaction energetics,<sup>19</sup> since it describes the variations of the interfacial field *local* to the reaction site. We relate surface-charge  $\sigma$ -dependent energetics (Figure 4(a,b)) to potential-dependent energetics through the interfacial capacitance  $C$  and potential of zero charge  $\phi_{pzc}$  as follows

$$\phi = \frac{1}{C}\sigma + \phi_{pzc} \quad (2)$$

Both quantities can, in principle, be determined from experiment.

The energy of a given adsorbate ( $E$ ) is a function of its dipole moment  $\mu$  and polarizability  $\alpha$  as follows

$$E = E_0 + \mu|\vec{E}| - \frac{\alpha|\vec{E}|^2}{2} \quad (3)$$

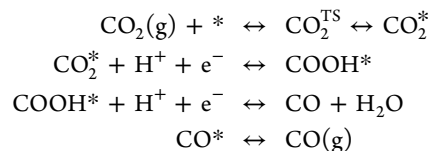
where  $E_0$  is the energy of the zero charge state, and  $|\vec{E}|$  is the interfacial electric field.  $\sigma$  and  $|\vec{E}|$  can be related by Gauss' law. Assuming a constant interfacial dipole, the dipole moment for a given adsorbate is given by

$$\mu = \epsilon A(\Phi_0^{\text{FS}} - \Phi_0^{\text{IS}}) \quad (4)$$

where  $\Phi_0^{\text{IS}}$  is the measured work function of the initial states,  $\Phi_0^{\text{FS}}$  is that of the final state, and  $A$  is the surface area. Figure 4 shows a linear relationship between  $\Delta E_{\text{CO}_2}$  and  $\sigma$ . This dependence indicates that  $\alpha$  is negligible for reasonably small values of  $\sigma$ . We determine the dipole moment as  $\epsilon_0 \frac{dE}{d\sigma}$ , where  $\epsilon_0$  is the absolute permittivity, and  $\frac{dE}{d\sigma}$  is the slope of the lines shown in Figure 4.

For DV4N, the effect of the dipole moment of CO<sub>2</sub> is higher than in the case of DV2N (Figure 4a), and hence, the energy drop with potential is steeper. As compared with transition metal catalysts such as gold and silver shown in Figure 4b, dipole moments of key reaction intermediates are significantly larger for these FeNC systems. While CO<sub>2</sub> dipoles on gold and silver step surfaces are below 0.2 eÅ, dipoles on both graphene vacancies are larger than 0.4 eÅ. A larger dipole implies a stronger stabilization from its interaction with the interfacial electric field<sup>33</sup> and could imply a larger symmetry factor for the reaction.<sup>34</sup> The impact of the dipole moment on the resulting kinetics of the CO<sub>2</sub>R are detailed in the next section.

**Microkinetic Model.** Based on the field-dependent energies calculated above, we develop a mean-field microkinetic model to determine the potential-dependent rate of CO production from CO<sub>2</sub>. The reaction steps considered are



pH-dependent kinetic measurements strongly suggest that proton–electron transfer is not involved in the rate-limiting step.<sup>8,18</sup> The rate for the competing hydrogen evolution reaction (HER) shows a marked pH dependence on an SHE scale under acidic to neutral pH. This pH dependence indicates that a proton–electron transfer step limits the rate and that hydronium ions are active as proton donors, since H<sub>2</sub>O as proton donors show no pH dependence.<sup>35</sup> In contrast to HER, CO production at the same range of pH is pH-independent of an SHE scale. Thus, the rate-limiting step for the CO<sub>2</sub>R reaction does not involve a hydronium ion nor an associated proton–electron transfers.

The experimental observations are consistent with the computed free energy diagram, shown in Figure 5 on both

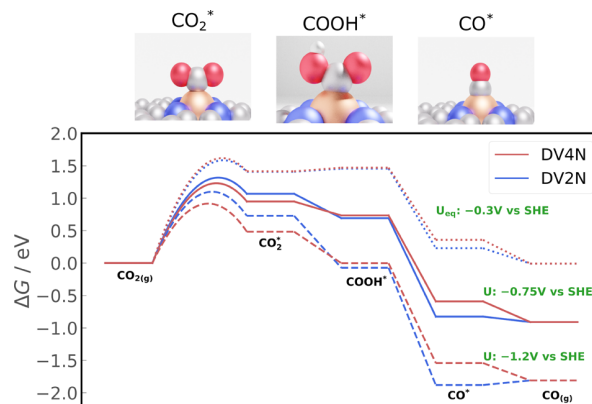


**Figure 5.** Free energy diagram at the theoretical equilibrium potential  $U_{\text{eq}} = -0.3$  V and at two other potentials:  $-0.75$  and  $-1.2$  V vs SHE for DV4N and DV2N vacancies at a pH of 2.

DV4N and DV2N vacancies. The \*CO<sub>2</sub> state, under relevant potentials, is the highest in energy, and the steps to the subsequent intermediates, \*COOH and \*CO, are all exergonic. From previous work, we found proton–electron transfers toward oxygen species to be generally facile,<sup>36</sup> and so, we assume no additional barrier for \*COOH formation. \*COOH to \*CO involves breaking a C–O bond and can sometimes be rate-limiting, especially at low overpotentials.<sup>37,38</sup> However, in this particular case, given the exergonicity of the step, even an extremely high hypothetical intrinsic barrier of 1.5 eV does not make it rate-limiting at the cathodic potentials considered (see SI Note 13 for further description). For the rest of this work, we therefore assume the reaction energetics are barrierless after CO<sub>2</sub> adsorption.

Figure 6 shows a comparison of experimental<sup>8,18</sup> and theoretical relative turnover frequencies (TOFs) (normalized to those at  $-0.6$  V vs SHE). Experimental activity data were taken from refs 18 and 8. In the former, the activity was measured at a range of acidic pH values from 1 to 7.25, while

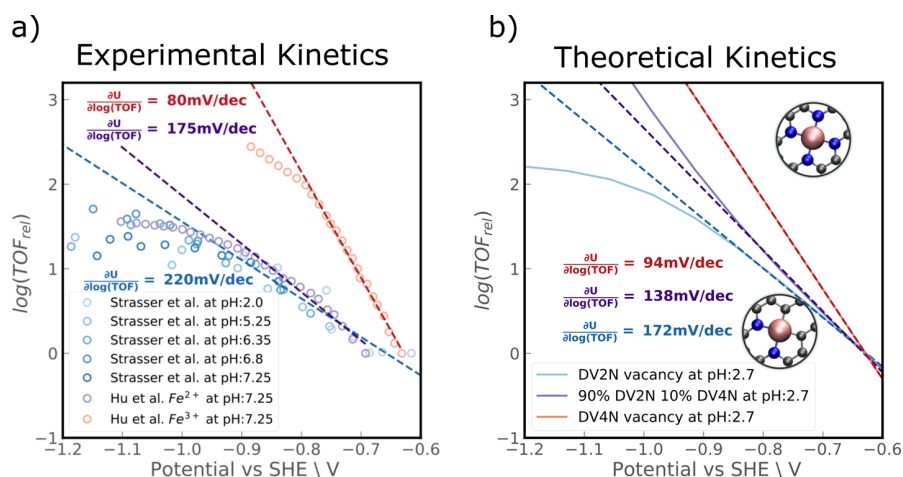


**Figure 6.** (a) TOF taken from two publications: Strasser et al.<sup>18</sup> and Hu et al.<sup>8</sup> Current densities were converted to TOF by assuming all iron sites were involved in catalytic activity. (b) TOF obtained from mean-field microkinetic modeling; TOFs are normalized to the activity at  $-0.6$  V vs SHE, to emphasize relative trends.

in the latter, the activity was measured at a fixed pH of 7.25 using FeNC fabricated by using either pyridinic or pyrrolic precursors. It was previously shown that the chemical identity of the N-doped vacancy can be varied based on the choice of precursor.<sup>39</sup> On the basis of *operando* XAS measurements, the more active catalyst was suggested to have an Fe  $3^+$  oxidation state, and the less active one was suggested to have an oxidation state of Fe  $2^+$ . The experimental TOFs were calculated by assuming all Fe sites are single-atom catalysts that are present on the surface and contribute to production of CO from  $\text{CO}_2$ .

Since  $\text{CO}_2$  adsorption is the rate-limiting step, the Tafel slope corresponding to activity from a given site is determined by the corresponding adsorbate dipole as follows<sup>38</sup>

$$\begin{aligned} \text{Tafel slope}^{-1} &= \frac{\partial \log(\text{TOF})}{\partial \Phi} \\ &= \frac{\partial \log(\text{TOF})}{\partial \Delta G_{\text{CO}_2}} \frac{d \Delta G_{\text{CO}_2}}{d \Phi} \\ &= -\frac{1}{k_B T} \frac{d \Delta G_{\text{CO}_2}}{d \sigma} \frac{d \sigma}{d \Phi} \\ &= -\frac{1}{k_B T} \frac{d \Delta G_{\text{CO}_2}}{d \sigma} C \\ &= \frac{1}{k_B T} \frac{C}{\epsilon} \mu \end{aligned} \quad (5)$$

where  $\epsilon$  is the permittivity of free space,  $\Delta G_{\text{CO}_2}$  is the free energy of  $\text{CO}_2$  adsorption, and the TOF was written as  $\exp\left(\frac{-\Delta G_{\text{CO}_2}}{k_B T}\right)$ . Thus, the Tafel slope depends solely on the rate of change of free energy as a function of the interfacial electric field.

As previously mentioned,  $\text{CO}_2^*$  at DV4N has a larger dipole moment as compared to that at DV2N. This is consistent with the lower Tafel slope obtained in the case of DV4N over DV2N as shown in Figure 6. Since pyrolysis is the experimental method of choice to generate these catalysts, it is not yet possible to obtain atomic precision over the active site. To show how the slope shifts when multiple sites are

contributing to the activity, we show the case of 10% DV4N and 90% DV2N sites, which gives an intermediate Tafel slope.

These Tafel slopes are in line with experimentally observed ones. Hu et al.<sup>8</sup> observed Tafel slopes of 80 mV/dec for the more active sample and 126 mV/dec for the less active sample. This difference is captured in our simple two-site model, with DV4N being significantly more active than DV2N. Strasser et al. also observed Tafel slopes of close to 200 mV/dec, which is similar to that obtained for DV2N. These results suggest that increasing the  $\mu$  of active sites through, for example, the coordination environment and metal atom identity could lead to lowering of Tafel slopes and more efficient catalysts.

It is important to note that we consider here *relative*, rather than *absolute*, reaction rates due to the inherent uncertainties in quantifying TOFs from both experiment and theory. Uncertainties in the experimental determination of absolute TOFs for example lie in the assumption that all Fe atoms loaded onto the sample are catalytically active while also presuming the same distribution of active Fe sites in samples that were prepared via different synthesis methods.<sup>8,18</sup> On the other hand, theoretical DFT calculations using GGA and hybrid functionals are known to suffer from systematic errors in describing O–C–O backbone structures.<sup>40–42</sup> This error is believed to mainly affect the gas-phase reference leading to a constant energy offset. Ultimately, this constant energy shift yields unrealistically high reaction energies and barriers for adsorbing  $\text{CO}_2(\text{g})$  (such as the 1 eV barrier shown in Figure 5) and an uncertainty of 5 to 7 orders of magnitude in the resulting absolute TOFs. While recent studies mitigate this issue by adding 0.30–0.45 eV corrections to gas-phase  $\text{CO}_2$  energies,<sup>40,41</sup> we choose here to focus only on *relative* TOFs. This allows for circumventing the application of empirical corrections to the computed DFT energetics, and our results are directly comparable to experimental data that have been normalized in the same way in Figure 6. Most importantly, we note that all (experiment and theoretical) uncertainties in absolute TOF values do not affect the main conclusion of this study, which focuses on the unique ability of single-site catalysts to tune  $^*\text{CO}_2$  dipoles and hence significantly change the predicted Tafel slopes (which are invariant to whether absolute or relative TOFs are considered). For reasons of completeness, we nevertheless include both absolute and



relative TOF values as a function of applied potential in the SI. We also note that solvation energies are critical to accurate prediction of onset potential and reaction kinetics.<sup>14</sup> By referring to *relative* rather than *absolute* rates, however, we effectively cancel out any systematic errors associated with implicit solvation for a given surface species.

Another point of difference between the vacancies is that CO desorption becomes rate-limiting for DV2N at large potentials, while CO<sub>2</sub> adsorption stays rate-limiting throughout the explored potential range for DV4N. The shift in rate-limiting step is shown in a degree of rate control (sensitivity) analysis,<sup>43</sup> coverage of CO, and change in Tafel slope. A degree of rate control analysis was carried out as follows.

$$\text{DRC} = \frac{d(\log(\text{TOF}))}{dG_i} \quad (6)$$

where  $G_i$  is the free energy of each intermediate. SI Figure S8 shows that at very reducing potentials, the rate is largely influenced by CO binding free energies. The rate would be increased by decreased CO<sub>2</sub> transition-state energies over the whole potential range. Corresponding coverage plots for DV2N are shown in SI Figure S7. The increase in CO coverage corresponds to the change in Tafel slope seen in Figure 6.

We also consider the pathway to CH<sub>4</sub>, which is a minor product formed on these materials. For potential ranges where coverages of CO would be very small, there would be little to no CH<sub>4</sub> production. However, once the coverage of CO becomes substantial, the Faradaic efficiency of CH<sub>4</sub> as compared to CO would increase. For a possible reaction pathway, intermediate binding energies as a function of surface charge were calculated. SI Figure S10 shows the TOF obtained from the model as well as those from Strasser et al.<sup>18</sup> CH<sub>4</sub> production in both cases is pH-dependent, indicating that a proton–electron transfer step would be rate-limiting for electrochemical reduction of CO to CH<sub>4</sub>. Since these are based on thermodynamic variations in energy alone, we focus here on the qualitative pH dependence.

The above microkinetic analysis, in summary, shows the following: (1) Tafel slopes can be tuned by appropriately designing sites that induce large dipole moments in adsorbates and (2) consideration of the effects of pH as well as potential and electric field in simulations are essential to an accurate mechanistic description of CO<sub>2</sub>R on FeNC catalysts.

## CONCLUSIONS

In this work, we presented an *ab initio* investigation of the activity of Fe–N–C catalysts for CO<sub>2</sub> reduction. We showed that a combination of state-of-the-art methods, hybrid functionals, an implicit electrolyte, and potential-dependent electrochemical reaction energetics are all required for a rigorous mechanistic analysis. We find that the rate-limiting step on these materials is generally a field-driven CO<sub>2</sub> adsorption step, which gives rise to the dramatic pH independence that is observed experimentally. This physical explanation appears to be in accordance with the latest experimental studies. We find that the activity is highly dependent on the configuration of the active site, with significant differences in the Tafel slope between DV2N and DV4N sites. Using this Tafel slope, we postulate that the DV4N site corresponds to those observed in a recently reported, highly active FeNC catalyst, assigned an oxidation

state of +3 from XPS studies. The present study provides a rigorous basis for the study of single-atom catalysts for CO<sub>2</sub>R and beyond, from both the fundamental and catalyst development perspectives.

## METHODS

Density functional theory calculations were carried out using the Vienna Ab initio Software Package (VASP).<sup>44</sup> Implicit solvation and counter charge was added to calculations by using VASPsol.<sup>45</sup> Core electrons were described using projector augmented wave (PAW) potentials.<sup>46</sup> Valence electrons were described by plane waves with kinetic energy up to 500 eV. Gaussian smearing with a width of 0.1 eV is used. The RPBE<sup>47</sup> functional was used for GGA-DFT calculations, while the HSE06<sup>48,49</sup> functional was used for hybrid calculations. Single-point energies with the HSE06 functional on RPBE+U geometries are reported throughout the text. The validity of this approximation is reported in SI Note 4. Hubbard-U corrections were added to the d orbitals of iron using the implementation of Dudarev.<sup>23</sup>

Single-layer 3 × 3 graphene was used as a model system.<sup>50</sup> Structures were prepared using the Atomic Simulation Environment.<sup>51</sup> The lattice for undoped graphene was optimized using a 12 × 12 × 1 Monkhorst–Pack<sup>52</sup> *k*-point mesh. The 3 × 3 single-layer graphene structures were made with the obtained lattice parameter. All structures were then treated with a 4 × 4 × 1 Monkhorst–Pack<sup>52</sup> *k*-point mesh with at least 16 Å of vacuum. Depending on the vacancy type, carbon atoms in the graphene structure were replaced by nitrogen and iron atoms. The structure obtained after creating vacancies and doping was subjected to an optimization of both position and lattice constants (VASP<sup>44</sup> keyword *ISIF* = 3) before adding an adsorbate to the unit cell. All geometries are optimized until forces are less than 0.025 eV Å<sup>-1</sup>. Transition-state geometries and energies were obtained by using the climbing image nudged elastic band (CI-NEB)<sup>53</sup> implemented within VASP. Forces on the climbing image were considered as converged if they are lower than 0.05 eV Å<sup>-1</sup>. The density of states for transition states were obtained by carrying out a single-point with HSE06 at the image associated with the transition state with an 8 × 8 × 1 *k*-point mesh and Gaussian smearing of 0.1 eV.

VASPsol<sup>45</sup> places a continuum charge distribution in the vacuum region of the cell with a charge density of an opposite sign to the excess or deficient charge on the surface. A Debye screening length of 3 Å was chosen, as this corresponds to a bulk ion concentration of 1 M. Similar to recent published work,<sup>29</sup> the nonelectrostatic parameter *TAU* was set to zero to avoid numerical instabilities. The continuum charge was varied from 0 to 1e in increments of 0.25e.

The computational hydrogen electrode (CHE)<sup>54</sup> was used to determine reaction energies as a function of potential for reactions with an electron in the reactant or product. The chemical potential of the proton and electron is related to that of H<sub>2</sub> at 0 V vs RHE.

$$\mu_{\text{H}^+} + \mu_{\text{e}^-} = \frac{1}{2}\mu_{\text{H}_2(\text{g})} \quad (7)$$

Field effects for all adsorbates were included in the model by assuming a linear dependence of binding energies with the surface charge.

$$\Delta E_{\sigma} = a_0 + a_1\sigma \quad (8)$$

We note that this linear variation of energy with  $\sigma$  is valid only for small additions of electrons in the unit cell. At large surface charges, second order terms would need to be taken into account. However, 4(a,b) both show good fits to lines ( $R^2$  values in the caption), which suggests the second order terms are negligible.

We calculated the adsorption energies and projected DOS for relevant intermediates and transition states of all intermediates as a function of the excess charge, applied by varying the number of electrons in the simulation cell. The same charging scheme was applied along the entire reaction pathway. We assume that our finite cell size simulations approximate those from an infinitely large cell where both the surface-charge density and work function approach a constant value along the reaction pathway. This assumption was validated through a convergence test (Figure S16), which shows negligible change in the calculated dipole moment between cell sizes of  $4 \times 4$  to  $5 \times 5$ . We relate the energetics as a function of charge to those at a function of potential with eq 2, where we have applied experimental pzcs and capacitances. Reliable estimates of the pzc cannot be obtained for single-layer 2D materials with an implicit solvent setup, because symmetric unit cells cannot be constructed. Thus, we used an experimental value of the pzc.

The capacitance of pristine graphene  $21 \mu\text{F}/\text{cm}^{255}$  and the experimental pzc<sup>56</sup> of  $-0.07 \text{ V}$  was used. While the work functions of DV4N and DV2N vacancies are different ( $\Phi_{\text{DV2N}} = 3.95 \text{ V}$  and  $\Phi_{\text{DV4N}} = 3.74 \text{ V}$ ), we approximate both vacancies to have the same potential of zero charge. This is because the doping concentrations in experiment are between 2 and 3%<sup>8</sup> by weight, which would give rise to a negligible shift in pzc from pristine graphene.

Microkinetic modeling was carried out using CatMAP,<sup>57</sup> which uses a multiple-precision Newton root finding algorithm to determine rates and coverages. A decimal precision of 100, along with a rate convergence tolerance value to  $10^{-25}$  was used. Surface-charge density dependence of each state was included to describe the effect of field on each adsorbate.

Experimental binding energies are estimated based on Redhead's<sup>58</sup> analysis of a TPD peak. It is assumed that there is no interaction between CO molecules adsorbed on the surface. This is a reasonable assumption, because the iron loading is less than 0.1 mass percent of the catalyst.<sup>18,59</sup> Ref 59 also shows that the TPD peak is first order in nature. This is expected for CO desorption, and the rate equation can be written as

$$\text{rate} = \frac{k_{\text{B}}T}{h} \exp\left(-\frac{G_{\text{TS}} - G_{\text{IS}}}{k_{\text{B}}T}\right) \quad (9)$$

For this estimate, we assume that  $G_{\text{TS}} - G_{\text{IS}} = E_{\text{FS}} - E_{\text{IS}}$ . This is reasonable, because the transition state of CO desorption is final-state-like. Further details are provided in the SI.

## ■ ASSOCIATED CONTENT

### Supporting Information

The Supporting Information is available free of charge at <https://pubs.acs.org/doi/10.1021/acscatal.0c01375>.

Contains coverages from RPBE energetics, CO adsorption energy from experiment, effect of dispersion correction and relaxation, sensitivity to Hubbard-U, pathway to methane, continuum charging details, gas-

phase references, vibrational frequencies and atomic coordinates of CO<sub>2</sub> transition states in xyz format (PDF)

## ■ AUTHOR INFORMATION

### Corresponding Author

Karen Chan – *CatTheory, Department of Physics, Technical University of Denmark, DK-2800 Kgs. Lyngby, Denmark;*  
✉ [orcid.org/0000-0002-6897-1108](https://orcid.org/0000-0002-6897-1108); Email: [kchan@fysik.dtu.dk](mailto:kchan@fysik.dtu.dk)

### Authors

Sudarshan Vijay – *CatTheory, Department of Physics, Technical University of Denmark, DK-2800 Kgs. Lyngby, Denmark;*

✉ [orcid.org/0000-0001-8242-0161](https://orcid.org/0000-0001-8242-0161)

Joseph A. Gauthier – *SUNCAT Center for Interface Science and Catalysis, Department of Chemical Engineering, Stanford University, Stanford, California 94305, United States;*

✉ [orcid.org/0000-0001-9542-0988](https://orcid.org/0000-0001-9542-0988)

Hendrik H. Heenen – *CatTheory, Department of Physics, Technical University of Denmark, DK-2800 Kgs. Lyngby, Denmark;*

✉ [orcid.org/0000-0003-0696-8445](https://orcid.org/0000-0003-0696-8445)

Vanessa J. Bukas – *CatTheory, Department of Physics, Technical University of Denmark, DK-2800 Kgs. Lyngby, Denmark;*

✉ [orcid.org/0000-0002-0105-863X](https://orcid.org/0000-0002-0105-863X)

Henrik H. Kristoffersen – *CatTheory, Department of Physics, Technical University of Denmark, DK-2800 Kgs. Lyngby, Denmark;*

✉ [orcid.org/0000-0001-6943-0752](https://orcid.org/0000-0001-6943-0752)

Complete contact information is available at:

<https://pubs.acs.org/10.1021/acscatal.0c01375>

### Notes

The authors declare no competing financial interest.

## ■ ACKNOWLEDGMENTS

Financial support was provided by V-Sustain: The VILLUM Centre for the Science of Sustainable Fuels and Chemicals (#9455) from VILLUM FONDEN.

## ■ REFERENCES

- (1) Nitopi, S.; Bertheussen, E.; Scott, S. B.; Liu, X.; Engstfeld, A. K.; Horch, S.; Seger, B.; Stephens, I. E.; Chan, K.; Hahn, C.; Nørskov, J. K.; Jaramillo, T. F.; Chorkendorff, I. Progress and Perspectives of Electrochemical CO<sub>2</sub> Reduction on Copper in Aqueous Electrolyte. *Chem. Rev.* **2019**, *119*, 7610–7672.
- (2) Seh, Z. W.; Kibsgaard, J.; Dickens, C. F.; Chorkendorff, I.; Nørskov, J. K.; Jaramillo, T. F. Combining Theory and Experiment in Electrocatalysis: Insights into Materials Design. *Science (Washington, DC, U. S.)* **2017**, *355*, eaad4998.
- (3) Jouny, M.; Luc, W.; Jiao, F. General Techno-Economic Analysis of CO<sub>2</sub> Electrolysis Systems. *Ind. Eng. Chem. Res.* **2018**, *57*, 2165–2177.
- (4) Chen, Y.; Li, C. W.; Kanan, M. W. Aqueous CO<sub>2</sub> Reduction at very Low Overpotential on Oxide-derived Au Nanoparticles. *J. Am. Chem. Soc.* **2012**, *134*, 19969–19972.
- (5) Möller, T.; Ju, W.; Bagger, A.; Wang, X.; Luo, F.; Ngo Thanh, T.; Varela, A. S.; Rossmeisl, J.; Strasser, P. Efficient CO<sub>2</sub> to CO Electrolysis on Solid Ni-N-C Catalysts at Industrial Current Densities. *Energy Environ. Sci.* **2019**, *12*, 640–647.
- (6) Su, H.; Zhao, X.; Cheng, W.; Zhang, H.; Li, Y.; Zhou, W.; Liu, M.; Liu, Q. Hetero-N-Coordinated Co Single Sites with High Turnover Frequency for Efficient Electrocatalytic Oxygen Evolution in an Acidic Medium. *ACS Energy Lett.* **2019**, *4*, 1816–1822.

- (7) Shen, J.; Kolb, M. J.; Göttle, A. J.; Koper, M. T. DFT Study on the Mechanism of the Electrochemical Reduction of CO<sub>2</sub> Catalyzed by Cobalt Porphyrins. *J. Phys. Chem. C* **2016**, *120*, 15714–15721.
- (8) Gu, J.; Hsu, C. S.; Bai, L.; Chen, H. M.; Hu, X. Atomically Dispersed Fe<sub>3+</sub> Sites Catalyze Efficient CO<sub>2</sub> Electroreduction to CO. *Science (Washington, DC, U. S.)* **2019**, *364*, 1091–1094.
- (9) Cheng, M. J.; Kwon, Y.; Head-Gordon, M.; Bell, A. T. Tailoring Metal-Porphyrin-Like Active Sites on Graphene to Improve the Efficiency and Selectivity of Electrochemical CO<sub>2</sub> Reduction. *J. Phys. Chem. C* **2015**, *119*, 21345–21352.
- (10) Ringe, S.; Clark, E. L.; Resasco, J.; Walton, A.; Seger, B.; Bell, A. T.; Chan, K. Understanding Cation Effects in Electrochemical CO<sub>2</sub> Reduction. *Energy Environ. Sci.* **2019**, *12*, 3001.
- (11) Hong, S.; Rahman, T. S. Rationale for the Higher Reactivity of Interfacial Sites in Methanol Decomposition on Au<sub>13</sub>/TiO<sub>2</sub>(110). *J. Am. Chem. Soc.* **2013**, *135*, 7629–7635.
- (12) Leung, K.; Rempe, S. B.; Schultz, P. A.; Sproviero, E. M.; Batista, V. S.; Chandross, M. E.; Medforth, C. J. Density functional theory and DFT+U study of transition metal porphines adsorbed on Au(111) surfaces and effects of applied electric fields. *J. Am. Chem. Soc.* **2006**, *128*, 3659–3668.
- (13) Keith, J. A.; Carter, E. A. Theoretical Insights into Pyridinium-based Photoelectrocatalytic Reduction of CO<sub>2</sub>. *J. Am. Chem. Soc.* **2012**, *134*, 7580–7583.
- (14) Gray, C. M.; Saravanan, K.; Wang, G.; Keith, J. A. Quantifying Solvation Energies at Solid/Liquid Interfaces using Continuum Solvation Methods. *Mol. Simul.* **2017**, *43*, 420–427.
- (15) Bagger, A.; Ju, W.; Varela, A. S.; Strasser, P.; Rossmeisl, J. Single Site Porphyrin-like Structures Advantages over Metals for Selective Electrochemical CO<sub>2</sub> Reduction. *Catal. Today* **2017**, *288*, 74–78.
- (16) Ju, W.; Bagger, A.; Wang, X.; Tsai, Y.; Luo, F.; Möller, T.; Wang, H.; Rossmeisl, J.; Varela, A. S.; Strasser, P. Unraveling Mechanistic Reaction Pathways of the Electrochemical CO<sub>2</sub> Reduction on Fe-N-C Single-Site Catalysts. *ACS Energy Lett.* **2019**, *4*, 1663–1671.
- (17) Zhang, C.; Yang, S.; Wu, J.; Liu, M.; Yazdi, S.; Ren, M.; Sha, J.; Zhong, J.; Nie, K.; Jililov, A. S.; Li, Z.; Li, H.; Yakobson, B. I.; Wu, Q.; Ringe, S.; Xu, H.; Ajayan, P. M.; Tour, J. M. Electrochemical CO<sub>2</sub> Reduction with Atomic Iron-Dispersed on Nitrogen-Doped Graphene. *Adv. Energy Mater.* **2018**, *8*, 1703487.
- (18) Varela, A. S.; Kroschel, M.; Leonard, N. D.; Ju, W.; Steinberg, J.; Bagger, A.; Rossmeisl, J.; Strasser, P. PH Effects on the Selectivity of the Electrocatalytic CO<sub>2</sub> Reduction on Graphene-Embedded Fe-N-C Motifs: Bridging Concepts between Molecular Homogeneous and Solid-State Heterogeneous Catalysis. *ACS Energy Lett.* **2018**, *3*, 812–817.
- (19) Gauthier, J. A.; Dickens, C. F.; Heenen, H. H.; Vijay, S.; Ringe, S.; Chan, K. Unified Approach to Implicit and Explicit Solvent Simulations of Electrochemical Reaction Energetics. *J. Chem. Theory Comput.* **2019**, *15*, 6895–6906.
- (20) Hou, Z.; Wang, X.; Ikeda, T.; Terakura, K.; Oshima, M.; Kakimoto, M. A.; Miyata, S. Interplay between Nitrogen Dopants and Native Point Defects in Graphene. *Phys. Rev. B: Condens. Matter Mater. Phys.* **2012**, *85*, 165439.
- (21) Sahaie, N. R.; Kramm, U. I.; Steinberg, J.; Zhang, Y.; Thomas, A.; Reier, T.; Paraknowitsch, J. P.; Strasser, P. Quantifying the Density and Utilization of Active Sites in Non-precious Metal Oxygen Electroreduction Catalysts. *Nat. Commun.* **2015**, *6*, 8618.
- (22) Luo, F.; Choi, C. H.; Primbs, M. J.; Ju, W.; Li, S.; Leonard, N. D.; Thomas, A.; Jaouen, F.; Strasser, P. Accurate Evaluation of Active-Site Density (SD) and Turnover Frequency (TOF) of PGM-Free Metal-Nitrogen-Doped Carbon (MNC) Electrocatalysts using CO Cryo Adsorption. *ACS Catal.* **2019**, *9*, 4841–4852.
- (23) Dudarev, S. L.; Botton, G. A.; Savrasov, S. Y.; Humphreys, C. J.; Sutton, A. P. Electron-energy-loss Spectra and the Structural Stability of Nickel Oxide: An LSDA+U study. *Phys. Rev. B: Condens. Matter Mater. Phys.* **1998**, *57*, 1505–1509.
- (24) Patel, A. M.; Ringe, S.; Siahrostami, S.; Bajdich, M.; Nørskov, J. K.; Kulkarni, A. R. Theoretical Approaches to Describing the Oxygen Reduction Reaction Activity of Single-Atom Catalysts. *J. Phys. Chem. C* **2018**, *122*, 29307–29318.
- (25) Bukas, V. J.; Kim, H. W.; Sengpiel, R.; Knudsen, K.; Voss, J.; McCloskey, B. D.; Luntz, A. C. Combining Experiment and Theory to Unravel the Mechanism of Two-Electron Oxygen Reduction at a Selective and Active Co-catalyst. *ACS Catal.* **2018**, *8*, 11940–11951.
- (26) Kim, H. W.; Bukas, V. J.; Park, H.; Park, S.; Diederichsen, K. M.; Lim, J.; Cho, Y. H.; Kim, J.; Kim, W.; Han, T. H.; Voss, J.; Luntz, A. C.; McCloskey, B. D. Mechanisms of Two-electron and Four-electron Electrochemical Oxygen Reduction Reactions at Nitrogen-doped reduced Graphene Oxide. *ACS Catal.* **2020**, *10*, 852–863.
- (27) Nørskov, J. K.; Studt, F.; Abild-Pedersen, F.; Bligaard, T. *Fundamental Concepts in Heterogeneous Catalysis*; Wiley Blackwell, 2014.
- (28) Gauthier, J. A.; Fields, M.; Bajdich, M.; Chen, L. D.; Sandberg, R. B.; Chan, K.; Nørskov, J. K. Facile Electron Transfer to CO<sub>2</sub> during Adsorption at the Metal–Solution Interface. *J. Phys. Chem. C* **2019**, *123*, 29278–29283.
- (29) Gauthier, J. A.; Ringe, S.; Dickens, C. F.; Garza, A. J.; Bell, A. T.; Head-Gordon, M.; Nørskov, J. K.; Chan, K. Challenges in Modeling Electrochemical Reaction Energetics with Polarizable Continuum Models. *ACS Catal.* **2019**, *9*, 920–931.
- (30) Garza, A. J.; Bell, A. T.; Head-Gordon, M. Mechanism of CO<sub>2</sub> Reduction at Copper Surfaces: Pathways to C<sub>2</sub> Products. *ACS Catal.* **2018**, *8*, 1490–1499.
- (31) Cheng, T.; Fortunelli, A.; Goddard, W. A. Reaction Intermediates during Operando Electrocatalysis Identified from Full Solvent Quantum Mechanics Molecular Dynamics. *Proc. Natl. Acad. Sci. U. S. A.* **2019**, *116*, 7718–7722.
- (32) Huang, J.; Hörmann, N.; Oveisi, E.; Louidice, A.; De Gregorio, G. L.; Andreussi, O.; Marzari, N.; Buonsanti, R. Potential-induced Nanoclustering of Metallic Catalysts during Electrochemical CO<sub>2</sub> Reduction. *Nat. Commun.* **2018**, *9*, 3117.
- (33) Kim, D.; Shi, J.; Liu, Y. Substantial Impact of Charge on Electrochemical Reactions of Two-Dimensional Materials. *J. Am. Chem. Soc.* **2018**, *140*, 9127–9131.
- (34) Nie, X.; Luo, W.; Janik, M. J.; Asthagiri, A. Reaction Mechanisms of CO<sub>2</sub> Electrochemical Reduction on Cu(1 1 1) Determined with Density Functional Theory. *J. Catal.* **2014**, *312*, 108–122.
- (35) Strmcnik, D.; Uchimura, M.; Wang, C.; Subbaraman, R.; Danilovic, N.; Van Der Vliet, D.; Paulikas, A. P.; Stamenkovic, V. R.; Markovic, N. M. Improving the Hydrogen Oxidation Reaction Rate by Promotion of Hydroxyl Adsorption. *Nat. Chem.* **2013**, *5*, 300–306.
- (36) Dickens, C. F.; Kirk, C.; Nørskov, J. K. Insights into the Electrochemical Oxygen Evolution Reaction with ab initio Calculations and Microkinetic Modeling: Beyond the Limiting Potential Volcano. *J. Phys. Chem. C* **2019**, *123*, 18960–18977.
- (37) Shi, C.; Chan, K.; Yoo, J. S.; Nørskov, J. K. Barriers of Electrochemical CO<sub>2</sub> Reduction on Transition Metals. *Org. Process Res. Dev.* **2016**, *20*, 1424–1430.
- (38) Ringe, S.; Morales-Guio, C. G.; Chen, L. D.; Fields, M.; Jaramillo, T. F.; Hahn, C.; Chan, K. Double Layer Charging Driven Carbon dioxide Adsorption Limits the Rate of Electrochemical Carbon dioxide Reduction on Gold. *Nat. Commun.* **2020**, *11*, 33.
- (39) Leonard, N.; Ju, W.; Sinev, I.; Steinberg, J.; Luo, F.; Varela, A. S.; Roldan Cuenya, B.; Strasser, P. The Chemical Identity, State and Structure of Catalytically Active Centers during the Electrochemical CO<sub>2</sub> Reduction on Porous Fe-nitrogen-carbon (Fe-N-C) Materials. *Chem. Sci.* **2018**, *9*, 5064–5073.
- (40) Peterson, A. A.; Abild-Pedersen, F.; Studt, F.; Rossmeisl, J.; Nørskov, J. K. How Copper Catalyzes the Electroreduction of Carbon Dioxide into Hydrocarbon Fuels. *Energy Environ. Sci.* **2010**, *3*, 1311–1315.
- (41) Studt, F.; Abild-Pedersen, F.; Varley, J. B.; Nørskov, J. K. CO and CO<sub>2</sub> Hydrogenation to Methanol Calculated using the BEEF-vdW Functional. *Catal. Lett.* **2013**, *143*, 71–73.



- (42) Christensen, R.; Hansen, H. A.; Vegge, T. Identifying Systematic DFT Errors in Catalytic Reactions. *Catal. Sci. Technol.* **2015**, *5*, 4946–4949.
- (43) Campbell, C. T. The Degree of Rate Control: A Powerful Tool for Catalysis Research. *ACS Catal.* **2017**, *7*, 2770–2779.
- (44) Kresse, G.; Furthmüller, J. Efficient Iterative Schemes for *ab initio* Total-energy Calculations using a Plane-wave Basis Set. *Phys. Rev. B: Condens. Matter Mater. Phys.* **1996**, *54*, 11169–11186.
- (45) Mathew, K.; Kolluru, V. S.; Mula, S.; Steinmann, S. N.; Hennig, R. G. Implicit Self-consistent Electrolyte Model in Plane-wave Density-functional Theory. *J. Chem. Phys.* **2019**, *151*, 234101.
- (46) Kresse, G.; Joubert, D. From Ultrasoft Pseudopotentials to the Projector Augmented-wave Method. *Phys. Rev. B: Condens. Matter Mater. Phys.* **1999**, *59*, 1758–1775.
- (47) Hammer, B.; Hansen, L. B.; Nørskov, J. K. Improved Adsorption Energetics Within Density-functional Theory Using Revised Perdew-Burke-Ernzerhof Functionals. *Phys. Rev. B: Condens. Matter Mater. Phys.* **1999**, *59*, 7413–7421.
- (48) Heyd, J.; Scuseria, G. E.; Ernzerhof, M. Erratum: Hybrid functionals based on a screened Coulomb potential. *J. Chem. Phys.* **2006**, *124*, 219906.
- (49) Heyd, J.; Scuseria, G. E.; Ernzerhof, M. Hybrid functionals based on a Screened Coulomb Potential. *J. Chem. Phys.* **2003**, *118*, 8207–8215.
- (50) Tripkovic, V.; Vanin, M.; Karamad, M.; Björketun, M. E.; Jacobsen, K. W.; Thygesen, K. S.; Rossmeisl, J. Electrochemical CO<sub>2</sub> and CO Reduction on Metal-functionalized Porphyrin-like Graphene. *J. Phys. Chem. C* **2013**, *117*, 9187–9195.
- (51) Hjorth Larsen, A.; Jørgen Mortensen, J.; Blomqvist, J.; Castelli, I. E.; Christensen, R.; Dulak, M.; Friis, J.; Groves, M. N.; Hammer, B.; Hargus, C.; Hermes, E. D.; Jennings, P. C.; Bjerre Jensen, P.; Kermode, J.; Kitchin, J. R.; Leonhard Kolsbjerg, E.; Kubal, J.; Kaasbjerg, K.; Lysgaard, S.; Bergmann Maronsson, J.; Maxson, T.; Olsen, T.; Pastewka, L.; Peterson, A.; Rostgaard, C.; Schiøtz, J.; Schütt, O.; Strange, M.; Thygesen, K. S.; Vegge, T.; Vilhelmsen, L.; Walter, M.; Zeng, Z.; Jacobsen, K. W. The Atomic Simulation Environment - A Python Library for Working with Atoms. *J. Phys.: Condens. Matter* **2017**, *29*, 273002.
- (52) Monkhorst, H. J.; Pack, J. D. Special Points for Brillouin-zone Integrations. *Phys. Rev. B* **1976**, *13*, 5188–5192.
- (53) Henkelman, G.; Uberuaga, B. P.; Jónsson, H. Climbing Image Nudged Elastic Band Method for Finding Saddle Points and Minimum Energy Paths. *J. Chem. Phys.* **2000**, *113*, 9901–9904.
- (54) Nørskov, J. K.; Rossmeisl, J.; Logadottir, A.; Lindqvist, L.; Kitchin, J. R.; Bligaard, T.; Jónsson, H. Origin of the Overpotential for Oxygen Reduction at a Fuel-cell Cathode. *J. Phys. Chem. B* **2004**, *108*, 17886–17892.
- (55) Chen, J.; Li, C.; Shi, G. Graphene Materials for Electrochemical Capacitors. *J. Phys. Chem. Lett.* **2013**, *4*, 1244–1253.
- (56) Choi, C. H.; Lim, H. K.; Chung, M. W.; Chon, G.; Ranjbar Sahraie, N.; Altin, A.; Sougrati, M. T.; Stievano, L.; Oh, H. S.; Park, E. S.; Luo, F.; Strasser, P.; Dražić, G.; Mayrhofer, K. J.; Kim, H.; Jaouen, F. The Achilles' Heel of Iron-based Catalysts during Oxygen Reduction in an Acidic Medium. *Energy Environ. Sci.* **2018**, *11*, 3176–3182.
- (57) Medford, A. J.; Shi, C.; Hoffmann, M. J.; Lausche, A. C.; Fitzgibbon, S. R.; Bligaard, T.; Nørskov, J. K. CatMAP: A Software Package for Descriptor-Based Microkinetic Mapping of Catalytic Trends. *Catal. Lett.* **2015**, *145*, 794–807.
- (58) de Jong, A. M.; Niemantsverdriet, J. W. Thermal Desorption Analysis: Comparative Test of Ten Commonly Applied Procedures. *Surf. Sci.* **1990**, *233*, 355–365.
- (59) Varela, A. S.; Ranjbar Sahraie, N.; Steinberg, J.; Ju, W.; Oh, H. S.; Strasser, P. Metal-Doped Nitrogenated Carbon as an Efficient Catalyst for Direct CO<sub>2</sub> Electroreduction to CO and Hydrocarbons. *Angew. Chem., Int. Ed.* **2015**, *54*, 10758–10762.

## 10.4 Paper 4

### Unified mechanistic understanding of CO<sub>2</sub> reduction to CO on transition metal and single atom catalysts

Sudarshan Vijay, Wen Ju, Sven Brückner, Sze-Chun Tsang, Peter Strasser, Karen Chan

Reproduced from Nat Catal **2021**, 4, 1024-1031.



# Unified mechanistic understanding of CO<sub>2</sub> reduction to CO on transition metal and single atom catalysts

Sudarshan Vijay<sup>1,3</sup>, Wen Ju<sup>2,3</sup>, Sven Brückner<sup>2</sup>, Sze-Chun Tsang<sup>1</sup>, Peter Strasser<sup>2,4</sup>✉ and Karen Chan<sup>1,4</sup>✉

**CO is the simplest product from CO<sub>2</sub> electroreduction (CO<sub>2</sub>R), but the identity and nature of its rate-limiting step remain controversial. Here we investigate the activity of transition metals (TMs), metal–nitrogen-doped carbon catalysts (MNCs) and a supported phthalocyanine, and present a unified mechanistic picture of the CO<sub>2</sub>R to CO for these catalysts. Applying the Newns–Andersen model, we find that on MNCs, like TMs, electron transfer to CO<sub>2</sub> is facile. We find CO<sub>2</sub>\* adsorption to generally be limiting on TMs, whereas MNCs can be limited by either CO<sub>2</sub>\* adsorption or by the proton–electron transfer reaction to form COOH\*. We evaluate these computed mechanisms against pH-dependent experimental activity measurements on the CO<sub>2</sub>R to CO activity. We present a unified activity volcano that includes the decisive CO<sub>2</sub>\* and COOH\* binding strengths. We show that the increased activity of MNC catalysts is due to the stabilization of larger adsorbate dipoles, which results from their discrete and narrow *d* states.**

The electrochemical reduction of CO<sub>2</sub> (CO<sub>2</sub>R) has the potential to store renewable energy in the form of high-value chemicals<sup>1–3</sup>. The simplest product obtained during the reduction of CO<sub>2</sub> is CO, which can be used as a renewable feedstock for the Fischer–Tropsch reaction<sup>4</sup>. This process is also the first CO<sub>2</sub>R reaction to be realized commercially, with Ag gas-diffusion electrodes that yield up to 300 mA cm<sup>−2</sup> CO towards the production of polymers<sup>5</sup>. Nanostructured forms of gold and silver are currently the state-of-the-art catalysts for this reaction. Aside from their cost, these transition metal (TM) catalysts also catalyse the competing hydrogen evolution reaction, which reduces the selectivity for CO. A recently proposed alternative for CO<sub>2</sub>R to CO is metal–nitrogen-doped carbon (MNC), which is low cost and Earth abundant<sup>6</sup>. These catalysts also have the advantage that they are less selective towards the hydrogen evolution reaction than are TM catalysts, with Faradaic efficiencies of H<sub>2</sub> of less than 20% under typical operating conditions of −0.6 V versus the reversible hydrogen electrode<sup>7,8</sup>, which is consistent with the scaling of the H\* and CO\* binding energies on these materials<sup>6</sup>.

CO<sub>2</sub>R to CO requires two proton–electron transfers. In acid:



Despite its apparent simplicity, its mechanism remains debated in recent work. First, the rate-limiting step has been proposed to be CO<sub>2</sub> adsorption on Au (refs. <sup>9,10</sup>), Fe- and Ni-doped MNC catalysts (FeNC and NiNC)<sup>8,11</sup>, COOH\* formation on noble metals<sup>12,13</sup> or COOH\* to CO(g) on Ag from C–O bond breaking<sup>14</sup>. Tafel slopes of 60 or 120 mV dec<sup>−1</sup> are sometimes taken as indicators of certain rate-limiting steps<sup>9,12</sup>; however, a recent comprehensive analysis of existing data showed silver, gold, copper, zinc and tin catalysts to have no intrinsic preference for such cardinal values, consistent with models of electron transfer in electrochemistry<sup>15</sup>.

Furthermore, the nature of the CO<sub>2</sub> adsorption step is a source of some controversy. CO<sub>2</sub> adsorption was suggested to give rise to a unit-charged CO<sub>2</sub><sup>−</sup> species on both Au (refs. <sup>16,17</sup>) and FeNC catalysts, which is untreatable with ground-state density functional theory (DFT) methods<sup>18</sup>. This hypothesis may originate from the reduction process of CO<sub>2</sub>(aq) to CO<sub>2</sub><sup>−</sup>(aq), which occurs at extremely negative potentials of −1.9 V versus the standard hydrogen electrode (SHE)<sup>19</sup>, or from homogeneous catalysis<sup>20,21</sup>. Solvent reorganization, as first considered through Marcus theory, has also been hypothesized to be a major contributor to the energetics of CO<sub>2</sub> adsorption<sup>17,22</sup>. Alternatively, it has been proposed that CO<sub>2</sub>\* adsorption is driven by the interaction of the dipole of CO<sub>2</sub>\* with the interfacial electric field<sup>23,24</sup>; given the facile electron transfer on metals, there is no distinct, extra-charged CO<sub>2</sub><sup>−</sup> species versus a polarized CO<sub>2</sub>\* adsorbate, no different from any other surface adsorbate, such as CO\* and OH\* (ref. <sup>25</sup>). The CO<sub>2</sub>\* dipole has similarly been described in terms of a partial charge transfer from the metal to adsorbate<sup>11,26</sup>.

In this work, we present a unified mechanistic picture of CO<sub>2</sub>R to CO on both these classes of catalysts. By consideration of the width of adsorbate-induced density of states, we found that on MNCs, as for TMs, electron transfer to CO<sub>2</sub> is extremely facile, such that a field-driven CO<sub>2</sub> adsorption step is treatable with standard ground state DFT methods. Using DFT with an explicit consideration of adsorbate–field interactions, we found CO<sub>2</sub>\* formation to generally be limiting on TMs, whereas MNCs could be limited by either CO<sub>2</sub>\* adsorption or COOH\* formation. We evaluated these computed mechanisms against pH-dependent activity measurements on the CO<sub>2</sub>R to CO activity for Au, FeNC, NiNC and supported cobalt phthalocyanine (CoPc). We present a unified kinetic activity volcano with CO<sub>2</sub>\* and COOH\* binding strengths as the descriptors, which reflects how the formation of either can be rate limiting, and with consideration of the decisive adsorbate–dipole interactions.

<sup>1</sup>CatTheory, Department of Physics, Technical University of Denmark, Lyngby, Denmark. <sup>2</sup>Department of Chemistry, Chemical Engineering Division, Technical University Berlin, Berlin, Germany. <sup>3</sup>These authors contributed equally: Sudarshan Vijay and Wen Ju. <sup>4</sup>These authors jointly supervised: Peter Strasser and Karen Chan. ✉e-mail: [pstrasser@tu-berlin.de](mailto:pstrasser@tu-berlin.de); [kchan@fysik.dtu.dk](mailto:kchan@fysik.dtu.dk)

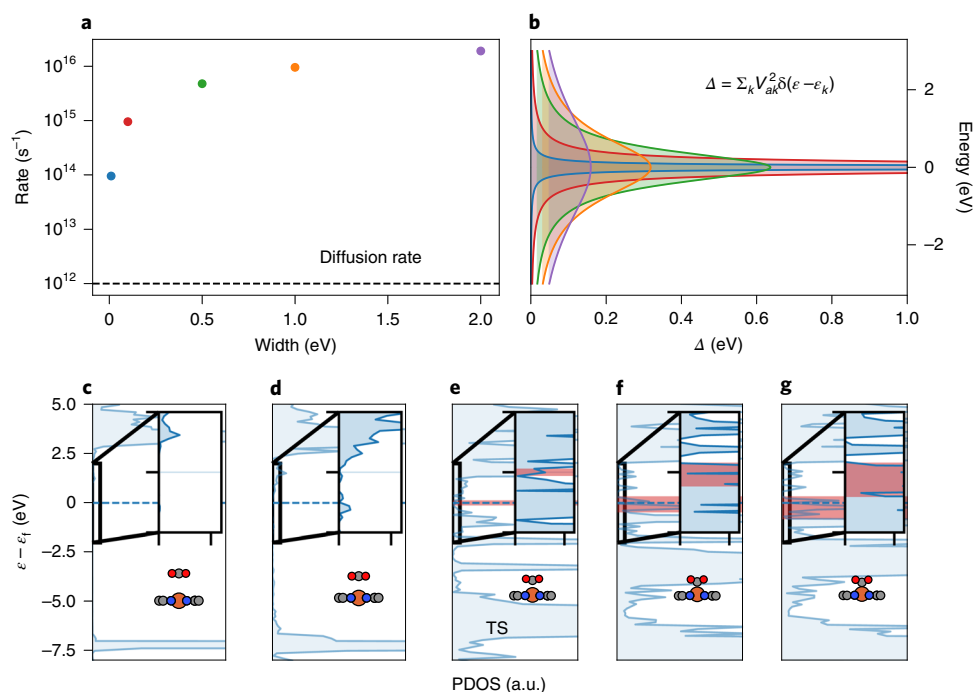


**Fig. 1 | Rate of electron transfer on MNC  $\approx 10^{14} \text{ s}^{-1}$ .** **a, b**, Rate of electron hopping (**a**) for the different idealized Lorentzian peaks shown in **b**. **c–g**, Densities of states projected onto  $\text{CO}_2$   $s$  and/or  $p$ -states for selected images of a  $\text{CO}_2$  adsorption climbing image nudged elastic band run on  $\text{FeN}_4$  show a short timescale of electron transfer. Insets: zoomed-in parts of the highlighted region; red bands indicate the estimated width of the states at the Fermi level,  $\epsilon_x$ , a.u., arbitrary units.

We furthermore showed that MNC catalysts are tunable towards a higher activity away from TM scaling, due to the stabilization of larger  $\text{CO}_2^*$  dipoles that result from narrower metal  $d$  states. We discuss the implications of these findings for catalyst design, namely that the optimization of the  $\text{CO}_2^*$  dipole is a critical descriptor in addition to the adsorption energies of key intermediates.

## Results

**Electron transfer is not rate-limiting on MNC catalysts.** Previous reports proposed the formation of a  $\text{CO}_2^-$  state as the rate-limiting step for  $\text{CO}_2$  R to CO. This step has been suggested to be limited by solvent reorganization<sup>17,22</sup> or by electron transfer to an uncharged  $\text{CO}_2^*$  state to give an excited, charged  $\text{CO}_2^-$  state, which cannot be modelled with workhorse, ground-state periodic DFT methods<sup>18</sup>. Here we show that electron transfer to adsorbates is not limiting (and therefore adiabatic) on MNC catalysts, which allows us to determine the  $\text{CO}_2$  R energetics by computing the one and only  $\text{CO}_2^*$  state using conventional, periodic DFT, along with the application of a stabilizing surface charge.

As in Gauthier et al.<sup>25</sup> for an Au surface, we determined the rate of electron hopping between the  $s$  and  $p$  states of the adsorbate and the states of the surface,  $k$ . We compared this rate against concurrent processes, such as the adsorbate diffusion to the surface. If the timescale for the electron transfer is very small in comparison, it will not be rate-limiting to species such as  $\text{CO}_2^*$ , and we would only need to consider the adiabatic pathway for  $\text{CO}_2$  adsorption. In the Newns–Anderson<sup>27–29</sup> model of chemisorption, the width of the adsorbate-induced states is  $\Delta = \sum_k |V_{ak}|^2 \delta(\epsilon - \epsilon_k)$ , where  $V_{ak}$  is the coupling matrix element between  $k$  and individual  $s$  and  $p$  states,  $\epsilon$  is the single particle energy of the adsorbate  $s$  and  $p$  states and  $\epsilon_k$  is the energy of the surface states.  $\Delta$  can be determined from the projected density of states (PDOS) onto the  $s$  and  $p$  states of  $\text{CO}_2$  through the width of the peak at the Fermi level<sup>25</sup>. We obtained the rate of electron transfer from Fermi's Golden Rule,  $\frac{2\pi}{\hbar} \Delta$ . To illustrate

this idea, Fig. 1a shows the rates of electron transfer associated with a range of idealized peaks of different width, shown in Fig. 1b. For a very small width of 0.1 eV, the rate of electron hopping is extremely fast, greater than  $10^{14} \text{ s}^{-1}$ , and is larger with increased broadening. For comparison, an estimate for the diffusion rate of ions in solution is of the order  $10^{12} \text{ s}^{-1}$ , shown by the dashed line in Fig. 1a<sup>30</sup>.

We then applied this methodology to PDOS obtained from DFT computations. Figure 1c–g shows the PDOS for the reaction path of  $\text{CO}_2$  adsorption on  $\text{FeN}_4$  (a prototype for MNC). The  $s$  and  $p$  states of  $\text{CO}_2$  broaden as it approaches the surface, which is expected for adsorption processes in general<sup>31</sup>. At the transition state (TS) and further along the reaction pathway, the peaks at the Fermi level are greater than 0.1 eV. The corresponding rate of electron transfer is approximately  $10^{14} \text{ s}^{-1}$ , which implies a timescale of  $10^{-14} \text{ s}$ . This rate is, in turn, two orders of magnitude greater than that of competing processes, which implies that it will not be rate limiting on  $\text{FeN}_4$ . As the states at the Fermi level on MNC catalysts are typically the  $s$  and  $p$  states of graphene at reducing potentials, at which oxide species are absent (Supplementary Note 2), we expect this analysis to hold for all MNC catalysts considered in this work<sup>32</sup>. Thus, only the adiabatic pathway for  $\text{CO}_2$  adsorption needs to be calculated to obtain the energetics for all the elementary steps on the MNC and TM catalysts. Non-adiabatic behaviour might be present in molecules such as CoPc adsorbed on a support, with rates of electron transfer on the order of the magnitude of diffusion as shown in Fig. 1<sup>33</sup>. In Supplementary Note 2 we show that with even a slight increase in doping concentration on the graphene sheet, hybridization between all the components of the system ( $\text{CO}_2$ , CoPc and  $n$ -doped graphene) improves, which would lead to an increase in the rate of electron transfer through a larger value of  $\Delta$ .

We do not exclude the possibility here that solvent reorganization could contribute to the energetics of the  $\text{CO}_2$  adsorption step, as has been considered in Brown et al.<sup>17</sup>. The magnitude of this contribution, however, has been estimated to be only  $\sim 0.2 \text{ eV}$  from the

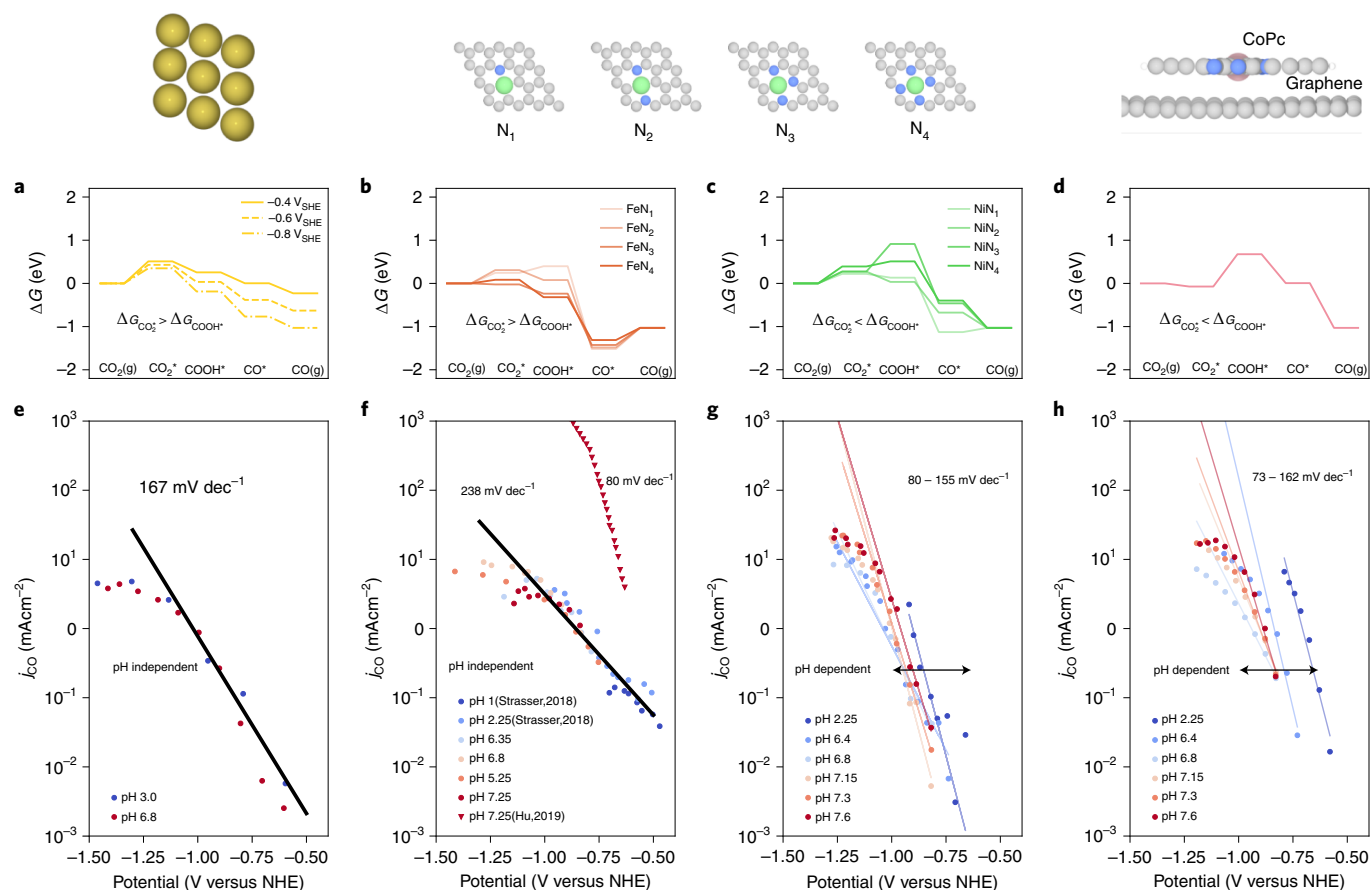
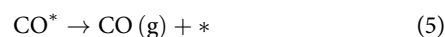
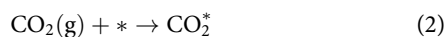


**Fig. 2 | Both CO<sub>2</sub>\* adsorption and COOH\* formation can be rate limiting.** **a–c**, Free energy diagram of CO<sub>2</sub> to CO for Au(211) at  $U = -0.6, -0.8$  and  $-1.0 V_{SHE}$  (**a**), FeNC (**b**), NiNC (**c**) and CoPc adsorbed on graphene (**d**) at  $U = -0.8 V_{SHE}$  and pH = 2. The schematics of the calculated surfaces are shown above their respective free energy diagrams, with the four double-vacancy MnCs. **e–h**, Experimental current densities plotted against NHE potential for polycrystalline Au (from Ringe et al.<sup>23</sup>) (**e**), FeNC (from Varela et al.<sup>8</sup> and Gu et al.<sup>74</sup> (reversed triangles)) (**f**), NiNC (this work) (**g**) and CoPc on CNT (this work) (**h**).

timescale of reorganization<sup>34,35</sup>. Recent investigations based on the Marcus–Hush–Chidsey model suggest that it can be up to 0.6 eV in the presence of certain electrolytes<sup>36</sup>.

**Both CO<sub>2</sub>\* adsorption and COOH\* formation can be rate limiting.** We now present the mechanism and rate-limiting step for Au, FeNC, NiNC and carbon nanotube (CNT)-supported CoPc determined from potential-dependent DFT calculations and evaluate them against pH-dependent activity measurements. We considered the following reaction pathway (written for acidic solutions):



We assumed that the barriers associated with all steps are small. As evaluated in Vijay et al.<sup>24</sup> for FeN<sub>2</sub> and FeN<sub>4</sub>, the CO<sub>2</sub> adsorption barrier is well approximated by the adsorption energy (differences between barrier and reaction energies of at most 0.2 eV); the protonation of CO<sub>2</sub>\* is facile, in line with general trends in electrochemical barriers for the protonation of oxygen<sup>37</sup>, and the COOH\* to CO\* step

for CO-producing catalysts is generally so downhill under reducing potentials that the corresponding barriers are unlikely to be limiting (Fig. 2b–d). This reduction of the barrier for COOH\* protonation is due to the two preceding potential-dependent steps and the reducing potentials at which CO<sub>2</sub>R occurs. The rate-limiting step at a given potential is, in this case, determined by the state with the highest free energy, ΔG. Each ΔG derives its potential dependence either from the presence of a proton–electron pair as the reactants and/or from the interaction between the dipoles of participating reaction intermediates with the interfacial field. The energetic stabilisation caused by the interaction of a dipole μ with an interfacial field ξ is μξ (ref. 38). At reducing potentials, fields set up by the double layer can be as large as 10<sup>10</sup> V m<sup>-1</sup>, which gives rise to a large stabilization of CO<sub>2</sub>\* on MNCs of 0.75–1 eV on MNCs (see Supplementary Note 1 for detailed information about the methodology used). Figure 2a shows the free energy diagram for Au(211) at -0.6, -0.8 and -1 V<sub>SHE</sub> at a pH of 2. At -0.6 V<sub>SHE</sub>, COOH\* is the intermediate with the highest ΔG, whereas at -0.8 V<sub>SHE</sub> and -1 V<sub>SHE</sub>, it is CO<sub>2</sub>\*. Thus, the computations predicted a change in rate-limiting step from COOH\* formation to CO<sub>2</sub>\* adsorption when the overpotential is increased, in line with previous work<sup>23</sup>. We note that this change in rate-limiting step occurs at -0.7 V versus SHE.

We evaluated the rate-limiting step with pH-dependent measurements. The activity was pH dependent on an absolute scale (for example, versus the SHE or normal hydrogen electrode (NHE)) when COOH\* formation was rate-limiting, as a proton–electron transfer was involved. CO<sub>2</sub>\* adsorption, however, did not involve a proton–electron transfer, so when it was rate limiting, the activity



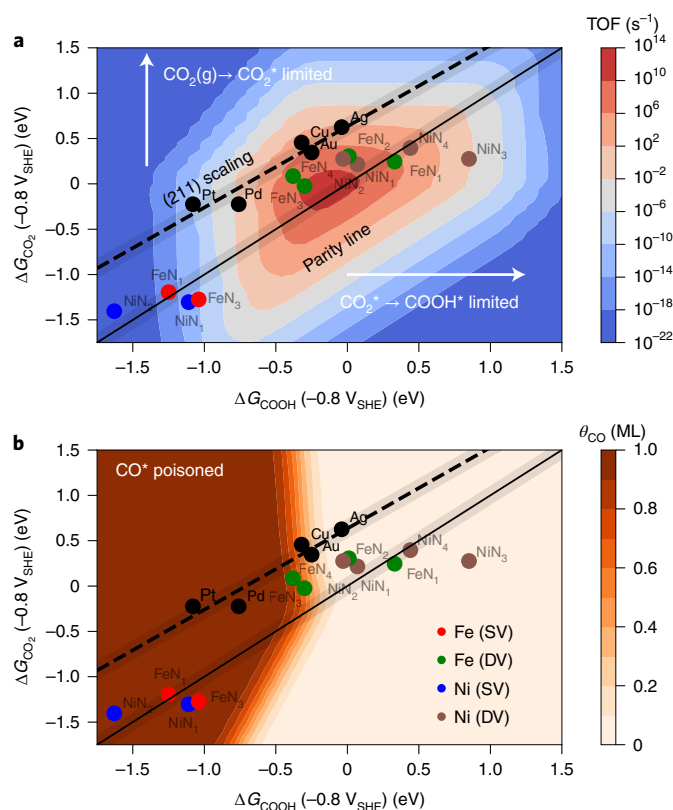


**Fig. 3 | General activity volcano for  $\text{CO}_2\text{R}$  to  $\text{CO}$ .** **a**, Rate map at  $-0.8 V_{\text{SHE}}$  and pH 2 for  $\text{CO}_2\text{R}$  to  $\text{CO}$  obtained from the (211) TM scaling line. The annotated points show MNCs either at SVs or DVs. The (211) scaling line has the best fit.  $\Delta G_{\text{CO}_2^*} = 0.94\Delta G_{\text{COOH}^*} + 0.51$ . **b**, Coverage map  $\theta_{\text{CO}}$  in monolayers (ML) with the same points showing which surfaces are poisoned by  $\text{CO}$ .

was pH independent on an absolute scale. Figure 2e shows the measured current densities versus potential on a NHE scale. The current densities show no pH dependence at high potentials (greater than  $-0.8 V_{\text{SHE}}$ ). At lower overpotentials, the scatter in the points could be indicative of  $\text{COOH}^*$  formation being the rate-limiting step.

With the same arguments, we show that the FeNC catalysts were limited by the energetics of  $\text{CO}_2^*$  adsorption, whereas the NiNC catalysts and supported CoPc catalysts were limited by the  $\text{CO}_2^* \rightarrow \text{COOH}^*$  step. Figure 2b shows the free energy diagram for FeNC catalysts computed at  $-0.8 V_{\text{SHE}}$  and a pH of 2 for various nitrogen coordinations around the metal centre for double vacancies (DVs) (metals on single vacancies (SVs) tend to overbind  $\text{CO}^*$ , see below). For  $\text{FeN}_2$ ,  $\text{FeN}_3$  and  $\text{FeN}_4$ , the computations predict  $\text{CO}_2^*$  adsorption to be rate limiting for potentials more cathodic than  $-0.8 V_{\text{SHE}}$ , which is in line with the completely pH-independent experimental rates (Fig. 2f, Strasser data<sup>8</sup>). The  $\text{FeN}_4$  vacancy configuration has also been stipulated to be the active site for  $\text{CO}_2\text{R}$  based on a comparison of the cyclic voltammograms and X-ray spectral features with those of molecular analogues<sup>39</sup>. In contrast,  $\text{FeN}_1$  was limited by  $\text{COOH}^*$  formation at this potential, and the lack of pH dependence in the experiments suggests that its population on the catalyst surface was small. All the NiNC catalysts investigated (Fig. 2c), except for  $\text{NiN}_2$ , were limited by  $\text{COOH}^*$  formation, consistent with the pH dependence of experimental rates, as shown in Fig. 2g (see Supplementary Note 3 for the total currents and Faradaic efficiencies). Recent works<sup>40,41</sup> also reported large  $\text{COOH}^*$  free energies for  $\text{NiN}_4$ , in line with the results shown in Fig. 2c. Molecular  $\text{NiN}_4$  analogues

also showed large  $\text{COOH}^*$  free energies in comparison with that of  $\text{CO}_2^*$  (ref. 42). Similarly, supported CoPc catalysts also had  $\text{COOH}^*$  formation as the rate-limiting step, as shown in Fig. 2d, which were realized in the pH-dependent experiments shown in Fig. 2h. Thus, the combination of simple field-dependent thermodynamic computations and pH-dependent measurements suggests that  $\text{CO}_2^*$  adsorption is rate limiting at higher overpotentials on Au and for all potentials on FeNC, and that  $\text{CO}_2^* \rightarrow \text{COOH}^*$  is rate limiting on NiNC and supported CoPc catalysts.

The adsorbate binding strengths in more detailed models of the electrochemical interface, but the electrostatic effects are in line with experimentally observed pH dependencies for the systems considered here, which suggests they are the predominant factor in the energetics. In Supplementary Note 6, we show, with an ab initio molecular dynamics simulation of explicit water on FeNC, an explicit solvation energy of  $\sim 0.3$  eV for  $\text{CO}^*$  versus the solvation energy self-consistently determined through an implicit solvent model in this work; in contrast, the  $0.75$  eÅ dipole moment of  $\text{CO}_2^*$  gives rise to a much larger  $-0.75$  eV change in its adsorption energy over a 1 V range.

Finally, the experimental Tafel slopes in Fig. 2e–h do not show the cardinal values of 60 or  $120 \text{ mV dec}^{-1}$ , which echoes a comprehensive study of the recent literature of TM catalysts for  $\text{CO}_2\text{R}$ <sup>15</sup>. These slopes reflect the magnitude of the dipole ( $\text{slope}^{-1} \approx \frac{C}{e}\mu$ , where  $C$  is the capacitance<sup>23,24</sup> and/or the symmetry factor ( $0 < \alpha < 1$ ) of the associated proton–electron transfer and therefore are not constrained to these values. The slopes may also be affected by mass transport and buffer equilibria<sup>23,43</sup>. Furthermore, the fitted value depends on the number of points used to make the fit. For example, by changing the number of fitted points in Fig. 2a by two, we would obtain a value different from the Tafel slope of  $167 \text{ mV dec}^{-1}$ . We therefore considered mechanistic interpretations of the experiments only on the basis of the pH dependence, and not the specific Tafel slopes obtained.

**Activity volcano determined by both  $\text{COOH}^*$  and  $\text{CO}_2^*$  free energies.** In this section we consolidate the mechanistic insights into a general kinetic activity volcano for  $\text{CO}_2\text{R}$  to  $\text{CO}$  determined by two activity descriptors, the free energy of adsorption of  $\text{CO}_2$ ,  $\Delta G_{\text{CO}_2^*}$ , and that of  $\text{COOH}$ ,  $\Delta G_{\text{COOH}^*}$ . Figure 3a shows this unified activity volcano for the  $\text{CO}$  production for both TM and MNC catalysts, and corresponds to the energetics in Fig. 2. The theoretical maximum in activity (represented by the turnover frequency (TOF)) occurs at intermediate  $\Delta G_{\text{CO}_2^*}$  values and at  $\Delta G_{\text{COOH}^*} \approx 0$ , that is, where both the  $\text{CO}_2$  and  $\text{COOH}$  formation steps are facile. The parity line corresponds to the case in which the free energies of  $\text{COOH}^*$  and  $\text{CO}_2^*$  are equal,  $\Delta G_{\text{CO}_2^*} = \Delta G_{\text{COOH}^*}$ . The  $\text{CO}$  adsorption energy generally scales with those of the other two intermediates<sup>13</sup>; thus, its energetics are included in the volcano through the calculated scaling relationships in the kinetic model (Supplementary Note 4).

Figure 3a shows several trends in the binding of  $\text{CO}_2\text{R}$  intermediates for TMs and MNCs. First, the TMs show a scaling line (the dashed black line) between  $\Delta G_{\text{CO}_2^*}$  and  $\Delta G_{\text{COOH}^*}$ , whereas the MNCs show more scatter. Furthermore, metals doped into SVs tend to bind reaction intermediates more strongly than those in DVs, and are poisoned by  $\text{CO}$ . Fig. 3a,b also allows us to determine which step is rate limiting in  $\text{CO}_2\text{R}$  to  $\text{CO}$  at any given potential, using computed  $\text{CO}_2^*$ ,  $\text{COOH}^*$  and  $\text{CO}^*$  free energies. In Fig. 3a, if the point lies below the parity line, then  $\text{CO}_2^* \rightarrow \text{COOH}^*$  is the rate-limiting step. Meanwhile, if it is above the parity line,  $\text{CO}_2$  adsorption is rate limiting. At very negative adsorption energies, the surface is poisoned by  $\text{CO}$ , as shown in Fig. 3b, which leads to  $\text{CO}^*$  desorption being rate limiting on TMs, such as Pd and Pt. All the TM (211) facets lie above the parity line, which indicates that  $\text{CO}_2$  adsorption or  $\text{CO}$  desorption is rate limiting at the studied potentials. Some NiNC catalysts lie below the parity line, which shows that  $\text{CO}_2^* \rightarrow \text{COOH}^*$

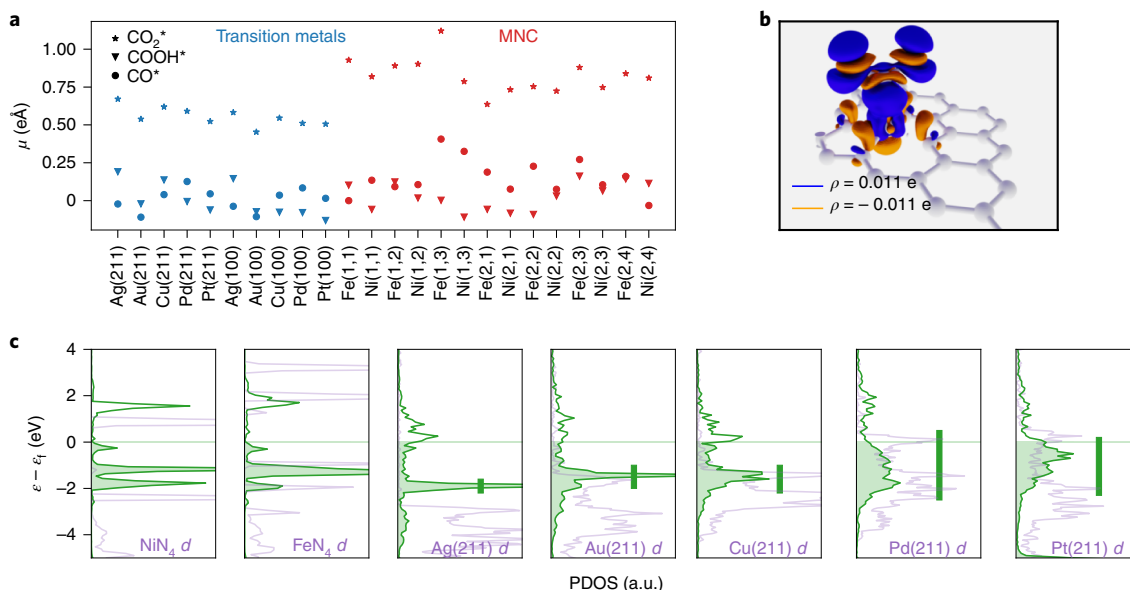


**Fig. 4 | Narrow  $d$  states stabilize larger dipoles.** **a**, Vacuum dipole moments for (211) and (100) TM surfaces (blue) and Fe and Ni MNCs (red). The MNCs (first index indicates the type of vacancy, 1 for single and 2 for double; second index indicates the number of substituting N atoms) have larger dipole moments as compared with those of the TMs. **b**, Charge density difference plot for  $\text{CO}_2$  adsorbed on  $\text{NiN}_4\text{C}$ . **c**, Density of states projected onto the  $s$  and  $p$  states of  $\text{CO}_2^*$  (green) and the  $d$  states of TMs (purple) show that the adsorbate states are much narrower on MNCs than they are on TMs.

is rate-limiting, in line with the experimental finding in Fig. 3f. Note that our approach, in contrast to that of Hansen et al.<sup>13</sup>, includes the effects of the adsorbate–field interactions for all the intermediates (Supplementary Note 1) and the consideration of  $\text{CO}_2$  adsorption as an elementary step, these effects that are critical to determining the activity trends. Supplementary Note 4 also shows the potential dependence versus SHE of the rate map shown in Fig. 3a.

We generally do not expect there to be only a single site motif present after the synthesis procedure for these materials<sup>44–47</sup>. Temperature-programmed desorption experiments (Supplementary Fig. 12 and Supplementary Note 5) show that FeNC, but not NiNC, have a peak above 300 K. This result suggests strong binding sites, such as those from SVs to be present on FeNC to a greater extent than on NiNC (ref. 48). Note that doped SV sites, or other binding sites of similar binding strength that we have not considered, are not active sites for  $\text{CO}_2\text{R}$ , as they would be poisoned by CO.

#### MNCs have a higher activity because they stabilize larger dipoles.

We now show that MNCs deviate from TM scaling because they stabilize large dipole moments on  $\text{CO}_2^*$ . Figure 4b shows charge density difference isosurfaces for  $\text{CO}_2^*$  on  $\text{NiN}_4\text{C}$ , which shows a perturbation of the electron density near the surface on adsorption. This change in electron density is captured by the dipole moment, given by  $\mu = \int \rho dz$ , where  $\rho$  is the charge density and  $z$  is the axis of integration, and is shown in Fig. 4a for (211) and (100) TM surfaces, as well as Fe- and Ni-doped MNC catalysts in both SVs and DVs of various N concentrations. The figure shows that the dipole moments for  $\text{CO}_2^*$  are larger than those for other adsorbates, such as  $\text{CO}^*$  and  $\text{COOH}^*$ . Furthermore, the  $\text{CO}_2^*$  dipoles are significantly higher on MNCs than on TMs. MNCs therefore have  $\text{CO}_2^*$  adsorption energies that are stabilized more at reducing potentials, at which the surface is generally negatively charged. This electrostatic stabilization caused by the dipole–field interaction gives rise to the offset of MNCs from the TM scaling line shown in Fig. 3.

We rationalize the differences in dipole moments with the PDOS on the  $s$  and  $p$  states of  $\text{CO}_2^*$ . The strength of the adsorbate–surface interaction is determined by both the position and shape of

the  $d$  states, and is reflected in the width of the  $s$  and/or  $p$  adsorbate states<sup>49</sup>. As shown in Fig. 4c for a selected set of surfaces (in green), the width of the  $s$  and  $p$  states increases in the order  $\text{FeN}_4$ ,  $\text{NiN}_4$ , Ag, Au, Pd and Pt.

In  $\text{FeN}_4$  and  $\text{NiN}_4$  catalysts, the sharp  $s$  and/or  $p$  states of  $\text{CO}_2^*$  mean they resemble those of their molecular counterpart, which indicates a weak interaction (poor hybridization) with the surface. A poor overlap between the  $s$  and/or  $p$  states close to the Fermi level ( $\pm 1 \text{ eV}$  in either direction) of  $\text{CO}_2$  and the  $d$  states of the surface means that  $\text{CO}_2^*$  retains a greater charge polarization between its two poles, that is a larger dipole (see Supplementary Note 7 for an explanation of this effect through the News–Muscat model). The same effect is present to a lesser extent on the weakly binding metals, Ag and Au, which, in comparison with the strongly binding ones, have slightly narrower  $d$  states and correspondingly slightly larger dipoles. In the strongly binding Pt and Pd catalysts, the broadened states indicate a large interaction<sup>27</sup>, and a lower charge polarization results from the mixing of adsorbate states with those of the surface and a lower resultant surface dipole. Overall, the trends in the width of the  $s$  and/or  $p$  PDOS of  $\text{CO}_2^*$  are consistent with the larger dipole moments of MNC catalysts.

TM alloys, in contrast to MNC catalysts, generally have wide  $d$  states, as with pure TMs<sup>50</sup>. In view of the results, improvements in activity through alloying can be attributed not to the stabilization of larger dipoles, but to the tuning of the  $\text{CO}_2^*$  binding strengths through the degree of hybridization with the surface.

The activity volcano of Fig. 3 and electronic structure arguments of Fig. 4 give two simple design principles. As shown in the TOF of Fig. 3, the ideal  $\text{CO}_2\text{R}$  catalyst has moderate  $\Delta G_{\text{CO}_2}$  and  $\Delta G_{\text{COOH}}$  of 0.25–0.5 eV and  $\Delta G_{\text{CO}} > 0 \text{ eV}$  (to prevent  $\text{CO}^*$  poisoning). It must, additionally, be able to stabilize a large dipole moment of  $\text{CO}_2^*$ , such that  $\text{CO}_2$  adsorption does not require a significant overpotential (and thereby deviate from the scaling of TMs in the direction of a higher activity, shown in Fig. 3). These larger dipole moments are stabilized for MNC catalyst materials through their narrow  $d$  states. We suggest that other materials that have similar discrete and narrow  $d$  states, such as supported single atoms<sup>51,52</sup>, molecules and clusters<sup>53,54</sup>, as well as two-dimensional materials and ionic com-

pounds<sup>32,55,56</sup>, could also be active CO<sub>2</sub>R catalysts, provided that hydrogen evolution is not competitive or suppressed through a decrease in water activity<sup>57</sup>. This principle could also be relevant for other processes in which dipole-field interactions are decisive, such as in C<sub>2</sub> product formation<sup>4,58</sup>.

## Conclusions

In summary, we present a unified picture of CO<sub>2</sub>R to CO on both TM and MNC catalysts that resolves the existing controversies on the identity and nature of the rate-limiting step. Considering the widths of the projected densities of states of an adsorbing CO<sub>2</sub>, we showed that, as for TMs, the electron transfer to CO<sub>2</sub> is not limiting in MNCs, and that CO<sub>2</sub> adsorption is driven by adsorbate dipole-field interactions. With a combination of field-dependent DFT and pH-dependent activity measurements, we showed that CO<sub>2</sub>\* adsorption is limiting on TMs over relevant potentials, whereas either CO<sub>2</sub>\* adsorption or COOH\* formation is rate limiting on MNCs. We present a unified kinetic activity volcano, based on critical COOH\* and CO<sub>2</sub>\* binding as the descriptors, that accounts for the decisive adsorbate dipole-field interactions. The volcano shows that ideal catalysts should have both a moderate binding strength of COOH\* and CO<sub>2</sub>\*, as well as large adsorbate dipoles on CO<sub>2</sub>\*. We furthermore showed that MNCs deviate favourably from TM scaling through the stabilization of large CO<sub>2</sub>\* dipoles, due to the localized narrow *d* states of these materials.

These results suggest that MNCs or other materials with similarly narrow *d* states, such as supported single atoms, molecules and clusters, as well as two-dimensional materials and ionic compounds, can be optimized for large dipoles and correspondingly higher catalytic activity beyond TM scaling. This principle can be relevant for other processes in which adsorbate-field interactions are decisive. The presented kinetic activity volcano and catalyst design rules should be used as the basis for computation-guided catalyst development of CO<sub>2</sub>R to CO catalysts.

## Methods

**Computational methods.** DFT calculations were carried out using the Vienna Ab Initio Software Package (VASP)<sup>59</sup>. Core electrons were described using projector augmented wave potentials<sup>60</sup>. Valence electrons were described with plane waves with a kinetic energy up to 500 eV. Gaussian smearing with a width of 0.1 eV was used. In the case of density of states plots, smearing was reduced to 0.05 eV. For relaxations, we applied the RPBE<sup>61</sup> functional. Hybrid calculations with the HSE06<sup>62,63</sup> were performed for the density of states calculations in Fig. 1. In the case of FeNC calculations, a Hubbard-U<sup>64</sup> parameter of *U* = 2 eV was added to the *d* orbitals of iron, in line with previous benchmark calculations<sup>24</sup>.

TMs were modelled using a 3 × 3 × 3 slab, with the bottom two layers fixed. MNC systems were modelled using a 3 × 3 graphene layer. All the structures were prepared using the Atomic Simulation Environment<sup>65</sup>. The lattice for all the TM and MNC catalysts were relaxed using a 12 × 12 × 1 Monkhorst-Pack<sup>66</sup> *k*-point mesh. All the supercells were treated with a 4 × 4 × 1 Monkhorst-Pack *k*-point mesh. All the geometries were optimized until the forces were lower than 0.025 eV Å<sup>-1</sup>. TS geometries and energies were obtained using the climbing image nudged elastic band<sup>67</sup> implemented within VASP. All the density of states plots used twice the *k*-point sampling used in the relaxation and/or TS calculations. DFT energies were converted into free energies at 298.15 K using vibrations obtained from VASP calculations using IBRION = 5. The ASE<sup>65</sup> Thermochemistry class was used to determine the Helmholtz free energy from harmonic thermochemistry and the Gibbs free energy from ideal gas thermochemistry.

Implicit solvation and continuum charge were added using VASPsol<sup>68</sup>. A Debye screening length of 3 Å was chosen, as it corresponds to a bulk ion concentration of 1 M. The non-electrostatic parameter, TAU, was set to zero for purposes of convergence<sup>30</sup>. Continuum charge was varied in increments of 0.25 e.

The computational hydrogen electrode<sup>69</sup> was used to determine the reaction energetics as a function of the potential with a proton-electron pair was in the reactant. The chemical potential of the proton can be related to that of H<sub>2</sub> at 0 V versus the reversible hydrogen electrode:

$$\mu_{\text{H}^+} + \mu_{\text{e}^-} = \frac{1}{2} \mu_{\text{H}_2(\text{g})} \quad (6)$$

The incorporation of the dipole-field interactions is described in detail in Supplementary Note 1.

Microkinetic modelling was performed using CatMAP<sup>70</sup>. The rate of a given elementary step was

rate =  $k_+ \Pi \theta_i \Pi p_j - k_- \Pi \theta_i \Pi p_j$ , where '+' indicates the forward reaction and '-' the reverse reaction. The rate constants are  $k_+ = \exp\left(-\frac{G_{a,+}}{k_B T}\right)$  and  $k_- = \exp\left(-\frac{G_{a,-}}{k_B T}\right)$ , where  $G_{a,+}$  and  $G_{a,-}$  are the free energy barriers. In the absence of electrochemical barriers, the free energy is used, which is given as  $\Delta G = \Delta G^\circ + neU + \Delta G_{\text{red}}$ , where  $\Delta G^\circ$  is the free energy for the reaction at the potential of zero charge, *n* is the number of proton-electron pairs transferred and  $\Delta G_{\text{red}}$  is the dipole-field contribution.

A multiprecision Newton root-finding algorithm was used to determine the steady-state rates and coverages. A decimal precision of 100 along with a convergence tolerance value of 10<sup>-25</sup> were used.

**Synthesis.** The polyaniline-derived NiNC catalyst is identical to that reported in our previous studies<sup>71,72</sup>. Aniline (3 ml), NiCl<sub>2</sub>·6H<sub>2</sub>O (5 g) and ammonium persulfate (5 g) were added to 0.5 l of 1 M HCl and stirred for 1 h. This suspension was then mixed with 0.4 g of a dispersed activated Ketjen 600 carbon black support (washed in HCl for purification and HNO<sub>3</sub> for oxygen doping), stirred for 48 h and then dried in the air at 95 °C for 24 h. The residual solid-state mixture was ball milled with Zr<sub>2</sub>O<sub>3</sub> balls for 20 min. We conducted the pyrolysis protocol in a furnace at 900 °C (ramp of 30 °C min<sup>-1</sup>) for 1 h under N<sub>2</sub> conditions, followed by acid washing steps (2 M H<sub>2</sub>SO<sub>4</sub> at 90 °C overnight) to remove the excessive Ni particles. We performed heat treatment four times and acid washing three times and the catalyst was obtained after the fourth pyrolysis.

**Synthesis of CoPc/CNT.** CoPc/CNT was synthesized following an analogous protocol reported in the literature<sup>73</sup>. CoPc (1 mg) was mixed with 30 mg of a multiwall CNT in 30 ml dimethylformamide solution and stirred for 24 h. The suspension became transparent. The final suspension was washed using EtOH and H<sub>2</sub>O within a centrifuge to remove the dimethylformamide, and after that was freeze-dried to give the final catalyst.

**Electrode preparation.** Carbon paper (1 cm × 2.5 cm, Freudenberg C2H23) was sonicated in ethanol and deionized water for 15 min and dried as the electrode substrate. The catalyst ink was prepared using 4.0 mg of catalyst mixed with 60 μl of Nafion solution (5% in ethanol, Sigma-Aldrich), 200 μl of isopropanol and 200 μl of deionized water. After 15 min of sonification, the ink was deposited on the microporous layer of carbon paper to achieve an area of 1 cm<sup>2</sup> with catalyst loading of 1 mg cm<sup>-2</sup>.

**Electrochemical measurement.** The electrochemical CO<sub>2</sub>R performance was measured in a regular three-electrode H-cell divided by a Nafion N117 membrane. The working electrode was the catalyst-coated carbon paper mentioned above, and a Pt mesh was deployed as the counter electrodes. A leak-free Ag/AgCl electrode was used as the reference. The current density was normalized to the working electrode's geometrical area (1 cm<sup>2</sup>). All the electrochemical experiments were performed in a CO<sub>2</sub>-purged electrolyte (CO<sub>2</sub> flow rate, 30 ml min<sup>-1</sup>). The pH value of each is presented in Supplementary Table 1.

**Product analysis.** A Shimadzu 2014 on-line gas chromatograph was utilized for product quantification. The gas stream was separated by Hayesep Q + R columns and then analysed by a thermoconductivity detector and flame ionization detector. The thermoconductivity detector detects the volume percentage of the H<sub>2</sub> product, and the flame ionization detector measures the CO after methanization. On all the NiNC type catalysts, no liquid product was found after the electrolysis. Calculations of the production rate, partial current density and Faradaic efficiency are given in the Supplementary Methods.

## Data availability

All computational data, which include the adsorption energies of CO<sub>2</sub>, COOH and CO, optimized atomic coordinates, data for plotting density of states and microkinetic analysis are available at <https://doi.org/10.24435/materialscloud:ws-7t>.

## Code availability

Python analysis scripts to reproduce all the figures in the manuscript are available at <https://github.com/CatTheoryDTU/kinetic-modelling-CO2R>.

Received: 16 April 2021; Accepted: 13 October 2021;  
Published online: 25 November 2021

## References

- Jouny, M., Luc, W. & Jiao, F. General techno-economic analysis of CO<sub>2</sub> electrolysis systems. *Ind. Eng. Chem. Res.* **57**, 2165–2177 (2018).
- Seh, Z. W. Combining theory and experiment in electrocatalysis: insights into materials design. *Science* **355**, aad4998 (2017).



3. Anastasiadou, D., Hensen, E. J. M. & Figueiredo, M. C. Electrocatalytic synthesis of organic carbonates. *Chem. Commun.* **56**, 13082–13092 (2020).
4. Nitopi, S. et al. Progress and perspectives of electrochemical CO<sub>2</sub> reduction on copper in aqueous electrolyte. *Chem. Rev.* **119**, 7610–7672 (2019).
5. Haas, T., Krause, R., Weber, R., Demler, M. & Schmid, G. Technical photosynthesis involving CO<sub>2</sub> electrolysis and fermentation. *Nat. Catal.* **1**, 32–39 (2018).
6. Bagger, A., Ju, W., Varela, A. S., Strasser, P. & Rossmeisl, J. Single site porphyrine-like structures advantages over metals for selective electrochemical CO<sub>2</sub> reduction. *Catal. Today* **288**, 74–78 (2017).
7. Clark, E. L. et al. Influence of atomic surface structure on the activity of Ag for the electrochemical reduction of CO<sub>2</sub> to CO. *ACS Catal.* **9**, 4006–4014 (2019).
8. Varela, A. S. et al. pH effects on the selectivity of the electrocatalytic CO<sub>2</sub> reduction on graphene-embedded Fe–N–C motifs: bridging concepts between molecular homogeneous and solid-state heterogeneous catalysis. *ACS Energy Lett.* **3**, 812–817 (2018).
9. Wuttig, A., Yaguchi, M., Motobayashi, K., Osawa, M. & Surendranath, Y. Inhibited proton transfer enhances Au-catalyzed CO<sub>2</sub>-to-fuels selectivity. *Proc. Natl Acad. Sci. USA* **113**, E4585–E4593 (2016).
10. Verma, S. et al. Insights into the low overpotential electroreduction of CO<sub>2</sub> to CO on a supported gold catalyst in an alkaline flow electrolyzer. *ACS Energy Lett.* **3**, 193–198 (2018).
11. Prslja, P. & López, N. Stability and redispersion of Ni nanoparticles supported on N-doped carbons for the CO<sub>2</sub> electrochemical reduction. *ACS Catal.* **11**, 88–94 (2021).
12. Dunwell, M. et al. The central role of bicarbonate in the electrochemical reduction of carbon dioxide on gold. *J. Am. Chem. Soc.* **139**, 3774–3783 (2017).
13. Hansen, H. A., Varley, J. B., Peterson, A. A. & Nørskov, J. K. Understanding trends in the electrocatalytic activity of metals and enzymes for CO<sub>2</sub> reduction to CO. *J. Phys. Chem. Lett.* **4**, 388–392 (2013).
14. Chen, L. D., Urushihara, M., Chan, K. & Nørskov, J. K. Electric field effects in electrochemical CO<sub>2</sub> reduction. *ACS Catal.* **6**, 7133–7139 (2016).
15. Limaye, A. M., Zeng, J. S., Willard, A. P. & Manthiram, K. Bayesian data analysis reveals no preference for cardinal Tafel slopes in CO<sub>2</sub> reduction electrocatalysis. *Nat. Commun.* **12**, 703 (2021).
16. Hori, Y., Wakebe, H., Tsukamoto, T. & Koga, O. Electrocatalytic process of CO selectivity in electrochemical reduction of CO<sub>2</sub> at metal electrodes in aqueous media. *Electrochim. Acta* **39**, 1833–1839 (1994).
17. Brown, S. M. et al. Electron transfer limitation in carbon dioxide reduction revealed by data-driven Tafel analysis. Preprint at *ChemRxiv* <https://doi.org/10.26434/chemrxiv.13244906.v1> (2020).
18. Ju, W. et al. Unraveling mechanistic reaction pathways of the electrochemical CO<sub>2</sub> reduction on Fe–N–C single-site catalysts. *ACS Energy Lett.* **4**, 1663–1671 (2019).
19. Benson, E. E., Kubiak, C. P., Sathrum, A. J. & Smieja, J. M. Electrocatalytic and homogeneous approaches to conversion of CO<sub>2</sub> to liquid fuels. *Chem. Soc. Rev.* **38**, 89–99 (2009).
20. Göttle, A. J. & Koper, M. T. M. Proton-coupled electron transfer in the electrocatalysis of CO<sub>2</sub> reduction: prediction of sequential vs. concerted pathways using DFT. *Chem. Sci.* **8**, 458–465 (2016).
21. Gennaro, A. et al. Mechanism of the electrochemical reduction of carbon dioxide at inert electrodes in media of low proton availability. *J. Chem. Soc. Faraday Trans.* **92**, 3963–3968 (1996).
22. Zhang, B. A., Costentin, C. & Nocera, D. G. Driving force dependence of inner-sphere electron transfer for the reduction of CO<sub>2</sub> on a gold electrode. *J. Chem. Phys.* **153**, 094701 (2020).
23. Ringe, S. et al. Double layer charging driven carbon dioxide adsorption limits the rate of electrochemical carbon dioxide reduction on gold. *Nat. Commun.* **11**, 33 (2020).
24. Vijay, S. et al. Dipole-field interactions determine the CO<sub>2</sub> reduction activity of 2D Fe–N–C single atom catalysts. *ACS Catal.* **10**, 7826–7835 (2020).
25. Gauthier, J. A. et al. Facile electron transfer to CO<sub>2</sub> during adsorption at the metal|solution interface. *J. Phys. Chem. C* **123**, 29278–29283 (2019).
26. Verma, A. M., Honkala, K. & Melander, M. M. Computational screening of doped graphene electrodes for alkaline CO<sub>2</sub> reduction. *Front. Energy Res.* **8**, 388 (2021).
27. Newns, D. M. Self-consistent model of hydrogen chemisorption. *Phys. Rev.* **178**, 1123–1135 (1969).
28. Anderson, P. W. Localized magnetic states in metals. *Phys. Rev.* **124**, 41–53 (1961).
29. Grimley, T. B. Overlap effects in the theory of adsorption using Anderson's Hamiltonian. *J. Phys. C* **3**, 1934–1942 (1970).
30. Gauthier, J. A. et al. Challenges in modeling electrochemical reaction energetics with polarizable continuum models. *ACS Catal.* **9**, 920–931 (2019).
31. Nørskov, J. K., Studt, F., Abild-Pedersen, F. & Bligaard, T. *Fundamental Concepts in Heterogeneous Catalysis* (Wiley, 2014).
32. Kim, D., Shi, J. & Liu, Y. Substantial impact of charge on electrochemical reactions of two-dimensional materials. *J. Am. Chem. Soc.* **140**, 9127–9131 (2018).
33. Mehdipour, H. et al. Dependence of electron transfer dynamics on the number of graphene layers in  $\pi$ -stacked 2d materials: insights from ab initio nonadiabatic molecular dynamics. *Phys. Chem. Chem. Phys.* **21**, 23198–23208 (2019).
34. Hansen, H. A., Viswanathan, V. & Nørskov, J. K. Unifying kinetic and thermodynamic analysis of 2 e<sup>-</sup> and 4 e<sup>-</sup> reduction of oxygen on metal surfaces. *J. Phys. Chem. C* **118**, 6706–6718 (2014).
35. Limmer, D. T., Willard, A. P., Madden, P. & Chandler, D. Hydration of metal surfaces can be dynamically heterogeneous and hydrophobic. *Proc. Natl Acad. Sci. USA* **110**, 4200–4205 (2013).
36. Huang, B. et al. Cation-dependent interfacial structures and kinetics for outer-sphere electron-transfer reactions. *J. Phys. Chem. C* **125**, 4397–4411 (2021).
37. Patel, A. M. et al. Theoretical approaches to describing the oxygen reduction reaction activity of single-atom catalysts. *J. Phys. Chem. C* **122**, 29307–29318 (2018).
38. Mortensen, J. J., Hammer, B. & Nørskov, J. K. Alkali promotion of N<sub>2</sub> dissociation over Ru(0001). *Phys. Rev. Lett.* **80**, 4333–4336 (1998).
39. Marshall-Roth, T. et al. A pyridinic Fe–N<sub>4</sub> macrocycle models the active sites in Fe/N-doped carbon electrocatalysts. *Nat. Commun.* **11**, 5283 (2020).
40. Sa, Y. J. et al. Thermal transformation of molecular Ni<sup>2+</sup>–N<sub>4</sub> sites for enhanced CO<sub>2</sub> electroreduction activity. *ACS Catal.* **10**, 10920–10931 (2020).
41. Hossain, M. D., Huang, Y., Yu, T. H., Goddard, W. A. & Luo, Z. Reaction mechanism and kinetics for CO<sub>2</sub> reduction on nickel single atom catalysts from quantum mechanics. *Nat. Commun.* **11**, 2256 (2020).
42. Kim, H. et al. Identification of single-atom Ni site active toward electrochemical CO<sub>2</sub> conversion to CO. *J. Am. Chem. Soc.* **143**, 925–933 (2021).
43. Marcandalli, G., Villalba, M. & Koper, M. T. M. The importance of acid–base equilibria in bicarbonate electrolytes for CO<sub>2</sub> electrochemical reduction and CO reoxidation studied on Au(*hkl*) electrodes. *Langmuir* **37**, 5707–5716 (2021).
44. Luo, F. et al. Accurate evaluation of active-site density (SD) and turnover frequency (TOF) of PGM-free metal–nitrogen-doped carbon (MNC) electrocatalysts using CO cryo adsorption. *ACS Catal.* **9**, 4841–4852 (2019).
45. Kramm, U. I. et al. Structure of the catalytic sites in Fe/N/C-catalysts for O<sub>2</sub>-reduction in PEM fuel cells. *Phys. Chem. Chem. Phys.* **14**, 11673–11688 (2012).
46. Jiang, K. et al. Transition-metal single atoms in a graphene shell as active centers for highly efficient artificial photosynthesis. *Chem* **3**, 950–960 (2017).
47. Jiang, K. et al. Isolated Ni single atoms in graphene nanosheets for high-performance CO<sub>2</sub> reduction. *Energy Environ. Sci.* **11**, 893–903 (2018).
48. Luo, F. et al. Surface site density and utilization of platinum group metal (PGM)-free Fe–NC and FeNi–NC electrocatalysts for the oxygen reduction reaction. *Chem. Sci.* **12**, 384–396 (2021).
49. Vojvodic, A., Nørskov, J. K. & Abild-Pedersen, F. Electronic structure effects in transition metal surface chemistry. *Top. Catal.* **57**, 25–32 (2014).
50. Xin, H., Vojvodic, A., Voss, J., Nørskov, J. K. & Abild-Pedersen, F. Effects of *d*-band shape on the surface reactivity of transition-metal alloys. *Phys. Rev. B* **89**, 115114 (2014).
51. Greiner, M. T. et al. Free-atom-like *d* states in single-atom alloy catalysts. *Nat. Chem.* **10**, 1008–1015 (2018).
52. Thirumalai, H. & Kitchin, J. R. Investigating the reactivity of single atom alloys using density functional theory. *Top. Catal.* **61**, 462–474 (2018).
53. Larsen, A. H., Kleis, J., Thygesen, K. S., Nørskov, J. K. & Jacobsen, K. W. Electronic shell structure and chemisorption on gold nanoparticles. *Phys. Rev. B* **84**, 245429 (2011).
54. Li, L. et al. Investigation of catalytic finite-size-effects of platinum metal clusters. *J. Phys. Chem. Lett.* **4**, 222–226 (2013).
55. Ji, Y., Nørskov, J. K. & Chan, K. Scaling relations on basal plane vacancies of transition metal dichalcogenides for CO<sub>2</sub> reduction. *J. Phys. Chem. C* **123**, 4256–4261 (2019).
56. Zhao, X. & Liu, Y. Unveiling the active structure of single nickel atom catalysis: critical roles of charge capacity and hydrogen bonding. *J. Am. Chem. Soc.* **142**, 5773–5777 (2020).
57. Singh, A. R. et al. Computational design of active site structures with improved transition-state scaling for ammonia synthesis. *ACS Catal.* **8**, 4017–4024 (2018).
58. Birdja, Y. Y. et al. Advances and challenges in understanding the electrocatalytic conversion of carbon dioxide to fuels. *Nat. Energy* **4**, 732–745 (2019).
59. Kresse, G. & Furthmüller, J. Efficient iterative schemes for ab initio total-energy calculations using a plane-wave basis set. *Phys. Rev. B* **54**, 11169–11186 (1996).
60. Joubert, D. From ultrasoft pseudopotentials to the projector augmented-wave method. *Phys. Rev. B* **59**, 1758–1775 (1999).
61. Hammer, B., Hansen, L. B. & Nørskov, J. K. Improved adsorption energetics within density-functional theory using revised Perdew–Burke–Ernzerhof functionals. *Phys. Rev. B* **59**, 7413–7421 (1999).
62. Heyd, J., Scuseria, G. E. & Ernzerhof, M. Hybrid functionals based on a screened Coulomb potential. *J. Chem. Phys.* **118**, 8207–8215 (2003).
63. Heyd, J., Scuseria, G. E. & Ernzerhof, M. Erratum: hybrid functionals based on a screened Coulomb potential. *J. Chem. Phys.* **124**, 219906 (2006).

64. Dudarev, S. & Botton, G. Electron-energy-loss spectra and the structural stability of nickel oxide: an LSDA+U study. *Phys. Rev. B* **57**, 1505–1509 (1998).
65. Hjorth Larsen, A. et al. The atomic simulation environment—a Python library for working with atoms. *J. Phys. Condens. Matter* **29**, 273002 (2017).
66. Monkhorst, H. J. & Pack, J. D. Special points for Brillouin-zone integrations. *Phys. Rev. B* **13**, 5188–5192 (1976).
67. Henkelman, G., Uberuaga, B. P. & Jónsson, H. Climbing image nudged elastic band method for finding saddle points and minimum energy paths. *J. Chem. Phys.* **113**, 9901–9904 (2000).
68. Mathew, K., Kolluru, V. S. C., Mula, S., Steinmann, S. N. & Hennig, R. G. Implicit self-consistent electrolyte model in plane-wave density-functional theory. *J. Chem. Phys.* **151**, 234101 (2019).
69. Nørskov, J. K. et al. Origin of the overpotential for oxygen reduction at a fuel-cell cathode. *J. Phys. Chem. B* **108**, 17886–17892 (2004).
70. Medford, A. J. et al. CatMAP: a software package for descriptor-based microkinetic mapping of catalytic trends. *Catal. Letters* **145**, 794–807 (2015).
71. Luo, F. et al. P-block single-metal-site tin/nitrogen-doped carbon fuel cell cathode catalyst for oxygen reduction reaction. *Nat. Mater.* **19**, 1215–1223 (2020).
72. Möller, T. et al. Efficient CO<sub>2</sub> to CO electrolysis on solid Ni–N–C catalysts at industrial current densities. *Energy Environ. Sci.* **12**, 640–647 (2019).
73. Zhang, X. et al. Molecular engineering of dispersed nickel phthalocyanines on carbon nanotubes for selective CO<sub>2</sub> reduction. *Nat. Energy* **5**, 684–692 (2020).
74. Gu, J., Hsu, C. S., Bai, L., Chen, H. M. & Hu, X. Atomically dispersed Fe<sup>3+</sup> sites catalyze efficient CO<sub>2</sub> electroreduction to CO. *Science* **364**, 1091–1094 (2019).

### Acknowledgements

The research leading to these results received funding from the European Union's Horizon 2020 research and innovation program under grant agreement no. 851441,

SELECTCO<sub>2</sub>, and from the VILLUM Centre for the Science of Sustainable Fuels and Chemicals (no. 9455) from VILLUM FONDEN. Research leading to some of these results received funding from the Fuel Cells and Hydrogen 2 Joint Undertaking under grant agreement no. 779366, CRESCENDO. The authors acknowledge computational resource from PRACE (project ID: prpa85) and the Juelich Supercomputing Centre. We thank G. Kastlunger for helpful discussions.

### Author contributions

S.V. and K.C. designed the computational study and wrote the first draft of the paper. S.V. and S.-C.T. performed the DFT calculations and the data analysis. P.S. designed the experiments, and W.J. and S.B. performed them. All the authors contributed to revising the manuscript.

### Competing interests

The authors declare no competing interests.

### Additional information

**Supplementary information** The online version contains supplementary material available at <https://doi.org/10.1038/s41929-021-00705-y>.

**Correspondence and requests for materials** should be addressed to Peter Strasser or Karen Chan.

**Peer review information** *Nature Catalysis* thanks Yang Hou, Hyungjun Kim and the other, anonymous, reviewer(s) for their contribution to the peer review of this work.

**Reprints and permissions information** is available at [www.nature.com/reprints](http://www.nature.com/reprints).

**Publisher's note** Springer Nature remains neutral with regard to jurisdictional claims in published maps and institutional affiliations.

© The Author(s), under exclusive licence to Springer Nature Limited 2021